Application de la BOS3D à l'étude des instationnarités de jets chauds et sous-détendus

Lorenzo Lanzillotta

To cite this version:

Lorenzo Lanzillotta. Application de la BOS3D à l'étude des instationnarités de jets chauds et sous-détendus. Mécanique des fluides [physics.class-ph]. Institut Supérieur de l'Aéronautique et de l'Espace (ISAE-SUPAERO), 2021. Français. ⟨NNT : 2021ESAE0002⟩. ⟨tel-03220875⟩

HAL Id: tel-03220875
https://hal.science/tel-03220875v1

Submitted on 7 May 2021

THÈSE

En vue de l'obtention du

Doctorat de l'Université de Toulouse

Délivré par : *l'Institut Supérieur de l'Aéronautique et de l'Espace (ISAE-SUPAERO)*

Spécialité : *Dynamique des Fluides*

Présentée et soutenue le 13/01/2021 **par :**

Lorenzo LANZILLOTTA

Application de la BOS3D à l'étude des instationnarités de jets chauds et sous-détendus

JURY

Peter JORDAN	Rapporteur
Markus RAFFEL	Rapporteur
Guillaume POLIDORI	Examinateur
Didier SAURY	Examinateur
Pierre MILLAN	Directeur de thèse
Guy LE BESNERAIS	Codirecteur de thèse
Frédéric CHAMPAGNAT	Encadrant
David DONJAT	Encadrant

École doctorale :
ED MEGEP (ED468)
Unité de Recherche :
ONERA/DMPE
Date :
13 January 2021 (version validée par le jury)

Dissertation submitted for the degree of

Doctor at the University of Toulouse

Awarded by: *l'Institut Supérieur de l'Aéronautique et de l'Espace (ISAE-SUPAERO)*

Specialty: *Fluid Dynamics*

Defended on January 13, 2021 by:

Lorenzo LANZILLOTTA

Application de la BOS3D à l'étude des instationnarités de jets chauds et sous-détendus

Date:

January 13, 2021 (version approved by the committee)

To cite this dissertation:

Lorenzo Lanzillotta. Application de la BOS3D à l'étude des instationnarités de jets chauds et sous-détendus. ISAE-SUPAERO, Université de Toulouse, 2021.

BibTEX entry:

```
@phdthesis{lanzillotta2021dissertation,
author={Lanzillotta, Lorenzo},
title={Application de la BOS3D a l'etude des instationnarites
   de jets chauds et sous-detendus},
school={ISAE-SUPAERO, Universit\'{e} de Toulouse},
year={2021},
address={Toulouse, France}
}
```

Application de la BOS3D à l'étude des instationnarités de jets chauds et sous-détendus

by

Lorenzo Lanzillotta

PhD dissertation defended on
January 13, 2021.
ISAE-SUPAERO, Université de Toulouse, France.

Abstract

The work carried out during the PhD is part of the development of metrological instruments for fluid mechanics, particularly in the field of flow visualisation.

Background Oriented Schlieren (BOS) is a technique that is capable of providing instantaneous 3D fields of density or temperature. This is a technique that has been developed at ONERA during the PhDs of V. Todoroff and F. Nicolas and belongs to measurement techniques based on the deviation of light rays through a non-homogeneous optical index medium.

It consists of imaging a textured pattern once without flow and then a second time with the flow between the camera and the background. Variations in the optical index within the flow due to density fluctuations (temperature and/or pressure fluctuations) bend the path of the light rays. An apparent shift in the texture of the background is observed and calculated through digital image correlation techniques such as those commonly used in PIV. By carrying out a simultaneous acquisition from different points of view, it is possible to reconstruct the associated density field by solving a regularised inverse problem.

To further develop the technique, we have studied some technical solutions to improve the spatial resolution without degrading the sensitivity of the measurement. Among the solutions studied are retroreflective backgrounds, telecentric objectives and the use of speckle to generate BOS background.

A first experimental campaign on an under-expanded supersonic jet allowed us to verify the improvements in terms of spatial resolution and to study the screech, an aeroacoustic phenomenon. Through BOS measurements coupled with acoustic measurements, it was possible to reconstruct two specific screech dynamics.

A second campaign was conducted at F2 ONERA wind tunnel on a hot cross-flow jet in cross flow. The problems encountered due to the complex geometry of the jet and the arrangement of the cameras led to synthetic studies to understand which solutions can be used in the future to improve the BOS acquisition.

Keywords: BOS, Density, Schlieren, Speckle, Tomography, Under expanded jet, Screech, Spatial resolution, Retroreflective background, Telecentric lens, POD, Hot cross-flow jet in cross flow, Acoustic measurements.

Contents

List of Figures

List of Tables

Acronyms

ART	Algebraic Reconstruction Technique
BOS	Background Oriented Schlieren
BOSCO	BOS using celestial objects
CCD	Charge-Coupled Device
CFD	Computational Fluid Dynamics
COC	Circle of Confusion
CPU	Central Processing Unit
DOF	Depth of Field
FBP	Filtered Back Projection
GPU	Graphics Processing Unit
IW	Interrogation Window
LDV	Laser Doppler Velocimetry
LED	Light Emitting Diode
NASA	National Aeronautics and Space Administration
Nd:YAG	Neodymium-doped Yttrium Aluminium Garnet
NPR	Nozzle Pressure Ratio
ONERA	Office National d'Etudes et de Recherches Aérospatiales
PIV	Particle Image Velocimetry
POD	Proper Orthogonal Decomposition
PSP	Pressure Sensitive Paint
PTV	Particle Tracking Velocimetry
RANS	Reynolds Averaged Navier-Stokes
SPL	Sound Pressure Level
TSP	Temperature Sensitive Paint

Notation

Greek letters

μ	dynamic viscosity
ν	frequency
ρ	density
ω	angular frequency
Σ	wavefront
ε	light deviation
δ	spatial resolution
λ	regularization parameter

Roman letters

A	wave amplitude
B	magnetic field
E	electric field
v	speed of propagation in a medium
T	period
k_0	wave vector in vacuum
k	wave vector in medium
$\mathbf{u}$	unitary vector
x	spatial coordinate
t	time
c	speed of light in vacuum
n	refractive index
L	optical path
I	luminous intensity
f	focal length
$f_{\#}$	objective f-number
D	lens aperture
l_{pix}	pixel size
M	magnification
l	background-flow distance
m	camera-flow distance
s	flow-speckle generator distance
z	image distance
$L_{tot} = m + l$	camera-background distance

S	sensitivity
h	sensor size
H	size of the test volume
G	Gladstone-Dale constant
d_{out}	exit direction of a light beam
d_{in}	entry direction of a light beam
d_{out}^*	estimated exit direction of a light beam
I_{in}	entry position of a light beam
I_m	middle position
I_{out}	exit position of a light beam
I_{out}^*	estimated exit position of a light beam
$\mathcal{J}$	regularised least-squares criterion
$\mathcal{R}$	regularization term

Operator

A	observation operator
D	differential operator
T	tomographic operator

Introduction

A major role of ONERA is to develop fluid mechanics simulation codes on behalf of large aeronautical companies such as Airbus and Safran. In recent years the tendency of these companies has been to rely on simulation as much as possible to reduce costly and time-consuming experimental wind tunnel campaigns. Yet, experimental results are still required as a reference, and will always be needed to develop new models and validate simulation results.

The mission of the DMPE (Département multi-physique pour l'énergétique) is to deepen the knowledge of the phenomena encountered in fluid mechanics relating to aerodynamics, aerothermics and multiphase flows and to describe them in the form of physical models. This approach contributes to the development of ONERA's major fluid mechanics calculation codes. These major codes are based on the Navier-Stokes equations that are non-linear partial differential equations which describe the movement of Newtonian fluids (ordinary viscous liquids and gases) in the approximation of continuous media.

The exact solution of these non-linear equations is currently not possible due to the limited calculation capacity available. Approximate solutions are then usually sought for practical engineering applications, thus relying on simplified models for turbulent transport of momentum and heat. Such models used in RANS (Reynolds Averaged Navier-Stokes) solvers must be validated, a process that is usually performed relying on experimental data. For this reason, it is of prime importance to provide accurate measurements, and to develop new techniques to extensively describe the considered flow.

Numerous measurement techniques have been developed and used over the years to improve our probing capacity of a flow. Some of these techniques are able to directly measure the physical quantity sought through the use of dedicated sensors. These sensors are generally intrusive, i.e. they are immersed in the flow and can disturb it by modifying its dynamics. They usually provide a local and not global measurement, imposing the need to move the probe in space to have a measurement in multiple points. The most common sensors that fall into this category are: temperature probes, pressure probes, flowmeters, accelerometers, strain gauges, etc.

With new technological advances and in particular with the advent of lasers, computers and CCD sensors, new measurement techniques have been developed to obtain properties that cannot be measured by a sensor or to make measurements less intrusive and more global. In this context, techniques for velocity measurement such as LDV (laser doppler velocimetry)and PIV (particle image velocimetry), for temperature measurement such as infrared thermography and TSP (temperature sensitive paint), for pressure measurement (PSP pressure sensitive paint) and density measurement such as shadowgraph, Schlieren and interferometry have been developed.

All these techniques are local methods or methods that allow to have information in one plan (2D). This implies that it is necessary to scan the flow to know the properties in the full three-dimensional field. This step is long and does not allow the complete characterization of an instantaneous three-dimensional field. The increase in available computational power and the continuous improvement of laser technologies over the past twenty years have allowed to consider nowadays full 3D and time-resolved measurements and thus a better description of turbulence that is 3D by nature and unsteady phenomena. In this line, PIV has undergone a series of evolutions that have made it possible to perform time-resolved measurements (TR-PIV) and to extend the measurement to the third dimension of space (TOMO-PIV). Today, PIV and PTV (Particle Tracking Velocimetry) allow to study complex phenomena in laboratory providing 3D velocity fields and, in some cases, also pressure fields. However, 3D information is limited to volumes of a few cm^3 because a large amount of light energy is required.

BOS is a measurement technique that has benefited from this context and that is capable of providing instantaneous 3D fields of density or temperature. It belongs to measurement techniques based on the deviation of light rays through a non-homogeneous optical index medium. Among these we find the shadowgraph, Schlieren and interferometry techniques that allow to reveal invisible phenomena by showing internal density gradients in air flows. These techniques have been used extensively in aerodynamics to study different types of flows and they are attractive since they do not disturb the flow in any way and do not require seeding.

Interferometry provides a quantitative measurement, but remains rather difficult to implement because it requires the use of an optical table and high quality optical elements. While the shadowgraph is limited to the visualization of intense phenomena (shock waves), the sensitivity of the Schlieren technique can be adjusted by moving the knife blade and therefore it is suitable for flow visualisation of several dynamics. Although shadowgraph and Schlieren are easier to setup than interferometry, it is difficult to perform quantitative measurements: difficult calibrations either using a grey scale or a colour filter are needed. Moreover, Schlieren can only measure one optical index gradient at a time, depending on the orientation of the knife blade.

The BOS technique is comparatively younger since it has been introduced at the beginning of the 21^{st} century. It is usually considered as the result of the work of Dalziel et al. (2000) and Raffel et al. (2000a) who presented for the first time a measurement technique very similar to classical Schlieren but with a simplified experimental setup. It consists of imaging a textured pattern once without flow and then a second time with the flow between the camera and the background. Variations in the optical index within the flow due to density fluctuations (temperature and/or pressure fluctuations) bend the path of the light rays. An apparent shift in the texture of the background is observed. The displacement between the reference image and the image acquired in the presence of the flow is calculated through digital image correlation techniques such as those commonly used in PIV. Knowing the geometry of the measurement system, one can deduce from these displacement fields quantitative information on the density gradients of the flow. BOS is an integral measurement technique, i.e. the measured displacement is proportional to the integral of the density gradient along the light ray. To determine the density field there are several solutions: either the flow has a particular symmetry and its value can be determined from a unique projection, or a tomographic reconstruction has to be carried out from projections taken with various point of views. In this case, the symmetry or stationary hypotheses make it possible to work with a single camera recording different images in succession. In order to reconstruct instantaneous flows, it is necessary to use a multi-camera system to capture images from many points of view at the same time. Ihrke (2008) and Atcheson et al. (2008), thanks to their 16-camera system, they were able to reconstruct convective flows in 3D.

3D BOS has been developed at ONERA during the PhDs of Todoroff (2013) and Nicolas (2017). During Violaine Todoroff's PhD, the 3D BOS technique was developed with the aim of measuring instantaneous density fields. This initial work led to the construction of a 12 camera 3D BOS system and consistent reconstructions of aerothermal flows. During François Nicolas' thesis, the 3D BOS was employed in ONERA's largest wind tunnels to improve its use in these environments rich in constraints such as vibrations and complex geometries to be respected.

Objectives

The work presented in this dissertation is part of the further development of 3D BOS at ONERA. Our objective is to improve the spatial resolution without degrading the sensitivity of the measurement.

The approach consisted initially in carrying out a state of the art study of density measurement methods and more particularly of 3D BOS. Principles of optics are recalled in the first place and the measurement techniques based on the deviation of light rays are then presented. A section is dedicated to exposing the basic equations of sensitivity, resolution and depth of field. Afterwards are presented different variants of the BOS technique that use different backgrounds, light sources and the different types of lenses to try to improve the BOS measurement. Finally, the development of the BOS technique at ONERA is presented in details.

The second chapter is dedicated to the study of methods to improve the spatial resolution of the BOS technique. The effects of the resolution on the measurement are first recalled and three solutions to improve the resolution are presented with their pros and cons. Among these were tested reflective backgrounds, telecentric lens and a series of setups using a speckle pattern as a background for BOS.

Subsequently, the reflective backgrounds proved to be very efficient in improving the resolution of the measurement and therefore an initial experience was carried out to test these backgrounds on a underexpanded supersonic jet. The third chapter is dedicated to the results obtained through the study of underexpanded supersonic jets featuring a global instability known as the screech phenomenon for the loud acoustic tone it generates. 3DBOS acquisitions are performed together with near-field acoustic measurements in order to investigate screech phenomena through their 3D features.

Reflective backgrounds were later used in a large wind tunnel to study a hot jet in cross-flow in the presence of a flat plate. After a bibliographic study on jet in cross-flow and a section dedicated to the description of the conditions of the experiment, the 2D and 3D BOS setups are described. In order to better describe the flow, other measurements were made in parallel with the BOS: LDV, PIV and thermocouple measurements. Subsequently are presented the results obtained with 2D BOS and the study of the best configuration that can be used with 3D BOS. As the experimental configuration revealed not suitable for precise 3D reconstructions, a series of density reconstructions from real data and a CFD simulation were performed. Finally, we provide perspectives and some possible suggestions and improvements for future experiences in the presence of a flow with similar experimental constraints.

Chapter 1

State of the art

Contents

In this chapter dedicated to the state of the art, the principles of optics necessary for the understanding of the following sections are recalled in the first place.
The second section presents the measurement techniques based on the deviation of light rays, including holography, shadowgraph, Schlieren and background oriented schlieren (BOS), the technique that is the object of this doctorate's study.
Next section discusses the mounting features, including sensitivity, resolution and depth of field, that are investigated in the following chapters.
The fourth section is dedicated to the different variants of the BOS technique that use different backgrounds to try to improve the BOS measurement.
Afterwards, the light sources and the different types of lenses used in the BOS are presented.
Finally, in section 1.7, the development of the BOS technique at ONERA is presented in detail.
The experimental and algorithm choices were made to have a measurement technique capable of reconstructing instantaneous 3D density fields.

1.1 Notions of optics

1.1.1 Characteristics of light wave

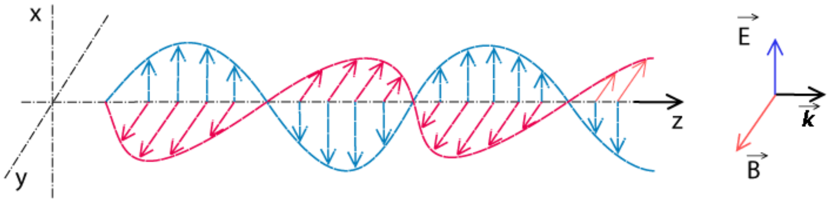

Figure 1.1. Electromagnetic wave: the electric field and the magnetic field perpendicular to each other and to the direction of motion. (Byjus ©)

Optics is made up of all phenomena that are perceived by the eye. Light was studied very early in the history of science and geometric and wavelike optics have been known for over two hundred years. In 1876 Maxwell concluded that light is an electromagnetic wave that vibrates at a frequency oscillating around $5{\times}10^{14}$Hz and that it propagates at a speed in vacuum of about $3{\times}10^{8}$ m/s. He also states that light is a transversal wave: the vectorial quantities that characterize it (the electric field $\mathbf{E}$ and the magnetic field $\mathbf{B}$) are perpendicular to the direction of propagation (figure 1.1). All waves can be seen as the superposition of ideal waves called monochromatic or sinusoidal waves of the form:

$$A\cos\omega\left[\left(t-\frac{x}{v}\right)\right] \tag{1.1}$$

where A is the amplitude, ω the angular frequency and v the speed of propagation of the wave in an isotropic medium. The other necessary quantities that characterize a wave are:

- The frequency: $\nu = \omega/2\pi$
- The period: $T = \nu^{-1}$
- The wavelength in vacuum and in medium: $\lambda_0 = c/\nu$ and $\lambda = v/\nu$
- The wave vector in vacuum and in medium: $\mathbf{k}_0 = (2\pi/\lambda_0\mathbf{u})$ and $\mathbf{k} = (2\pi/\lambda\mathbf{u})$ where $\mathbf{u}$ is the unitary vector defined by the direction of propagation.

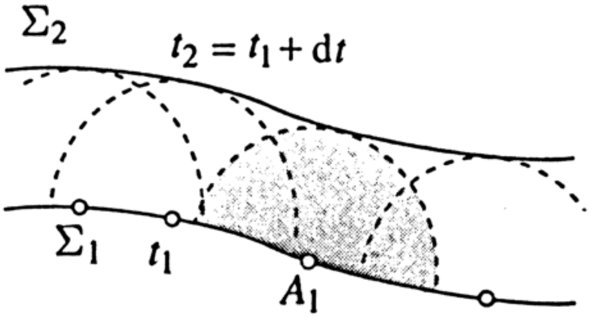

Figure 1.2. Wavefront propagation on the principle of Huygens (Pérez 2000).

1.1.2 Huygens' principle

The principle of Huygens is the basis of the wave theory of light. Remembering that a wave is a physical phenomenon characterized by a quantity that depends on time t and where x is the spatial coordinate and assuming that the propagation medium of the wave is isotropic, i.e. that the propagation speed is constant in all directions, the statement of the principle states: *every point of an advancing wave front is a new center of disturbance from which emanates independent wavelets whose envelope constitutes a new wave front at each successive stage of the process.*

What follows is that if the wavefront is flat, the wave is flat; if it is spherical, the wave is spherical. To construct the wave at time $t_2 = t_1 + dt$, as shown in the figure 1.2, it is necessary to start from the wavefront Σ_1 at the instant t_1 and draw for each point of it a sphere centred on the wavefront of origin and with a radius equal to the duration of propagation of the light wave dt. By calling ds the distance travelled by the wave in time dt, we can write the relation linking time to the speed of propagation of the wave: $dt = ds/v$.

1.1.3 The refractive index

The refractive index, by definition, is the ratio between the speed of light in vacuum c and the speed of light in the medium considered v.

$$n = \frac{c}{v} \tag{1.2}$$

It is therefore a dimensionless number that describes how quickly light propagates in a given medium. The refractive index is therefore higher than the unit (except for metamaterials) and also strongly depends on the state of the matter. For the gaseous state the refractive index is very close to the unit (air $n = 1.000293$), for water $n = 1.333$ and in solids it ranges over different values (n=1.31 in ice, $n = 1.52$ in glass and it reaches n=2.42 in diamond). After introducing the refractive index, we can write the time t, which allows to define the the wavefront Σ_2 starting from Σ_1 on figure 1.2:

$$dt = \frac{ds}{v} = \frac{nds}{c} \tag{1.3}$$

In the case of finite propagation between two points A and B, the corresponding optical path is given by the integral:

$$L = \int_{t_A}^{t_B} cdt = \int_A^B nds = c(t_B - t_A) \tag{1.4}$$

This curvilinear integral must be calculated along the direction of wave propagation which, at any point, is normal at the wavefront in an isotropic medium. The optical path is therefore the distance travelled by the light in vacuum during the propagation time in the medium considered.

1.1.4 The principle of least time

In 1657, Pierre de Fermat enunciated the following principle that bears his name: *light travels through the path in which it can reach the destination in least time.*

This principle can be seen by using the notion of optical path, which is a different way to evaluate the duration of the path, and therefore we speak of stationarity of the optical path ($dL = 0$).

The main consequences of this theorem are two: a rectilinear propagation of light in a homogeneous medium and the reversibility of the light path. In a homogeneous medium (constant refractive index), the light propagates in a straight line:

$$L = \int_{AB} nds = n\widehat{AB} \tag{1.5}$$

The optical path L is minimal when the distance $\widehat{AB}$ corresponds to the straight line between these two points. For most optical needs, the assumption of homogeneous or piecewise homogeneous media can be used; the light rays are then presented as broken lines.

Bearing in mind a non-homogeneous medium, a ray of light will be curvilinear and the optical path passing through points A and B can be written as:

$$L(AB) = \int_{AB} nds = \int_{BA} n(-ds) \tag{1.6}$$

where $-ds$ coincides with the curvilinear element from B to A, consequently $L(AB) = L(BA)$. It can therefore be said that the path of light does not depend on the direction of travel.

1.1.5 Fundamental equation of geometric optics and law of Snell-Descartes

This paragraph introduces the main equations that describe the behaviour of light in a non-homogeneous medium, i.e. with refractive index variations.

Taking into consideration two wavefronts Σ_0 and Σ (figure 1.3), consisting of the set of points of the same light perturbation at moments t_0 and $t_0 + \tau$, the optical path is calculated along a curved light beam RL that passes through points A_0 of Σ_0 and A of Σ:

$$L = \int_{A_0}^{A} nds \tag{1.7}$$

By fixing point A_0 and leaving point A mobile, then the optical path calculated depends only on $\mathbf{r}$ since the RL curve is the path taken by the light.

$$\int_{\mathbf{r_0}}^{\mathbf{r}} nds = L(\mathbf{r}) \quad \text{and} \quad dL = \mathbf{grad} L \cdot d\mathbf{r}$$

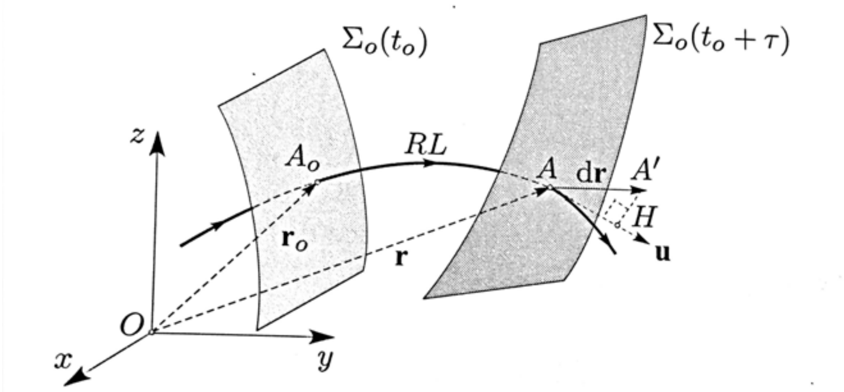

Figure 1.3. Trajectory of a ray of light between two wavefronts (Pérez 2000).

this elementary variation can also be written as:

$$dL = nds = nAH = n(d\mathbf{r}\cdot\mathbf{u})$$

where **u** is the unitary vector defined by the direction of propagation. Therefore:

$$nd\mathbf{r}\cdot\mathbf{u} = \mathbf{grad}L\cdot d\mathbf{r}$$

since $d\mathbf{r}$ is arbitrary:

$$n\mathbf{u} = \mathbf{grad}L \quad \text{and} \quad n = |\mathbf{grad}L| \tag{1.8}$$

The result is the Eikonal equation. It binds the refractive index of the medium to the norm of the gradient of the optical path.

Figure 1.4. Heat haze: the heat produced by F1 engines is distorting the image captured by the camera. (Darren Heath ©)

Through a differential variation of the vector ($n\mathbf{u}$) in function of the curvilinear abscissa s, it is possible to demonstrate that this last equation can be written in the form of a differential equation such that:

$$\frac{d(n\mathbf{u})}{ds} = \mathbf{grad}n \tag{1.9}$$

This equation is considered the fundamental equation of geometric optics and equivalent to the Fermat principle. It respects the rectilinear propagation of light in the presence of a homogeneous medium ($\mathbf{grad}n = 0$). On the contrary, if the light encounters a change in the refractive index, the light beam will be bended in the direction of the gradient. It is possible to see with the naked eye this phenomenon in the presence of strong gradients as in the case of the heat produced by F1 engines that distorts the image captured by the camera (figure 1.4). The equation can be used to explain certain phenomena such as mirages, atmospheric aberrations or the light behaviour through lenses and optical fibres.

1.1.6 Gladstone-Dale relation

As we have seen in the previous paragraph, the Eikonal equation describes how light rays deviate in a medium as the refractive index varies.

Considering that this thesis develops in the field of aerodynamics, the medium that interests us most is air. Gladstone Dale's relation provides for a gas a link between the refractive index and the density as follows:

$$n - 1 = G\rho \tag{1.10}$$

where G is the Gladstone-Dale constant which depends mainly on the characteristics of the gas and to a lesser extent on the wavelength of the light passing through it. The value used for air at ambient pressure and temperature ($P = 1\text{atm}$ and $T = 20°\text{C}$) is $0.23 \times 10^3 \text{m}^3/\text{kg}$.

By joining the Eikonal and Gladstone-Dale relations, and measuring in some way the deviations of light in the medium, it is therefore possible to determine the density gradient of the air. However, it must be taken into account that it is necessary to work in such conditions that the Gladstone-Dale constant remains constant (without modification of the gas components).

We must also keep in mind that for a real case the variations of the refractive index are very small. If the index is calculated for two density values $\rho_1 = 1.205\text{kg/m}^3$ and $\rho_2 = 0.457\text{kg/m}^3$, corresponding to temperatures $T_1 = 20°\text{C}$ and $T_2 = 500°\text{C}$, a $\Delta n = 1.72 \times 10^{-4}$ is obtained, corresponding to a variation of $1.72 \times 10^{-2}\%$. These values seem to be extremely small but are not negligible: the techniques for measuring these values must be very sensitive and precise.

1.2 Measurement techniques based on the deviation of light rays

In the measurement techniques used based on the deviation of light rays, we find interferometry, shadowgraph, Schlieren, speckle photography and Background Oriented Schlieren. For all these techniques the object of interest is between a light source and an observation plane (figure 1.5). The deviations of the light rays induced by the density gradients cause displacements that occur on the observation plane. These displacements depend not only on the deviations induced by the object under study but also on the characteristic distances of the installation.

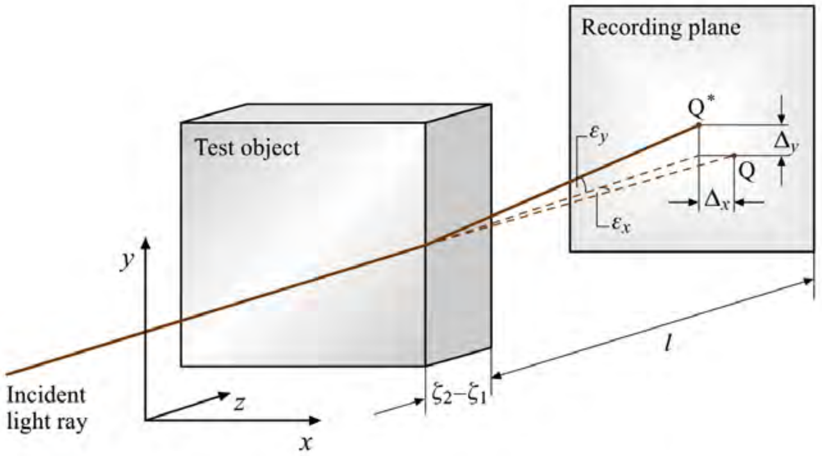

Figure 1.5. Trajectory of a light ray within an inhomogeneous index volume (Tropea et al. 2006).

Considering a volume V of non-homogeneous refractive index, and integrating the fundamental equation of geometric optics (equations 1.9) between the point of entry and exit, it is found the following expression:

$$\boldsymbol{\varepsilon} = \mathbf{d_{out}} - \mathbf{d_{in}} = \frac{1}{n_{ext}} \int_{s_{out}}^{s_{in}} \nabla n(\mathbf{x}(s))ds \tag{1.11}$$

where $\mathbf{d_{out}}$ and $\mathbf{d_{in}}$ are respectively the exit and entry directions in the volume of interest. Using the relationship of Gladstone-Dale (Eq 1.10) in the light deviation equation (Eq 1.11):

$$\boldsymbol{\varepsilon} = \frac{G}{n_{ext}} \int_{s_{out}}^{s_{in}} \nabla \boldsymbol{\rho}(\mathbf{x}(s))ds \tag{1.12}$$

The deviation vector can be decomposed into the three Cartesian components ($\boldsymbol{\varepsilon}_\mathbf{x}$, $\boldsymbol{\varepsilon}_\mathbf{y}$ and $\boldsymbol{\varepsilon}_\mathbf{z}$).

These measurement methods have in common the fact that they are integral: the result on the observation plane is the result of an integration, and therefore of a sum, along each individual optical path. As result, we obtain a 2D image of a three-dimensional phenomenon. Consequently, to obtain spatially resolved 3D information within the volume of interest it is necessary to use several 2D fields captured at different angles of view, except in specific axi-symmetric configurations.

As explained in more detail below, techniques for flow visualisation exploit in different ways the deviation of light induced by the density gradients.

1.2.1 Interferometry

Interferometry is the measurement technique that estimates a phase change of the light wave that passes through the flow.

To create an interferogram, the visible signal pattern obtained with this technique (figure 1.7 and 1.9), it is necessary to make two light waves interact, making sure that at least one of them crosses the flow. This feature makes it possible to have two different types of interferometers: differential or Schlieren interferometry and interferometry with one reference beam.

In the first case, both light waves pass through the flow (figure 1.6), but spaced by a certain distance d, they then combine in the interferometer and generate the interferogram. A Wollaston

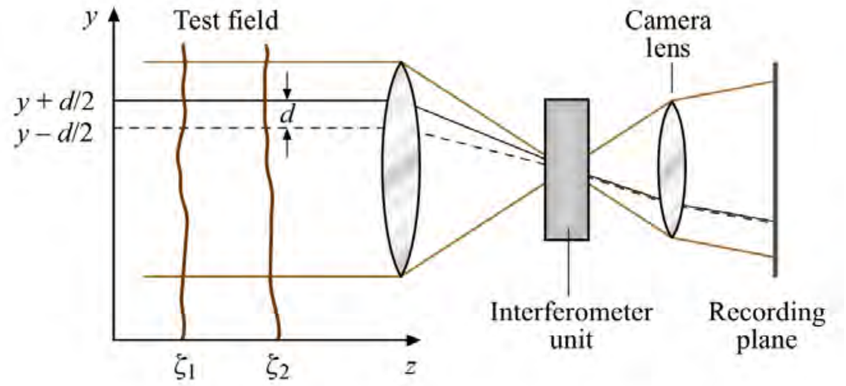

Figure 1.6. Scheme of a differential interferometer (Tropea et al. 2006).

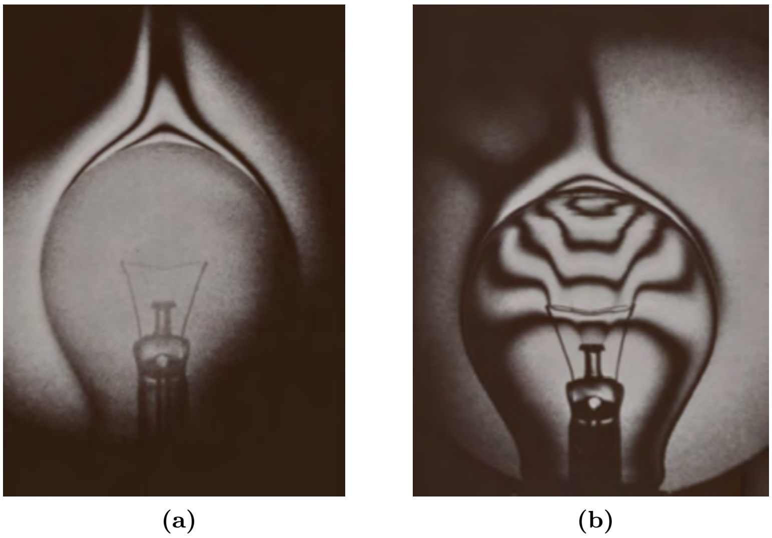

(a) **(b)**

Figure 1.7. (a): Mach-Zehnder interferogram visualising the plume rising from a light bulb. (b): Holographic interferogram allows to compensate the disturbances caused by the bulb glass and to visualize the temperature field inside the bulb. (Tropea et al. 2006)

prism is usually used in differential interferometry and allows separating the light into two separate polarized beams with orthogonal polarization. This technique is the central topic of the recent PhD of Olchewsky (2017) conducted at ONERA.

Instead, the other type of interferometry can be traced back to Mach-Zehnder's interferometer, where the light wave is divided through a beam splitter creating two beams (figure 1.8): the first passes through the test object and the other serves as a reference. The two light beams are then recombined to generate the interferogram. This setup requires optical devices of great size, high quality, difficult to handle and is highly sensitive to vibration. The invention of holography has greatly facilitated the use of this interferometer by giving birth to holographic interferometry. With holography it is possible to record the information of two light waves on the same holographic plate. With holographic interferometry two consecutive holographic exposures are acquired: the first without the flow and the second with the object of interest. In this process the first exposure acts as a reference while the second one contains the flow information. The difficulties encountered with the completion of a Mach-Zehnder interferometer are eliminated thanks to the holographic interferometer (figure 1.7). As shown in figure 1.7, with holographic

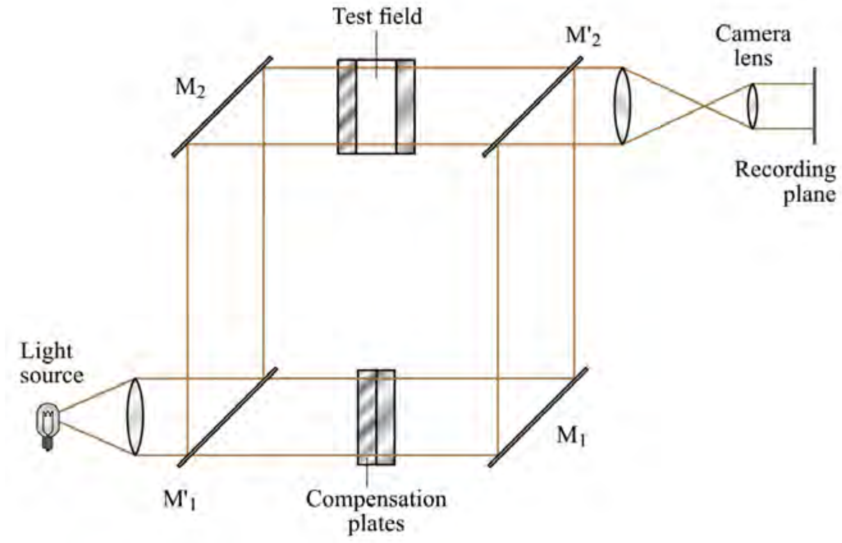

Figure 1.8. Mach-Zehnder's interferometer setup (Tropea et al. 2006).

interferogram it is possible to visualize the temperature inside the bulb, which is not possible with a Mach-Zehnder interferogram.

It is possible to determine from a quantitative point of view the information related to the refractive index (and thus calculate the density thanks to the Gladstone-Dale relationship) through the study of the distance between the fringe S and their shift ΔS.

For reference interferometer the signal is directly proportional to the refractive index in the direction perpendicular to the fringes:

$$\frac{\Delta S(x,y)}{S} = \frac{1}{\lambda}\int_{\zeta_1}^{\zeta_2} n(x,y,z)dz - const \tag{1.13}$$

This setup avoids the passage of the integration that is necessary in differential interferometer: in this configuration the signal is proportional to the gradient of the index, hence is very suitable for the study of thermal flows (figure 1.9):

$$\frac{\Delta S(x,y)}{S} = \frac{d}{\lambda}\int_{\zeta_1}^{\zeta_2} \frac{\partial}{\partial y} n(x,y,z)dz - const \tag{1.14}$$

In recent decades, much progress has been made through digital image processing. Thanks to digital phase-stepping interferometry, a combination of holographic interferometry and computer-based signal evaluation, it is possible to retrieve information between two interference fringes not through an interpolation but through a physical process. In this way the sensitivity is greatly improved and the resolution of digital phase stepping is estimated to be between a hundredth and a millionth of a wavelength.

Improvements in these techniques are generally associated with the use of different wavelengths for the light beams, resulting in colour interferograms. On this subject it is worth remembering the studies conducted at ONERA by J. Desse (2002), J. Desse and Tribillon (2009) and Olchewsky et al. (2019).

Interferometry is a method particularly suitable for the study of axisimmetric or two-dimensional phenomena. It has a great sensitivity that is able to capture the smallest variations in density and the treatment of results does not require steps of integration. The weak points of this technique are certainly the difficulty of implementing a complex optical setup with high costs and limiting in terms of size. Nevertheless, Olchewsky and Desse have implemented a multi-viewpoints interferometry technique for the reconstruction of no-axi-symmetric phenomena (Olchewsky et al. 2018a). The analysis of fringes is also complicated.

Figure 1.9. Mach-Zehnder interferogram of Bénard convection: fringes enclose zones with constant temperature (Tropea et al. 2006).

1.2.2 Shadowgraph

Shadowgraph, in its simplest form, does not require any kind of optical device and can be observed in different situations outside of a laboratory. An example is the shadow produced by petrol vapours when refuelling the car on a sunny day.

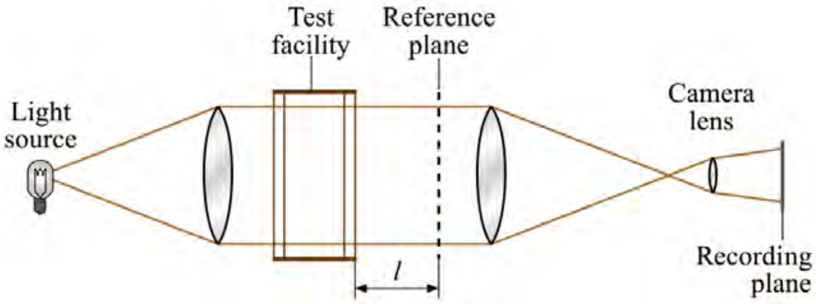

Figure 1.10. Shadowgraph configuration with parallel beams through the test section (Tropea et al. 2006).

This technique requires a light source and a plane, possibly flat, where to observe the shadow generated. With the use of a camera the assembly is slightly complicated: the plane of the sensor is focused through camera lens in a plane that is at a distance l from the object. In this way it is possible to obtain some sensitivity but the object is blurred in the shadowgraph. The more advanced shadowgraph setups use parallel rays through the test facility (figure 1.10).

The light rays that pass through the object of study are refracted and bent according to the fundamental equation of geometric optics. What results is that the light intensity in an observation plane is no longer uniform but altered.

Through the study of the luminous intensity I and its variation, it is possible to go back to the refractive index according to the following equation (written in the approximation of small deviations):

$$\frac{\Delta I(x,y)}{I} = l \int_{\zeta_1}^{\zeta_2} \left(\frac{\partial^2 n}{\partial x^2} + \frac{\partial^2 n}{\partial y^2} \right) dz \tag{1.15}$$

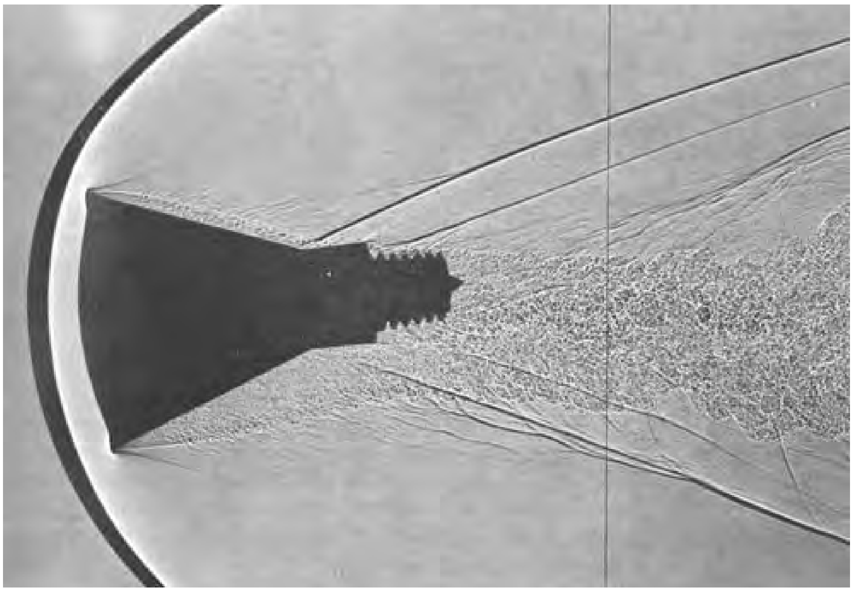

Figure 1.11. A shadowgraph of the Project Mercury reentry capsule, showing the bow-shock wave in front of it and the flow fields behind the capsule (NASA 1959).

where I is the light intensity, l the distance between the test object and the focusing plane.

The equation shows that shadowgraphy is sensitive to changes of the second derivative of the density. What follows is that this measurement technique is not suitable for a quantitative evaluation of density, since its evaluation requires a double integration that would lead to significant errors. Despite this inconvenient and with its ease of realization, the shadowgraphy is used for quick survey of flow fields. Another use is to validate the results obtained through numerical simulations: by inserting the computed density distribution in the shadowgraphy equation, it is obtained digitally a shadowgraph that is compared to the one obtained in an experimental way. However, one must be very careful because small deviations of the two patterns can produce large differences in the distribution of density (density related to the second derivative of the refractive index). For this reason, shadowgraphy remains particularly suitable for visualising shock waves, studying stationary supersonic flows or unsteady configurations within shock tubes (figure 1.11).

Shadowgraph has a very simple optical mounting, but its sensitivity is very low. Being sensitive to the second derivative of the density, it is impossible to use it for quantitative measurements.

1.2.3 Schlieren

The term “schliere”, that comes from German, refers to local optical inhomogeneities in transparent media. As stated by Schardin (1942) and G. Settles (2001), the Schlieren technique is used for the first time by Toepler to visualize density inhomogeneities in a flow.

The system consists of a light source, a system of lenses that allow to have light rays parallel through the test object, a knife edge positioned where the image of the light source is formed and finally a recording plane (figure 1.12). The camera lens focuses the test object on the camera sensor. Thus, the flow is in focus, and the formation of shadow effects is avoided.

When a flow is introduced into the test section, the initially parallel light beams are deflected. The rays that are deflected upwards are able to pass over the knife edge and arrive on the screen illuminating it. On the contrary all the rays that are deflected downwards are ‘captured’ by the knife edge and therefore the result is a darker area on the screen.

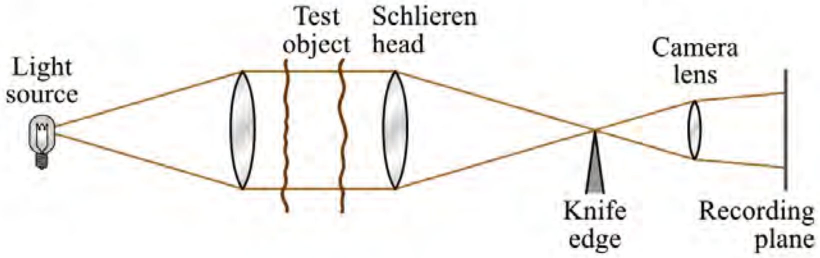

Figure 1.12. Schlieren setup with parallel beams through the test section (Tropea et al. 2006).

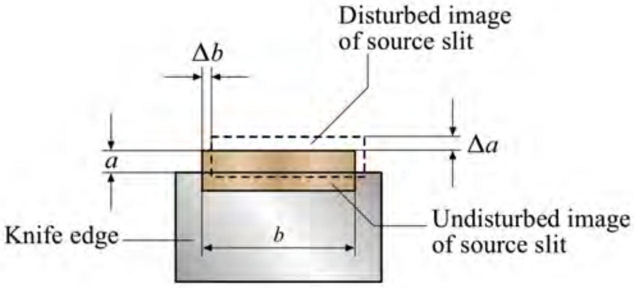

Figure 1.13. Knife edge and image of the light source placed in the focal plane of the schlieren head (Tropea et al. 2006).

The light intensity on the recording plane can be controlled by adjusting the knife edge (figure 1.13) by changing the distance parameter a. Under the assumption of small angles of deflection, the following equation can be written:

$$\frac{\Delta I(x,y)}{I} = \frac{f_2}{a}\int_{\zeta_1}^{\zeta_2} \frac{1}{n}\frac{\partial n}{\partial y} dz \tag{1.16}$$

where f_2 is the focal length of the Schlieren head.

As well as in previous techniques, the integration of information takes place along the trajectories of the light in the test section, from ζ_1 to ζ_2. In case the medium is a gas, the refractive index is equal to unity and by introducing the Gladstone-Dale constant the equation can be written as:

$$\frac{\Delta I(x,y)}{I} = \frac{G f_2}{a}\int_{\zeta_1}^{\zeta_2} \frac{\partial \rho}{\partial y} dz \tag{1.17}$$

This equation shows that the Schlieren method is sensitive to changes of the density derivative normal to the knife edge ($\partial\rho/\partial y$, because the knife edge is assumed to extend in the x direction). By turning by 90° the knife edge, the component $\partial\rho/\partial x$ is measured.

The sensitivity of this device is controlled by adjusting the knife edge. If the knife edge is very far from the axis, few light rays will be cut off and therefore the technique is similar to shadowgraph. If instead the knife edge is approached at the focal point, the smallest deviations are captured (figure 1.14).

With this device it is impossible to distinguish a strongly deviated beam from a barely deviated one, the two beams illuminate the screen in the same way. For this reason, over time, different modifications in the optical mount have been proposed, which have also allowed a

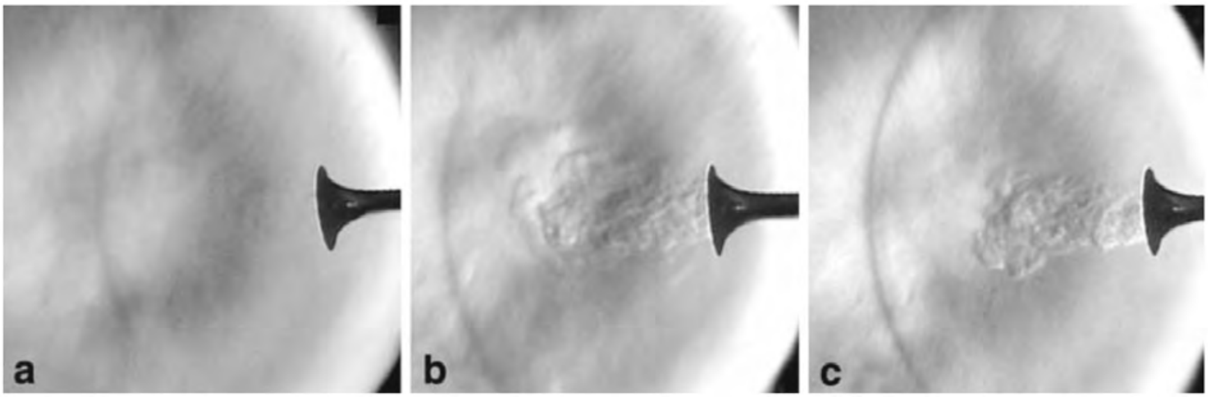

Figure 1.14. Schlieren images of shock waves observed while playing trumpet notes. a) Mezzo-forte high G. b) fortissimo middle C. c) fortissimo high G. The performer's turbulent breath is also seen emerging from the instrument (M. J. Hargather et al. 2010).

quantitative evaluation of the density. The most interesting one is the rainbow schlieren (figure 1.15): the knife is replaced by a transparent coloured filter: besides obtaining colour images, knowing the colour map of the filter it is possible to determine the deviations produced by the density perturbations.

Figure 1.15. Rainbow schlieren of acetylene torch operating unstably (Howes 1983).

Since Schlieren is a line-of-sight technique, information on $\partial\rho/\partial x$ and $\partial\rho/\partial y$ can only be obtained for a 2D object with $\rho = \rho(x, y)$. For a 3D reconstruction it is necessary to apply the techniques of optical tomography.

Schlieren is a technique with a great and adjustable sensitivity. Optical assembly is not very complicated, but large mirrors are necessary to obtain large fields of view. It is a more qualitative method even if there are some quantitative results.

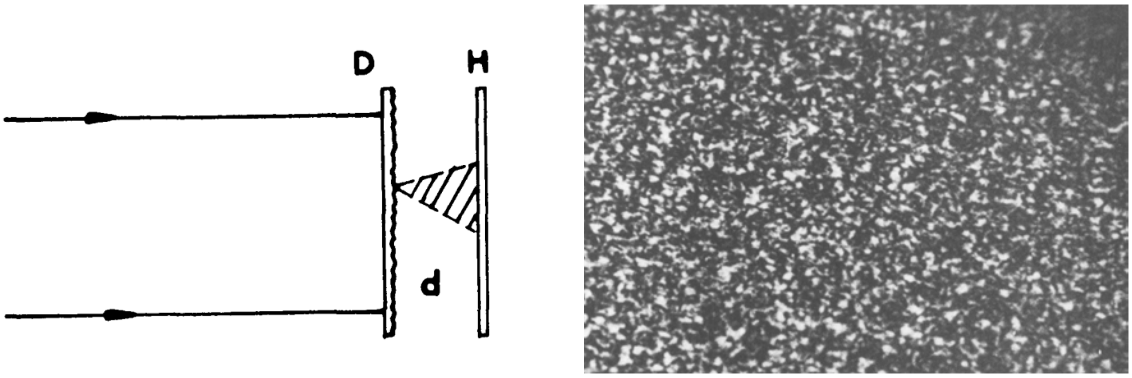

(a) (b)

Figure 1.16. a) Principle of speckle photography system proposed by (Debrus et al. 1972). D ground glass; H photographic plate; d the separation between D and H. b) Speckle pattern from ground glass plate (Sivasubramanian et al. 1984).

1.2.4 Laser Speckle Photography

The first article appeared in 1972 with Debrus et al. (1972). At the time there were no digital camera and all was analogic, the processes were longer and difficult with several steps where it was possible to make mistakes. However Debrus proposed a quite innovative method that simplified the previous methods that employed a large number of optical components. A photographic plate is used and two successive exposures are made on it: one without a transparent object and another with transparent object. After the exposures the photographic plate is examined with analogical methods in order to compute the displacements between the two different exposures. The experiment setup consists in a ground glass illuminated by a parallel beam of coherent light and a photographic plate H is placed behind it at a small distance *d* (figure 1.16a). The ground glass serves as the speckle-generating element, where speckle is a micro scale reference pattern of random geometry and is created when coherent light illuminates a suitably roughed screen (figure 1.16).

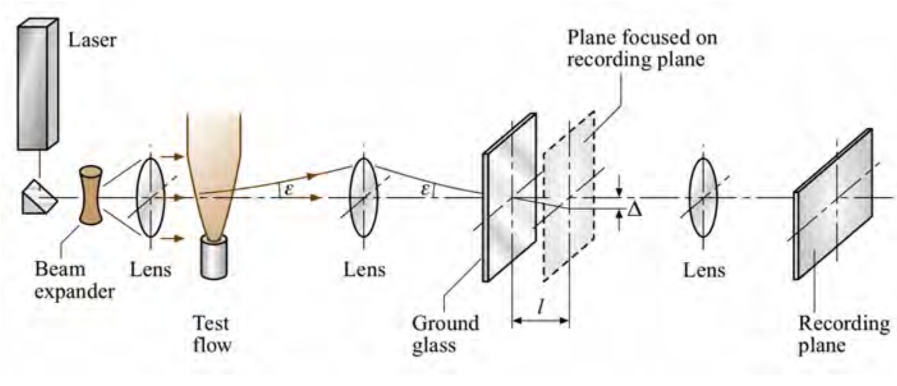

Figure 1.17. Setup for deflection mapping proposed by (Wernekinck and Merzkirch 1987).

Wernekinck and Merzkirch (1987) proposed an other set up (figure 1.17): the light from a laser source, a pulsed ruby laser, is expanded and passes as a parallel beam through the test field. A lens focuses a plane of the test field onto the ground glass plate. A second imaging lens focuses a plane at distance l from the ground glass onto the photographic plate. As usual, two exposures are taken: a reference exposure in the absence of the test field, and a second exposure with the test object in place. Due to the imaging of the test object on the ground glass, a light ray, deflected by an angle in the test field, will arrive at the ground glass at the same point where the corresponding, undisturbed ray of the reference exposure has arrived. However, the two rays form an angle between each other if a 1:1 imaging ratio is chosen. In the plane at distance l from the ground glass, the two rays are separated by $\Delta = \varepsilon \cdot l$. At the same time, Δ is the displacement of the respective speckles recorded in the double exposure, and Δ was determined with the point-by-point reconstruction technique via an evaluation of the respective systems of Young's fringes.

In recent years, first Fomin et al. (2006) and then Ko et al. (2011), have demonstrated the feasibility of a tomographic reconstruction. Furthermore, the analysis of the two images acquired with this technique are processed digitally through software such as those used for the particle image velocimetry.

Laser speckle photography aim to provide quantitative information about the light deflection in the test field. The optical setup is not complicated to adjust and is less sensitive to disturbances. With the advent of computers and image processing the evaluation of deviations is straightforward. However, the size of the test object remains limited, the sensitivity is reduced compared to Schlieren and the optical setup is a bit complex.

1.2.5 Background Oriented Schlieren

The first descriptions of the principle and application of background oriented schlieren appeared in publications from 2000 (Dalziel et al. (2000), Raffel et al. (2000a) and Raffel et al. (2000b)). In 2002 the background oriented schlieren was patented by G. Meier (2002). This relatively late appearance is linked to the fact that, as detailed below, BOS is closely linked to the required image processing which is impossible without modern computers.

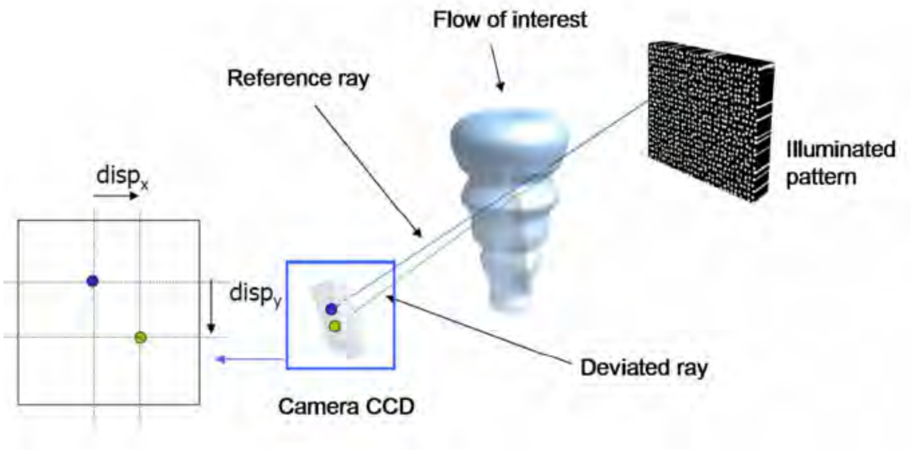

Figure 1.18. BOS set up. When a flow is introduced, motions of the background patterns can be observed on the CCD camera.

Over the years several different solutions, applications and different set up were proposed in order to develop and improve the techniques. Raffel (2015) has brought together and explained several contributions about BOS offered by the scientific community since 2000.

The BOS, compared to the techniques presented above, is a very simple technique from the point of view of the installation required. It is furthermore possible to obtain a quantitative information of the test object.

The setup consists of a structured background and a camera to capture an image. An example of its simplicity is demonstrated by the possibility of using a simple smartphone to capture images (G. S. Settles 2018). The camera, focused on the background, records an image with the flow and another without. When the test object is added, the light reflected from the background is diverted and impacts the camera sensor on a different pixel than the previous one in a $x + \Delta x$ position. Random patterns are indeed used even if they can be less efficient than non random ones; this choice is explained in detail in section 1.4. At this point the movements induced on the sensor are calculated with an image processing software (section 1.7.5), which can be the same as those used for the processing of the Particle Image Velocimetry data. The BOS then measures the displacements (Δx and Δy) that occur on the camera sensor, which are the result of light deviations induced by a flow. In terms of sensitivity the BOS technique is limited and more similar to shadowgraph than to Schlieren: for this reason are studied phenomena where the index gradients are more important.

BOS is a relatively simple measurement technique and there are no restrictions in terms of the size of the test object. Full-scale physical phenomena have been studied even outside the laboratories (shock waves in flying planes (section 1.4.7 figure 1.30), vortex formation from blade tips of helicopter (section 1.4.3 (Raffel et al. 2014))), but also thermal convection (M. Hargather and G. Settles 2010a), flows around wings (Klinge et al. 2003), under-expanded jets (Goldhahn and Seume 2007), (Barthe 2006) and (Iffa et al. 2011), supersonic flows (Venkatakrishnan and Suriyanarayanan 2009), (Ota and Maeno 2008), (Elsinga et al. 2004) and (Leopold et al. 2013), flows around turbine blades (Loose et al. 2000) etc. As explained in section 1.3.2, the resolution is lower than the previous techniques and it is complicated to have high sensitivities. The reduced spatial resolution of the measurement is related to the fact that the camera lens focuses on the background rather than on the volume under study; therefore in the presence of an object in the volume of interest, this not only remains out of focus but partly hides the background itself.

1.2.6 From 2D measure to 3D reconstruction

The measurement techniques presented above provide information integrated into the measurement volume, which is why certain assumptions have to be made to obtain a density field. Excluding a two-dimensional flow (where the thickness is negligible), in order to obtain a 3D density field it is therefore necessary to go for a 3D reconstruction.

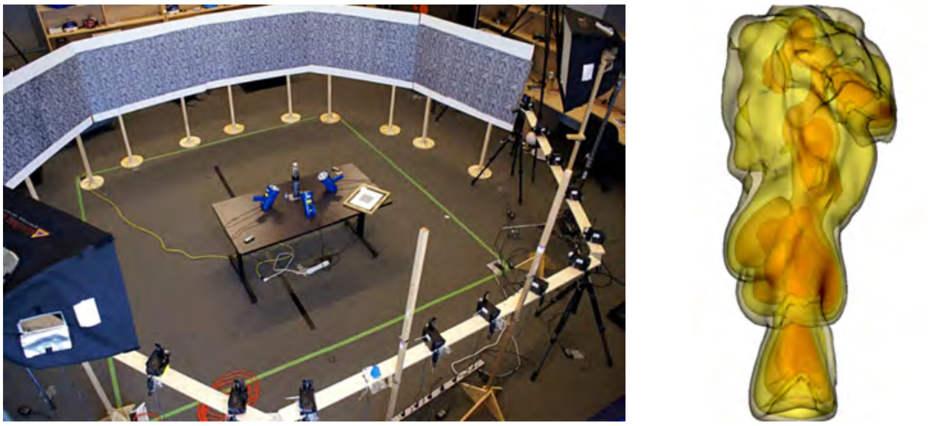
(a) (b)

Figure 1.19. a) BOS experimental device with 16 cameras by Atcheson et al. (2008). In the center is located the Bunsen burner, around it there are the cameras and panels with the BOS background pattern. b) 3D reconstruction of the convection plume above the Bunsen burner.

To reconstruct a stationary field, it is possible to carry out measurements with a unique device at different viewpoints obtained at different times. For stationary reconstructions around supersonic models, Ota et al. (2011) and Sourgen et al. (2012) rotate the models around their axes and therefore it is possible to obtain more viewpoints by keeping the BOS experimental device fixed.

When the phenomenon becomes unsteady, it is necessary to acquire the phenomenon simultaneously. For this reason, it is necessary to multiply the number of viewpoints by using several experimental devices. Figure 1.19a present a 3D measurement system made of several 2D BOS lines.

Since shadowgraph and Schlieren are mainly qualitative techniques, the candidates for a 3D reconstruction are interferometry, laser speckle photography and BOS. Because it involves the simplest optical setting, BOS appears much more convenient for 3D measurement than interferometry and laser speckle photography. However, both interferometry and speckle laser photography were used respectively by Olchewsky, J.-M. Desse, et al. (2018b) and Ko et al. (2011) for 3D reconstructions.

Ihrke (2008) and Atcheson et al. (2008) were the first to develop a multiple 3D BOS system to handle unsteady regimes. Their domain is not fluid dynamics nor optics but computer graphics, and their aim was to realistically simulate the optical distortions caused by a non-homogeneous medium present above flames. They developed a 3D BOS system using 16 cameras (figure 1.19a), reconstructing a density field over a Bunsen burner (figure 1.19b).

The reconstruction is divided into two stages: at the first step they reconstruct the three components of the gradient field by tomography with the algebraic reconstruction technique (ART), stopping the process before the convergence in order to to regularize the solution. Finally they obtain the density field by integrating the Poisson equation. Note that the ART, in contrast to other tomographic techniques like the Filtered Back Projection (FBP), can exploit a limited number of projections, simplifying the experimental setup.

1.3 BOS setup features

The sensitivity of BOS is related to the smallest deviation that can be measured by the BOS set-up: it has been studied in several works Bichal and Thurow (2013), Gojani et al. (2013) and Goldhahn and Seume (2007). Another important subject is the spatial resolution of BOS, which is discussed in Gojani et al. (2013), Goldhahn and Seume (2007) and Kirmse et al. (2011). While several causes affect the spatial resolution, we show in the following sections that the dominant cause is often the fact that the measurement volume is out of focus. Unfortunately it turns out that increasing the sensitivity and reducing the blur inside the measurement volume are antagonist needs. Ultimately, improving the measurement leads to increasing the depth of field by minimizing the aperture. Several parameters influence sensitivity, resolution and depth of field: focal length, diameter of the entrance pupil, focus plane and distances (camera-density field and density field background). We discuss these points in the following subsections.

1.3.1 Sensitivity

Figure 1.20 presents a schematic view of the BOS imaging configuration. When the reference image is being recorded, a feature from the background located at the point P is imaged in the point $x + \Delta x$. The introduction of the fluid flow with a variable refractive index n will deflect the beam for an angle ε and the imaged point now will be shifted of Δx.

Here below are the formulas taken from Bichal and Thurow (2013), Gojani et al. (2013) and Goldhahn and Seume (2007) to obtain an expression of sensitivity. The sensitivity of a measure

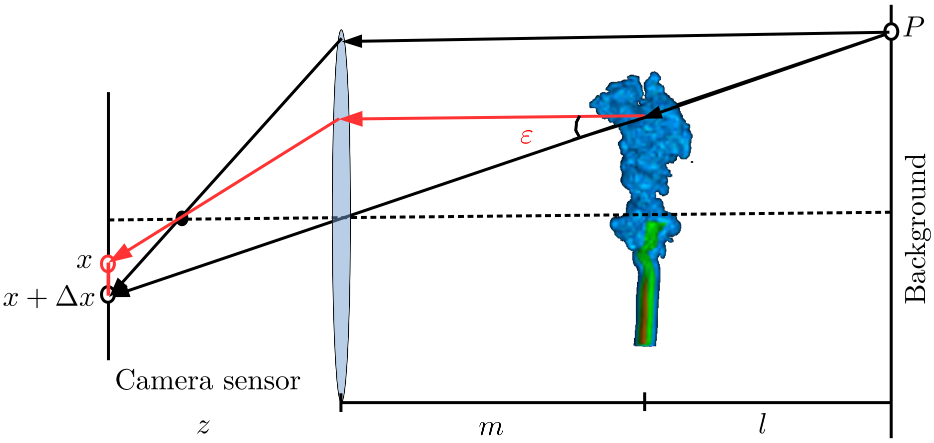

Figure 1.20. BOS imaging configuration: the light rays are deflected by the flow by an angle ε and consequently a displacement Δx is detected by the CCD.

is the ratio between the detected displacement Δx and the angle of deflection ε:

$$S = \frac{\Delta x}{\varepsilon} \tag{1.18}$$

In order to find out the smallest variation of the refractive index and so of the deflection angle, a great sensitivity is needed. By using the thin lens relation:

$$\frac{1}{f} = \frac{1}{z} + \frac{1}{m+l} \tag{1.19}$$

and the magnification of the system:

$$M = \frac{z}{m+l} = \frac{f}{m+l-f} \tag{1.20}$$

it is possible to write the displacement as function of the the deviation angle:

$$\Delta x = Ml \cdot \tan(\varepsilon) = \frac{fl}{m+l-f} \cdot \tan(\varepsilon) \simeq \frac{fl}{m+l} \cdot \varepsilon \tag{1.21}$$

Finally the sensitivity writes:

$$S \simeq \frac{fl}{m+l} \simeq \frac{zl}{m+l} \tag{1.22}$$

As the test section is placed between the background and the lens, the values of m falls in the range $0 < m < \infty$ and consequently the sensitivity of the BOS setup is:

$$0 < S < z \tag{1.23}$$

When the focal is fixed the sensitivity depends only on the positions of the background and the density field. The sensitivity improves rising the ratio l/m; pulling away the background ($l \to \infty$) or moving the density field closer to camera ($m \to 0$). An other way is increasing the focal length but this reduces the field of view.

1.3.2 Spatial resolution

The spatial resolution of a BOS measurement depends on several factors and has been discussed in details in the articles of Gojani et al. (2013) and Ota et al. (2015). It depends both on the optical settings and on the sensor resolution, i.e. the pixels size but it is also dependent on the size of the interrogation window used to estimate the apparent displacement of the image that is done through methods of numerical cross-correlation (details in section 1.7.5).

One of the best example of the problem of spatial resolution is reported by Kirmse et al. (2011). His test were conducted on a sphere at 12 and 22MJ/kg total specific enthalpies at Mach = 8.1. The interesting part is the comparison between CFD analysis and data obtained from BOS measurements.

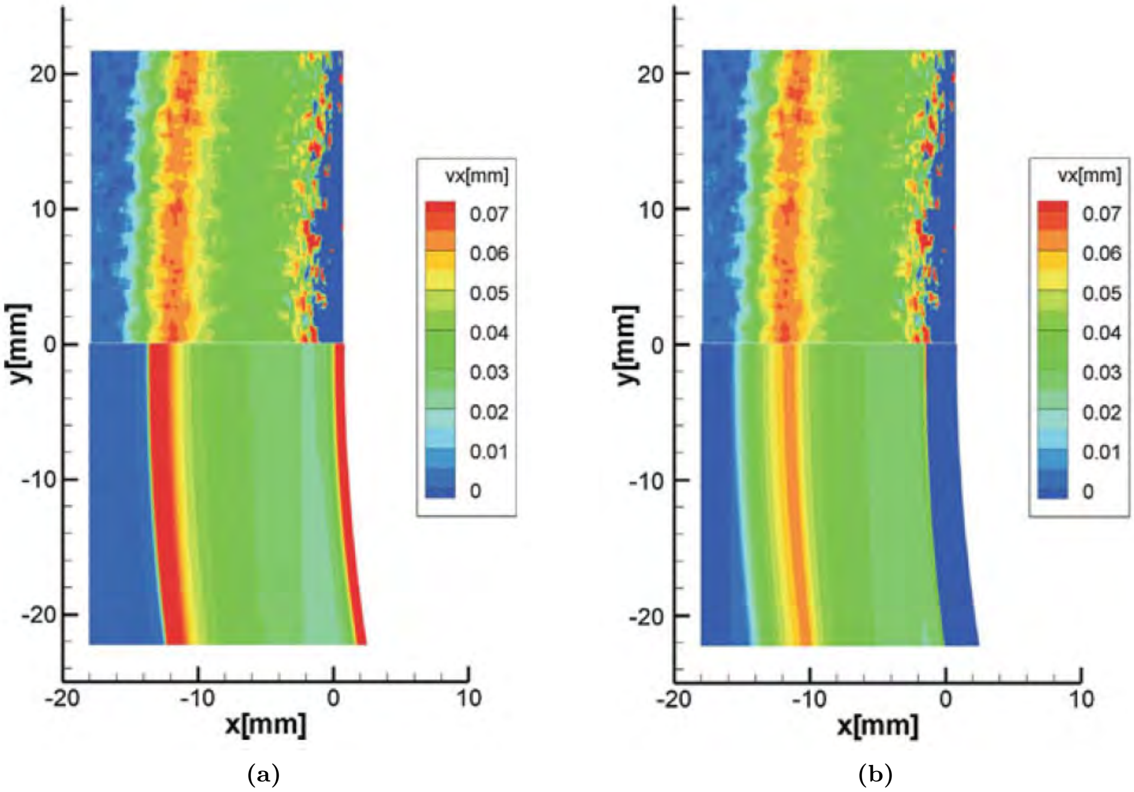

(a) (b)

Figure 1.21. In the upper parts of a) and b): measured data obtained from BOS. a) lower part: numerical data extracted from the computed flow field by the ray tracer technique b) lower part: computed flow field by the ray tracer technique and applying a moving-average filter with a window of 4.3 x 4.3mm. (Kirmse et al. 2011)

In figure 1.21 the displacement in the flow direction, vx[mm], obtained by the ray tracer (lower part of each figure) is compared to the results of the BOS measurement (upper part of each figure). In figure 1.21a the original ray tracer result is shown. The maximum displacement occurs at the shock front in the region of the highest density gradients. In the BOS results, the shock front seems to be blurred, the maximum displacement is half of the value determined by the ray tracer and its position is shifted towards the sphere. This difference between the numerical and experimental result is caused by the optical setup; in the simulation, one dot on the background is represented by a single ray, but in the measurement a dot on the background is imaged by a bundle of rays limited by the aperture of the camera. Even though the aperture was closed to an f-number of 32, the light cone had a diameter of 4.3 mm at the position of the sphere, introducing a spatial filter to the BOS result. For the present BOS setup, the spatial filter due to the optics dominates compared to the spatial averaging over the interrogation window of 1x1 mm. To take this effect into account in the ray tracer simulation, a moving-average window of 4.3x4.3 mm was applied, resulting in the displacement field depicted in figure 1.21b.

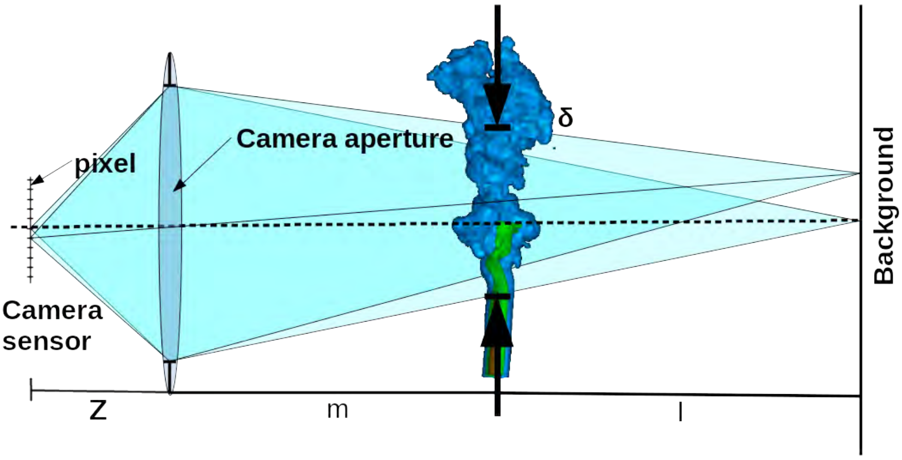

Figure 1.22. Circle of confusion in a BOS configuration.

After demonstrating the effect of the resolution, the parameters on which it depends are presented in detail below. First of all mention is made of the resolution related to the interrogation window and pixel size, then the resolution related to the optical configuration of the BOS technique.

As for the first one, while increasing the number of pixels for a given sensor size leads to a finer resolution and allows using a finer dotted pattern and smaller interrogation windows, it also comes with a decrease of the signal to noise ratio. However, such choices are constrained by the available technology. At the flow level this resolution is:

$$\delta_{pix} = \frac{l_{pix} \cdot IW \cdot m}{L_{tot} M} \tag{1.24}$$

where l_{pix} is the pixel dimension, IW the interrogation window size in number of pixels and $L_{tot} = m + l$ is the camera to background distance.

Ideally, the optical resolution limit stems from diffraction and is governed by the diameter D of the aperture. However, in BOS the resolution is often much lower and related to the notion of circle of confusion. Due to the fact that the flow is much larger than the lens, we do not work with a collimated light beams but with divergent light beams. As illustrated in figure 1.22, when the focus is on the background panel, the light received on a pixel comes from a pencil which has a width δ in the measurement volume. The circle of confusion is the circle of diameter δ modelling the spatial averaging which occurs in this volume.

As done by Gojani et al. (2013) and Ota et al. (2015) the spatial resolution considered below does not take into account the size of the interrogation area used to estimate the apparent displacement of the image. The circle of confusion at the density field is the sum of the light cone width emitted from one point on the background and the pixel size projected onto the refractive plane. Referring to figure 1.22: the first term is: $\delta_a = \frac{Dl}{m+l}$ and the second is $\delta_d = \frac{\delta_b m}{m+l}$ where $\delta_b = l_{pix}/M$ is the pixel size projected on the focusing plane (Nicolas 2017). Summing the two:

$$\delta = \frac{Dl}{m+l} + \frac{\delta_b m}{m+l} = \frac{M}{1+M}\frac{l}{f_\#} + \frac{l_{pix}}{M}\frac{m}{m+l} \tag{1.25}$$

where $f_\# = f/D$ is the objective f-number.

For BOS typical sizes the first term is predominant compared to the second one, e.g. in a setup carried out previously at ONERA in the F2 wind tunnel (Nicolas et al. 2017c): the first term is 4.11mm while the second is 0.13mm. What a pixel records is the average information contained on δ.

A decrease of the size of the aperture (D) reduces δ and improves the resolution as long as the diffraction does not appear.

Concerning the parameters of the geometrical configuration l and m, the resolution is improved by increasing m and decreasing l, which means positioning the measurement volume as close as possible from the background. To improve the spatial resolution on the camera sensor, in addition to the previous parameters, the focal must tend to zero ($f \rightarrow 0$). Changing these parameters improves the spatial resolution of the measurement but the sensitivity decreases, this is the topic of the following section.

As has been demonstrated by (Kirmse et al. 2011) the spatial resolution has an important influence on the results obtained with the BOS technique and therefore it is necessary to be careful with the measurements that are made and to take it into consideration.

1.3.3 Sensitivity versus spatial resolution

The purpose of this section is to discuss about the relationship between sensitivity and spatial resolution.

By combining sensitivity (eq. 1.22) and spatial resolution (eq. 1.25, where the second term has been neglected):

$$\delta = \frac{fl}{m+l}\frac{1}{f_\#} = \frac{\Delta x}{\varepsilon}\frac{1}{f_\#} = S\frac{1}{f_\#} \tag{1.26}$$

The spatial resolution is equal to sensitivity divided by the f-number.

All the tuning of l and m to increase the sensitivity will decrease the spatial resolution.

The only possibility to improve the spatial resolution without touching the sensitivity is decreasing the f-number. Since f cannot be decreased without decreasing the field of view, the only way is by minimizing the aperture D.

When f or m are changed, the visualized volume changes. If H is the width of the visible volume and h the size of the camera sensor:

$$\frac{h}{H} \approx \frac{f}{m} \tag{1.27}$$

Replacing this expression into 1.22:

$$S = \frac{h}{H}\frac{ml}{m+l} \tag{1.28}$$

When the apparent size of the density field ($h/H = const$) is kept constant , m and l have the same role on the sensitivity of the setup.

Increasing one or the other leads to an increase of sensitivity.

This result is interesting when one attempts to minimize the defocus blur in the presence of a model in the density field. The density field must be moved away from the camera so as to put it closer from the background which is on focus. According to equation 1.27, f must be increased to keep constant the captured density field.

The depth of field and the fact that the measurement volume is not within it are discussed in the next section.

1.3.4 Depth of field

The depth of field is defined as the distance between the nearest and farthest objects in a scene that appears acceptably sharp in an image. Although a lens can precisely focus at only one distance at a time, the decrease in sharpness is gradual on each side of the focused distance, so that within the DOF, the unsharpness is imperceptible under normal viewing conditions. Due to the fact that in the background oriented schlieren technique the focus is done on the background, the flow of interest is always out of focus, but the amount of blur depends on the depth of field of the setup.

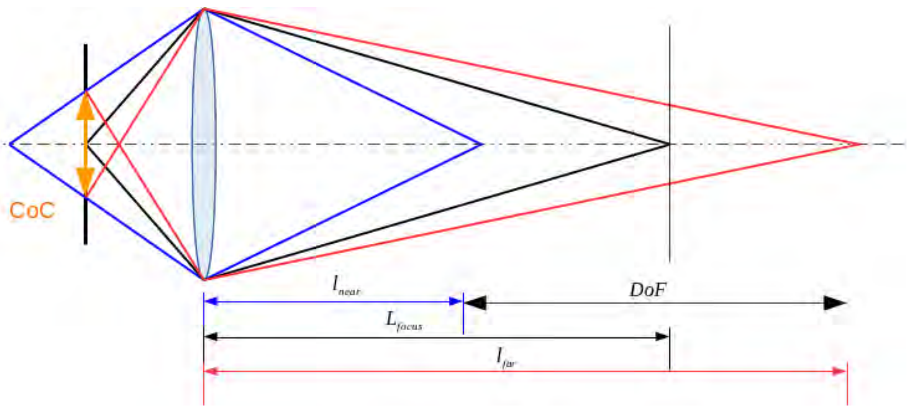

Figure 1.23. Depth of field.

Leopold et al. (2012) discussed this problem and observed that the distance between the flow field and the background is greater than the depth of field of the camera.

The lens is set to focus at a distance L_{focus} from the lens such that all points originating from this plane form a sharp image on the image sensor. Rays originating from in front or behind the focal plane will appear blurred. Inside the depth of field, these blurred spots are indistinguishable from the spots formed from a point source on the object plane. The size of the blur spot (on CCD), the circle of confusion (which is not to be confused with the one of section 1.3.2, which is the light cone at the position of the flow), is typically chosen to correspond to the size of a single (or integer multiple) pixel. L_{near} and L_{far} are the distances measured from the lens to the nearest and furthest planes in the DOF.

DOF is the region between L_{near} and L_{far}:

$$L_{far} = \frac{L_{focus} \cdot f^2}{f^2 - (L_{focus} - f) \cdot f_{\#} \cdot \Delta} \tag{1.29}$$

$$L_{near} = \frac{L_{focus} \cdot f^2}{f^2 + (L_{focus} - f) \cdot f_{\#} \cdot \Delta} \tag{1.30}$$

$$DoF = L_{far} - L_{near} \tag{1.31}$$

where the maximum acceptable circle of confusion is often defined as: $\Delta = d/1500$ where d is the diagonal length of the image sensor (https://lenspire.zeiss.com/photo/en/article/depth-of-field-and-manual-focusing).

Bichal and Thurow (2013) proposed a background oriented schlieren with a slightly out of focus background in order to improve the sensitivity of measurements.

The solution proposed by the authors is to place the background at the farthest point of the depth of field and the exit plane of the flow is at the nearest point in the depth of field. With this set up the spatial resolution of the background and the exit plane are equal. It is important to note that the nominal focus is not fixed at the background plane, but, rather, to a plane between the background and the exit plane. The optimized set up proposed by Bichal allows to improve the sensitivity and to limit the blur around the schlieren object. It should be noted that with the distances that have been used they limit the sensitivity and therefore this strategy can be used for a limited number of applications.

1.4 BOS backgrounds

The choice of a suitable background is essential for the technique: it must allow calculating the apparent displacements of pixels, also called optical flow. It is important to note that all of estimation methods require the presence of high frequency and highly contrasted patterns in the images in order to accurately measure the apparent motion. The most widely used solution is to print a random distribution of points that respect the rules of an ideal seeding for the PIV technique (Raffel et al. 2018): the size of the dots is between 2 and 3 pixels and each interrogation window must contain 4 to 8 dots. For different mounting dimensions or for different focal lengths (different setup magnifications), it is necessary to use backgrounds with a different dot size.

Different types of background have been used over time for the BOS technique and are presented below.

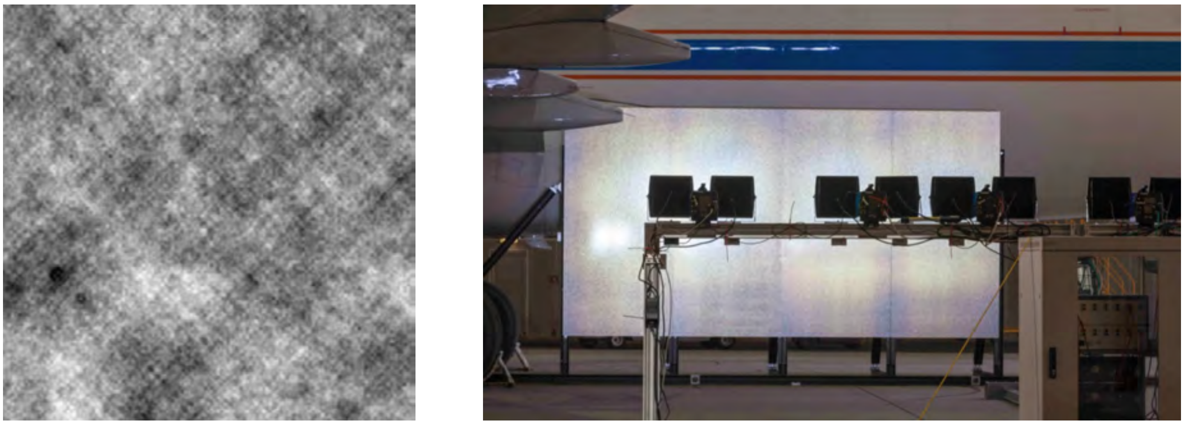

(a) (b)

Figure 1.24. a) Multi-scale noise pattern (Atcheson et al. 2009). b) Retro-reflective background (Schröder et al. 2014).

1.4.1 Multi-scale noise pattern

This type of pattern, proposed by Atcheson et al. (2009), is suitable for any type of setup: the details are distinguishable for each distance or focal used. This pattern is generated by summing up multiple independent noise functions with non-overlapping frequency spectra. This process ensures that the image contains sufficient high-contrast detail at any scale.

This type of background has been studied by Vinnichenko et al. (2012) who recommends it only when it is not possible to continuously change the dots size: he has shown that this pattern is highly vulnerable with respect to blur in the presence of strong density gradients.

1.4.2 Retro-reflective and back lighting backgrounds

These two techniques are presented together because they increase the light energy of the optical mounting.

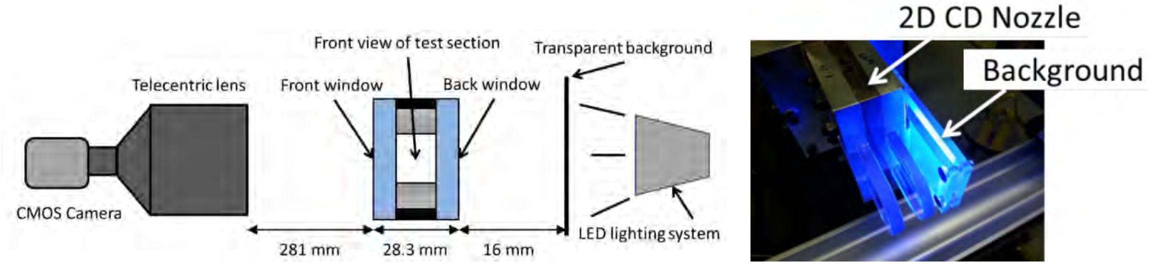

(a) (b)

Figure 1.25. Back lighting background illuminated by LED (Cozzi et al. 2017).

In the first case, the pattern is printed directly on retro-reflective panels: such material are made with retroreflective glass beads or micro-prisms and,unlike usual printed backgrounds that exhibit Lambertian reflectance, these retroreflective backgrounds reflect the light back to its source with minimum scattering. Because of the high directionality of the retroreflective backgrounds reflection, each camera needs its own light source. This type of background was used by Heineck et al. (2010) to visualize shock waves, the vortices from a full-scale helicopter rotor and a jet in cross-flow in adverse conditions where measures would not have been possible otherwise. The retroreflective BOS has been used by Schröder et al. (2014) to investigate an engine jet of an Airbus A320 with a high-speed BOS system.

With back lighting backgrounds the pattern is printed on a transparent panel and illuminated from behind by a light source Elsinga et al. (2004) , Ramanah et al. (2007) and Cozzi et al. (2017): the camera receives light directly from the source and not the light reflected from a surface, decreasing the amount of light lost, thus obtaining a greater amount of light available.

1.4.3 Natural backgrounds

The use of a natural background is certainly far from a optimum background that can be used in a laboratory. For this reason, these types of backgrounds have been studied by numerous teams active in the field of the research of large flows.

Since BOS is the only suitable technique for the visualization of large scale flows, a number of different natural backgrounds have been used in the literature. In this context, different scale screes, grass and forests have been used to perform in-flight measurements ((Leopold 2007), (Raffel et al. 2014), (Bauknecht et al. 2014b) and (Heineck et al. 2016)), to study helicopter blade tip vortices (Richard and Raffel 2001) and open-air explosions (Mizukaki et al. 2013).

Despite the use of different quality indicators for the image correlation, Kindler et al. (2007), Raffel et al. (2014), M. Hargather and G. Settles (2010b) and Bauknecht et al. (2014a) come to the conclusion that the difficulty lies in finding a pattern with high frequency (according to mounting distances) and high contrast.

1.4.4 Color BOS

The color BOS was developed by Leopold (2007). The technique involves the use of backgrounds with color dots on a black background and a color camera to capture images. The colours and the disposition of the dots are randomly distributed: the colours used are red, blue, green and other secondary colours obtained from a mixture of the previous ones. Because of the different colors present, it is possible to divide the image into eight elementary dot patterns (pure red, blue, green and mixtures of them figure 1.26a).

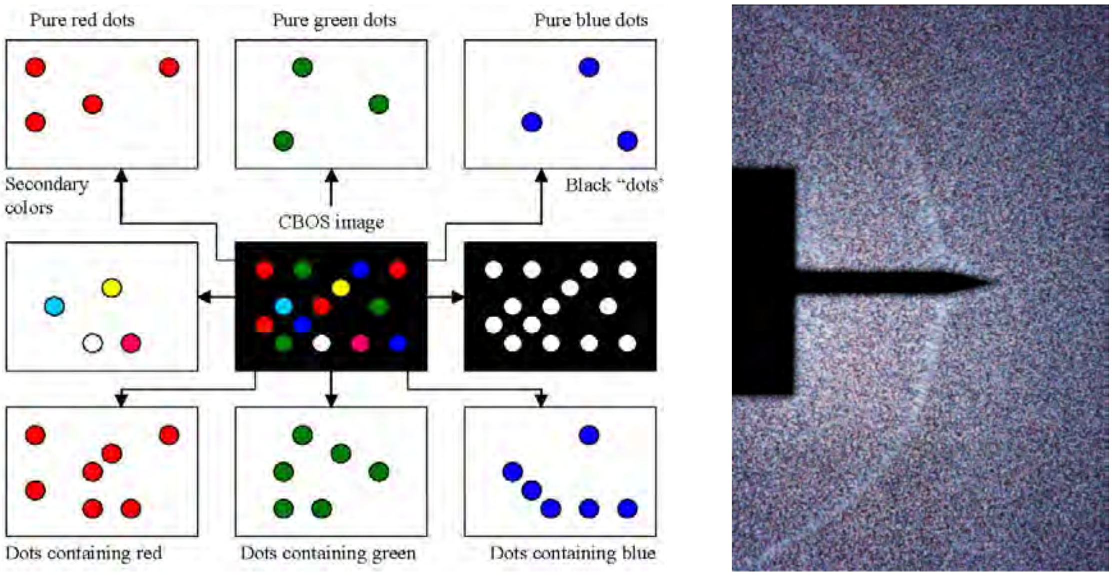

(a) (b)

Figure 1.26. Color-BOS (Leopold et al. 2013). a) Extraction of the different colour components. b) Compression shock around blurred spike and color BOS background.

The strategy consists in calculating the displacement field for each elementary image separately and then calculating the average value. In this way the standard deviation of the correlation is reduced. The advantage of this method is its ability to treat regions with strong density gradients where the background often appears blurred (figure 1.26b) by shifting one of the color with respect to the other two. The drawback is the computational cost, which is eight times higher, resulting in a very heavy burden when you have many images to process.

1.4.5 Colored-grid BOS

The colored-grid BOS was introduced by Ota et al. (2011). This technique differs in the utilization of an innovative background composed of two grids: one vertical red and one horizontal green. This technique, as for the color-BOS, involves the use of a color camera and a specific algorithm to treat the horizontal and vertical displacement of the fringes, based on methods used in holography (finite fringe analysis). The global displacement field is calculated by interpolation. Since the grid is known in advance, there is no need to acquire the reference image.

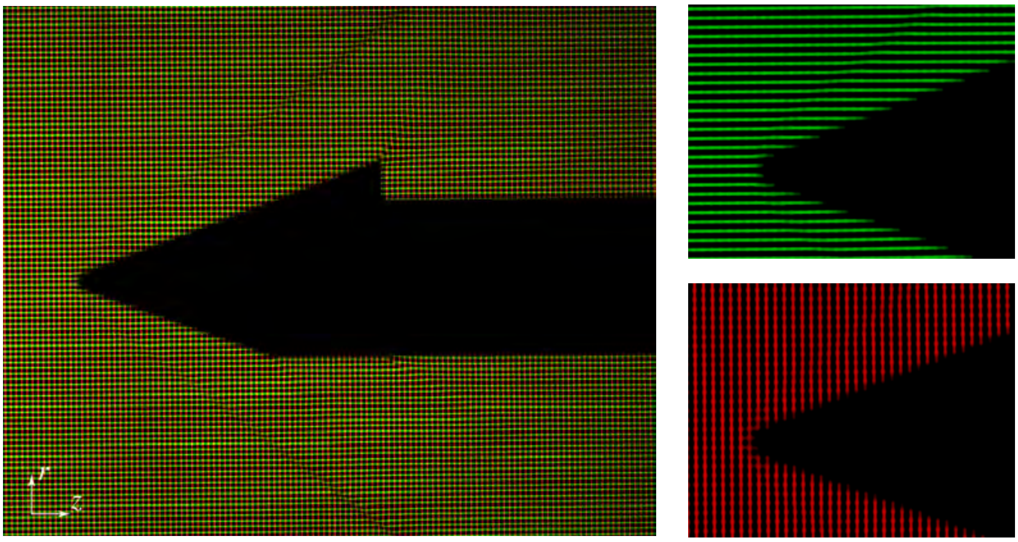

Figure 1.27. Color-Grid BOS on a truncated cone at Mach 2.0. On the left the full pattern and the horizontal green pattern and the vertical red pattern can be distinguished. The compression shock can be seen from the tip of the cone. (Ota et al. 2011)

1.4.6 Speckle BOS

Some authors have proposed to use speckle pattern generated by a coherent light source for BOS: this is the subject of the work published by A. H. Meier and Roesgen (2013).

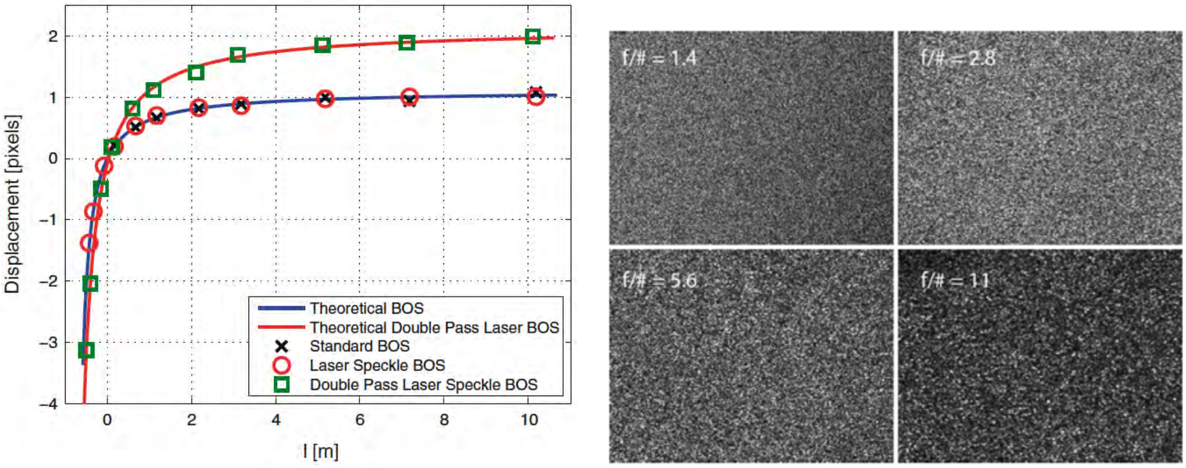

(a) Sensitivity for conventional and speckle BOS measurements: displacement as function of the lens imaging distance.

(b) Effect of the f-number $f_{\#}$ on the speckle size patterns. (A. H. Meier and Roesgen 2013)

Figure 1.28. Sensitivity and speckle size pattern of speckle BOS proposed by A. H. Meier and Roesgen (2013).

These patterns have been exploited in the previously mentioned "laser speckle photography" technique and are created when coherent light with a spatially random phase is interfering on a sensor surface, this happens when the BOS background is replaced by a suitably roughed speckle screen illuminated with laser light. The speckle diameter depends on the laser wavelength and on the imaging lens f-number as illustrated in figure 1.28b, the speckle spot diameter increases with $f_{\#}$.

First, Meier and Roesgen show that identical results can be obtained with conventional BOS and BOS with a speckle illumination, as illustrated in figure 1.29a. In both settings, the camera in-focus plane is located at the same distance of the camera (a large distance l=11m is chosen in order to reach the limiting sensitivity). For the conventional BOS, the background panel is located in the in-focus plane. In the speckle BOS, the scatter screen is close to the camera (100mm). The advantage is clear: asymptotic value can be reached without the need of placing the background at large distances. The scattering plane can be placed very close to the density field without losing sensitivity.

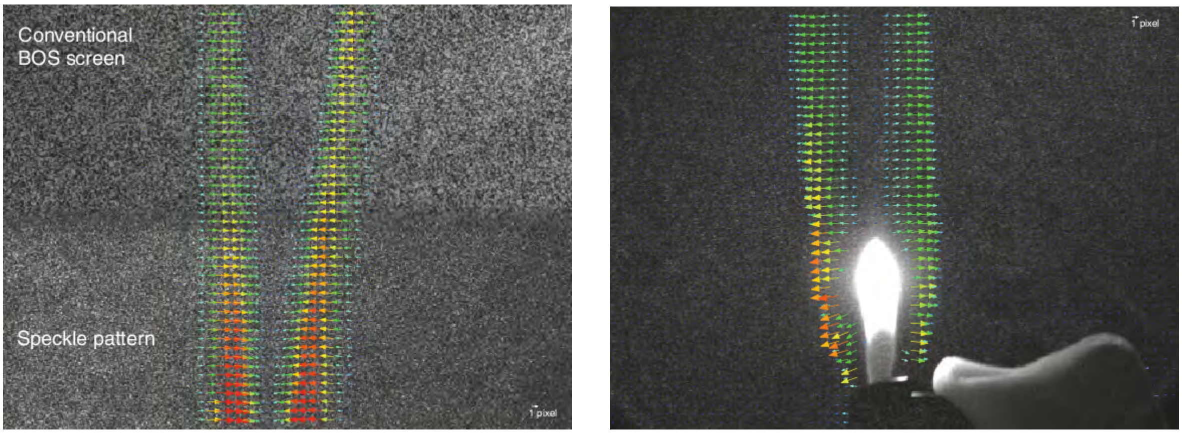

(a) Displacements induced by the convection of a candle plume with a conventional BOS background (upper part) and speckle pattern (lower part).

(b) Focused imaging using a double-pass speckle configuration.

Figure 1.29. Speckle BOS proposed by A. H. Meier and Roesgen (2013).

An other advantage is that the camera can be focused for negative l distances, by focusing on a plane placed between the density field and the camera. Figure 1.28a and equation 1.21 show how the displacements captured by the camera turn negative as soon as l turns negative and they grow rapidly to values higher than the asymptotic value obtained for very large l distances. With the speckle BOS it is therefore possible to achieve greater sensitivity than with classic BOS.

A possible solution for solving the problem of unfocused model and spatial resolution can be the double pass speckle by focusing on the object ($l = 0$) (A. H. Meier and Roesgen 2013). In this set up the laser illumination is performed coaxially with the camera view. In this configuration the laser beam passes two times into the distorting object. The displacement is negative and it can be increased by moving the speckle screen to large distances over the density field. In this manner the object can be kept in focus (figure 1.29b) while increasing the sensitivity by placing the speckle screen farther from the target.

Certainly the speckle setup is more complicated and more difficult to adjust than a classic BOS setup. Moreover it is sensitive to vibrations and relative motion between the camera and the scattering plane (consequence of the nature of the interferometric nature of the speckles).

1.4.7 Celestial objects BOS

An original application is definitely the BOS using celestial objects (BOSCO). This technique was developed to simplify as much as possible the installations previously used (Schlieren for Aircraft in Flight (SAF) (Weinstein 1994) and air-to-air BOS (AirBOS) (Heineck et al. 2016)) for real-size visualization of flight shocks.

NASA has developed this technique to study shock waves around real-size supersonic planes to try to reduce their noise.

In order to generate exploitable backgrounds, calcium-K or hydrogen-α band-filters have been used to filter certain wavelengths, highlighting the granular cells on the sun.

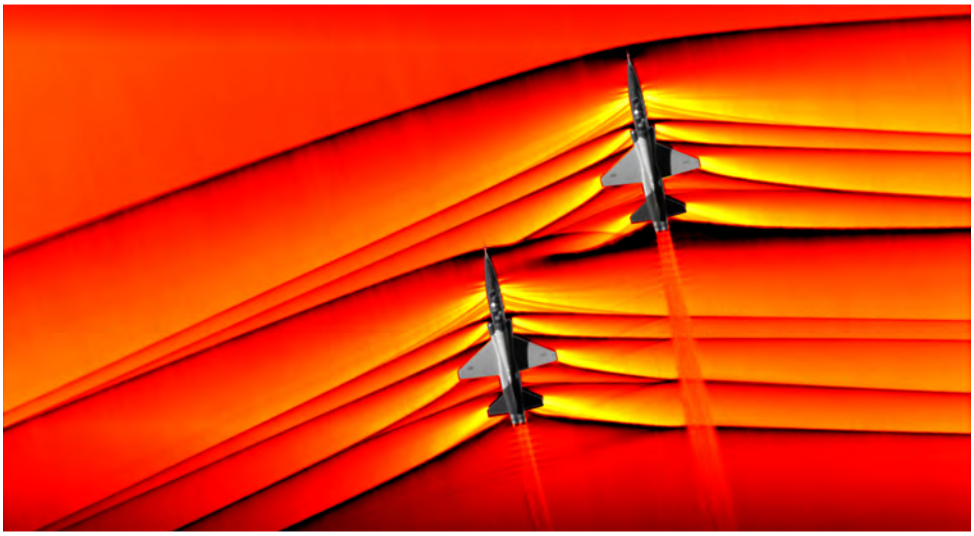

Figure 1.30. Air-to-air images of the interaction of shock waves from two T-38 supersonic aircrafts flying in formation using the schlieren photography technique (NASA).

1.5 Light sources

With the exception of the BOSCO (section 1.4.7) and the natural BOS (section 1.4.3), for which no additional light sources are needed, all other setups require a light source with characteristics that depend on the type of mounting and the type of phenomenon to investigate.

It must be taken into account that to avoid a temporal integration of the flow, it is necessary to be careful of exposure times that in supersonic flows must be in the order of a few tens of nanoseconds. In addition, a greater amount of light allows working with a smaller camera aperture and thus to improve the spatial resolution by reducing the circle of confusion.

The importance of illumination is already highlighted in the first publications on BOS: Richard and Raffel (2001) test two types of light source, a continuous white and a stroboscope light synchronized with the camera, obtaining different results. Atcheson et al. (2008) propose to use halogen spots combined with sunlight to minimize exposure times. Arc lamp and halogen spots are also being used by Kumar et al. (2011), Nicolas et al. (2016) and Venkatakrishnan (2005). As suggested by the latter, it would be preferable to use high-power short-duration flash to illuminate the background.

Pulsed lighting is required to visualize unsteady phenomena. Three different types of light sources are mainly used in these applications: Xenon strobes, lasers and LEDs.

Xenon strobes are employed by Augenstein et al. (2001), Ramanah et al. (2007) and Rouser et al. (2011) in an back-lighting background configuration to further increase its efficiency. Xenon flash lamps have a high repetition rate ($\sim$ 1000Hz) with 5-10μs pulse duration.

Pulsed lasers, such as Nd:YAG used for PIV measurements, are used by Kirmse et al. (2011), Jin et al. (2011), Venkatakrishnan et al. (2013), Yamamoto et al. (2014) and Nicolas et al. (2017c). These lasers are very powerful and, moreover, the duration of the flash is in the order of ten nanoseconds: the amount of light emitted is very significant.

In recent years more and more high intensity LEDs (Light Emitting Diodes) have been used due to the breakthroughs made in the field of electronics. By building dedicated circuits, it has been demonstrated by Heineck et al. (2010) that the amperage can be increased up to five times compared to the standard amperage in continuous mode operation: in this way a high-brightness and short-duration illumination is obtained. Impulse LEDs have also been used in BOS technique by Bencs et al. (2011), Hernandez et al. (2013) and Schairer et al. (2013).

Wilson et al. (2015) has shown that overdriven LEDs can be used for high-speed schlieren up to 50Kfps with exposure times of 1μs at a reduced cost: these same LEDs can be used for high-speed BOS.

1.6 Camera objectives

The use of a camera lens is necessary to be able to focus on the camera sensor the light coming from an object placed at a certain distance, in the specific case of BOS, the background. A single convex lens is sufficient for this purpose but to partially eliminate optical aberrations, the objective is made up of a series of lens elements that are multi-coated treated to transmit the maximum of light. In the next sections are presented the different camera objectives that have been used by different authors in the technique BOS.

1.6.1 Endocentric

Endocentric lens is the most common type of photographic lens and also the one that is typically used in BOS technique: this is why section 1.3 is developed around this type of lens. This type of lens can be simplified to the model of pinhole, very simple and very close to reality.

Its principles are outlined in figure 1.31a. In endocentric perspective, the further away an object is positioned from the projection center, the smaller it will be in the image (figure 1.32a). As explained in the next section, this is no longer valid in the case of bi-telecentric perspective.

The two fundamental parameters that distinguish it are the focal length and the aperture. The focal length determines the magnification of the system while the light intensity is controlled by the aperture. If the focal length determines the size of the field to be examined, the aperture strongly influences the spatial resolution of the measurement (section 1.3.2).

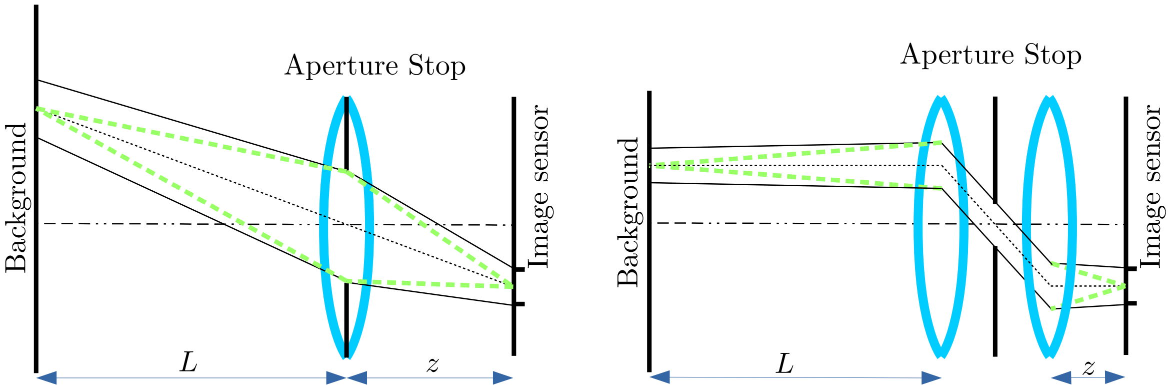

(a) Endocentric system perspective.

(b) Bi-telecentric system perspective.

Figure 1.31

1.6.2 Telecentric

The characteristic of a telecentric system is that it has the entrance or the exit pupil at infinity, in this way the chief rays are parallel to the optical axis. This is achieved by placing the aperture


(a) Endocentric lens **(b)** Bi-telecentric lens **(c)** Cubes arrangement

Figure 1.32. With an entocentric system (fixed focal length lens), the angular field of view produces a parallax error in the image and the two cubes appear to be of different sizes. (Edmund Optics)

stop in one of the focal points of the lens.

What interests us in this section are the bi-telecentric systems, which have been used in the BOS technique, by Ota et al. (2015), Leopold et al. (2013) and Cozzi et al. (2017), to improve spatial resolution and depth of field. A bi-telecentric lens, in its simplest version, is made up of two convex lenses placed at a distance equal to the sum of their focal lengths and with the aperture stop placed at the common focal point (figure 1.31b). Since the field of view is limited by the size of the lens, Ota and Leopold used a concave mirror to study larger fields, while Cozzi has just restricted his work to the use of lenses and therefore to the study of micro-nozzle. With this type of lens system, in addition to increasing resolution and depth of field, the magnification does not change in respect to depth (it depends only on the focal length ratio of the two lenses), and therefore the 3D effects of the perspective used in the conventional (endocentric) objectives are eliminated (figure 1.32a).

1.6.3 Plenoptic

A plenoptic camera uses an array of micro-lenses placed one focal length away in front of the camera sensor, this system is shown in Figure 1.33. With this camera you can capture the intensity of light in a scene, but also the light direction, unlike a conventional camera that can only record the light intensity.

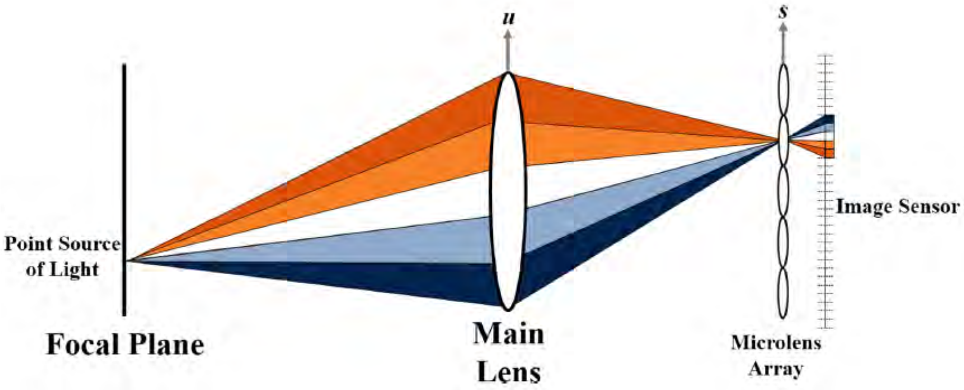

Figure 1.33. Schematic of imaging with a plenoptic Camera (Klemkowsky et al. 2017).

With this two pieces of information, after an image has been acquired, it is possible to generate synthetic images in two ways: by changing the perspective and by changing the focal plane. Using these cameras in the BOS technique means to be able to focus both on the background and on the flow of interest (increase in resolution) and to have different angles of view with only one camera to perform tomography reconstruction.

Plenoptic BOS is developed by the University of Auburn. Bichal (2015) conducted experimental and synthetic tests around a cone model at Mach 2.3, recently Klemkowsky et al. (2017) continued his studies on flows without models (single heated jet and two flame sources). Klemkowsky emphasizes the need to compare this technique with a conventional BOS system and also the need to use tomographic methods to determine the feasibility of reconstructing density field from multiple line-of-sight acquired from a single plenoptic camera.

Disadvantages include a limited resolution due to lens size in the lenses array and the solid angle at which the flow is observed is too small with only one plenoptic camera.

1.7 Development of 3D BOS technique at ONERA

The BOS has been developed at ONERA for several years through the PhDs of Todoroff (2013) and Nicolas (2017). The choice was to develop a technique capable of instantaneous 3D reconstructions: for this reason it was necessary to opt for a configuration with several cameras and a synchronized acquisition of images. The next step is to calculate the displacements and then the reconstruction of the density or temperature field.

This section describes in detail the equipment, means, processes and codes to obtain a BOS measurement with the technology and experience accumulated over the years in the laboratory.

1.7.1 Background

Todoroff has studied the influence of two very different backgrounds: a classic one with a random distribution of white dots on a black surface and a multi-scale background (figure 1.24a). In the presence of strong gradients, the multi-scale background is highly sensitive to astigmatism and the results are less reliable. The aleatory background has instead shown that the presence of large black areas or clots of white spots cause zones where correlation is not possible. For this reason we use a semi-random background (figure 1.34a): this remains random to the scale of the interrogation windows and regular beyond this size.

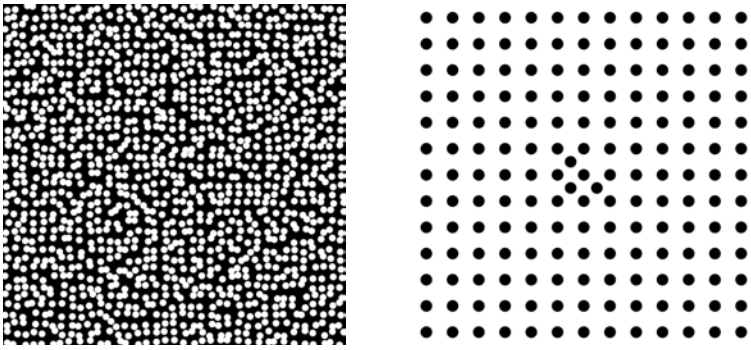
(a) (b)

Figure 1.34. a) The semi-random background guarantees a fixed number of dots within the correlation window with a random distribution within it. b) Calibration body.

For each different BOS mounting, a background suitable for the dimensions is generated: the size of the points (about 3 pixels to avoid aliasing phenomena) and the dimensions of the background are chosen. Usually these backgrounds are applied on aluminium plates to maintain a certain rigidity and avoid movements.

1.7.2 Light sources

To capture instantaneous phenomena it is necessary to perform the measurement in very short times, which for supersonic phenomena is a time of the order of a hundred nanoseconds. A measurement in larger times involves a temporal smoothing of the flow structures.

Since the minimum exposure time of the cameras is 64 μs, the choice has been made for pulsed PIV lasers. These are double-pulse Nd:YAG lasers capable of providing a powerful light source with a pulse duration of about 8ns: with this solution we are able to freeze the flow. The laser used is a Quantel Big Sky Laser Twin BSL 2x200mJ which can operate up to 15 Hz.

To uniformly illuminate large areas and better direct the light beam, the laser beam is split into four or eight beams using a separation table made of seven 50:50 beamsplitter plates. Liquid guides equipped with diverging lenses are then used to direct this light toward the backgrounds.

500W halogen spots have been used for flows with shorter characteristic times. Since the light is emitted continuously, the acquisition time is no longer given by the laser pulse but by the exposure time of the camera (the exposure time is no longer in the order of ns but of μs). This configuration has been used by Nicolas et al. (2016) in the geode for the acquisition around a candle plume.

1.7.3 Camera and acquisition system

The cameras used are black and white JAI BM500GE 8-bit with a resolution of 2058 x 2456 pixels. The choice fell on this type of camera for the small size of the pixels (3.45μm) which help, as seen in section 1.3.2, to improve the resolution of the measurement. The minimum exposure time is 64μs. The camera can be equipped with Schneider C-mount 23, 50 or 70mm optics. Cameras are synchronized through a TTL generator with 24 independent outputs. Is the TTL generator that synchronizes the acquisition of images with the light emitted by the laser. To record images from twelve 5 Mpx cameras at a rate of about 10Hz, an Enterays C5G124-24 switch is used, connected through a 20Gb/s network card to a dedicated PC where the images are saved on the 64Gb RAM memory. In a 12 camera configuration it is possible to record about 900 images in about 4min 30 sec (1 min 30s for acquisition and 3min for the storage).

The arrangement and the number of cameras needed for the measurement has been studied by (Nicolas et al. 2016). If the residual error decreases asymptotically as the number of cameras increases, in a realistic configuration these are limited to 12 which seems to be a good compromise between the amount of information recorded and the complexity of the assembly and the amount of data.

For a flow that has a geometrical main axis (such as free jet), it has been verified that a coplanar configuration, where the cameras are on a plane orthogonal to the main axis, is the most suitable. A cluster arrangement of the cameras strongly influences the reconstruction which is shown to be degraded and the information is spread out along camera axis. In addition, due to the principle of light reversibility, it is not necessary to add cameras with a solid angle greater than 180°, since the same information would be recorded several times.

1.7.4 Calibration

Calibration of a multi-camera system is an essential step in performing a tomography reconstruction. This process consists of identifying the camera's internal parameters, such as focal length, principal points and distortion parameters, but also the position and orientation in a global coordinate system. Calibration parameters are obtained through a non-linear least-squares minimization of the retroprojection errors computed for all the features of the calibration body (figure 1.34b).

During calibration not all the dots are seen by all the cameras at the same time, for this reason the process consists in acquiring a series of images moving the calibration body in the measurement volume in order to obtain a sufficient number of common features.

Another problem related to calibration is focusing: since this is done at the background, the calibration body may be more or less blurred depending on the depth of field of the BOS setup. The calibration process takes about 1 hour in terms of calculation, because it is necessary to process about 100 images per camera. To speed up the process we use a CPU-GPU implementation.

All details of the calibration can be found in Le Sant et al. (2014).

1.7.5 Image correlation and displacements estimation

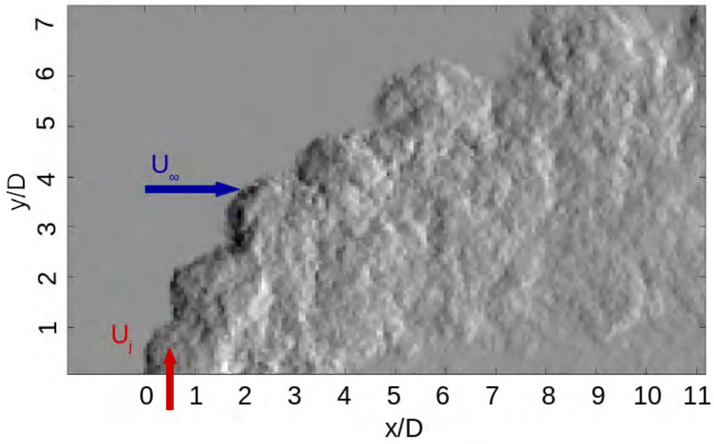

Figure 1.35. Instantaneous horizontal displacements seen by a camera in a 3D BOS configuration.

The calculation of the displacements from the acquired images of reference and with the flow is done through methods of numerical cross-correlation: in this way we obtain a map of the displacements (x, y) on the whole figure. We use FOLKI-SPIV, an ONERA software implemented on GPU to speed up the process (5Mpix images are processed in about 30ms). Folki is based on an iterative Lucas-Kanade process that relies on local interrogation windows (additional details can be found in Champagnat et al. (2011)). The result is a dense displacement map, i.e. a vector of displacements per pixel, but the spatial resolution remains bounded and limited by the size of the interrogation windows.

1.7.6 Deviations

In BOS, in order to reconstruct the density field, the inverse problem to be solved is formulated according to the deviation maps. However, the measured quantities are the displacement fields and not the deviation maps. To establish the relationship between these two magnitudes, it is necessary to make some assumptions.

The calculation of the deviations from the displacements is carried out making an approximation proposed by Atcheson et al. (2008) it consists in considering that the deviations take place in the middle point of the volume of interest. The entry (I_{in}) or exit (I_{out}) points can also be used but these lead respectively to underestimate or overestimate the deviations. More details are available in Nicolas (2017).

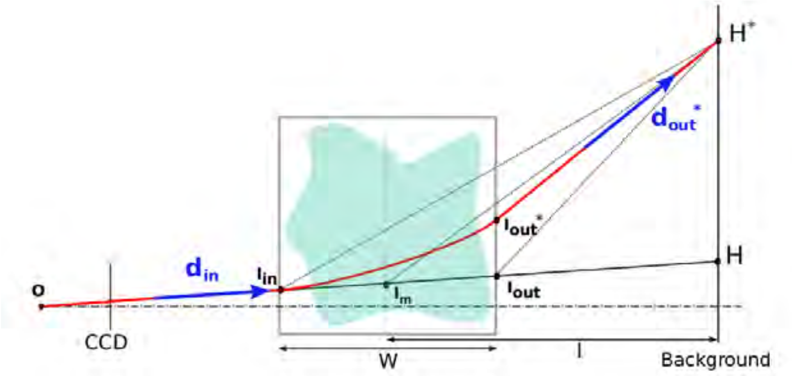

Figure 1.36. Approximation of the mid-point volume for the deviation determination (Nicolas 2017).

This process is shown in figure 1.36. A ray coming out of the camera enters the volume with density gradient, is deflected, and comes out of it with an d^*_{out} direction and ends up at the background in the H^* position. The light deviation is the result of the difference between the two vectors of exit (d^*_{out}) and entry (d_{in}) into the volume. With the calibration and the calculation of the displacements the points I_{in}, H and H^* and the direction of the vector d_{in} are known. On the other hand d^*_{out} and ε are unknown and moreover d^*_{out} depends on the position of the point of exit I^*_{out} which is also unknown.

The actual deviation $\varepsilon = d^*_{out} - d_{in}$, is then approximated in:

$$\varepsilon = \boldsymbol{H^* I_m} - \boldsymbol{d_{in}} \tag{1.32}$$

1.7.7 3D Mask

The use of a 3D mask is necessary to improve the optimization of the reconstruction process. This is calculated from the displacements map obtained from each camera: the user must trace for each camera a 2D mask that encloses only the areas where displacements are present. The 3D mask is created by the retro-projection of the set of 2D masks in the reconstruction volume.

The 3D mask is also used to impose boundary conditions and validate rays; this aspect is discussed in section 1.7.8.4.

1.7.8 3D BOS reconstruction

The reconstruction process is the final step in obtaining a 3D BOS field.

Since the tomography methods allow to reconstruct the gradient field of ρ, an integration is necessary to determine the density. One of the possibilities is to use the Poisson equation by deriving the gradient field $\partial^2\rho/\partial x^2 + \partial^2\rho/\partial y^2 + \partial^2\rho/\partial z^2 = \Delta\rho$. Ota proposes an integration that is carried out iteratively using the SOR (Successive Over Relaxation) method (Ota et al. (2011) and Ota et al. (2012)). A simpler solution is the method used by Leopold et al. (2013) that relies on finite differences to integrate the gradient field in the three directions of space. The choice that has been made at ONERA differs from the works in the literature, the end-to-end operator which combines both the integration over light rays and the spatial gradient is considered in the inversion algorithm, this allows a direct reconstruction of the density field (Todoroff et al. 2014) and (Nicolas 2017).

Executing the reconstruction algorithm requires the valid deviations fields, calibration and 3D mask.

1.7.8.1 Discretization

Remembering the equation that binds the deviations to the density: $\varepsilon_i = \frac{G}{n_0}\int_s \frac{\partial\rho}{\partial i} ds$ where $i = x, y, z$ the three directions of space, it can be written in the form of a linear system as follows (Todoroff et al. 2014) and (Nicolas 2017):

$$\varepsilon = TD_i\rho = A\rho \tag{1.33}$$

where the observation operator A is made up of the the tomographic operator T and the finite difference matrix D_i of the density volume ρ. The matrix T is composed of positive weights that indicate the contribution of each volume voxel to a specific deviation. According to computed tomography, a constant and piecewise discretization of the volume is chosen and therefore T is a sparse matrix. Calibration makes possible to calculate the T matrix, but since it is enormously large, it is not saved during reconstruction but calculated on-the-fly.

1.7.8.2 Regularization

Since measuring and calculating deviations involves errors, they must be added to equation 1.33: $\varepsilon = A\rho + e$ where e takes into account the errors in the estimation of ϵ and measurements noise. There are several problems related to the resolution of this equation. First, because the interest is to make instantaneous measurements, it is impossible to decrease the noise by averaging several images. Second, since A is neither regular nor square, it can only be inverted in the least-square sense by calculating the minimizer of $\|\varepsilon - A\rho\|^2$. The last problem is that A is a ill-conditioned matrix and therefore the error introduced in the measurement is amplified solving the least-square problem. For these reasons a process of regularization has been necessary.

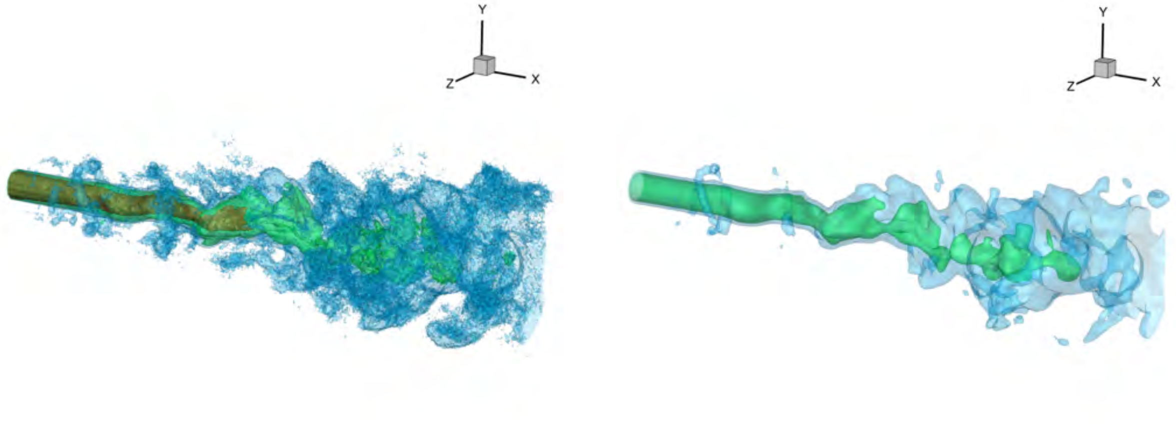

(a) Under-regularized solution ($\lambda = 1.0 \times 10^{-6}$). **(b)** Over-regularized solution ($\lambda = 1.0 \times 10^{-3}$).

Figure 1.37. Effect of the regularization parameter. (Nicolas et al. 2016)

The choice was to use a first-order Tikhonov regularization (Tikhonov and Arsenin 1977) implemented by choosing the $\mathcal{L}2$ norm of the density spatial gradient as the regularisation term:

$$\mathcal{J}(\rho) = \|A\rho + \varepsilon\|^2 - \lambda\mathcal{R}(\rho) \tag{1.34}$$

with $\mathcal{R}(\rho) = \|\bar{D}\rho\|^2 = -\rho^T \Delta \rho$ where $\bar{D}$ is the upwinded discrete gradient operator and Δ the discrete Laplacian operator. The first term of the equation 4.5 is the least-square criterion while the second is the regularization term: the solution is a balance between these two and is regulated by the regularization parameter $\lambda > 0$. Regularisation tends to smooth out the solution and reduces the propagation of noise.

The smoothing parameter is chosen according to the L-curve criterion proposed by Hansen (1992). This method takes its name from the L-shaped graph obtained by drawing the regularization term with respect to the data term for a set of solutions of (4.5) with several values of the regularization parameter.

λ is selected by choosing the point of the curve with the greatest curvature, this choice tends to balance the sensitivity of both terms of (4.5), and is also proven to minimize the average risk in a quadratic setting.

1.7.8.3 Optimization

For the need to treat very large problems, of the order of 10^7 voxels, it is necessary to use an optimization process to speed up the reconstruction: it has been chosen a conjugate gradients optimization method.

The method of conjugated gradients was introduced by Nocedal and Wright (1999) to solve large linear systems in an iterative way and later used for 3DBOS reconstruction by Ihrke and Magnor (2004) and Atcheson et al. (2008) to solve equation 1.33.

In our case it was used to solve equation 4.5.

Because it is an iterative method, the volume is updated at each iteration k as follows:

$$\rho_k = \rho_{k-1} + \alpha_k d_k \tag{1.35}$$

where d_k is the descent direction:

$$d_k = -g_k + \beta_k d_{k-1}, \quad \text{and} \quad d_0 = -g_0$$

and

$$g_k = \nabla \mathcal{J}(\rho_k) = 2\left(A^T\left(A\rho_k - \varepsilon\right) - \lambda \Delta \rho_k\right)$$

and β_k is selected in order to respect the orthogonal descent direction:

$$\beta_k = \frac{\|g_{k+1}\|^2}{\|g_k\|^2}$$

where α_k the descent step is given by:

$$\alpha_k = -\frac{g_k^T d_k}{d_k^T\left(A^T A - \lambda \Delta\right) d_k}$$

Since the residual varies from one type of reconstruction to another, a certain number of iterations are set and then its convergence is verified.

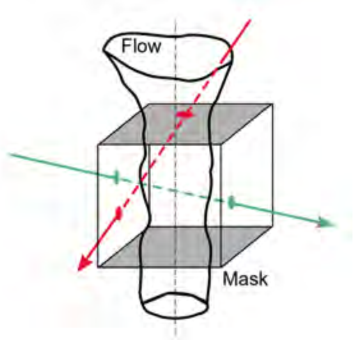

Figure 1.38. Boundary conditions and rays validation. The two grey faces are crossed by the flow, while the remaining ones remain outside it. A valid ray is in green and one to be discarded in red.

1.7.8.4 Boundary conditions and valid rays

Inside the parallelepiped given by the maximum dimensions of the 3D mask, there are active voxels (where there are density gradients) and other inactive, outside the mask where the density does not vary and remains equal to the external value ρ_0.

The boundary conditions are imposed to external density on the edges of the 3D mask. However, it is necessary to eliminate these conditions where the flow passes through the mask (figure 1.38 grey faces): here a free condition is set.

Another important step is the ray validation. When a beam is projected towards the measurement volume, it must not encounter density gradients outside it. Otherwise, the captured deviation contains a part of the information coming from an area outside the reconstruction volume: these rays must be discarded (red rays). This step ensures that the deviations used for reconstruction occur only within the reconstructed volume. The rays validation is carried out on the deviation map, discarding unsuitable areas.

1.7.9 Synthetic 3D BOS reconstruction

In order to test the reconstruction code, the possibility of using CFD simulations and not experimental data has been implemented. In this way it is possible to test different situations that in reality would be impractical or their realization would require long mounting times. For this purpose it is necessary to have a CFD simulation but also to define the characteristics of the virtual cameras, a model of propagation of the light rays to obtain a deviation map, and to add a quantity of noise on the data.

The camera model has been simplified and reduced to a pinhole model. In this way, distortions caused by the lens are not taken into account. For simulation, the number of cameras, the number of pixels of the sensor, the focal length and their position and orientation must be defined.

Rays casting is performed through a discrete volume where the mesh is structured with an equal and regular shape and size of cubes. The model of propagation is not based on the rectilinear propagation of rays but on the equations (Ihrke 2008):

$$p_{i+1} = p_i + \frac{\Delta s}{n} d_i \tag{1.36}$$

$$d_{i+1} = d_i + \Delta s \nabla n \tag{1.37}$$

By means of these, realistic deviations can be obtained even in the case of non-linear phenomena.

The deviations obtained in this way can be considered perfect, without measurement errors and noise. For a simulation more similar to a real case, it is necessary to add a noise to the measurement: a white and homogeneous Gaussian noise is added directly to the deviations. The variance of the noise added is chosen in such a way as to obtain a noise on displacements of about 0.1 pixels, which is a typical value for errors due to image correlation.

1.8 Conclusion and objectives

The BOS is certainly a technique of great interest that has been a great success since its inception. The reasons for this are surely due to the simple set-up and implementation, but also to its ability to build large fields and the possibility of having a non-intrusive and quantitative measure.

For these reasons, ONERA has developed this technique through two PhDs and a team of experts in different fields. The system developed consists of 12 cameras thanks to which it is possible to reconstruct 3D instantaneous density fields. Thanks to the work of Nicolas, the possibility of its use in large wind tunnels has been demonstrated but some difficulties have also been encountered.

The following is the original contribution to the state of the art divided into three different sections.

The potential of the technique is certainly great but it is partly constrained by the resolution that remains limited due to its intrinsic nature. For this reason, different types of setups have been tested experimentally to try to increase the resolution (Chapter 2).

After the choice of the best method for increasing the resolution, the technique has been used to study in detail the screech phenomenon on a supersonic under-expanded jet, improving the measurements previously made by Nicolas et al. (2017b) (Chapter 3). During this campaign, the BOS has been coupled for the first time to acoustic measurements.

Finally, the BOS technique has been used in a slightly more complex situation of a hot jet in cross-flow. Here, some difficulties were emphasized related to the flow geometry, presence of a flat plate and the arrangement of the cameras (Chapter 4). This experiment has highlighted the areas of improvement that still need to be addressed.

Chapter 2

Study of methods for improving the spatial resolution of the BOS technique

Contents

In this chapter, dedicated to the study of methods to improve the spatial resolution of the BOS technique, the effects of the resolution on the measurement are first of all recalled and some solutions to improve the resolution are presented.

The second section presents some details of how the resolution is closely related to the sensitivity and size of the field to be measured. It also describes how to select the characteristic lengths (i.e. l = camera-object distance and m = object-background distance) to optimize a BOS setup.

The following sections focus on some of the methods studied to improve the resolution.

Section 2.3 presents different retroreflective backgrounds and shows the advantages they bring in terms of spatial resolution.

Section 2.4 is dedicated to the use of telecentric lenses in a BOS setup: the equations describing the problem are detailed and compared with those of a classic lens to understand under which conditions it is convenient to use which kind of lens.

Finally, in the last section a series of setups using a speckle pattern as a background for BOS are presented. Here are discussed problems and advantages that are introduced with the use of the speckle. The results obtained with a double-pass speckle setup are compared with measurements obtained with a classic BOS one. Lastly, two BOS setups for the study of small fields are compared.

2.1 Introduction

This chapter stems from the need to find methods to improve the spatial resolution of the BOS technique, which is often not satisfactory for measuring certain types of flow where high resolution is required.

Looking at the data presented in the table 2.1, one notices that some of the installations presented in the literature have rather rough spatial resolutions and consequently they are not fully able to capture the fine details of the flow. The resolutions obtained by these authors range from 1.3 to 6 mm and they depend strongly on the camera aperture (Nicolas et al. 2017b). Surely a resolution of 6 mm is not enough to perfectly describe the flow around a candle where the diameter of the heat flow generated is definitely less than 3 cm. Moreover in Nicolas et al. (2017c) 4.3 mm are likely insufficient to fully capture the relevant scales of a turbulent flow. As far as supersonic flows are concerned, the thickness of the shock is about 200 nm, so even the best resolution equivalent to 1.3 mm, obtained by Nicolas et al. (2017b) with a 70mm lens closed to $f_{\#}$=22, will yield overfiltered measurements in some regions of the flow.

Reference	Flow type	f	$f_{\#}$	δ
Nicolas et al. (2016)	hot and candle plumes	23 mm	2	6 mm
Nicolas et al. (2017c)	hot co-flowing jet	23 mm	2.8	4.3 mm
Nicolas et al. (2017b)	underexpanded jet	70 mm	7.1, 8, 11, 16	2.8, 2.5, 1.8, 1.3 mm
Kirmse et al. (2011)	hypersonic with shock	300 mm	32	4.3 mm

Table 2.1. Comparison of spatial resolution δ of some BOS installations present in the literature.

Indeed, it was demonstrated by the simulation made by Kirmse et al. (2011) that the spatial integration due to the optics alters the position and magnitude of BOS displacements. The same behaviour was observed by Nicolas et al. (2017b) (figure 2.1): in the presence of strong density gradients, spatial filtering yields an underestimation of displacements and a failure to capture high gradients.

This lack of resolution of the BOS technique with respect to the type of phenomena to be studied has required the need to deepen this subject in order to try to improve and understand

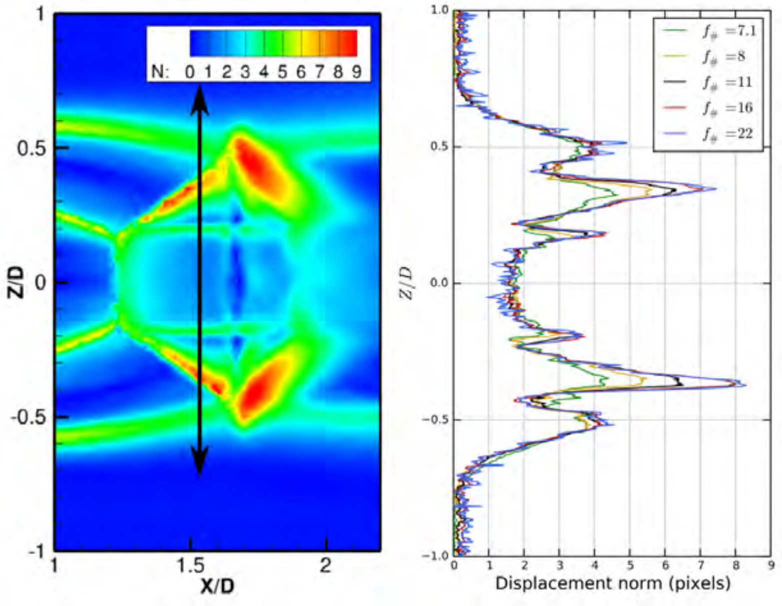

Figure 2.1. Effect of spatial filtering on displacement norm profiles extracted at axial location $X/D = 1.53$ for different $f_\#$ on an underexpanded supersonic jet (Nicolas et al. 2017b).

what the resolution depends on and what strategies can be implemented to reduce the effect of spatial integration on the measurement.

Recalling section 1.3.3, the resolution δ is related to the sensitivity S of the measurement according to the relationship (equation 1.26):

$$\delta = S\frac{1}{f_\#}. \tag{2.1}$$

As a consequence, for a given sensitivity of a setup, a reduction of the spatial resolution is obtained by working with the smallest possible lens aperture, and thus the highest $f_\#$.

Building on this idea and as presented in Chapter 1, solutions exist to improve the resolution of the BOS. Before describing in details the three solutions that were considered, the reasons for the exclusion of some methods and the choice of others are presented.

A first solution is to act on the luminance to reduce the lens aperture as much as possible. It is therefore necessary to use powerful light sources to illuminate the BOS background in order to be able to operate at high f-numbers. As the relative luminance of the image decreases with the square of the f-number, we can write:

$$I_{f_{\#_2}} = \frac{I_{f_{\#_1}}}{\left(\frac{f_{\#_2}}{f_{\#_1}}\right)^2} \tag{2.2}$$

where $I_{f_{\#_1}}$ is the luminance, at the f-number equal to $f_{\#_1}$ and $I_{f_{\#_2}}$ is the new luminance at $f_{\#_2}$. Moreover, since BOS is especially interesting for displaying relatively large fields, it is not possible to concentrate the light beam (to increase the luminance) but it is necessary to illuminate large surfaces. Surely a first solution could be to use light sources capable of producing large amounts of light. For this reason, pulsed lasers are already in use, such as those employed in PIV, which are able to produce large amounts of energy with short pulse durations. There are alternatives such as LEDs, arc lamps and Xenon strobes, but their luminous intensity is still far from that achievable with lasers. The advantage that they offer is that being non-coherent light sources, unlike lasers, no speckle is produced that in some way could degrade the quality of the measurement.

If we exclude the use of new light sources, we can then act on the background with two different strategies. The first is to use a backlit background (Cozzi et al. 2017). This situation immediately appeared to us not suitable for our application: the realization of this type of lighting of backgrounds in a experimental facility as the geode (Nicolas et al. 2016) was not considered easy because of the large dimensions of panels required. Surely it is feasible in the case of small test volumes and mainly applicable in cases with a single surface background. The second solution is the use of retro-reflective backgrounds. In this case the light entering the camera is increased because of the ability of this background to reflect the light. The drawback in this application is that each camera must have its own light source aligned with the optical axis. This approach is detailed further in section 2.3.

Other proposals in the literature put into question the type of lens used in the camera. For instance, it was proposed the use of bi-telecentric lenses. By using these lenses, that work with parallel beams in the test volume, we can obtain higher f-numbers than an endocentric objective. This solution was also investigated during the present work and is further detailed in section 2.4, but it should be borne in mind that these objectives are much more expensive than conventional ones and the field of view is limited by the size of the lenses.

The last method to improve the resolution of the technique is to use a different mounting from the classic setup where the cameras focus on a background placed at a certain distance from the flow of interest. Our attention is drawn to the mounting proposed by A. H. Meier and Roesgen (2013) where in a double pass configuration, exploiting the features of the speckle, it is possible to obtain a maximum resolution by focusing on the test volume while having a non-zero sensitivity. This last type of mounting is the object of interest in section 2.5.3 for its characteristics even if its application to a case with more than one camera may be very complicated from a practical point of view (Buhlmann 2020).

This chapter discusses the three methods investigated to improve the spatial resolution of the measurement, but before that in the next section is analysed the relationship between sensitivity and resolution and the method with which the distances for a BOS assembly are chosen.

2.2 Spatial resolution considerations

In this section the equation of the spatial resolution of the BOS technique (equation 1.25) is resumed, showing how this is related not only to the sensitivity but also to the size of the measuring field; in addition, the dependence on the lens aperture is studied showing that there is theoretically an optimum for a given configuration. The second part is dedicated to the study of the minimum sensitivity necessary to capture a certain temperature step and to the sizing of a BOS setup that optimizes the resolution of the measurement.

2.2.1 Basic equations

As reported in the state of the art, in section 1.3.2, we can write the spatial resolution δ as the sum of two terms (equation 1.25):

$$\delta = \frac{Dl}{m+l} + \frac{\delta_b m}{m+l} = \frac{M}{1+M}\frac{l}{f_{\#}} + \frac{l_{pix}}{M}\frac{m}{m+l} \tag{2.3}$$

where $M = \frac{f}{m+l-f}$ is the magnification factor. The first term of the equation $\delta_a = \frac{Dl}{m+l}$ is related to the circle of confusion and is the width at the density field level of the light cone

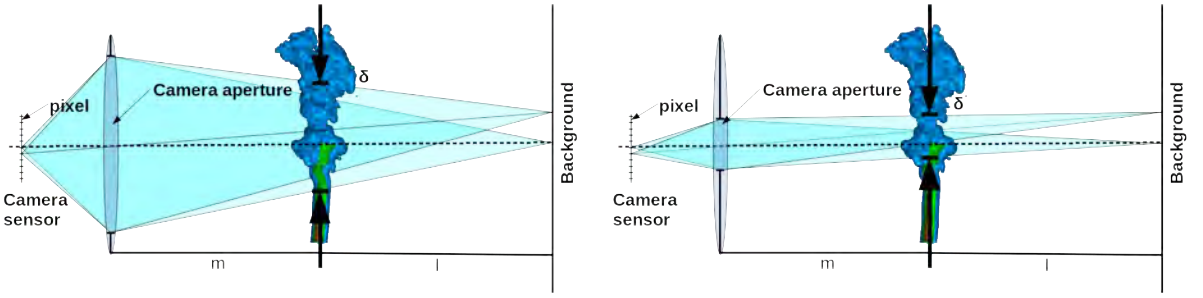

(a) Big camera aperture $f_\#$ leads to big circle of confusion.

(b) Small camera aperture $f_\#$ leads to small circle of confusion.

Figure 2.2. Influence of the lens aperture on the spatial resolution of BOS technique.

emitted from one point on the background. The second is $\delta_d = \frac{l_{pix}/Mm}{m+l}$ and corresponds to the pixel size projected onto the refractive plane.

If we now take diffraction in consideration, the smallest point at which a lens can focus a beam of light is the size of the Airy disk:

$$\delta_{airy} = 1.22\lambda f_\# \tag{2.4}$$

In other words, nothing smaller than the Airy disk can be distinguished because of diffraction. Working for example at $f_\#$=16 and considering a wavelength of 532nm (green), the Airy disk corresponds to 10.38μm, three times the size of our camera pixels (3.45μm). For this reason, the equation should be rewritten by replacing the pixel size with the airy disk:

$$\delta = \frac{M}{1+M}\frac{l}{f_\#} + \frac{1.22\lambda f_\#}{M}\frac{m}{m+l} \tag{2.5}$$

Writing this last expression as a function of the sensitivity S necessary for the measurement and size of the test volume H:

$$\delta = \frac{Sl}{(S+l)\,f_\#} + 1.22\lambda f_\# \frac{H}{h} \approx \frac{S}{f_\#} + 1.22\lambda f_\# \frac{H}{h} \tag{2.6}$$

where h is the camera sensor width.

The resolution of the measurement is therefore directly proportional to the sensitivity and the size of the field to be displayed. Once these two parameters are set, the resolution can be improved only by choosing the lens aperture that minimizes equation 2.6. Moreover, it must be taken into consideration that to improve the resolution it is necessary to reduce the field of view as much as possible by selecting appropriate focal lengths and distances.

Figure 2.3 shows the influence of the camera aperture on the resolution of the measurement. This example shows the measurement resolution as a function of the camera aperture for an installation with typical BOS dimensions. The background-flow distance l is 400 mm, the camera-flow distance m is 1000 mm and the focal length 70 mm. The resulting sensitivity is 21 mm/rad while the displayed range is 115 x 97 mm.

The resolution of the measurement in red (δ), improves when working at smaller apertures, closing the diaphragm of the lens. Acting in this way is the first term, $\delta_a = \frac{Dl}{m+l}$ (in blue), which is strongly reduced and improves the resolution. Conversely, the second term ($\delta_d = \frac{l_{pix}/Mm}{m+l}$)

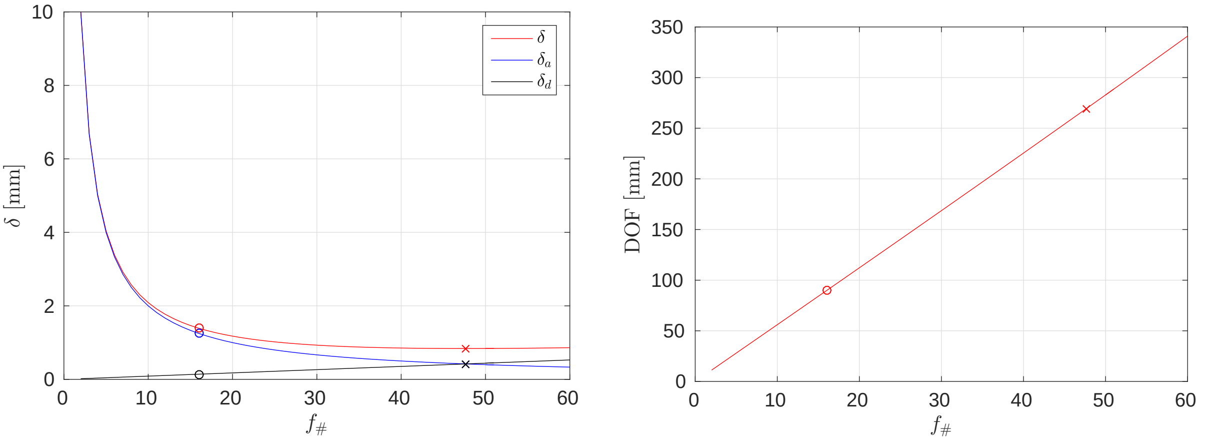

(a) In red the spatial resolution of the measurement δ, sum of the two terms δ_a and δ_d.

(b) The depth of field has a linear relationship with the lens aperture.

Figure 2.3. Spatial resolution and depth of field of the BOS measurement as a function of the lens aperture $f_\#$ for $m = 1$ m, $l = 400$ mm and $f = 70$ mm.

increases and degrades the resolution of the technique. There is an optimal point where the spatial resolution of the measurement is the best: this is reached, in this configuration, at an f-number of 47.65 (red and black crosses). This value is a theoretical value that cannot be reached in reality because of for lack of luminance which, as equation 2.2 shows, must be very high in order to obtain an image where it is possible to distinguish the background patterns with a sufficient signal/noise level to perform image correlation. The optimum lens aperture is therefore impossible to reach with the current light sources and therefore it is not possible to close the diaphragm to reach these values: consequently an f-number that can be reached with the available light sources is about $f_\#$ =16: in the two figures this point is marked with circles and the resolution obtained with this aperture is 1.39 mm.

By analysing the depth of field (figure 2.3b), to see if an object within the area of interest is still sharp or not, it can be seen that the depth of field increases linearly as the f-number increases. Closing the lens to $f_\#$ =16, and focusing on the background, placed at 1.4 m from the camera, the depth of field is about 90 mm and then our object is outside the focus range. Even if the aperture could be closed at $f_\# = 47.65$, the value to obtain the optimal spatial resolution, this would not be enough to have the zone of interest within the depth of field. This shows that BOS is a technique where the flow always remains outside the depth of field even if a very high f-number equivalent to the maximum theoretical resolution could be used.

2.2.2 Dimensioning of a BOS assembly

Once the equation governing the spatial resolution of the measurement was clarified, this section shows the method used to dimension a BOS setup by optimizing the spatial resolution after selecting the type of flow to be studied.

The first step consists in choosing the sensitivity required to have a setup sensitive to a certain deviation induced by the flow. In his reference book on shadowgraphy, G. Settles (2001) provides some of the orders of magnitude of deflection angles for subsonic and supersonic phenomena:

- hot air generated by the friction of the thumb and middle finger: 5-10 arcseconds.
- convection plume over a low-power reading lamp: 10 arcseconds.
- revolver bullet moving just below the speed of sound: 70 arcseconds.

- gas bubble in the air $\varepsilon_{min} = 2\left(1 - \frac{n}{n_0}\right)$ where n is the refractive index inside the bubble and n_0 is that of the surrounding atmosphere. This is the greatest refractions that occurs at the periphery of the bubble through an adaptation of thin-lens of geometrical optics proposed by Keagy Jr and Ellis (1948).

Once we have identified the minimum deviation that our mounting must capture ε_{min} and introduced the minimum displacement that the image correlation algorithm can calculate Δ_{min}, it is possible to find the minimum sensitivity required to detect ε_{min}:

$$S = \frac{\Delta_{min}}{\varepsilon_{min}} \tag{2.7}$$

Then, once the flow size H, focal length f and sensitivity S required for the measurement are selected, the distances can be calculated to achieve the desired sensitivity and field of view. The magnification is obtained according to the sensitivity required for the measurement S, the size of the field H, the focal length selected f and the size of the camera sensor h. An equation of second degree is obtained by considering equations 2.9 ($M = f/(L - f)$), 1.22 ($S = Ml$) and $M = hm/HL$ obtained by simple geometrical optics:

$$fH \cdot M^2 + (fH - hf) \cdot M + Sh - hf = 0 \tag{2.8}$$

In this equation we find the magnification of the system and some quantities that are determined: the focal length f (by choosing the type of lens), the size of the CCD h (by choosing the camera), the size of the flow to capture H and the sensitivity S. Solving this equation yields the magnification as function of h, H, S and f:

$$M = \frac{-\left(fH - hf\right) + \sqrt{\left(fH - hf\right)^2 - 4\left(Sh - hf\right)fH}}{2Hf} \tag{2.9}$$

and consequently the distances write:

$$\begin{aligned} l &= \frac{S}{M} \\ m &= \frac{fM - S + f}{M} \end{aligned} \tag{2.10}$$

This result shows that once the camera is selected (i.e. the CCD size h is fixed) and the lens (focal length f), and a certain sensitivity S and the field to be captured H are selected, the background-flow l and flow-camera m distances are fixed and consequently the resolution of the measurement δ only depends on the lens aperture $f_{\#}$. Varying the distances l and m therefore leads to changes in sensitivity, field of view and consequently in resolution. Hence, in order to improve the resolution of the measurement, once the sensitivity and the field of view are fixed, it is only possible to close the lens diaphragm up to the point where the light is sufficient to be able to distinguish the background patterns with a sufficient signal/noise level to perform image correlation.

2.3 Retroreflective backgrounds

As demonstrated in the previous section, in order to improve the spatial resolution of the measurement it is necessary to close the lens aperture to get closer to the optimal point. What does not allow the optimal $f_{\#}$ to be reached is a lack of light that forces to work at larger apertures, because the relative luminance of the image decreases with the square of the f-number (eq. 2.2).

This section therefore proposes to use a retroreflective background that allows to obtain a greater amount of reflected light compared to a traditional background, thus enabling to work at higher f-numbers and hence improving the resolution of the measurement.

2.3.1 Principle

These backgrounds are characterized by a directional reflection, they reflects the light back to its source with minimum scattering.

There are mainly two different types of reflective bases: the first was invented by 3M in 1930 and consists of glass beads (figure 2.4), the second was introduced 30 years later by Reflexite and is made up of micro-prisms (figure 2.5).

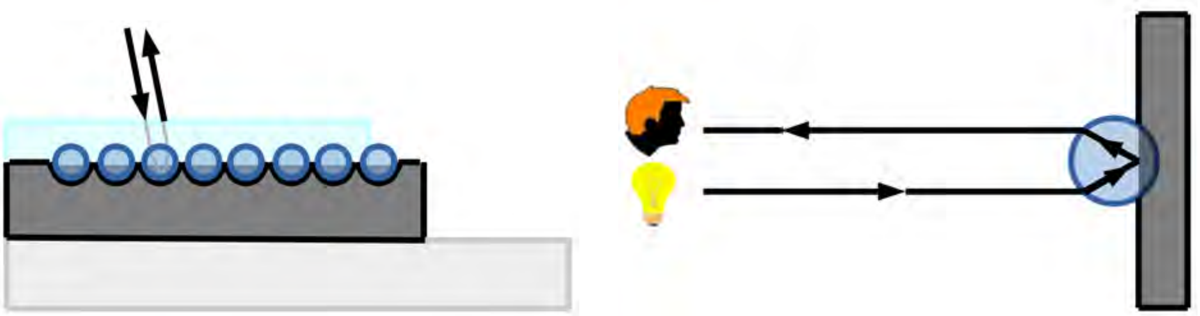

(a) Glass beads based retro-reflective background structure

(b) Glass beads background operating principle.

Figure 2.4. The light entering a perfect glass bead is refracted and then reflected by a reflective film and sent back in the direction of the light source.

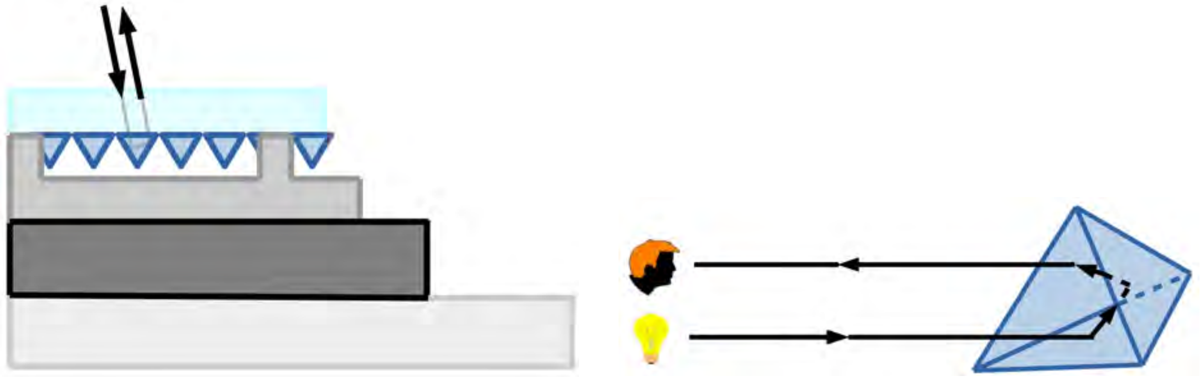

(a) Micro-prismatic based retro-reflective background structure

(b) Micro-prismatic background operating principle

Figure 2.5. Prismatic based retro-reflective backgrounds exploit the geometry of a prism to reflect the light in the direction of the light source.

The first type is based on the principles of light refraction and reflection (figure 2.4b). The light entering a perfect glass bead, with a different refractive index, is refracted and then reflected by a reflective film and sent back in the direction of the light source. As shown in the figure (2.4a), the beads are held on the reflecting surface (black layer) by a transparent resin (blue layer) and then is glued by the adhesive layer (grey).

Microprismatic backgrounds are an evolution of the glass beads ones. They are composed of a series of micro prisms aligned and adjacent to each other. The operating principle is different because it uses the geometry of a prism to reflect the light in the direction of the light source (figure 2.5b). These backgrounds are more efficient than those with glass beads and moreover their distribution is uniform while in the first case there may be dead spaces or overlaps of several beads on top of each other causing a non-homogeneous reflections. Their structure is also different because of the presence of a layer of air that serves to keep the prisms in place (figure 2.5a). For this reason the surface is interrupted by bridges that serve to create these air spaces: here it is not possible to place the prisms and therefore the surface is not retroreflective.

I tested these two different types of backgrounds (section 2.3.3), in particular three products of 3M, white 780mC and Scotchlite 13150 (made with glass beads) and white Scotchlite 823-10 (made with micro prisms). The latter two types of reflective backgrounds were created for warn-marking film for vehicles and road signs while the first was conceived to wrap commercial vehicles.

For glass beads products, data specifications are provided only at a $\beta = 5°$ entrance angle and a $\alpha = 0.2°$ observation angle (angles are compared to the normal of the background): the coefficient of reflection is 75-100 $\mathrm{cd}/\left(\mathrm{lx}\cdot\mathrm{m}^2\right)$. coefficients of reflection for the micro prismatic background are given in table 2.2 for different angles.

α	β	Coefficient of Retroreflection $\mathrm{cd}/\left(\mathrm{lx}\cdot\mathrm{m}^2\right)$
0.2°	5°	250
	30°	150
	40°	110
0.33°	5°	180
	30°	100
	40°	95
2°	5°	5
	30°	2.5
	40°	1.5

Table 2.2. Retroreflection coefficient for micro prisms reflective background (3M Scotchlite 823-10).

Comparing the two materials with the data specifications at similar entrance and observation angles, it can be seen that the surface consisting of prisms has a retroreflective power two and a half times greater.

2.3.2 Constraints

From the table it can be understood that the behaviour of this type of background is strongly dependent on the angle of observation: when an observer is almost in axis with the light source ($\alpha = 0.2°$), the background reflects at its maximum, instead when this angle is increased by 2°, the background loses its effectiveness and the observer is reached only by 2% of the light reflected in the previous configuration. The directional response of this background is very high and therefore the cameras should be mounted as close as possible to the light sources: for example, with a distance of 1.5 m between the camera and the background, the angle of observation between the light source and the camera is 2° when they are only 52 mm away.

In micro-prismatic backgrounds, due to the presence of the bridges necessary for the practical construction of this type of retroreflective film, the surface is not uniformly reflective and therefore in certain areas, due to the absence of micro prisms, there is a lack of information.

For this reason it was decided to use backgrounds made with glass beads. It should be noted that in this case the printed dots must not be too small: a certain amount of beads must be present inside the point to ensure a minimum of reflected light.

One of the problems encountered in the use of these backgrounds is the ink used to print them. First of all, a quick-drying solvent-based Mimaki SS21 ink was used. This ink is suitable for these backgrounds and particularly resistant to scratches but its drawback is that it is brilliant. By positioning the camera in line with the light source, not only are the reflections of the reflective background taken, but the light is also strongly reflected by the ink: the result is a large central spot where the camera is saturated and it is impossible to distinguish any dots of the BOS background.

For this reason it was necessary to use an opaque ink, the Lus170. This is a UV-curable ink and it is cured and adhered to the media by UV radiation. This ink has a wide range of applications and it is suitable for our needs due to its non-reflective nature.

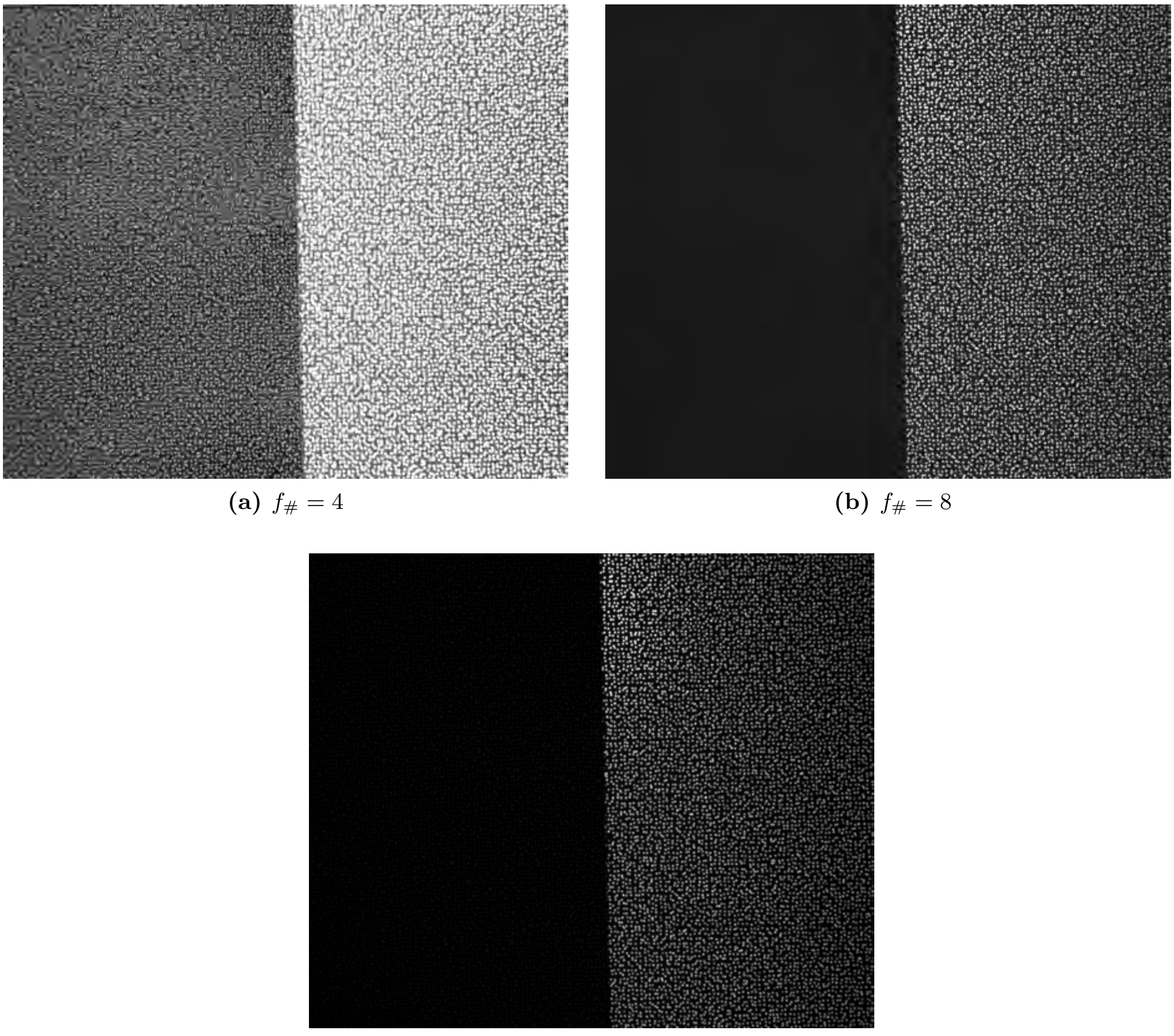

(a) $f_{\#} = 4$ **(b)** $f_{\#} = 8$

(c) $f_{\#} = 16$

Figure 2.6. Photo obtained by combining two backgrounds printed on two different types of material, maintaining the same size and density of the dots: on the left on plain paper and on the right on retroreflective material (3M Scotchlite 13150). The exposure time was kept constant for all three photos ($t = 2$ms).

2.3.3 Retroreflective backgrounds effectiveness test

To demonstrate the advantages of using retroreflective backgrounds, some images were acquired with the same exposure times (2 ms) and with the same illumination, a halogen spotlight located on the axis and next to the camera, of a classic Lambertian BOS background printed in the left half on plain paper and in the right half on a Scotchlite 13150 type retroreflective background. The only parameter that was changed is the camera aperture ($f_{\#}$ =4, 8 and 16). The images thus obtained are shown in figure 2.6. For each image it can be seen that the left part is much darker than the right part where the retroreflective material is present.

A particular attention is given to figures 2.6a and 2.6c: if in the first one because of the great aperture, the background on retroreflective paper results to be saturated, vice versa, increasing the f-number, the zone printed on plain paper results to be completely black. If instead we compare the background printed on plain paper for $f_{\#}$ =4 and the background printed on retroreflective material for $f_{\#}$ =16, it can be seen how the light intensities are comparable: this means that, with the same amount of light used and exposure times, it is possible to switch from an aperture of 4 to 16. Using the formula 2.2, that links the aperture of a lens to the light intensity that passes through it, it can be concluded that the gain in terms of light captured by the camera sensor using a retroreflective background is about 16 times.

The use of retroreflective backgrounds is definitely more expensive compared to plain paper and it is also necessary to take into account that printing is more expensive and complex. Another inconvenience comes from the directional response of the backgrounds and therefore it is necessary to have a light source for each camera: the installation is more complicated and it could be impossible to use several cameras simultaneously. As in the experimentations presented in chapters 3 and 4, the number of cameras used was limited to 8, due to the system used to split the laser beam into as many beams. This type of background definitely brings a great gain, about 16 times, in terms of the light captured by the camera and is an effective method to increase the amount of reflected light by acting only on the background that we identified.

2.4 Telecentric objective

As discussed in the state of the art in section 1.6.2, a telecentric lens is a system in which the chief rays are parallel to the optical axis: this is achieved by placing the aperture stop in one of the focal points of the lens. The image is formed by the parallel projection of the object onto the image plane: the resulting magnification, unlike a common lens, is independent of the distance of the object. These lenses can be divided into two categories: the ones that are either telecentric in object or image space and those that are telecentric in object and image space. In the following it will only be discussed in relation to this latter type of telecentric lens which are also known as bi-telecentric lens due to the double side telecentricity.

What interests us in this section are the bi-telecentric systems, which were used in the BOS technique, by Ota et al. (2015), Leopold et al. (2013) and Cozzi et al. (2017), to improve spatial resolution and depth of field.

2.4.1 Principle and state of the art

To our knowledge, only two different authors have ventured into the use of telecentric lenses for the BOS technique. These are Ota et al. (2015) and Cozzi et al. (2017) and have carried out a series of BOS measurements on different types of flows. Leopold et al. (2013) also used a telecentric lens for BOS measurements but in his particular application he employed the system previously developed by Ota.

Ota et al. (2015) propose to use a bi-telecentric type objective to improve the spatial resolution of BOS measurement. The authors propose to increase the depth of field through a telecentric lens to make possible BOS measurements around models in the flow of interest. This solution is certainly very attractive because it allows to perform measurements around bodies in the measurement volume, which are not possible with a normal lens, because of the limited depth of field, as also described by Leopold et al. (2012): in BOS applications the flow of interest is always outside the depth of field and therefore an object would be blurred degrading the measurement region around it.

Ota et al. (2015) have built a telecentric system using a concave mirror and a camera lens: the decision of choosing a mirror lies in the fact that in this way larger fields can be observed. The BOS measurements were made in the supersonic wind tunnel of the JAXA/ISAS at Mach=2 and the cone model studied has a diameter of 40 mm, a length of 270 mm and a semi apex angle of 20°. Ota et al. (2015) observed numerous improvements due to the use of the telecentric objective compared to a diverging ray observation obtained through the use of a common camera objective. Using the telecentric lens the captured shocks are thinner (thanks to parallel rays observation) and the density gradients through the shock are captured more efficiently. This is possible thanks to the increase in spatial resolution of the measurement which, according to the authors, increases from 1.39-2.9 mm for divergent ray observation, to 0.43-0.58 mm with the use of the telecentric system. Moreover, the depth of field encountered is increased and equal to 1.7 m, for this reason Ota focuses the objective on the model managing to have the BOS background in the depth of field: with this solution both the background and the model in the flow are within the depth of field and therefore BOS measurements are still possible around the model. Through these improvements the authors succeeded in observing Mach waves caused by the surface roughness, which had not been observed with a diverging ray observation.

Also Cozzi et al. (2017) propose to use a telecentric lens to improve the accuracy of the measurement and to eliminate the 3D effects introduced by the use of a conventional lens characterized by a divergent light recording. The Schlieren object studied by Cozzi et al. (2017) is a 2D type flow so that there is no need for a tomographic algorithm for the 3D reconstruction of the density field. The flow is a supersonic 2D over-expanded jet coming out of a convergent-divergent type nozzle of small size: its exit section measures 30 mm. The telecentric lens used by Cozzi et al. (2017) was made in the laboratory and its two main elements are two thin positive focal length lenses distant from each other by the sum of the two focal lengths. A diaphragm is placed in the common focal and the whole is enclosed in a tube so as to collect only light from the front of the lens. A schematic diagram of this lens is presented in figure 2.7. As proposed by Berger (2002), the system was designed to work for conjugated distances so as to have $L = f_1$ and $z = f_2$ in order to minimize the sensitivity to axial positioning errors of optical elements.

2.4.2 Equations driving the depth of field

Following the example of the telecentric lens developed by Cozzi et al. (2017), the equations that characterize the depth of field and the spatial resolution of the measurement are obtained below as a function of some fundamental characteristics of a BOS setup such as the sensitivity and the dimensions of the flow to be displayed.

We emphasize here that this section particularly discusses the properties of the depth of field obtained with such telecentric optical setups since, as detailed later, depth of field and resolution of the BOS measurement are strongly linked: improving the depth of field leads to an increase in resolution.

Referring to image 2.7 which schematically shows the components and characteristic lengths of a telecentric lens and starting from the thin lens equation, it is possible to write this equation for the first lens of this system lenses, (the outermost lens, closest to the flow):

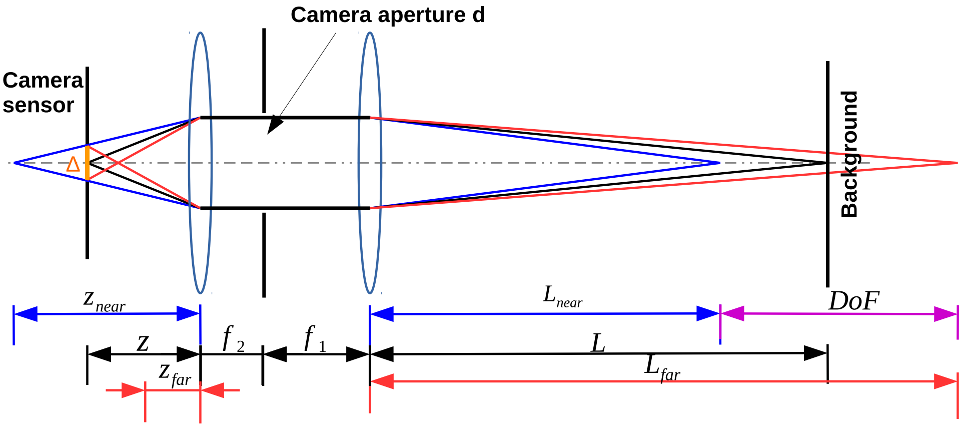

Figure 2.7. Schematic diagram of a BOS setup with a double telecentric lens consisting of two focal length lenses f_1 and f_2 separated by a distance equal to the sum of the two focal lengths and a diaphragm placed at the common focal point of the two lenses. The focusing distances and the corresponding depth of field are plotted.

$$\frac{1}{f_1} = \frac{1}{L} + \frac{1}{z'} \tag{2.11}$$

where L is the focusing distance, ideally the distance between the lens and the BOS background; f_1 is the focal length of lens 1 and z' is the image distance.

By writing the same equation for lens 2, the innermost and closest to the camera sensor:

$$\frac{1}{f_2} = \frac{1}{(f_1 + f_2 - z')} + \frac{1}{z} \tag{2.12}$$

where the focus distance is $f_1 + f_2 - z'$ and z the image distance.

By combining the two equations 2.11 and 2.12, it is possible to obtain the equation describing the image distance for a telecentric system consisting of two focal lenses f_1 and f_2:

$$z = f_2 \left[\frac{f_2}{f_1} \left(1 - \frac{L}{f_1} \right) + 1 \right] \tag{2.13}$$

The image distance is dependent on the focusing distance and on the focal lengths of the two lenses. This equation can be written for different focusing distances, in particular for L_{far} and L_{near} distances that corresponds to the far and near limits of the depth of field of the lens.

$$\begin{aligned} z_{far} &= f_2 \left[\frac{f_2}{f_1} \left(1 - \frac{L_{far}}{f_1} \right) + 1 \right] \\ z_{near} &= f_2 \left[\frac{f_2}{f_1} \left(1 - \frac{L_{near}}{f_1} \right) + 1 \right] \end{aligned} \tag{2.14}$$

As shown in figure 2.7 it can be seen that when the lens is set to focus on the background at L distance, a point at a distance L_{far} or L_{near} corresponds to a certain area on the camera sensor called circle of confusion Δ. This is usually a standard value equal to the diagonal of the camera sensor divided by 1500: in our case, having a CCD sensor of 8.47×7.1 mm, the circle of confusion is 7.37 μm. This is the maximum acceptable circle of confusion: objects outside the depth of field produce larger circles of confusion and the image obtained is blurred.

Knowing the geometry of our lens system and the diameter of the diaphragm d we can write the following ratios that link the circle of confusion Δ to the distances z, z_{far} and z_{near}.

$$
\begin{aligned}
\Delta &= d\frac{z - z_{far}}{z_{far}} \\
\Delta &= d\frac{z_{near} - z}{z_{near}}
\end{aligned}
\tag{2.15}
$$

By introducing the magnification of the system defined as:

$$M = \frac{f_2}{f_1} \tag{2.16}$$

The magnification for a telecentric lens can also be written as $M = h/H$. Where in this case h is the width of the camera sensor and H is the field of view that for a telecentric lens, since it is characterized by parallel rays, is constant and does not vary with the distance from it.

As proposed Ota et al. (2015), the f-number of a telecentric lens is defined as:

$$f_{\#,tele} = \frac{f_1}{d} \tag{2.17}$$

Using equations 2.13, 2.14, 2.15, 2.16 and 2.17, it is now possible to derive L_{far} and L_{near} distances as a function of the focus distance, lens aperture and magnification of the system:

$$L_{far} = \frac{f_2\left(LM + f_{\#}\Delta M + f_{\#}\Delta\right)}{M\left(f_{\#}\Delta M + f_2\right)} \tag{2.18}$$

$$L_{near} = \frac{f_2\left(-LM + f_{\#}\Delta M + f_{\#}\Delta\right)}{M\left(f_{\#}\Delta M - f_2\right)} \tag{2.19}$$

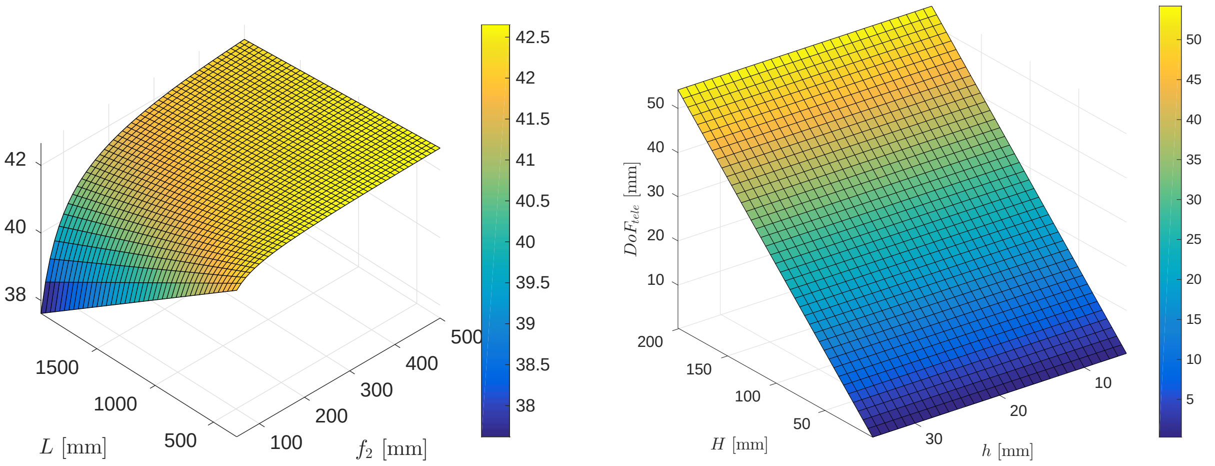

(a) Telecentric lens: $f_{\#} = 155$. Camera sensor size: $h = 8.47$mm. Flow size: H =150mm. Sensitivity: $S = 20$mm/rad.

(b) Telecentric lens: $f_{\#} = 155$. Sensitivity of the BOS setup: $S = 20$mm/rad.

Figure 2.8. Depth of field of a BOS setup, using a telecentric lens, depending on the focusing distance L, the focal lengths chosen in the lens construction f_1 and f_2, the flow size to be captured H, and the size of the camera sensor h.

With these two equations it is possible to determine the depth of field of a telecentric lens and since $M \ll f_2$ the terms in the parenthesis containing M can be deleted by obtaining an equation that is only a function of the maximum acceptable circle of confusion, magnification and f-number.

$$\begin{aligned} DoF_{tele} &= \frac{2 f_2 f_\# \Delta \left(L M^2 - M f_2 - f_2\right)}{M \left(f_\#^2 \Delta^2 M^2 - f_2^2\right)} \\ &\simeq 2\frac{\Delta f_\#}{M} \simeq 2\frac{\Delta f_\# H}{h} \simeq \frac{2}{1500} f_{\#,tele} D = \mathcal{F}\left(D(H), f_{\#,tele}\right) \end{aligned} \tag{2.20}$$

The depth of field can then be written according to some characteristic quantities of the flow to be studied and the camera used: once the camera is chosen, the dimensions of the sensor (h) and the maximum permissible circle of confusion (Δ) are fixed. Then the dimensions of the field (H) are dictated by the type of flow to visualize and finally the diaphragm is stopped as much as possible to have the greatest depth of field and therefore the best resolution, as explained below, at the level of the flow to be analysed. Using the diagonal of the field to be observed (D), it is immediate to understand that the depth of field depends only on the dimensions of the field and the camera aperture $f_{\#,tele}$.

An analysis of orders of magnitude shows that the depth of field of a telecentric lens is slightly dependent on the focal lengths of the two lenses $(f_1$ and $f_2)$ chosen and the focusing length (L). In figure 2.8a this relationship is shown for typical values of a BOS setup: for a fixed sensitivity $S = 20$ mm/rad, a flow size of 150 mm and a f-number of 155, the depth of field given by the approximate formula is 40.4 mm and as it can be seen, using the exact formula and varying L and f_2 the value of the depth of field varies little around the approximate value (for typical values of a BOS setup). The approximation of not taking into account the choice of the two lens focal lengths and focusing distance in the depth of field formula for a telecentric lens can therefore be considered correct.

Figure 2.8b instead shows how the depth of field is independent from the size of the camera sensor: since Δ is defined as the diagonal of the sensor divided by 1500, the formula 2.20 is simplified and is no longer dependent on the size of the sensor h. The graph of the depth of field with respect to the sensitivity is not shown because, as is evident in the formula, this is not dependent on the sensitivity.

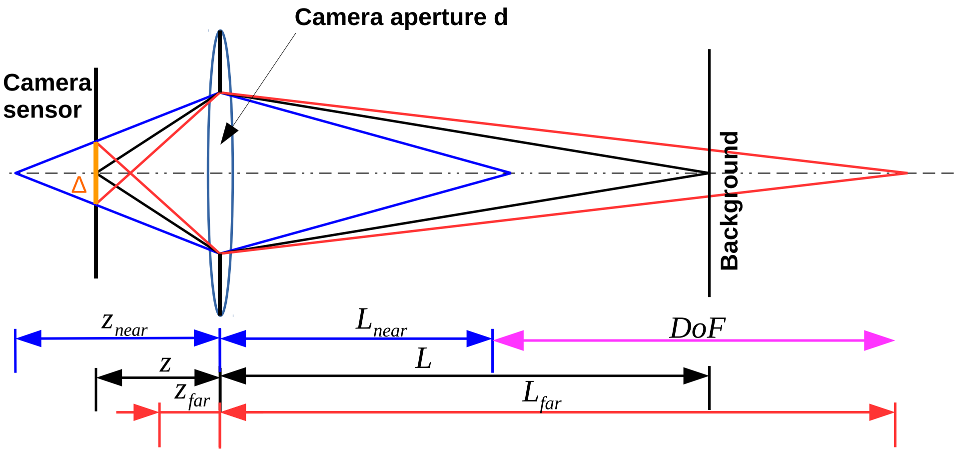

Figure 2.9. Schematic diagram of a BOS setup with a entocentric lens consisting of one lens lens f a diaphragm. The focusing distances and the corresponding depth of field are plotted.

The depth of field of a telecentric lens is now compared with the depth of field of an entocentric lens. The depth of field of an entocentric lens is derived in the same way as before and thus the equations for L_{far} and L_{near} (equations 1.29 and 1.30) presented in section 1.3.4 are obtained. Figure 2.9 shows the characteristic lengths of a telecentric lens for depth of field determination. The depth of field is:

$$
\begin{aligned}
DoF_{ento} &= -2\,\frac{L f^2\,(L-f)\,f_{\#}\,\Delta}{(f_{\#}\,\Delta\,L - f_{\#}\,\Delta\,f - f^2)\,(f_{\#}\,\Delta\,L - f_{\#}\,\Delta\,f + f^2)} \\
&= 2\,\frac{f^2\,(M+1)\,f_{\#}\Delta}{M^2 f^2 - \Delta^2 {f_{\#}}^2} \\
&\simeq 2\frac{\Delta f_{\#}\,(M+1)}{M^2} = \mathcal{F}\left(S, H, h, f, f_{\#,ento}, \Delta\right)
\end{aligned}
\tag{2.21}
$$

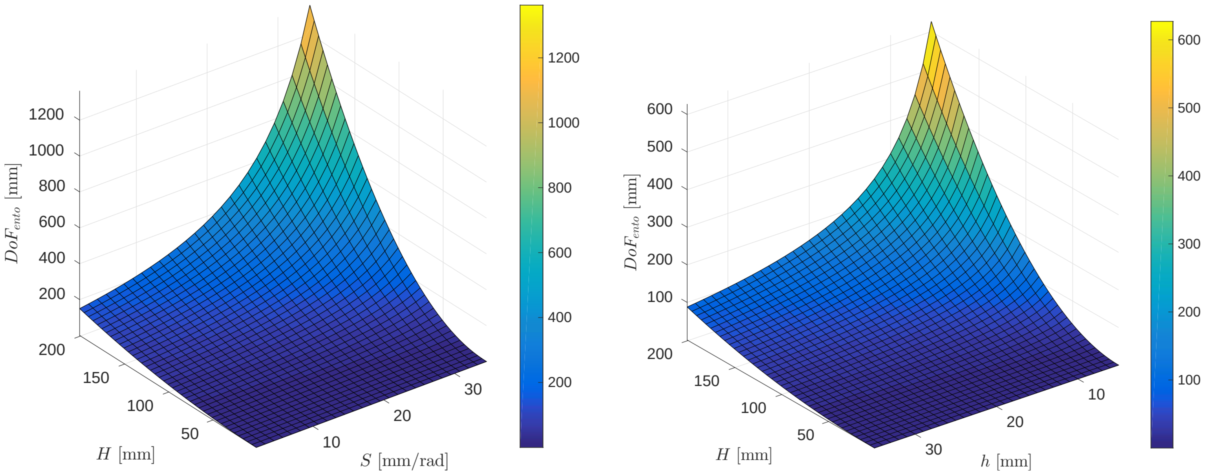

(a) Entocentric lens: $f = 50$mm, $f_{\#} = 16$. Camera sensor size: $h = 8.47$mm.

(b) Entocentric lens: $f = 50$mm, $f_{\#} = 16$. Sensitivity of the BOS setup: $S = 20$mm/rad.

Figure 2.10. Depth of field of a BOS setup, using an entocentric lens, depending on the sensitivity S, the size of the flow to be captured H and the size of the camera sensor h.

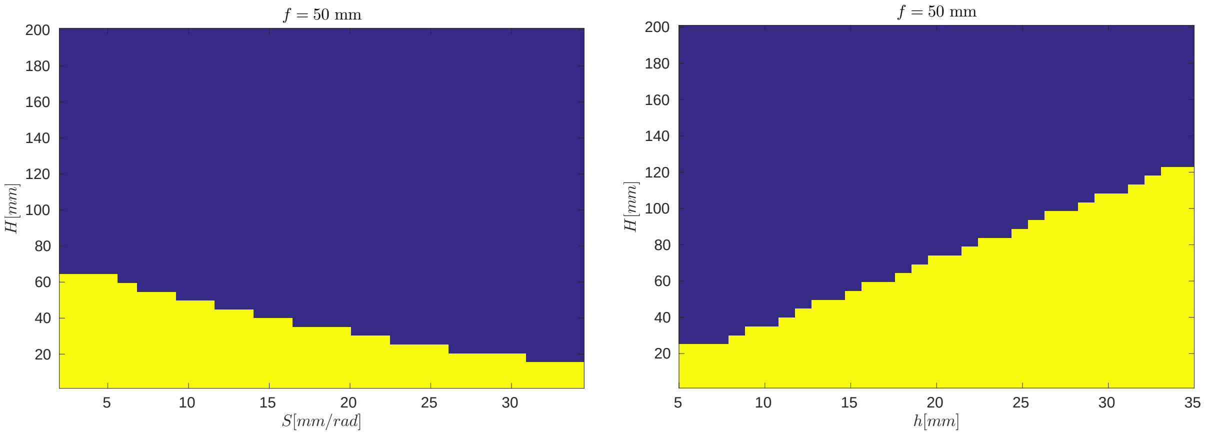

(a) Entocentric lens: $f = 50$mm, $f_{\#} = 16$. Telecentric lens: $f_{\#} = 155$. Camera sensor size: $h = 8.47$mm.

(b) Entocentric lens: $f = 50$mm, $f_{\#} = 16$. Telecentric lens: $f_{\#} = 155$. Sensitivity of the BOS setup: $S = 20$mm/rad.

Figure 2.11. Graphs that highlight where an entocentric or telecentric lens should be used to improve the depth of field for a given setup. In yellow the area where the use of a telecentric lens improves the depth of field of the BOS measurement.

By fixing the field to be displayed (H), selecting the camera (h) and the lens (f) the DoF_{ento} can be written as a function of magnification, thus eliminating the focusing distance. As discussed above in section 2.2 with equation 2.9, the magnification depends exclusively on the sensitivity required for the measurement S, the size of the field H, the focal length selected f and the size of the camera sensor h. The depth of field for an entocentric lens therefore depends on these elements plus the maximum acceptable circle of confusion Δ and the f-number $f_\#$.

Unlike a telecentric lens, the depth of field for an entocentric lens is dependent on both the sensitivity and the size of the camera sensor, as well as the size of H. This dependence is shown in figure 2.10a and 2.10b where the depth of field is plotted as a function of H and S and then H and h.

The two graphs in figure 2.11 show where the depth of field of a telecentric lens is greater than the depth of field obtained with an entocentric lens obtained under the same conditions (camera h, sensitivity of the BOS system S and size of the flow to capture H). The part in yellow corresponds to the area where $DoF_{tele} > DoF_{ento}$ and therefore it designates the conditions under which a telecentric lens should be used to increase the depth of field.

As demonstrated in this section, the depth of field of a telecentric system depends on different parameters than that of an entocentric system. In particular, for a telecentric lens, the depth of field depends only on the size of the flow to be observed H and the aperture of the lens $f_{\#,tele}$; for an entocentric lens there is the same type of dependence, but in addition to these two parameters the sensitivity of the measurement S, the size of the CCD h, the focal length f and the circle of confusion Δ have to be added. It should be noted that the depth of field for a telecentric lens does not depend on the sensitivity required to perform the measurement. The easiest way to increase the depth of field for both lenses is to close the lens as much as possible. As explained in the following section, depth of field and resolution of the BOS measurement are closely linked.

2.4.3 Equations driving the resolution

In this section, as has been done for the depth of field, the spatial resolution δ is obtained as a function of some fundamental characteristics of a BOS setup such as the sensitivity and the dimensions of the flow to be displayed.

The equation for the spatial resolution 2.5 for an entocentric lens can be rewritten as a function of the quantities that are fixed by choosing a certain camera and the characteristic parameter of the test setup needed for the measurement:

$$\begin{aligned}\delta_{t,ento} &= \frac{H\left(-f\left(Kf_\#{}^2+S\right)M_{ento}+Kf_\#{}^2\left(S-f\right)\right)}{f_\#\,h\left(-M_{ento}f+S-f\right)} \\ &\simeq \frac{S}{f_\#}+\frac{K\,f_\# H}{h}=\mathcal{F}\left(S,H,h,f_\#,\lambda\right)\end{aligned} \tag{2.22}$$

the expression that is obtained is a function of the required sensitivity S, the size of the field to be captured H, the size of the CCD h, the focal length f , the f-number of the lens $f_\#$ and the wavelength of the light λ (where $K = 1.22\,\lambda$). Once the camera and the lens are chosen, the lens aperture is closed as much as the light allows (section 2.2.1), and therefore it only depends on the flow to be studied (S and H).

As the sensitivity required for the measurement and the size of the flow to be captured increases, the resolution of the measurement decreases: the image 2.12a shows this effect and it can be seen that once the sensitivity required for the measurement is fixed, it is of fundamental importance to reduce the camera's field of view H as much as possible to improve the resolution. Figure 2.12b shows the spatial resolution as a function of the field to be observed and the size of the camera sensor: having large sensors helps to improve the resolution of the measurement. As explained in section 2.2, it must be taken into account that the size of the pixels is also

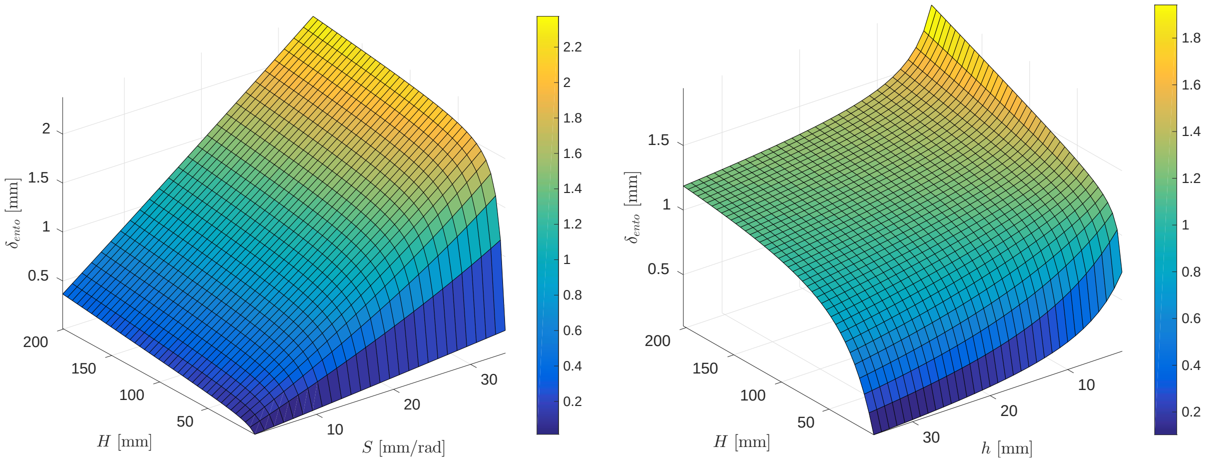

(a) Entocentric lens: $f = 50$ mm, $f_{\#} = 16$. Camera sensor size: $h = 8.47$mm.

(b) Entocentric lens: $f = 50$ mm, $f_{\#} = 16$. Sensitivity of the BOS setup: $S = 20$mm/rad.

Figure 2.12. Spatial resolution of a BOS setup, using an entocentric lens, depending on the sensitivity S, the size of the flow to be captured H and the size of the camera sensor h.

important: if these are larger than Airy's spot then it must be taken into account and the resolution is reduced.

If on the one hand with the use of an entocentric lens the BOS technique is capable of capturing large fields, on the other hand it is necessary to be careful to evaluate the spatial resolution to understand up to which scale the measurement correctly captures the small structures of the flow.

After having presented the spatial resolution of the BOS measurement using an entocentric lens, the parameters affecting the resolution of the measurement for a telecentric lens type are discussed below. For a telecentric objective the formula given by Cozzi et al. (2017) can be derived:

$$\delta_{t,tele} = \frac{l}{f_{\#,tele}} + \frac{\delta_{airy,tele}}{M_{tele}} = \frac{l}{f_{\#,tele}} + 1.22\,\lambda f_{\#,tele} \tag{2.23}$$

where $\delta_{airy,tele}$ is the size of the Airy disk for a telecentric system and defined as:

$$\delta_{airy,tele} = 1.22\,\lambda \frac{f_2}{d} \tag{2.24}$$

where d is the aperture of the lens.

Equation 2.25 can be written as a function of the field to be displayed, the size of the camera sensor and the aperture of the lens:

$$\delta_{t,tele} = \frac{K {f_{\#,tele}}^2 h + HS}{f_{\#,tele}\, h} = \mathcal{F}\left(S, H, h, f_{\#,tele}, \lambda\right) \tag{2.25}$$

The spatial resolution of the measurement, using a telecentric system, once the camera was selected and the type of flow to be studied, depends exclusively on the aperture of the lens.

The spatial resolution of a telecentric lens as a function of the field of view, the sensitivity required for the measurement and the size of the camera is plotted in figures 2.13a and 2.13b. It can be seen, from figure 2.13a, that as the field of view and sensitivity increase, the spatial resolution of the measurement degrades. The same phenomenon occurs when the size of the camera sensor decreases (figure 2.13b): this means that to obtain good spatial resolutions it is

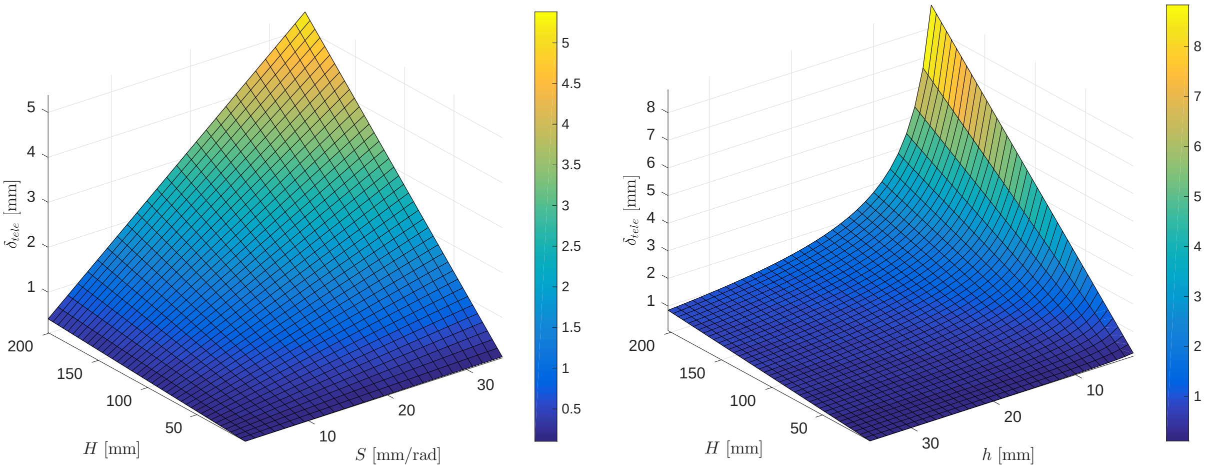

(a) Telecentric lens: $f_{\#} = 155$. Camera sensor size: $h = 8.47$mm.

(b) Telecentric lens: $f_{\#} = 155$. Sensitivity of the BOS setup: $S = 20$mm/rad.

Figure 2.13. Spatial resolution of a BOS setup, using a telecentric lens, depending on the sensitivity S, the size of the flow to be captured H and the size of the camera sensor h.

necessary to work at large magnifications, using cameras with larger sensors or observe smaller fields.

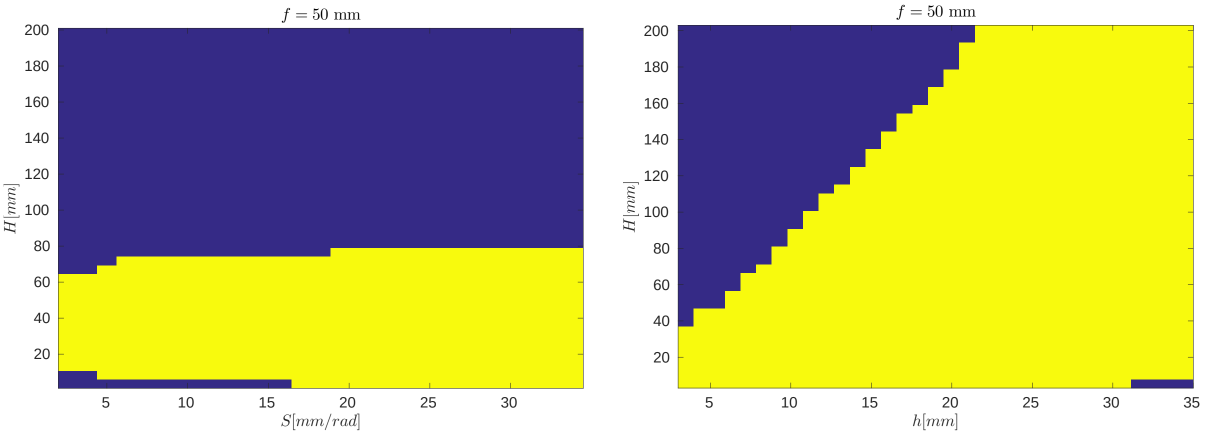

(a) Entocentric lens: $f = 50$ mm, $f_{\#} = 16$. Telecentric lens: $f_{\#} = 155$. Camera sensor size: $h = 8.47$mm.

(b) Entocentric lens: $f = 50$ mm, $f_{\#} = 16$. Telecentric lens: $f_{\#} = 155$. Sensitivity of the BOS setup: $S = 20$mm/rad.

Figure 2.14. Graphs that highlight where an entocentric or telecentric lens should be used to improve the spatial resolution. In yellow the area where the use of a telecentric lens improves the resolution of the BOS measurement.

As shown in figure 2.14a, it is advantageous to use telecentric lenses to work with small H fields of view. Moreover, from graph 2.14b, it can be observed how to increase the size of the sensor of the camera h, is of help to capture larger fields. It must be remembered that these are however the limits where it is convenient to use a type of lens or another one. Besides the convenience in the use of a certain type of lens, it must be considered that the telecentric lenses that are found in commerce have decidedly higher costs in comparison to the entocentric lenses, moreover it must be reminded, that to work with parallel rays, the optical parts of the telecentric objectives must be of the dimensions of the field to observe. In view of these considerations, it is necessary to state that it is not appropriate to use these objectives if the field of use is in an area close to the limit of convenience (yellow-blue border).

By using the approximate formula to calculate the spatial resolution of an entocentric lens 2.22 and making it equal to the spatial resolution of a telecentric lens 2.25, it is obtained the limit field of view for which the spatial resolution of the two types of lenses is equal. This depends only on the f-numbers ($f_{\#,tele}$ and $f_{\#,ento}$) of the two lenses and the size of the camera sensor h and is given by the relationship:

$$H_{lim} = \frac{f_{\#,tele}\, h}{f_{\#,ento}} \tag{2.26}$$

This formula therefore tells the maximum flow size beyond which to use a telecentric lens is not more convenient in terms of spatial resolution during a BOS measurement.

As an example, estimating the value for a typical BOS setup, taking an f-number of 16 for an entocentric lens and 155 for a telecentric lens (as used in Cozzi et al. (2017)) and considering the sensor size of our cameras h=8.47 mm, a limit size of 82 mm is obtained, beyond which it is no longer convenient to use a telecentric lens. It can be noted that this value is relatively small and therefore it can be concluded that the convenience in using telecentric lenses is limited to small fields. This value is significantly smaller than the dimensions of the phenomena of interest in our study, such as under-expanded jets and hot jets (Chapters 3 and 4), therefore it can be concluded that telecentric appears not adapted to our experimental contexts.

2.4.4 Conclusion

This section compared the characteristic equations of telecentric and entocentric lenses with respect to depth of field and spatial resolution in a BOS setup. These equations were rewritten by looking for the characteristics of the optical setup needed to make the measurement, such as sensitivity and size of the flow to be captured, and the fixed quantities once the type of camera and lens was chosen (sensor size and maximum f-number), remembering that in a BOS setup the object of interest is always outside the depth of field and that the feature that is of interest is the spatial resolution of the measurement. Spatial resolution for BOS techniques improves under certain conditions when a telecentric lens is used: through the equations of spatial resolution for a telecentric 2.25 and an entocentric 2.22 system (Figure 2.14) it was proven that the field of view must be small and therefore when displaying large fields of view it is convenient to use classic lenses. The maximum flow size H_{lim} beyond which an entocentric lens should be used is given by equation 2.26. In addition to convenience in one type of lens or another, it must be taken into account that telecentric lenses, since they work with parallel and not divergent rays, are limited by the size of the optical components that make it up: the diameter of the outermost lens determines the maximum size of the field of view.

We have characterized precisely the domains of interest of both entocentric and telecentric lenses, in a more systematic way than previous works on the subject, and we conclude that the telecentric lens is not well adapted to the dimensions of the phenomena that we intend to study here. Another factor not to be underestimated is the quality of the lenses, which must be of excellent quality and often is not sufficient to have an undistorted image: the telecentric lenses on the market are not made by only two lenses but by many, precisely to eliminate possible distortions. A telecentric lens was assembled and tested in the laboratory but the results obtained in terms of image quality were not at all satisfactory, probably due to the quality of the lenses used. The purchase of a telecentric lens to observe 150 × 200 mm fields was considered, but their high cost of 7 to 10 k€per lens, multiplied by 8 cameras, made us quickly change our mind.

For the reasons listed above, it was considered that the telecentric objective is not a valid solution to improve the spatial resolution of the BOS for the applications we considered. For this reason, other solutions such as the use of speckle are studied in the next Section to improve spatial resolution.

2.5 Speckle BOS

The objective of this section is to present the work aimed at improving the BOS resolution with backgrounds. Our attention is drawn to the mounting proposed by A. H. Meier and Roesgen (2013) where in a double pass configuration, exploiting the features of the speckle, it is possible to obtain a maximum resolution by focusing on the test volume while having a non-zero sensitivity in contrast to classical BOS.

After describing what speckle is, this section focuses on some properties, such as the distribution of light intensity and dot size, which are essential for its use as a projected background for BOS. In the following subsections three setups particularly investigated in this work are presented: an in-line speckle setup more similar to the classic BOS, a setup with a double passage of light through the flow and a speckle setup adapted to small fields.

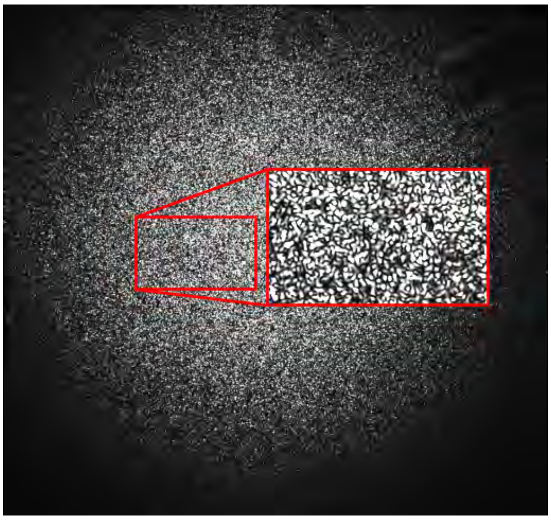

Figure 2.15. Details of a speckle pattern and its halo.

2.5.1 Principles of speckle generation

A speckle pattern is obtained whenever an optically rough surface is illuminated with highly coherent light (such as the one emitted by lasers): the speckle pattern presents a particular intensity distribution, which consists of a fine granular structure that alternates dark and bright spots of variable shapes, distributed in a random way. Moreover, the shape of this pattern has no relation to the macroscopic properties of the surface. This particular distribution of intensity is also obtained when coherent light is propagated through a medium that presents random variations in its refractive index.

Speckle can be registered by placing an image sensor at any distance from the object. For this reason it is not mandatory to use an image forming system to observe a speckle pattern.

To generate a speckle pattern one has to illuminate an optically rough surface with a coherent and collimated light of wavelength λ; such that the height variations of the illuminated surface are greater than λ: this is the case for most materials, since the wavelength is about 0.5 μm.

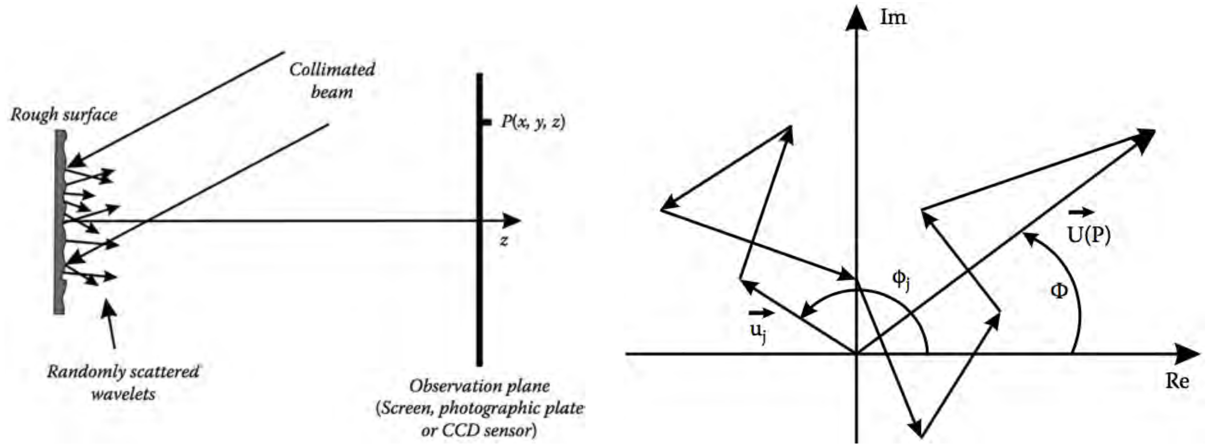

(a) Physical origin of speckle pattern: diffuse reflection of coherent light from rough surface.

(b) Sum in the complex plane of several scattered fields $u_j\left(P\right)$ with their respective random phases ϕ_j contributing to the total field $U\left(P\right)$.

Figure 2.16. The collimated light emitted by a laser impacts a rough surface, the light is reflected by the surface and after that it can be decomposed in several randomly scattered wavelets: all these interfere on an observation plane generating the speckle pattern. The contribution at a point P on the observation plane is the result of the sum of several scattered wavelets with random phases. Rabal and Braga Jr (2018)

After the light is reflected by the surface, as illustrated in figure 2.16a, the randomly scattered wavelets constructively of destructively interfere at points $P\left(x, y, z\right)$ on the observation plane, ultimately yielding a speckle pattern. In other words, each point in a speckle pattern is the sum of a large number N of components representing the contribution from all points on the scattering surface. As shown in figure 2.16b, we note $u_j\left(P\right)$ the N components of the scattered field arriving at point P on the observation plane, such that:

$$u_j\left(P\right) = \left|u_j\right| e^{i\phi_j} = \left|u_j\right| e^{ikr_j} \tag{2.27}$$

ϕ_j is a random phase, r_j is the distance between the point of origin of the considered light field on the rough surface and the point P on the observation plane, and k is the wavenumber. The total field at point P can then be expressed as a complex number such that:

$$U\left(P\right) = \frac{1}{\sqrt{N}} \sum_{j=1}^{N} u_j\left(P\right) = \frac{1}{\sqrt{N}} \sum_{j=1}^{N} \left|u_j\right| e^{i\phi_j} = \frac{1}{\sqrt{N}} \sum_{j=1}^{N} \left|u_j\right| e^{ikr_j} \tag{2.28}$$

Because of the random phases ϕ_j, the sum in equation 2.28 results in random motion in the complex plane, as also shown in figure 2.16b. Assuming that the amplitude u_j and the phase ϕ_j are statistically independent of each other and the phases ϕ_j are uniformly distributed on $(-\pi, \pi)$ and with a large number of N, Goodman (2007) demonstrated that the real and imaginary parts of the resultant field have Gaussian distributions. The joint probability density function is thus:

$$p_{r,i}\left(U^{(r)}, U^{(i)}\right) = \frac{1}{2\pi\sigma^2}\exp\left[\frac{\left(U^{(r)}\right)^2 + \left(U^{(i)}\right)^2}{2\sigma^2}\right] \tag{2.29}$$

where

$$\sigma^2 = \lim_{N\to\infty} \sum_{j=1}^{N} \frac{\langle |u_j| \rangle^2}{2}$$

and

$$U^{(r)} = \sqrt{I}\cos\Phi$$
$$U^{(i)} = \sqrt{I}\sin\Phi$$

where I and Φ are respectively the intensity and the phase of the resultant field $U\left(P\right)$. The probability density of the intensity and of the phase can be written as:

$$p\left(I\right) = \frac{1}{\langle I \rangle} e^{-\frac{I}{\langle I \rangle}} \qquad \text{for} \qquad I \geqslant 0 \tag{2.30}$$

and

$$p\left(\Phi\right) = \frac{1}{2\pi} \qquad \text{for} \qquad -\pi \leqslant \Phi \leqslant \pi \tag{2.31}$$

where $\langle I \rangle$ is the intensity mean value of a speckle pattern. Therefore, according to equations 2.30 and 2.31, the intensity distribution follows a negative exponential law, while the phase is uniformly distributed in the range $(-\pi,\, \pi)$. Examining image 2.15 that displays a speckle pattern, it is difficult to confirm this type of distribution where dark areas should be more frequent than bright areas. This result indicates that the intensity distribution of a speckle background is different from that of a classic BOS background (double peaked distribution), obtained through the printing of a dotted pattern on a sheet of paper or retro reflective material. The intensity distribution of a speckle background causes some speckle grains to have a small difference in intensity compared to the black background. As a result, the signal-to-noise ratio is lower than when using a classic BOS background.

After having exposed the characteristics of intensity distribution of a speckle background here below we analyse another fundamental parameter for BOS setup which is the size of the pattern: this, as already explained in section 1.7.1, must be optimized for the image correlation process that requires an optimal size of 3 pixels per dot. Speckle size was extensively discussed by Goodman (2007) and here in the follow is reported the main equation which is used to understand which parameters affect the size of the speckle dots.

An approximate average diameter of the speckle (Goodman 2007) can be estimated by:

$$\varnothing_{speckle} = \frac{4}{\pi}\lambda f_{\#} \tag{2.32}$$

Therefore, once the type of laser and hence the wavelength of light (λ) are chosen, it only depends on the aperture of the lens ($f_{\#}$) and is completely independent of distances m, l and s (distance between the flow and the speckle screen). What must be taken into consideration is that the size of the speckle can be adjusted independently of the geometry of the BOS setup acting only on the lens aperture; using a green laser (λ=532nm) and a lens aperture $f_{\#}$=16, the diameter of the speckle is 10.8μm.

2.5.1.1 Principles of double-pass speckle BOS

The double-pass speckle BOS setup was first proposed by A. H. Meier and Roesgen (2013) and is particularly interesting because of the possibility to focus on the flow of interest while having a measurement sensitivity different from zero: this is possible because of the double-pass of the laser through the flow. In this way, the measurement sensitivity is independent of

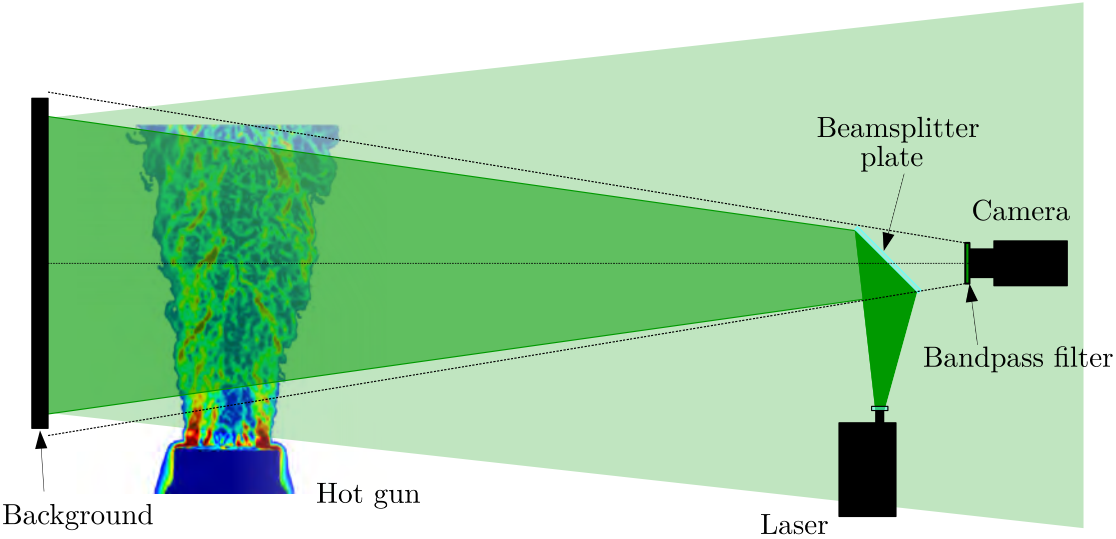

Figure 2.17. Diagram of a double-pass BOS set-up. In order to generate the speckle pattern and obtain a large amount of light, the background used is a sheet of retroreflective material. A 50:50 beamsplitter plate was used to align the laser with the axis of the camera.

the measurement resolution and is increased by varying the distance between the flow and the speckle screen (s). On the other hand, since the lens is focused on the flow, the resolution is the maximum possible achievable and moreover, an object in the field of interest would be sharp, eliminating the areas of incertitude introduced by the blurred region around the model.

The sensitivity formula is given by A. H. Meier and Roesgen (2013) and can be obtained through geometrical relationships. The sensitivity for a speckle BOS double-pass setup is given by:

$$S = M\,(2l - s) \tag{2.33}$$

It must be taken into account, however, that the distance l, between the flow of interest and the focus position, is zero because the lens is focused on the flow. For this reason the sensitivity is affected by shifting the background where the speckle is generated (by varying the flow-background distance s). Moreover, it is necessary to note the presence of the minus sign in front of the distance s: this, as illustrated in images 2.26a and 2.23 and in 2.28, influences the sign of the displacements that are countersigned with respect to the displacements obtained with a classic BOS setup. By focusing on flow the sensitivity that is achieved is:

$$S = -\frac{f}{m-f}\,s \tag{2.34}$$

The sensitivity thus depends on the focal length f, focus distance and position of the flow m and the distance between the flow and the screen generating the speckle s.

The sensitivity of a speckle BOS double-pass set-up is given by equation 2.34 (A. H. Meier and Roesgen 2013), whereas the resolution is given by equation 2.5 $\delta = \frac{M}{1+M}\frac{l}{f_\#} + \frac{1.22\lambda f_\#}{M}\frac{m}{m+l}$. In contrast to standard BOS one can improve the resolution by setting $l = 0$ (the focus is made on the flow) without setting the sensitivity to zero. The spatial resolution obtained by focusing on the flow in a double pass speckle setup is:

$$\delta = \frac{1.22\lambda f_\#}{M} \tag{2.35}$$

Taking an example, for a measurement range of 150mm, a spatial resolution of 0.18mm is obtained by working at a lens aperture of 16: this leads to 7 times the resolution improvement compared to a classic BOS setup.

In the next sections, we investigate three speckle BOS configurations: an in-line speckle setup more similar to the classic one (2.5.2), a setup with a double passage of light through the flow (2.5.3) and a speckle setup adapted to small fields(2.5.4).

Following theoretical details presented in the previous section, we now experimentally examine the benefits and the drawbacks of using speckle for BOS.

2.5.2 In-line single pass speckle BOS

To this end, we particularly consider the following configuration that allows to collect a significant amount of light on the camera sensor, thus providing low exposure times. This is shown in the diagram in figure 2.18 is referred to as the in-line single pass setup: pointing the laser in the direction of the camera and using a ground-glass as a speckle generator.

The purpose of this section and of this specific setup is to show how the speckle impacts the correlation of images and degrades the quality of the measurement.

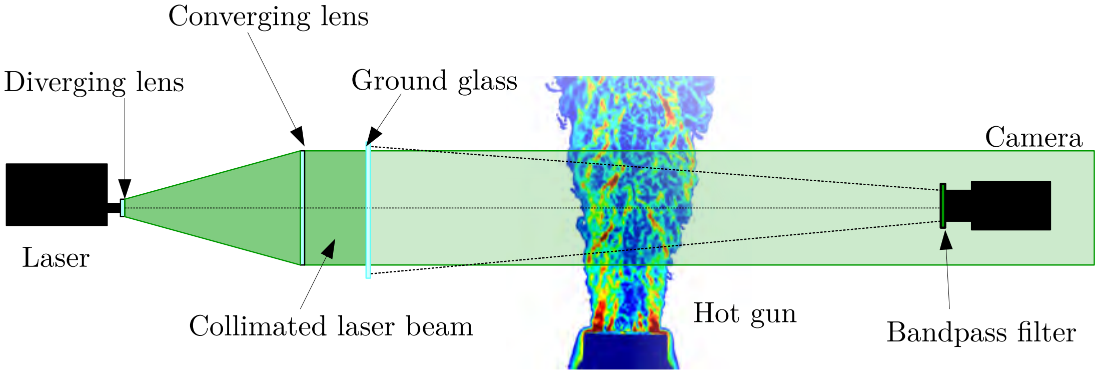

Figure 2.18. Diagram of a in-line single-pass speckle BOS setup. The laser is mounted in front of the camera to collect a greater amount of light. The speckle generator is composed of a ground glass.

2.5.2.1 Setup, sensitivity and spatial resolution

The light source used is a SLIM Oxxius continuous laser with a wavelength of 532nm, a power of 300mW and a long coherence length to have a stable speckle. The beam is collimated through two lenses, one diverging and then one converging, before passing through the ground glass. The flow, as in the case of a classic BOS setup, is between the camera and the background, in this case the ground glass generating the speckle. To recover only the light emitted by the laser, a bandpass filter of the same wavelength as the laser was used. The object of study is a hot jet issued from a hot air gun operated at a temperature of 250°C measured using a thermocouple. The aperture of the camera was adjusted to have a speckle size of about 3 pixels, which is optimal for the image correlation algorithm: in the current case the lens was stopped at $f_{\#}$=16 obtaining a speckle size of 3.3 pixels (equation 2.32 for speckle diameter).

Thanks to the characteristics of the speckle, it is possible to focus the lens at any distance, obtaining a pattern that is always in focus. For this reason the speckle is interesting to perform measurements where it is impossible to place a background due to limited distances or to perform measurements next to the wall where there would be zero sensitivity. This part was widely discussed by A. H. Meier and Roesgen (2013) where it is shown that the sensitivity is a function

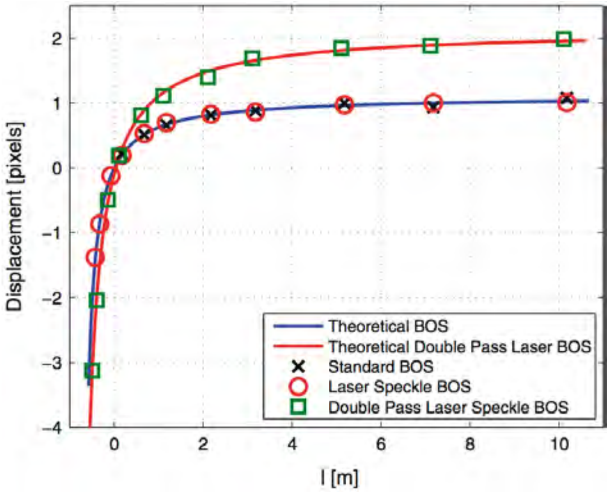

Figure 2.19. Displacement as function of the focusing distance for standard and speckle BOS measurements (A. H. Meier and Roesgen 2013).

of the focusing distance. As it can be seen from figure 2.19 the sensitivity of the measurement is greater for negative values of l, that is when the lens is focused between the camera and the flow.

The sensitivity formula for a single-pass speckle mount, as also given by A. H. Meier and Roesgen (2013), remains the same as for a classic BOS system. As stated in section 1.3.1 , the sensitivity is given by:

$$S = \frac{f\,l}{m + l - f} \tag{2.36}$$

As one can see, the sensitivity of the measurement depends only on the focal length f and the focusing position (m and l) and does not depend on the distance between the surface generating the speckle and the flow (s).

The resolution of the measurement also remains the same as in a classic BOS mount (equation 2.5), always paying attention to the focusing distance l:

$$\delta = \frac{M}{1+M}\frac{l}{f_\#} + \frac{1.22\lambda f_\#}{M}\frac{m}{m+l}$$

2.5.2.2 Main results

In the figure 2.20 the measurements made at two different sensitivities can be seen: in the left column with an approximately null sensitivity, by focusing on the mid-plane of the flow, and in the right column at a sensitivity of 12.4mm/rad by focusing at 200mm from the flow. As one would have expected the displacements obtained with a null sensitivity are approximately zero while they are not null for S=12.4mm/rad. Looking in detail at the displacements for zero sensitivity in figure 2.20a, it can be seen that they are not exactly zero and some areas characterized by a non-null displacement appear.

In the figure 2.20a, from the norm of displacement, one can distinguish the truncated cone shaped area where the flow is present: some displacements are detected by the camera. The cause of this unexpected effect can be attributed to two possible reasons: the first reason may be due to the depth of the flow and since the sensitivity can only be null in a plane, some displacements are detected by the camera while the second is related not to motion but to local changes of the speckle pattern as will be studied later on.

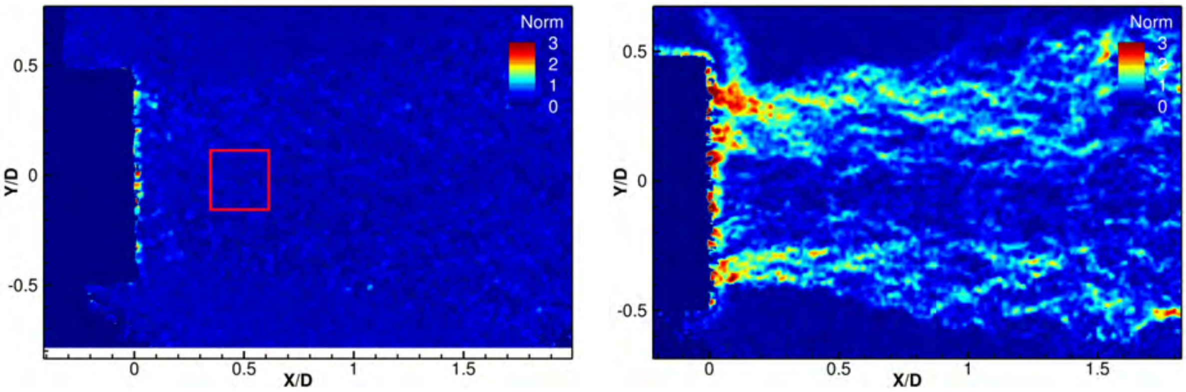

(a) Instantaneous displacements Norm for S = 0mm/rad. The red square is the area from which the speckle background in figure 2.21 was obtained. **(b)** Instantaneous displacements Norm for S = 12.4mm/rad.

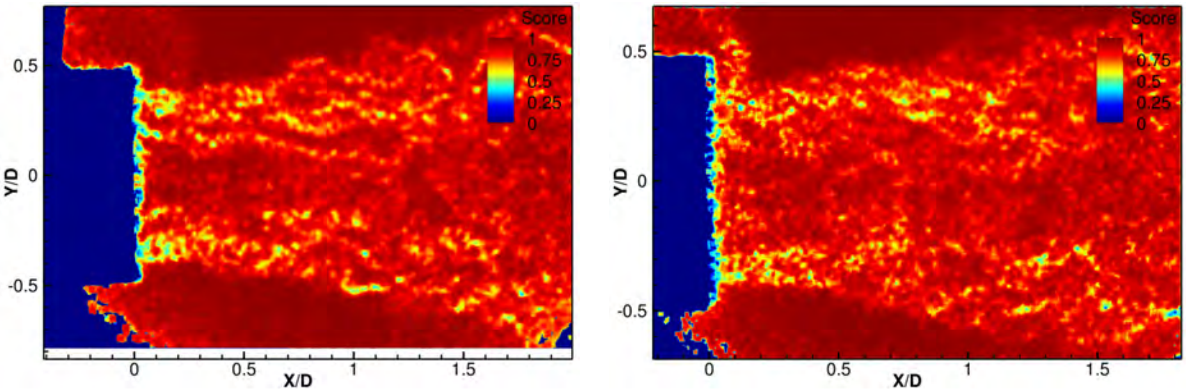

(c) Correlation Score for $S = 0$mm/rad. **(d)** Correlation Score for $S = 12.4$mm/rad.

Figure 2.20. Instantaneous results obtained using a hot gun in two configurations with different sensitivities: on the left the results are obtained with a zero measurement sensitivity on the right instead the mounting sensitivity is $S = 12.4$mm/rad.

Comparing the score of the correlation between the image acquired without flow and the one with the flow, it is possible to see that both are degraded. First of all it must be noted that the score is degraded in the same way in the measurements with zero sensitivity and with a sensitivity equal to 12.4mm/rad. This means that the confidence in the calculation of the displacements does not depend on the sensitivity of the measurement but on the use of the speckle as background.

Looking at the two images 2.20c and 2.20d it can be seen that the score is strongly impacted by the presence of the flow: outside of it, where the background does not change, the score remains close to the maximum value. In presence of the flow the score is strongly degraded where large displacements are observed (see figure 2.21b) and therefore where large density variations are present.

Furthermore, the resolution of the measurement does not influence the correlation score: in case of zero sensitivity the resolution of the measurement is maximum but the score is affected in the same way.

To investigate why the score decreases in the presence of a flow, the raw photos in figure 2.21 of the zero-sensitivity setup with zero displacements were analysed. Figures 2.21a and 2.21b are a zoom of the two images with and without flow taken in an area at the exit of the

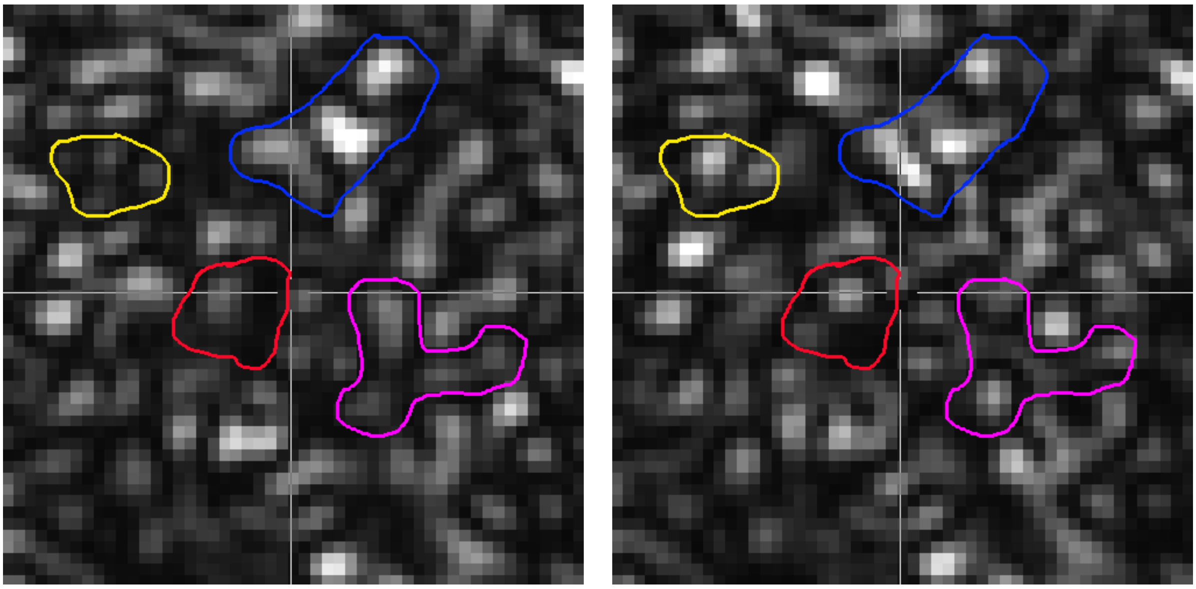

(a) Part of the raw image without flow.

(b) Part of the raw image with flow.

Figure 2.21. Shape and brightness changes of the speckle pattern caused by the presence of a flow for zero measurement sensitivity. There are no displacements due to zero sensitivity. This background area was grabbed in an area within the flow shortly after the hot gun exit, represented in the red square in figure 2.20a.

gun where the flow is present. As it can be seen for the points of the pattern formed by the speckle, the displacements are null but the pattern varies considerably. What is observed are strong variations in the light intensity of the speckle pattern that lead to a change in the shape of the pattern. In figures 2.21, local changes in the speckle pattern have been highlighted with coloured contours. Because of these pattern variations the algorithm for the estimation of the displacements yield poor correlation scores. Furthermore, variations in the brightness and shape of the pattern may induce apparent displacements that are not present but only an effect due to the changes mentioned above. This explains why the norm of displacements, for the zero sensitivity setup, is not zero (figure 2.20a).

Measurements with zero sensitivity have helped to understand the reason for this degradation because they have eliminated the pattern displacements introduced by the flow, maintaining only the effects of the flow on the variation of the speckle pattern. Even in the case with a sensitivity different from zero (figure 2.20b), apparent and spurious displacements are added to real displacements causing a degradation in the confidence in the calculation of the displacement actually introduced by the flow.

These first measurements with speckle BOS have shown that due to shape and brightness changes of the speckle pattern, spurious displacements are introduced that are not inherent to the observed flow. Moreover these variations affect the image correlation and degrade the quality of the measurement. To understand how much the measurement is affected by the changes introduced by the speckle, it is important to compare a BOS speckle measurement with a BOS measurement made with a classical background (printed on paper), this is done in section 2.5.3 on a double-pass speckle BOS setup.

2.5.2.3 Buhlmann results on speckle decorrelation

In parallel to the present work, Buhlmann (2020) completed a PhD on similar topics using a BOS setup using speckle as background. This subsection is dedicated to the presentation of the results he has achieved, in accordance with those presented in this section.

Buhlmann (2020) also observed intensity changes in speckle in the presence of strong light deflections, caused by strong refractive index gradients: he had to deal with measurements strongly influenced by speckle decorrelation.

Investigating on speckle decorrelation Buhlmann (2020) discovered that it depends on certain parameters: the interrogation window size, the lens aperture, the focus distance, the magnitude of refractive index gradients (in his case the temperature of the jet) and sensitivity of the measurement. In its investigation he observed higher decorrelations with small interrogation windows, large focusing distances ($L = \infty$), small lens aperture (e.g. $f_{\#} = 16$), high jet temperatures and great sensitivity.

Buhlmann (2020), for the speckle velocimetry, uses a reference image that is computed as a moving average over 300 flow images: this allow to reduce speckle decorrelation. In combination with this, he increases sensitivity of the measurement to improve the signal to noise ratio, but this causes an increase in decorrelation which is compensated by using larger interrogation windows.

The results obtained by Buhlmann leads us to conclude that the problem is quite complex and, once the type of flow has been selected, a careful analysis is necessary to optimise the set-up parameters and find the right compromise between speckle decorrelation, sensitivity but also spatial resolution of the measurement technique. Buhlmann does not discuss about the resolution of the measurement of his setups but this is strongly degraded by increasing the sensitivity (section 2.2) and by using large interrogation windows (section 1.3.2). Because of this degradation of the resolution, the settings proposed by Buhlmann have not been considered further in the present work.

In the next subsection a more complex setup, already present in the literature, is introduced: this is the double-pass speckle setup, which from a theoretical point of view brings great benefits in terms of spatial resolution of the measurement.

2.5.3 Double pass speckle BOS

The purpose of this section is not only to present the double-pass setup introduced by A. H. Meier and Roesgen (2013) but also to compare the results obtained with a classic setup under the same conditions (sensitivity and field of view) in order to verify the advantages and disadvantages of each.

2.5.3.1 Experimental implementation

The speckle double pass setup is shown in figure 2.17. The main feature is that the laser passes twice through the flow and is aligned with the axis of the camera. Aligning the laser with the axis of the camera requires a relatively complex optical assembly and is quite tricky: this can be achieved by using two different strategies.

The solution used is to employ a 50:50 beamsplitter plate tilted 45°: in this way the laser beam is deflected by 90 degrees aligning with the camera, then it impacts against the speckle screen and then it goes back through the separating blade and it enters into the camera. With this mounting, every time the beamsplitter plate is crossed, half of the light intensity is lost: assuming that the speckle generator is able to reflect 100% of the light, the light collected by the camera is only 25% of the light emitted by the laser, because the beamsplitter plate is crossed twice. To increase the light captured by the camera, the assembly proposed next was tested.

An alternate setup that can be used to align the laser with the camera axis was proposed by G. S. Settles et al. (2005) to perform shadowgraphy measurements with divergent light to capture large fields: the trick proposed is to use a mirror of very small size tilted 45° with respect to the camera axis glued on the last lens of the camera lens. Always assuming a maximum reflection of the speckle generator background, this assembly allows to exploit 100% of the light emitted by the laser. This latter setup was tested but excluded: the diameter of the available lens was too small compared to the size of the mirror glued on it, causing a spot in the center of the image degrading the measurement.

A sheet of retro-reflective material was used as a speckle generator background: for this purpose the sheet used was of the glass sphere type and was not printed with the typical BOS pattern. This background proved to be highly effective for collecting a large amount of light and working at relatively short exposure times. This solution brought significantly more satisfactory results than using a plain sheet of paper.

As in the previous case, a bandpass filter was used to recover only the light emitted by the laser. Finally, the focus of the lens, as discussed extensively above, was done on the flow: as a result, the flow-focusing distance l is zero.

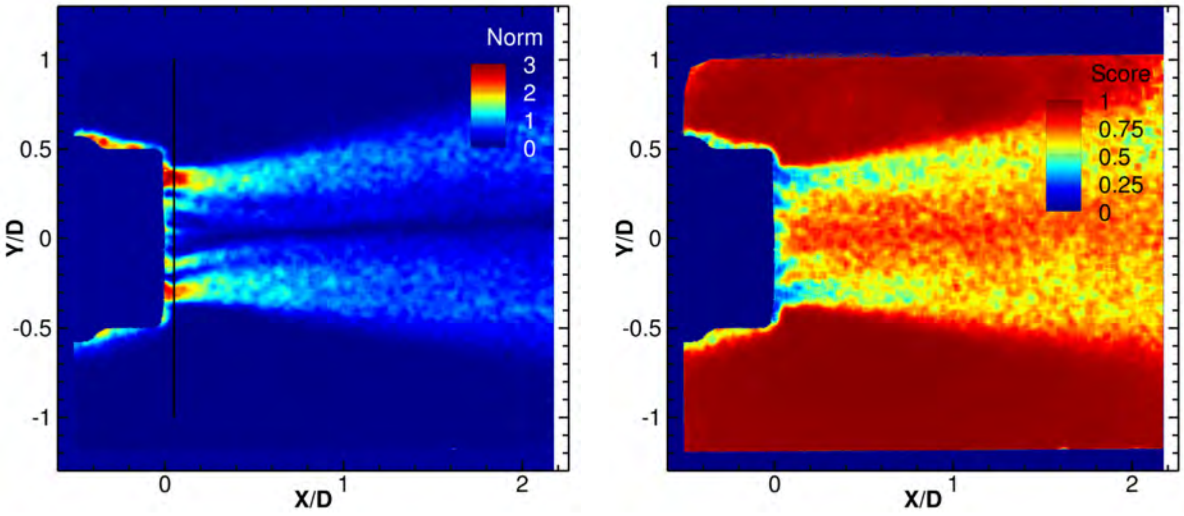

(a) Mean displacement norm.

(b) Mean image score correlation.

Figure 2.22. Results obtained through double-pass speckle BOS on a hot gun. In black is drawn the line for $X/D = 0.05$ for which the vertical displacements shown in Figure 2.27a were extracted.

The results obtained in figure 2.22 were acquired with a camera-flow distance of 740mm, a background-flow distance of 190mm, a 70mm focal length and a f-number of $2^{3.75}$ ($f_{\#}$=13.5). Obtaining with these mounting characteristics a measurement sensitivity of -19.9rad/mm and a captured field size of 105mm.

These results are discussed in detail later and compared to measurements made with a classic BOS setup with the captured field size of 115mm and a sensitivity of the measurement equals to 21mm/rad maintained almost unchanged compared to BOS double-pass setup. To obtain these characteristics, the classic BOS setup has a camera-flow distance of $m = 1000$mm, background-flow distance of $l = 400$mm using a focal length of 70mm with a f-number of 16. The objective of these measurements is to compare the displacement field obtained with the two different setups using the same sensitivity.

Before presenting the results obtained, it should be remembered that although the measurements were made keeping sensitivity unchanged, what differentiates the two setups is the resolution of the measurement. For the double pass BOS speckle this is maximum and equal to 0.08mm while for the classic mount the resolution strongly depends on the aperture of the camera, in this case, closing at 16 produces a maximum spatial resolution of 1.4mm.

The effect of spatial resolution is examined in the following section.

2.5.3.2 Experimental visualization of spatial resolution

In this section our aim is to visualize the effective gain in spatial resolution on the BOS measurements related to various tuning changing the theoretical resolution of the setup. The theoretical resolution of a BOS setup was studied before in this work and has been linked in particular to the aperture of the lens. To put it roughly, the higher the aperture, the better the spatial resolution of the setup. However, BOS measurements, image displacement or ray deviations, stem from complex operations, mainly an image correlation, and as such it is not straightforward that a gain in theoretical resolution of the setup leads to an improvement of the effective spatial resolution of the measurement. In this section we will use the terms "theoretical resolution" and "effective resolution" to distinguish between these two notions of spatial resolution.

To achieve that, a classic BOS mount was used in which the aperture of the lens was simply changed to vary the resolution. In our case three different apertures (4, 8 and 16) were tested for three different spatial resolutions equal to 5.0, 2.6 and 1.4mm. To obtain the same brightness in images, the laser was adjusted in power to balance the loss of brightness due to higher f-numbers.

The studied flow is the same used in the previous section for the in-line speckle type mounting but in this case, to make the effect of our changes of tuning more visible, average and not instantaneous flows were studied: in this way it is easier to compare the range of displacements in certain areas to actually understand how the change in theoretical resolution affects the measurement. Acquisitions are therefore obtained by calculating the instantaneous displacements field of 200 images (sufficient number to guarantee a convergence of displacements) and averaging them.

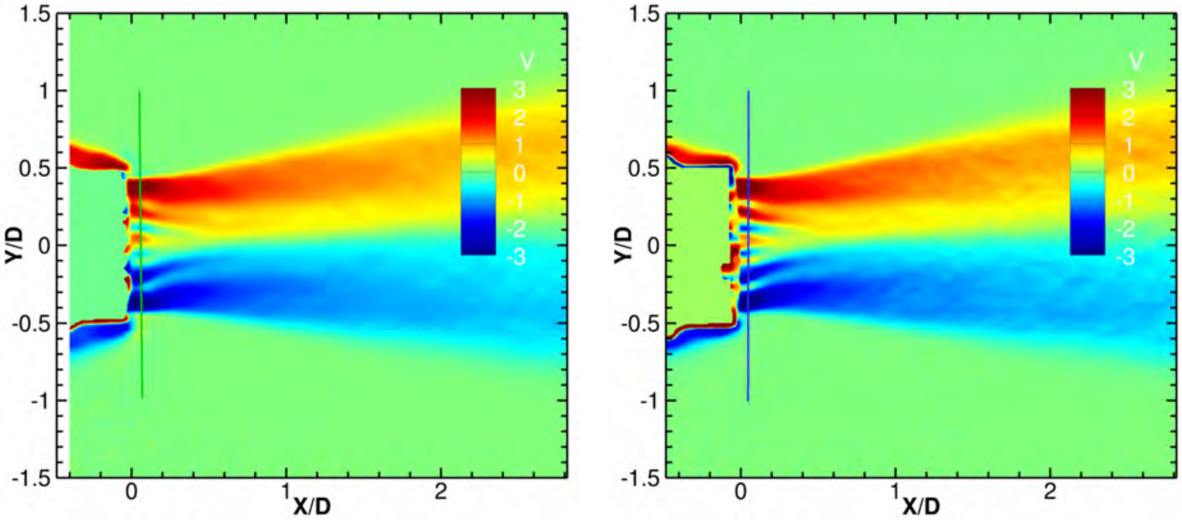

(a) $f_\# = 4$ (b) $f_\# = 16$

Figure 2.23. Mean vertical displacements obtained through a classic BOS configuration at different camera apertures. In green and blue are drawn the line for $X/D = 0.05$ for which the values shown in Figure 2.25a were extracted.

Figures 2.23a and 2.23b show the measurements performed as discussed above with the two extreme camera apertures ($f_\# = 4$ and 16), so that the naked eye can see the effect of the two

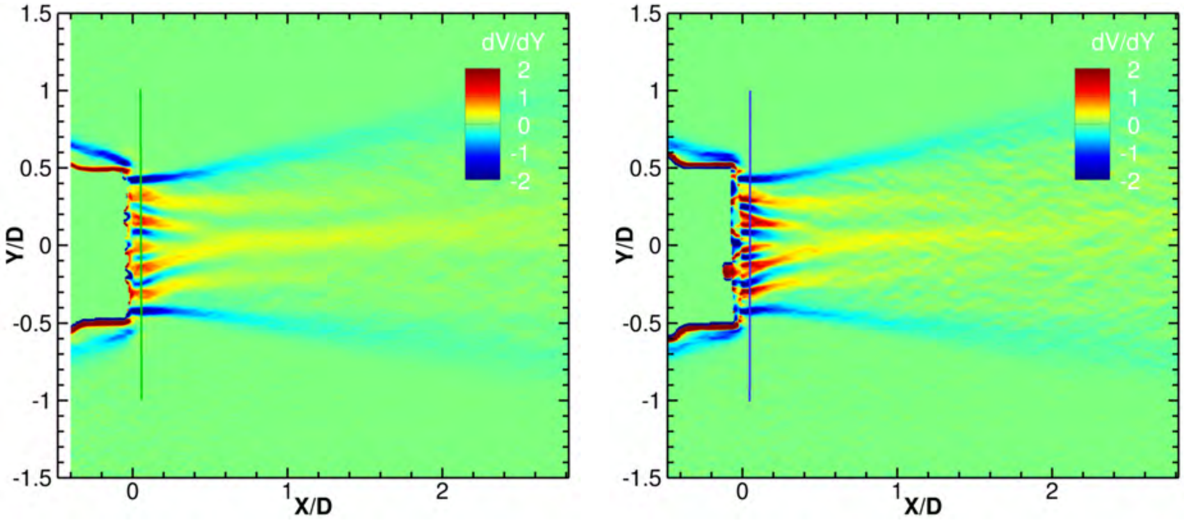

(a) $f_{\#} = 4$ **(b)** $f_{\#} = 16$

Figure 2.24. Gradient of mean vertical displacements obtained through a classic BOS configuration at different camera apertures. In green and blue are drawn the line for $X/D = 0.05$ for which the values shown in Figure 2.25b were extracted.

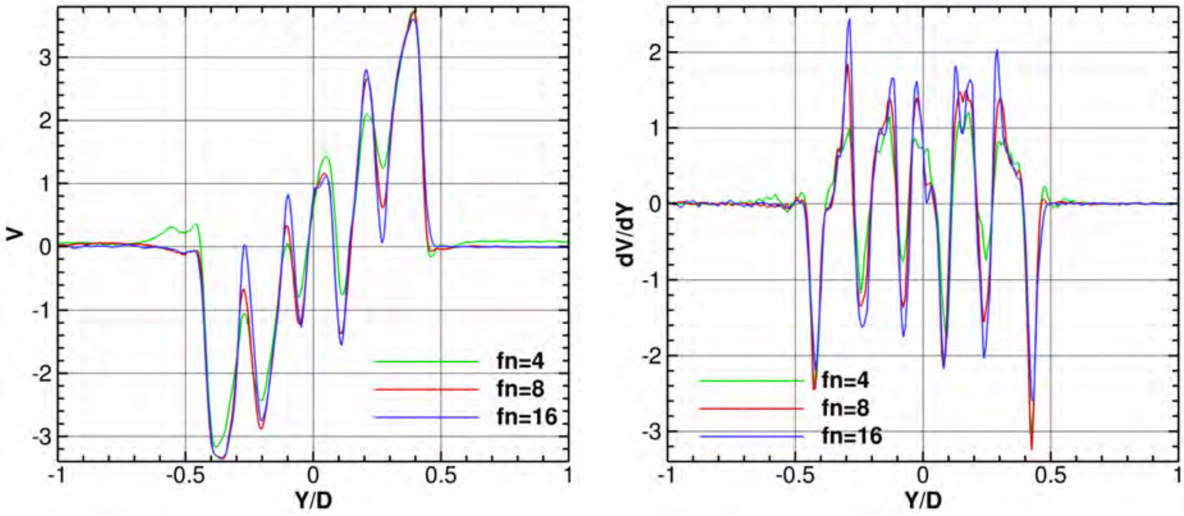

(a) Mean vertical displacements at $X/D = 0.05$. **(b)** Gradient of mean vertical displacements at $X/D = 0.05$.

Figure 2.25. The values plotted in these graphs are extracted for $X/D = 0.05$ to compare the data obtained through a classic BOS setup at different camera apertures.

chosen theoretical resolution (δ =5.0mm and 1.4mm) in the effective spatial resolution of the measured displacement field. These effects are particularly visible at the jet exit area of the hot gun and in the area around it: these are the areas where the strongest density gradients are present. Looking at the area at the exit of the gun, it can be seen that positive vertical displacements alternate with negative displacements: this is certainly due to a metal grid present at the exit of the gun. The size of these patterns is small and for this reason it is possible to capture them in a better way, i.e. with more detail and higher displacements with higher spatial resolution mounting.

To better visualize the change in effective resolution, the displacements extracted at $X/D = 0.05$ from the exit of the hot gun for the three different aperture were plotted (figure 2.25a). In these graphs it can be seen that with an higher aperture, the pattern are sharper and maximum displacements are greater. For this type of flow it can be seen that the most substantial difference in the results obtained is between the measurement made at $f_{\#} = 4$ and $f_{\#} = 8$: probably this is due to the fact that the theoretical resolution obtained at $f_{\#} = 8$ is already sufficient to resolve the smaller scales present in this type of flow. So even if at $f_{\#} = 16$ results are improved, for an $f_{\#} = 8$ results are already highly satisfactory.

To confirm what has just been said above, the gradient of the vertical displacements was plotted for the same position (figure 2.25b). Once again measurements made at higher theoretical resolutions confirm the ability to capture in a better way the stronger gradients present in the flow: at an aperture of $f_{\#} = 16$ the stronger gradients are captured. Moreover it is possible to observe certain details that are not perceived with $f_{\#} = 4$: a clear example is if one considers the part between Y/D=0.1 and 0.2 where a tiny local minimum appears only with the highest aperture or theoretical resolution of the setup. This characteristic is not visible at lower aperture because being a very small phenomenon, where the distance between the two maxima is about 0.06D, it is necessary a resolution of at least equal to their distance (2.1mm) that is reached only at $f_{\#} = 16$ ($\delta = 1.4$mm).

Change in effective resolution are also observed in the upper and lower areas of the gun where the natural convection caused by the overheated metal of the ending part is present. Looking at the images of figure 2.23 and 2.24 it is possible to notice some substantial differences. As far as the displacements are concerned, they are higher and concentrated near the walls of the gun when the measurement is made with the highest theoretical resolution: the abrupt jump between strong displacements and nil is correctly recorded and the spatial spread is limited. Surely the same thing cannot be said about the measurement made at an $f_{\#} = 4$ where the displacements are mitigated and distributed over a greater area than the physical phenomenon. The same effects can be found on the gradient of the vertical displacements: at $f_{\#} = 16$ the captured gradients are higher and cover a smaller area than the measurement made at a lower spatial resolution.

It is important to emphasize the difference in the depth of field that influences the measurement in the area around the gun: the raw photos are not shown but in the acquisition at the lowest aperture the gun remains blurred and the edges are not sharp; on the contrary for $f_{\#}$=16 the depth of field is high and the borders of the gun are easily distinguishable.

With these acquisitions it has therefore been demonstrated that the effect of changing the theoretical resolution of a BOS setup is visible in particular by modifying the norm of the displacements and capturing or not certain small scale phenomena.

2.5.3.3 Resolution comparison between a classic BOS and double-pass speckle BOS setup

After having presented the measurements carried out with a classic BOS assembly in section 2.5.3.2, now the measurements performed with the double-pass speckle setup are presented. As already mentioned above, one of the interests of this type of setup is the ability to perform acquisitions by focusing on the flow of interest and therefore in conditions of the highest possible resolution and with a potential model in focus without losing the information around it.

Figure 2.22a and 2.22b show the average displacement norm and the average image correlation score respectively. On these results it is observed the presence of apparent displacement due to strong noise: as previously explained this is strictly related to the use of the speckle as a background for BOS measurement. This phenomenon is strongly present and visible both on the displacements and on the score maps. In the flow the displacements appear in blocks and outside the flow they are not completely null both because of the signal/noise ratio which is lower than the classic BOS and because of slight changes over time in the speckle that add artificial displacements. As far as the score is concerned this is strongly degraded at the exit of the hot gun at the most important displacements: the strong temperature gradients vary strongly the shape of the speckle of the images acquired with the flow compared to the original pattern of the background. For this reason it is not possible to have complete confidence in the calculated displacements and therefore another weak point of the use of the speckle is highlighted: flows with strong gradients are not suitable for the use of this type of background.

To confirm this, measurements were taken (not reported here) with the same type of speckle double-pass BOS setup around a candle. The candle, reaching a maximum temperature of about 1400°C, has much higher temperature gradients than those found in the hot air gun previously used. The score is strongly degraded and more so than in the previous case, leading to a strongly degraded measurement. Decreasing the sensitivity of the measurement to reduce the displacements obtained does not improve the measurement because the changes in the speckle are directly related to the gradients present in the flow.

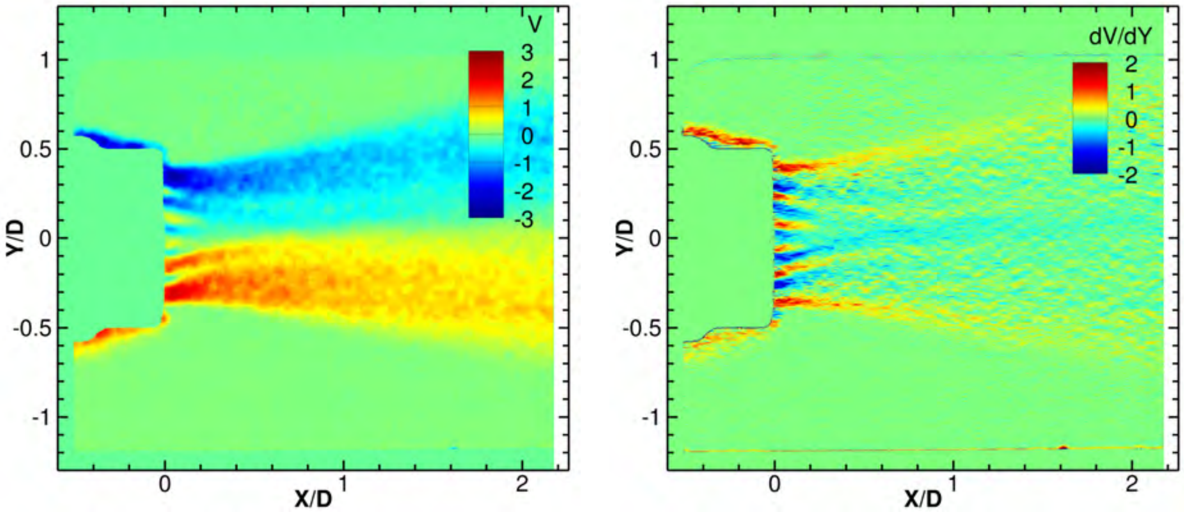

(a) Mean vertical displacements. **(b)** Gradient of mean vertical displacements.

Figure 2.26. Results obtained through double-pass speckle BOS on a hot gun.

In order to correctly evaluate the resolution of this type of BOS original setup, the vertical displacements acquired with the double-pass speckle setup and those acquired with the classic BOS setup at the highest resolution ($f_{\#}$ =16 and widely discussed above) are compared (figure 2.26a and 2.23b).

At first glance it is immediately noticeable that the displacements are strongly affected by the spurious displacements and comparing the results with those obtained with the classical BOS it can be seen that they are considerably degraded by no longer obtaining smooth and blunt displacements. Looking at the figure 2.27a where the vertical displacements obtained with the two types of BOS are compared, it can be seen that although the trend is the same, the values of the displacements reached with the double passage BOS are lower: this is an unexpected result because from a theoretical point of view the two mountings have almost the same sensitivity and moreover it is not to be attributed to a spatial integration effect due to a low resolution of the measurement. Always linked to the resolution it can be said, comparing the output of the hot gun in figures 2.26a (double-pass speckle BOS) and 2.23a (classic BOS), that this is improved compared to the measurement made at $f_{\#}$ =4 (δ =5.0mm) because it is possible to distinguish all the alternating positive and negative displacements.

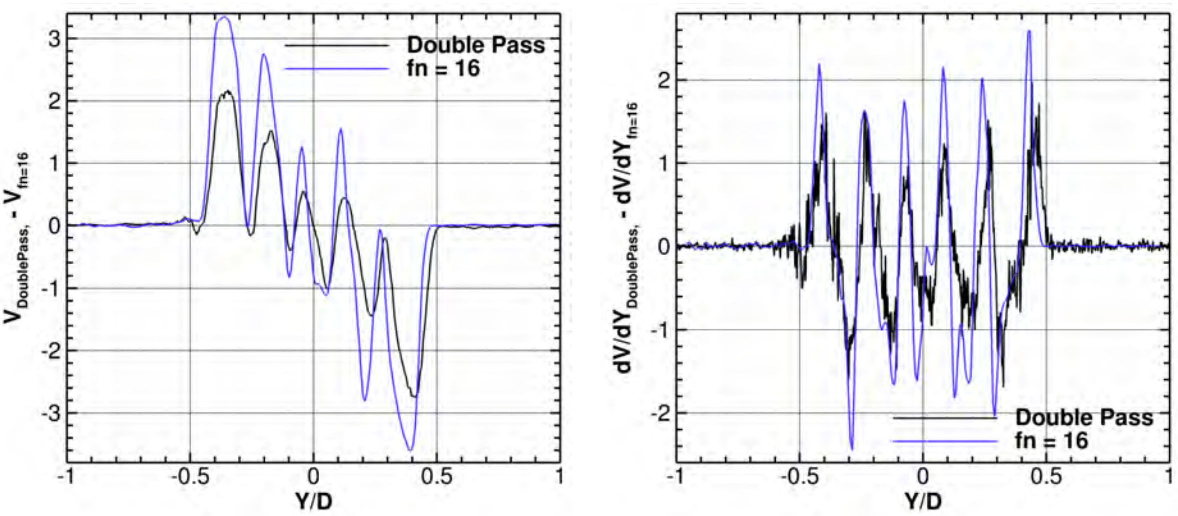

(a) Mean vertical displacements at $X/D = 0.05$.

(b) Gradient of mean vertical displacements at $X/D = 0.05$.

Figure 2.27. The values plotted in these graphs are extracted for $X/D = 0.05$ to compare the data obtained through a double-speckle setup and a classic BOS setup with the same measurement sensitivity. To have the same trend in the graph, the sign was changed to the displacements obtained through a classic BOS setup.

Finally, by comparing the measurements obtained by a double-pass speckle configuration and a classical configuration with the highest aperture, we could conclude that even if the potential resolution seems comparable (looking at the alternation of positive and negative displacements) the strong noise which affects the result of the double pass speckle BOS does not allow to conclude to an effective improvement of this setting.

Moreover, the measurements made with the double pass speckle setup showed a strong sensitivity of the speckle to high values of the density gradients which lead to even higher noise level on the measurements. The expected gains in spatial resolution are then not practically measurable because of speckle pattern fluctuations caused by strong refractive index gradients.

Hereafter we explore another context where speckle BOS has been found promising: the case of small-size fields. The volume of interest is small and the speckle is one of the possibilities for the study of this type of ranges where the printing of small patterns becomes impossible.

2.5.4 BOS with small measuring ranges

In the case of small fields, the manufacturing of a background with BOS pattern of suitable size is difficult and the use of speckle can be an alternative (Michalski et al. 2018). Two different setups are compared for the measurement of light deflection created by thermal gradients in the vicinity of a resistor. A classic BOS setup using a sheet of sand paper as the background and a double-pass BOS speckle setup with the use of a telecentric lens. A double-pass speckle BOS was chosen to have a great resolution at the level of resistor and to have the resistor in focus (figure 2.28b).

After presenting two different setups with the use of the speckle and highlighting the difficulties encountered in the measurement, this section exposes the results of some BOS measurements carried out around a small resistor of 5 watts powered at 9.7V and 0.45A, 4.8mm in diameter and 24mm in length.

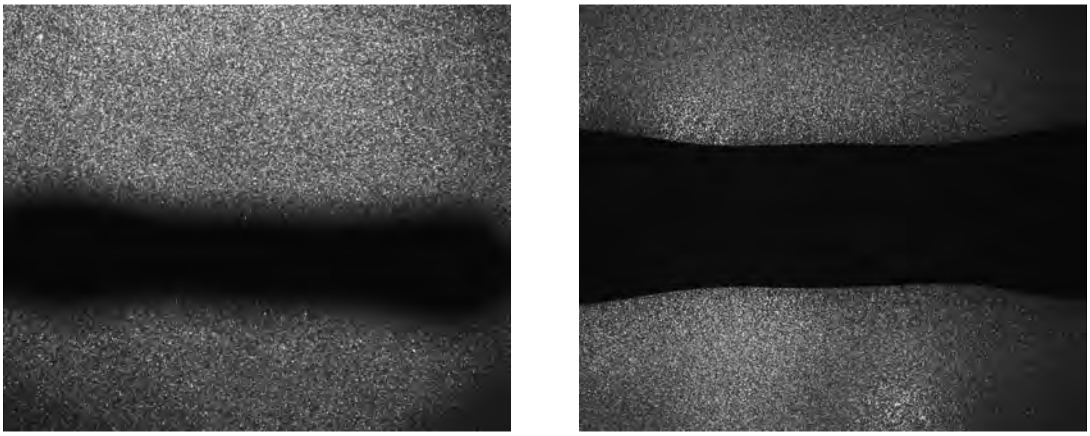

(a) Raw images of classic BOS setup using P220 grit sandpaper as background with 70mm lens at $f_\#$ =16.

(b) Raw images of double-pass speckle BOS using a retroreflective background as speckle generator and a telecentric lens at $f_\#$ =10.

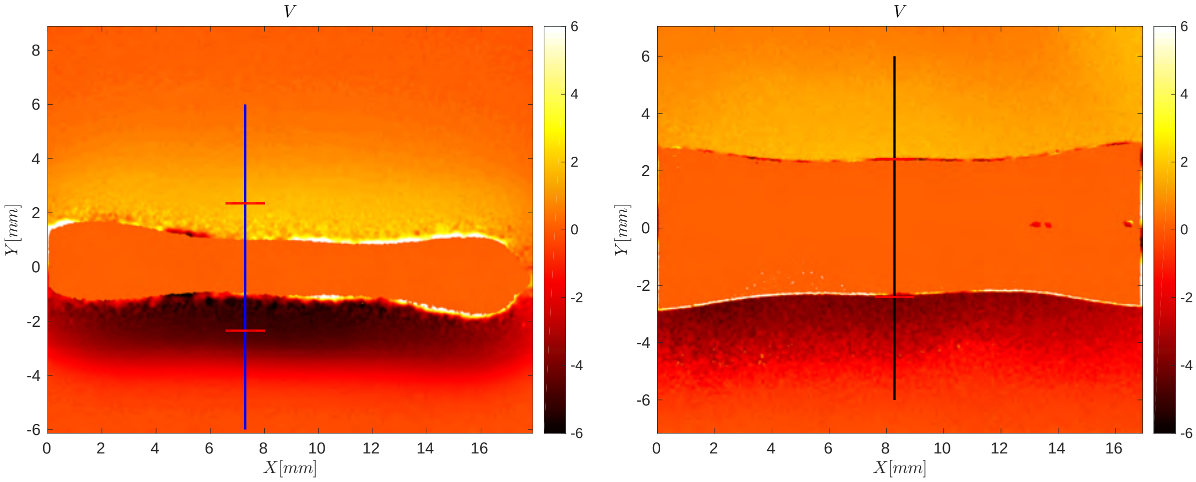

(c) Vertical displacements obtained with classic BOS from the correlation of a background image and another one taken at an instant Δt after the power supply of the resistor $S = 55$mm/rad. In blue the area around which the profile of figure 2.29 was extracted. The two red lines delimit the resistor.

(d) Vertical displacements obtained with double-pass speckle BOS from the correlation of a background image and another one taken at an instant Δt after the power supply of the resistor $S = -55$mm/rad. In black the area around which the profile of figure 2.29 was extracted. The two red lines delimit the resistor.

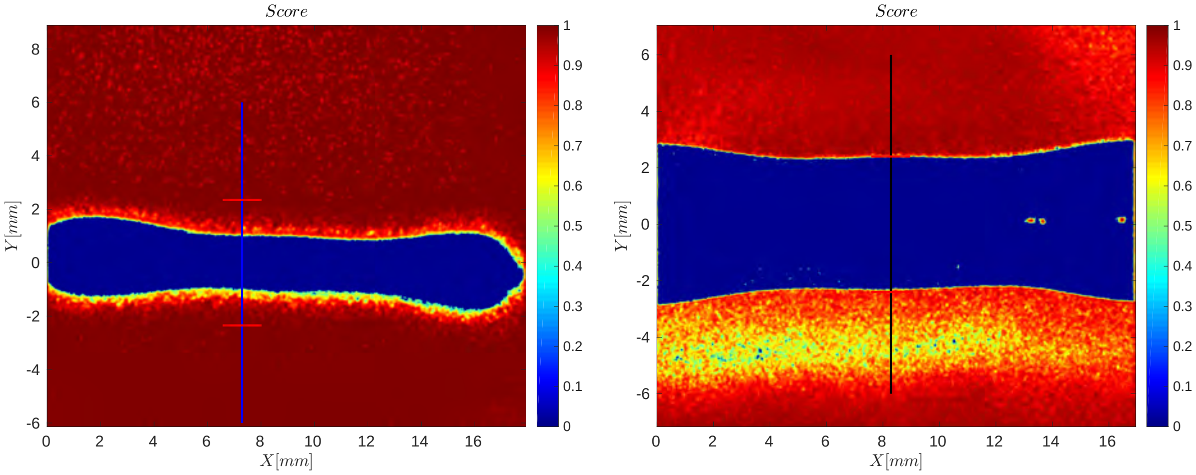

(e) Score correlation of two classic BOS images.

(f) Score correlation of two double-pass speckle BOS images.

Figure 2.28. Comparison of the results obtained with two different BOS setups at the same sensitivity with the same studied object, a 5W resistor powered at 9.7V and 0.45A. On the left a classic BOS setup with an entocentric lens, on the right a double-pass speckle BOS with a telecentric lens.

	m [mm]	l [mm]	s [mm]	f [mm]	$f_{\#}$	S [mm/rad]	δ [mm]
Classic BOS	170	370	/	70	16	55	3.02
Speckle Double Pass BOS	120	0	110	/	10	55	0.007

Table 2.3. Main specifications of BOS setups .

As already mentioned, the problem in the case of small fields is the need to generate a high spatial frequency pattern of small size. From the distances of the setups presented in table 2.3 the fields displayed are about 17×23mm at the flow level, resulting in magnifications of 0.5 for the double pass speckle setup and 0.15 for the classic one. Consequently it would be necessary to print dots for the creation of the BOS backgrounds of 20μm diameter in the first case and 70μm in the second case: even using printers able to print at 1200ppi (points per inch), this would not be enough because it would mean to have 1 dot per point of the BOS backgrounds in the worst case or 3.5 points, however insufficient to have a good quality pattern.

For this reason it was decided to test the BOS in a classic configuration using as BOS background a sandpaper where the diameter of the abrasive particles corresponds to about 3 pixels on the camera: the chosen sandpaper is a P220 with an average particle size of 68μm. While zooming the image it was observed that the size of a single grain is actually 3 pixels but there are some areas where more grains overlap forming light zones of larger size and up to 10 pixel. Observing the raw image it is observed that the pattern formed by the sand paper is very similar to a printed pattern (figure 2.28a): white dots alternate with gray or black areas creating a strong contrast. Moreover, due to the limited depth of field (about 15mm) our object is outside this area and the edges around the resistor are completely blurred. A consequence of the position of the resistor away from the focus zone and the limited depth of field is related to the size of the resistor in the BOS image. The resistor appears much smaller than the actual size due to the strong blur around it: this can be seen in images 2.28c and 2.28e where the extremes of the resistor are marked by two red lines. The resolution of the measurement, due to the high sensitivity required for the measurement, is 3.0mm so on a field of such small size it must be taken into account that strong density gradients can not be captured.

Looking at image 2.28e, it shows that the score is degraded in the border area around the resistor, this is due to the blurred area that surrounds it. Elsewhere the degree of confidence in the correlation of the images is at maximum and therefore it is stated that the sand paper background brings excellent results in terms of correlation between BOS images: the signal-to-noise ratio is high and the size of the points, although not always constant, is close to the optimal value corresponding to 3 pixels.

Looking at the vertical displacements, these are more important in the lower resistor area. This can be explained by the fact that the resistor, even if small in size, acts as a barrier to natural convection. These are rather important near the resistor but vanish a few millimetres away from it: this fact tells that there may be very high temperature gradients but they can't be well captured because of the problems previously mentioned related to the spatial resolution.

Passing now to the double pass speckle BOS setup (figure 2.28b), the resistor appears in-focus and not blurred this because the focus was made directly on it. Moreover the theoretical spatial resolution of the measure is the maximum possible because we focus on the resistor: spatial resolution is 6.9μm, the double of the size of a pixel because a telecentric lens of magnification equal to 0.5 is used. In this setup we faithfully find the resistor true dimensions, not as in the previous case where the resistor was considerably smaller than the real dimensions. The speckle size obtained at a f-number of 10 is equal to about 3 pixels.

Looking at the correlation score (figure 2.28f) between the two acquired images it can be seen how this is very high in the upper zone and also near the border zone between resistor and background: thanks to the double pass setup the model results to be in focus and the loss of correlation caused by the blurred zone (present in the classic setup Fig. 2.28e) is not present. Moreover, where the minor displacements and gradients are present (above the resistor), the score is weakly degraded by the variations of shape and light intensity of the speckle already observed in the cases previously exposed. Instead, in the zone below the resistor, where the major displacements are present, stronger variations in the speckle pattern are observed and the score is more degraded because of this changes. This further experience reinforces what was previously observed and presented in the previous sections.

As also observed in the previous cases, the displacements (figure 2.28d) suffer from great noise and speckle pattern fluctuations and spurious displacements are introduced into measurements: this is linked to the fact of using the speckle as a background for the BOS technique.

Despite the use of speckle degrades the measurement, it is nevertheless possible to compare the displacements generated by the density variations (figure 2.28c and 2.28d), acquired with the same sensitivity of the BOS setups (S = 55mm/rad). As described in the section 2.5.1.1, since the sensitivity for the two setups is the same but inverted in the sign, in figure 2.28d we have plotted the vertical displacements inverted in the sign ($-V$) to obtain a colour palette that is easily comparable between the two types of setups. At first sight, comparing the vertical displacements of figures 2.28c and 2.28d it can be seen that these are not of the same magnitude and that for the case of double-pass BOS speckle they are smaller. This is an unexpected result because from a theoretical point two mountings have the same sensitivity and moreover it is not to be attributed to a spatial integration effect due to a low resolution of the measurement.

To understand where this difference in displacement comes from, vertical displacement profiles averaged over a width of 100 pixels have been plotted to filter out the high noise present in the speckle BOS measurements in particular. To do this, the same area around the resistor was selected and the displacements were re-scaled to respect the different scales of the two setups. In order to have a more easily readable result, as before, the displacements of the speckle BOS double pass have been reversed in sign. The result thus obtained is presented in figure 2.29. The displacements that must be taken into consideration are those that are only located outside the resistor which is delimited by the two horizontal red lines. Both in the upper and in the lower part the displacement values at the borders of the resistor are totally compatible while their trend moving away from it is different. For the speckle BOS double pass setup, it decreases in

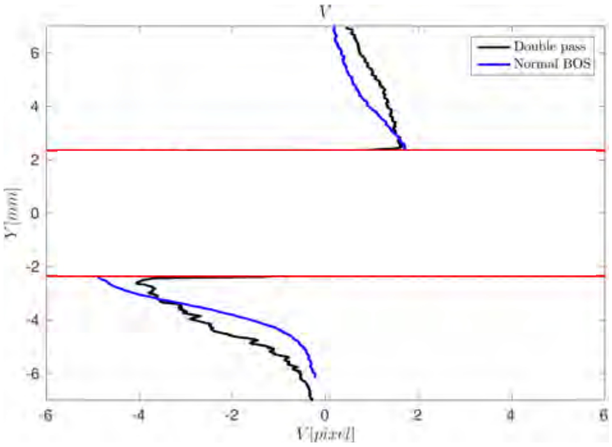

Figure 2.29. Vertical displacements extracted around the blue line for the classic BOS (figure 2.28c) and the black line for the double pass speckle BOS (figure 2.28d). The two red lines delimit the position of the 4.8mm wide resistor.

a linear way while for the classic BOS setup the decrease has a quadratic type trend. Probably this effect is given by the strong spatial integration introduced by the classic BOS setup where the resolution of the measurement δ (3mm) has the same order of magnitude as the resistor (4.8mm).

This measurements proves that it is possible to obtain an object in focus by focusing on it and a sensitivity different from zero succeeding in obtaining a BOS measurement all around the model without a zone of uncertainty affected by defocus. As far as the effective resolution of the measurement is concerned, it is difficult to say and find the effects introduced by the two different acquisitions made with different resolutions: probably in this type of flow characterized by natural convection, there are no strong gradients where it is possible to visualize difference in effective spatial resolution. In addition, the displacements map can be strongly influenced by theoretical resolution of the setup and the defocus zone around the resistance. This could be confirmed through a series of acquisitions at different $f_\#$ and therefore at different theoretical resolution of the setup.

In this section it was shown that even in the case of very small fields it is advisable to find alternative solutions to a printed BOS background type when it is no longer possible to print patterns of suitable size. The use of sand paper has led to excellent results from the point of view of the correlation between images eliminating the spurious displacements introduced with the use of the speckle. The score remains always high and not degraded as in the double pass setup where the speckle is subject to variations in light intensity and shape introduced by the perturbations generated by thermal gradients. Thanks to the double pass speckle BOS mounting, by focusing on the resistor, it is possible to perform the measurement next to the walls of the resistor, which is not possible in classic BOS setup because of the blurred area surrounding the body. Surely the double pass setup is interesting for measurements with the presence of an object in the flow but its realization is very complicated from a practical point of view, in addition to obtaining results degraded by spurious displacements that cause a loss of confidence in image correlation.

2.6 Conclusion

In this chapter the importance of the spatial resolution of the measurement and its effect of integration in acquisitions was demonstrated. One of the fundamental steps for the development and improvement of the BOS technique is certainly to try to increase the spatial resolution compared to the one that can be obtained through a classic BOS setup.

As demonstrated, the resolution is closely related to the sensitivity of the measurement and the size of the field to be captured. Once these two parameters were set, in a classic BOS setup, it is thus possible to act only on the aperture of the lens to improve the resolution.

The first solution tested acts on the background type to reflect as much light as possible to close the lens diaphragm at maximum. This is achieved through the use of retroreflective backgrounds. All the different types of backgrounds used have given very good results in terms of reflected light: using this type of backgrounds allows to gain a factor 16 in terms of light, being able to perform measurements at much higher $f_\#$ improving the spatial resolution. If the micro prism backgrounds reflect a greater amount of light and hence more suitable for our use, they were less effective because of the bridges that are necessary for the positioning of the micro prisms: in these areas the absence of retroreflective material generates a lack of pattern that negatively affects the BOS acquisition. For this reason the glass ball type backgrounds were preferred and were chosen for the study of an under-expanded supersonic jet (chapter 3.6) and for the study of a hot jet in cross flow (chapter 4.6). The use of this type of backgrounds also involves a more complex assembly as each camera must be placed next to a light spot due to the strong directional response of the background. As presented in the following two chapters, this has proved to be a very valid solution to make measurements with several cameras (in our case 8) without having to increase the aperture of the camera, thus obtaining instantaneous measurements of unsteady flows at high resolution.

Section 2.4, on the study of telecentric lenses, focuses on the theoretical study of the equations that characterize depth of field and spatial resolution. Since in a BOS measurement the flow is always outside the depth of field, the most important parameter is the spatial resolution. The results obtained show that the use of a telecentric lens increases the resolution only in certain specific conditions. After having demonstrated that the resolution both for an entocentric and a telecentric lens, once chosen the camera (sensor size), the focal length and fixed the $f_{\#}$, depends only on the sensitivity of the measure and the size of the flow to be captured, it was possible to draw the graphs 2.14a and 2.14b which shows where it is convenient to use a certain lens. Thus it was shown that the telecentric lens is advantageous only for small flows (<100mm) and it is useful to use cameras with large sensors. These lenses are not used in the following experimental studies because of their convenience limited to small fields, as well as the very high cost of purchase or their delicate manufacture.

The double-pass speckle setup proposed by A. H. Meier and Roesgen (2013) was then studied in detail. This succeeds in decoupling spatial resolution from measurement sensitivity using the speckle as the background for the BOS technique in a double-pass setup of the light beam through to the flow. Furthermore, focusing on the flow provides the highest possible measurement resolution.

The studies presented in section 2.5.2 have shown how the use of the speckle introduces a spurious displacements and the image correlation score is degraded. These two effects are caused by the change of shape and light intensity induced by the flow on the speckle pattern between a reference image and one with the flow. These changes are dependent on the type of flow observed: stronger density gradients have produced more important changes in the speckle, so measurements in the presence of strong gradients are almost impossible due to the great loss of confidence in the calculation of the displacements. The inline speckle setup, as well as facilitating the observation of these degradations related to the use of the speckle as background, was useful to understand that these are not linked to the sensitivity of the measurement but are introduced by the flow itself.

In section 2.5.3 a classic BOS setup was compared to a double speckle setup. In the first place, for the classic setup, it was varied $f_{\#}$ of the lens to demonstrate the effects of a different spatial resolution on the acquisitions. The comparison between the results obtained with the two different setups is rather difficult because the effects introduced by the speckle on the measurement are important and the noise is high. It is therefore difficult to conclude if the double-pass speckle BOS setup brings improvements in the effective spatial resolution of the measurement because the effects introduced may be greater than the possible improvements.

In the last section two setups for the visualisation of small flows were compared: because of the small size, it is not possible to print on paper the patterns used in a classic setup so the background was replaced by a sheet of sandpaper in one case and by the speckle background in the second test. The results obtained led us to conclude that in the case of small volumes it is possible to find alternative backgrounds to a printed background with good results. The use of the speckle results always critical introducing a strong noise in the measurement with a spurious displacements constantly occurring. In addition, with the classic BOS setup, the displacement map can be strongly influenced by the theoretical spatial resolution of the setup and the blurred area around an object.

The investigations in this chapter have brought out the importance of the resolution in the BOS technique and that this is closely related to the sensitivity of the measurement and the size of the flow to be acquired. After studying and testing different solutions, the most appropriate and effective way to improve the resolution for our applications was the use of retroreflective backgrounds.

Chapter 3

3D density reconstruction of a screeching supersonic jet by BOS

Contents

This chapter is dedicated to the study of underexpanded supersonic jets featuring a global instability known as the screech phenomenon for the loud acoustic tone it generates. Building on the conclusions drawn from the previous Chapter **??**, we rely on reflective BOS backgrounds to continue and improve the initial work performed by Nicolas et al. (2017a) and Nicolas et al. (2017b) on this subject.

3DBOS acquisitions are performed together with near-field acoustic measurements in order to investigate the connection between global 3D features found in reconstructed density fields using Proper Orthogonal Decomposition (POD) and the screech noise.

3.1 Underexpanded jets and Screech

Supersonic axisymmetric underexpanded jets are commonly found in aerospace and industrial applications, e.g. aircraft engines, space launchers or pressurised tank leakage. These jets were extensively studied in the past and their overall structure is well known (Franquet et al. 2015).

One particular feature of such jets is the possible development of a global instability, referred to as the screech phenomenon, driven by an aeroacoustic feedback mechanism yielding strong acoustic tones and large flow oscillations.

The main characteristics of underexpanded jets are presented below, followed by a detailed description of the screech.

3.1.1 Underexpanded jets

Supersonic jets issued from a convergent nozzle are often non-ideally expanded, such that the flow static pressure at the nozzle exit, p_0, is greater than the ambient one, p_a: pressure equilibrium is reached outside the nozzle through a series of shocks and expansions that characterise this type of flow.

The operating condition of these under-expanded jets is defined by the Nozzle Pressure Ratio NPR $\equiv p_{t0}/p_a$ where p_{t0} is the stagnation pressure at the nozzle exit. Equivalently, the ideally expanded Mach number, that corresponds to the Mach number that would be reached if the jet was perfectly expanded through isentropic processes, may be used. Using isentropic relations, one gets:

$$M_j \equiv \sqrt{\frac{2}{\gamma-1}\left(\mathrm{NPR}^{\frac{\gamma-1}{\gamma}}-1\right)} \tag{3.1}$$

where γ is the heat capacity ratio taken equal to 1.4 in the present work.

Referring to figure 3.1a, it is possible to identify a series of features typical of highly under-expanded jets. Starting from the nozzle outlet, there is an area of expansions fans ①, through which the pressure gradually decreases, that is delimited by the barrel shock ②. The Mach Disk ④ (MD) is a feature that appears only in highly under-expanded jets, otherwise the barrel shock merges to a point. The point identified with ⑤ is called triple point and is the point of intersection between the Mach Disk, the barrel shock and reflected shock ⑥ on the isobar line ③ of the mixing layer. The region after the normal shock (MD) is subsonic while the one beyond the oblique reflected shock remains supersonic: the line that delimits these two zones is called slip line ⑦.

Two characteristic lengths of supersonic jets having a MD are the Mach Diameter (D_{MD}) and its distance from the nozzle outlet (X_{MD}), depicted in figure 3.1a. The work of Franquet et al. (2015) summarises most of the studies carried out on these topics.

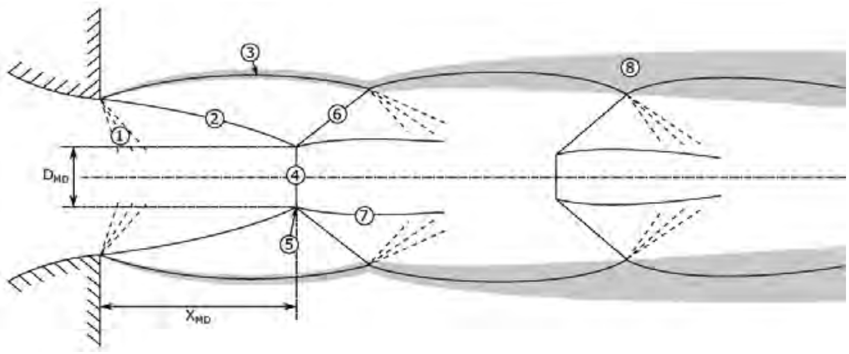

(a) Schematic view of an under-expanded jet at high NPR : $4-7$ (Nicolas et al. 2017a).

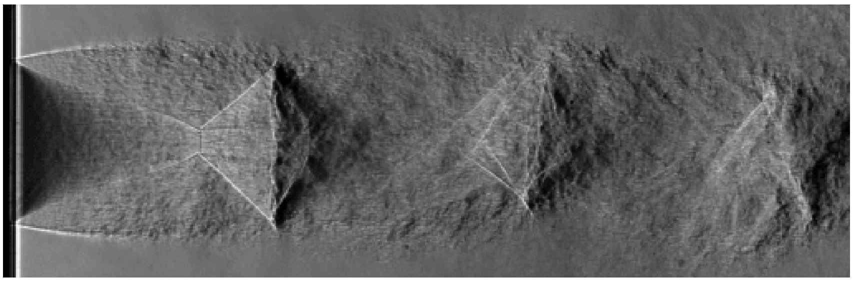

(b) Instantaneous schlieren visualisation of an under-expanded jet at NPR = 4.1: the strong pressure gradients caused by expansions and shocks are easily detectable using this technique (Donjat et al. 2017).

Figure 3.1. Shock cells structure of an under-expanded jet at high nozzle pressure ratios.

Figure 3.1b is an instantaneous visualisation of an under-expanded jet acquired at an NPR=4.1: from this picture it is possible to recognise all the features that were described previously and 3 shock-cell structures can be identified. The first one that starts at the nozzle exit is well defined and stable, while the following ones are less strong and are observed to oscillate, yielding instantaneous structures not aligned with the jet axis.

Another characteristic quantity of under-expanded jets is the fully expanded diameter D_j. This diameter corresponds to the diameter of the jet necessarily obtained through isentropic processes to reached M_j. It is related to the diameter D using isentropic relations and a condition of mass flux conservation (C. K. Tam and Tanna 1982), such that:

$$D_j = D \left[\frac{1 + \frac{M_j^2(\gamma-1)}{2}}{1 + \frac{(\gamma-1)}{2}} \right]^{\frac{\gamma+1}{4(\gamma-1)}} \left(\frac{1}{M_j} \right)^{0.5} \tag{3.2}$$

It is also finally useful to introduce the fully expanded jet velocity U_j, which serves for the definition of the Strouhal number $\left(St_j \equiv \frac{f D_j}{U_j} \right)$ where f is the frequency:

$$U_j = M_j \sqrt{\gamma R T_s} \tag{3.3}$$

where $T_s = T_{t0} \left(1 + \frac{\gamma-1}{2} M_j^2 \right)^{-1}$ is the static temperature of the ideally expanded jet.

3.1.2 Screech

The tonal component of the noise emitted by an under-expanded jet in screeching condition is generally clearly visible in acoustic spectra measured by near-field microphones. For example, several sharp peaks can be observed in figure 3.2a, illustrating the presence of the screech tone and its harmonics. This aeroacoustic phenomenon has been extensively studied since the early work of Powell (1953) who understood that these tones are the result of a feedback loop described below. Raman (1998) provided a comprehensive synthesis on the screech.

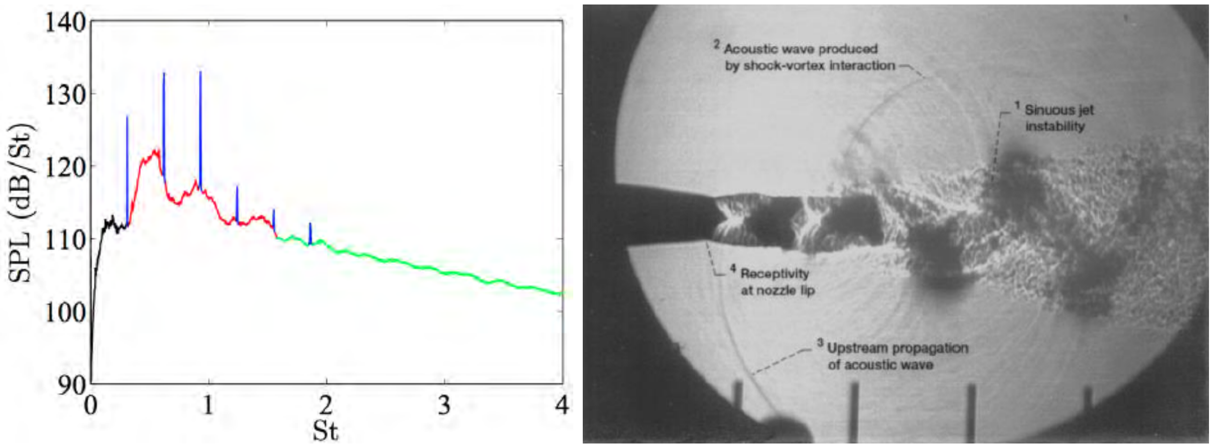

(a) Typical far-field spectrum emitted by an under-expanded nozzle at $M_j = 1.35$. Mixing noise in black, screech noise in blue, broadband noise in red and in green the combination between mixing and broadband noise. (André 2012).

(b) Schlieren image of an under-expanded jet operating at $M_j = 1.5$ with a rectangular nozzle: in the photo are highlighted the features of the screech feedback loop (Raman 1998).

Figure 3.2. Shock cells structure of an under-expanded jet at high nozzle pressure ratios.

3.1.2.1 Screech modes and cessation

As M_j increases, several screech modes can be identified, which are characterised by different frequencies and dynamical behaviours.

First Powell (1953) described four modes that he called A, B, C and D. These four modes can be identified in figure 3.3a over consecutive ranges of NPR values. The transitions from one mode to another, called staging, are made over sharp frequency intervals.

Only later Merle (1956) pointed out that the first mode can be divided into two modes, A1 and A2, and noted that these modes are not equally stable.

Later Davies and Oldfield (1962) used a fixed microphone and a second one rotating azimuthally around the jet axis to identify the dominant spatial structure of the different modes. They demonstrated that the sound fields associated with modes A1 and A2 are axisymmetric, and modes B and C are flapping and helical respectively. To complete this work, Powell et al. (1992), relied on Schlieren visualisations and acoustic measurements, to establish that mode D is antisymmetric, like mode B; Powell et al. (1992) have interpreted these two modes as the sum of two counter-rotating helices (also stated by M. K. Ponton and J. M. Seiner (1995)).

Secondary modes were also observed to coexist with dominant modes: e.g. modes b and d that are extensions of modes B and D in the range where the mode C is dominant.

In figure 3.3a, one can finally see that at high Mach numbers, screech ceases and no more characteristic frequencies appear; this is also evident from figure 3.3b where the sound pressure level (SPL) is plotted as function of the M_j.

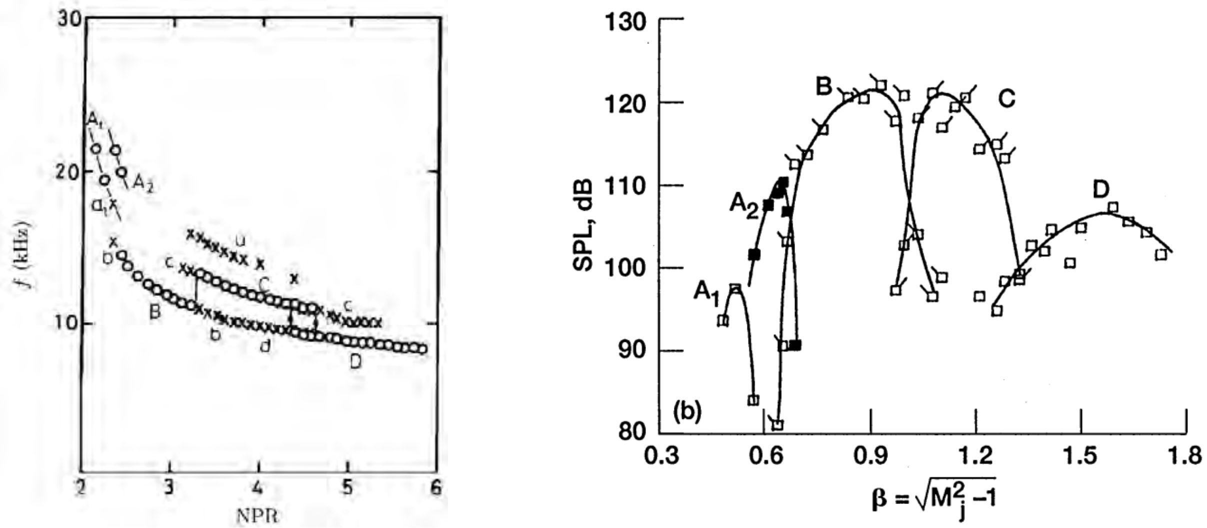

(a) Screech frequencies as function of the NPR. With ○ and capital letters are designed the dominant modes while with × and lowercase letters the non dominants ones (Powell et al. 1990).

(b) Amplitude of the screech fundamental as a function of jet condition (Norum and Shearin 1984).

Figure 3.3. Frequencies and SPL of different screech modes.

3.1.2.2 Mechanism

The feedback loop identified by Powell (1953) is as follows: the coherent structures associated with the jet shear-layer convective instabilities propagate downstream and interact with the shock cells, generating upstream-propagating waves (either freestream acoustic waves or neutral upstream modes inside the jet, see Edgington-Mitchell (2019) for a recent review) that, in return, excite the shear layer at the nozzle-lip, a highly receptive region.

Shen and C. K. Tam (2002) suggested the existence of two different closure mechanisms, in particular the feedback phenomenon may be closed by two kinds of disturbances propagating upstream.

The first type of mechanism consists of interactions between the shock cell and amplified disturbances that generate acoustic waves that propagate upstream, outside of the jet shear layer, reflecting on the nozzle lip and generating new instabilities. This mechanism is the one envisaged in figure 3.2b, where all the phases of the feedback loop are identified. This is the classic model most frequently proposed in the literature, starting with Powell (1953).

The second type of mechanism identifies another type of upstream-propagating waves which were identified for the first time by C. K. Tam and Hu (1989): unlike the acoustic waves, these waves propagate inside and outside of the jet. Recent studies conducted by Gojon et al. (2018) and Edgington-Mitchell et al. (2018) suggest for example that screech modes A and C can be satisfactorily modelled and explained relying on a simple vortex-sheet model where the screech feedback loop is sustained by the upstream neutral acoustic wave modes.

The existence of these two mechanisms, according to Shen and C. K. Tam (2002), explains the coexistence of two modes of screech simultaneously (figure 3.3a).

Despite decades of research effort and progress, a precise understanding of the mechanisms behind all these oscillation modes is still lacking. For example, open questions remain regarding the exact nature of the screech noise production process (that is the interaction of the downstream propagating instabilities and the shock cells), the possibility of coexistence of two screech

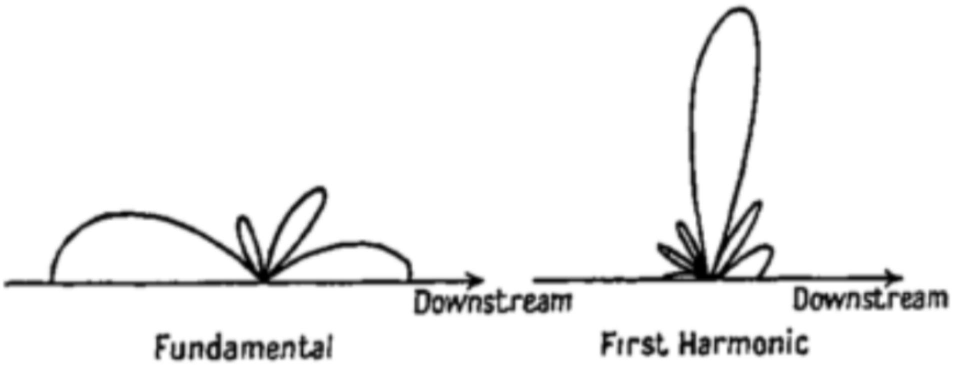

Figure 3.4. Screech intensity directivity (Powell 1953).

modes, or the nature of the upstream waves.

3.1.2.3 Directivity

According to the model proposed by Powell (1953) where phase-shifted monopoles are distributed on the jet boundary, each harmonic of the screech has a particular directivity, due to interference between sources. Screech is a strongly directional and numerous studies have confirmed what Powell observed.

For instance Norum (1983) has verified the validity of this model. The comparison between the measurements and Powell's prediction for the fundamental and the first two harmonics of mode B is in excellent agreement.

As the figure 3.4 shows, the screech fundamental frequency is more intense in the downstream and upstream directions, vice versa the first harmonic is stronger in the direction perpendicular to the direction of the jet.

3.1.2.4 Jet temperature influence

As the jet temperature T_s increases, the fully expanded jet velocity U_j given in equation 3.3 increases accordingly. As a result, the convective velocity U_c, the velocity of the coherent instabilities propagating inside of the mixing layer, being about $0.7U_j$ for round jets (Walker and Thomas 1997), also propagate at higher velocities. On the other hand, the shock-cell structures spacing does not depend on temperature (Shen and C. K. W. Tam 2000). These two facts lead to an increase in the frequency of screeching as the jet temperature increases ((Ahuja et al. 1997) and (Shen and C. K. W. Tam 2000)). However, as Shen and C. K. W. Tam (2000) demonstrated, the Strouhal number St_j is not dependent on temperature.

3.1.2.5 Nozzle lip thickness influence

It was shown in previous works that the lip thickness is an important parameter in the overall screech feedback process. More precisely, (M. Ponton and J. Seiner 1992) and Shen and C. K. W. Tam (2000) observed a delayed screech cessation (in terms of NPR or M_j values) as the lip thickness was increased, together with a significant increase in screech noise levels (also reported by Norum (1983) and Raman (1997)).

Furthermore, nozzle lip thickness was reported to induce slight shifts in screech frequencies by Aoki et al. (2006). Finally, this geometrical parameter was observed to play a determinant role in the transition between screech modes (Assunção (2018) M. Ponton and J. Seiner (1992)): first, in thick-lip configurations, an earlier transition in terms of NPR between modes B and

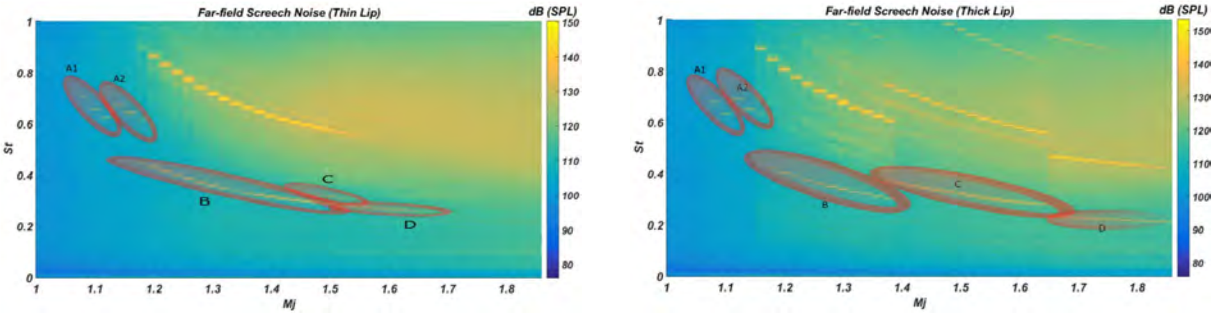

(a) Far-field screech noise with thin lip nozzle.

(b) Far-field screech noise with thick lip nozzle.

Figure 3.5. PSD of far-field noise of the screeching jets generated by a thin and a thick lip nozzle (Assunção 2018).

C was reported compared to thin-lip cases; second, the range of NPR over which intermittent switching between these two modes occurs was observed to be reduced; third, mode C was observed to extend over a larger range of NPR values, meaning that the transition to mode D should occur at larger NPR values compared to thin-lip cases. The impact of the nozzle thickness is visible in the graphs 3.5a and 3.5b where the cartography of the PSD of far-field noise is plotted at different operating points (M_j) (Assunção 2018).

3.2 Experimental configuration

3.2.1 Jet facility

The jet studied was issued from a contoured convergent nozzle of exit diameter $D = 22$ mm and designed to ensure a straight sonic condition at the exit.

A schematic of this nozzle is given in figure 3.6. The flow, supplied by 80 bar pressurised air tank, was regulated in mass-flow rate and temperature, such that the total temperature was set to $T_{t0} = 293$ K. This stagnation temperature and the Nozzle Pressure Ratio (NPR) were monitored throughout the experiment using respectively a thermocouple and a total pressure probe located 0.7 m upstream of the convergent nozzle (equivalent to $\approx 32D$). Different NPR were investigated, ranging from 1.7 to 8.

As illustrated in figures 3.6, 3.7 and 3.9, one particular feature of the nozzle considered in this work lies in its large lip thickness $t = 6.9$ cm $= 3.1D$. As observed by other authors (section 3.1.2.5), this geometry has a significant effect on the screech properties of the jet, this point being further developed in section 3.3.

3.2.2 3D BOS setup

BOS images were acquired using 8 cameras (JAI BM-500GE) placed on an azimuthal arc of 1 m radius centred on the jet axis and homogeneously distributed over an azimuthal angle of 135°, as schematically shown in figure 3.7. These 5MPx cameras have a 2/3 inch sensor with a pixel size of 3.45 μm and were equipped with 50 mm focal length lenses (Schneider). With this optical setup, each camera observed an area of about 16 cm × 14 cm in a plane containing the jet axis. Four background plates were placed on the opposite side, at a distance of 0.4 m from the jet axis. The BOS backgrounds were designed using a semi-random dot pattern printed with opaque UV ink on a glass beads retroreflective layer. These dots had a diameter of 0.35 mm, yielding a size of 3.5 px in the images. Unlike usual printed backgrounds that exhibit Lambertian reflectance,

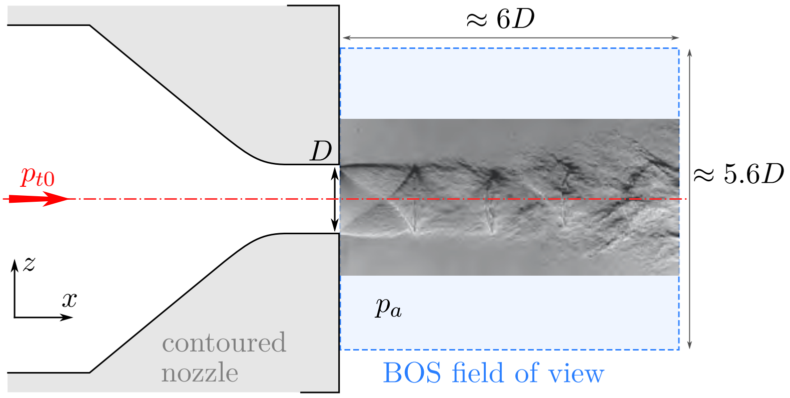

Figure 3.6. Schematic view of the contoured nozzle geometry studied issuing an under-expanded supersonic jet visualised using Schlieren photography; the field of view represented corresponds to the approximate one obtained with the 3D BOS setup.

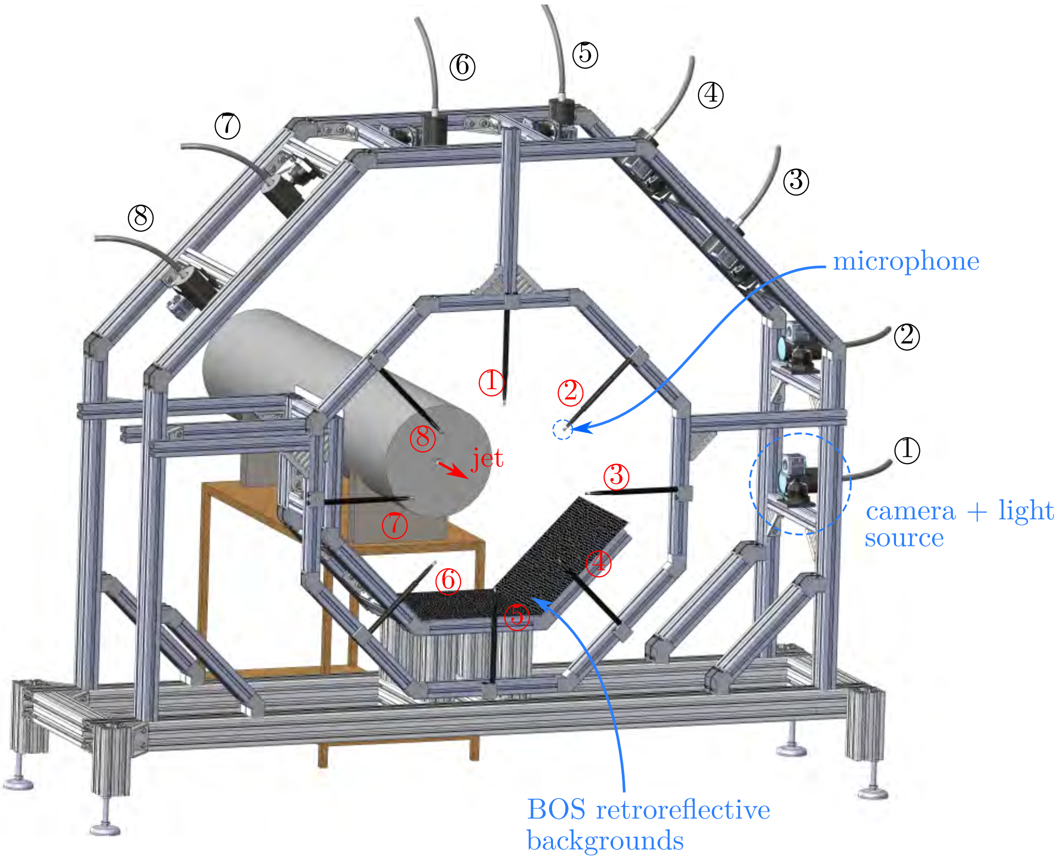

Figure 3.7. Schematic view of the 3D BOS setup mounted around the supersonic jet nozzle axis; the 8 cameras are placed on an arc covering an azimuthal angle of 135° and the 8 microphones are distributed on a circle every 45°.

these retroreflective backgrounds reflect the light back to its source with minimum scattering: the quantity of light reaching the camera is larger, enabling smaller apertures and thus finer spatial resolutions.

Illumination of the backgrounds was achieved using a 532 nm double-pulse laser (Quantel EverGreen 200). Only one laser pulse was used during the cameras exposure time, leading to an effective exposure time of about 10 ns, the pulse duration. This time scale ensured that the turbulent structures of the flow imaged by the cameras did not move more than about 0.1 px during each acquisition. This was regarded as sufficient in this work to consider the acquisitions as instantaneous images of the flow.

Because of the high directivity of the retroreflective backgrounds reflection, each camera needed its own light source. Consequently, the laser beam was split into eight beams using a separation table made of seven 50:50 beamsplitter plates (figure 3.8). Eight liquid guides equipped with diverging lenses were then used to direct this light toward the backgrounds. With such a setup, the amount of light collected by each camera was sufficient to operate at an optimal f-number $f_{\#} = 16$. Under these conditions, the circle of confusion of the optical system in the region of the flow has an approximate diameter of 0.9 mm. This value is similar to the size of the interrogation window used in the post-processing algorithm (15 px) back-projected to the flow region. It is then expected that the global spatial resolution of the present BOS measurements is about 1 mm.

The 8 cameras and the laser were synchronised using a TTL pulse generator, ensuring a synchronous observation of the flow by the cameras. During the acquisition, the camera images were transferred to a computer RAM and stored on a SSD disk. In order to obtain well converged first and second statistical moments of the BOS displacement fields, 6000 images were acquired for the 6 aerodynamic conditions tested, corresponding to NPR $\in \{2.1, 2.3, 2.7, 4.0, 5.0, 6.6\}$ as explained in section 3.3. A maximum acquisition rate of 5 Hz was achieved, yielding statistically independent realizations but no relevant information about the temporal dynamics of the flow, the typical fundamental screech frequency measured in the present experiments being around 5 kHz.

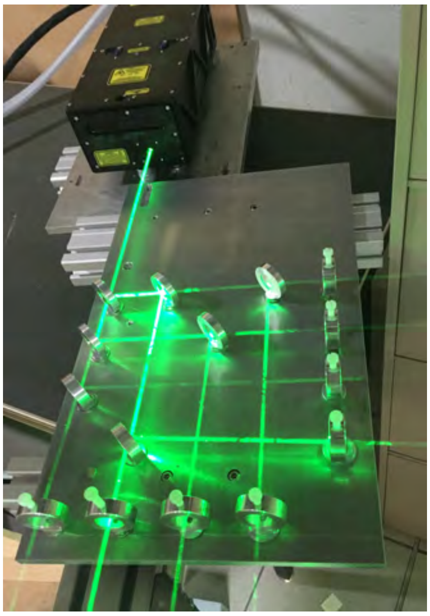

Figure 3.8. The laser beam coming out of Quantel EverGreen is separated into eight beams through a separating plate made of seven 50:50 beamsplitter plates. The photo does not include the liquid guides that bring light to the light spots located next to each camera.

3.2.3 Acoustic setup

The temporal dynamics of the jet flow was indirectly scrutinised through acoustic measurements. This was performed using 1/4inch microphones (GRAS 46DB) having a dynamic range upper

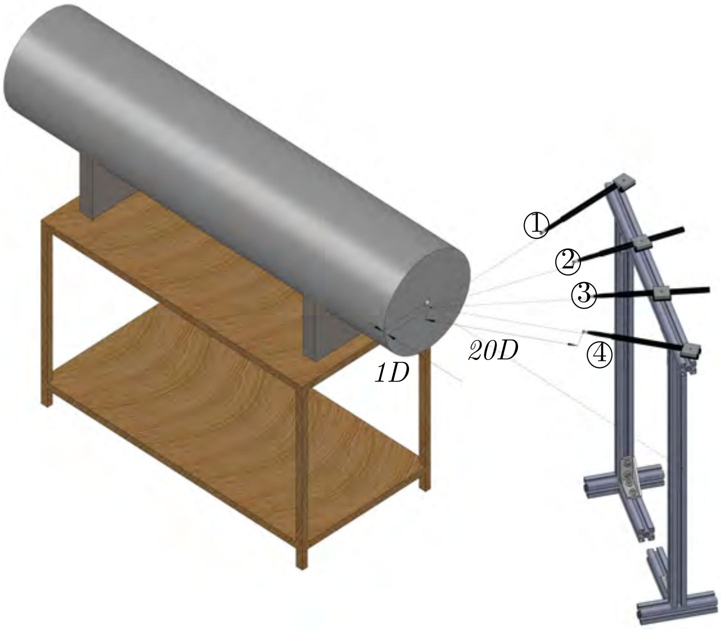

Figure 3.9. Microphone arrangement used to characterise the characteristic screech frequencies of this jet facility. The four microphones are placed radially on the horizontal plane at a distance of $20D$ (44cm) from a point placed on the axis of the jet at a distance of x = 1D from the exit, forming angles of $\theta = 30, 50, 70$ and 90° with the axis of the jet.

limit of 166dB and a frequency range of 70 kHz.

Two microphone setups were considered. In the first configuration, four microphones were mounted along an arc of radius r = 20D, centred on the jet axis at x = 1D and with polar angles measured from downstream θ = 30°, 50°, 70° and 90°. This setup allowed studying the jet noise directivity and was employed to analyse the screech properties of the jet presented in section 3.3.

In the second setup that is schematically represented in figure 3.7, eight microphones were evenly mounted (every 45°) on a ring centred on the jet axis in order to analyse the azimuthal distribution of the jet acoustic field. This ring was positioned at x = 21D and the microphones were located at r = 13D.

These acoustic measurements were not performed in anechoic conditions, but care was taken to attenuate the acoustic reflections on the floor and the walls of the facility as well as on the BOS structure itself using acoustic foam panels . These muffled conditions were observed to be sufficient for the present analysis. Indeed, very limited reflection artefacts were observed on the acoustic spectra.

Furthermore, it should be noted that this work is primarily focusing on the analysis of the jet screech effects that occur at very specific frequencies and with large sound pressure levels that easily emerge from the background noise.

Finally, it was verified that the presence of the 3D BOS bench did not modify the frequencies and the levels of the screech noise measured, ensuring the relative non-intrusivity of our setup and measurement technique.

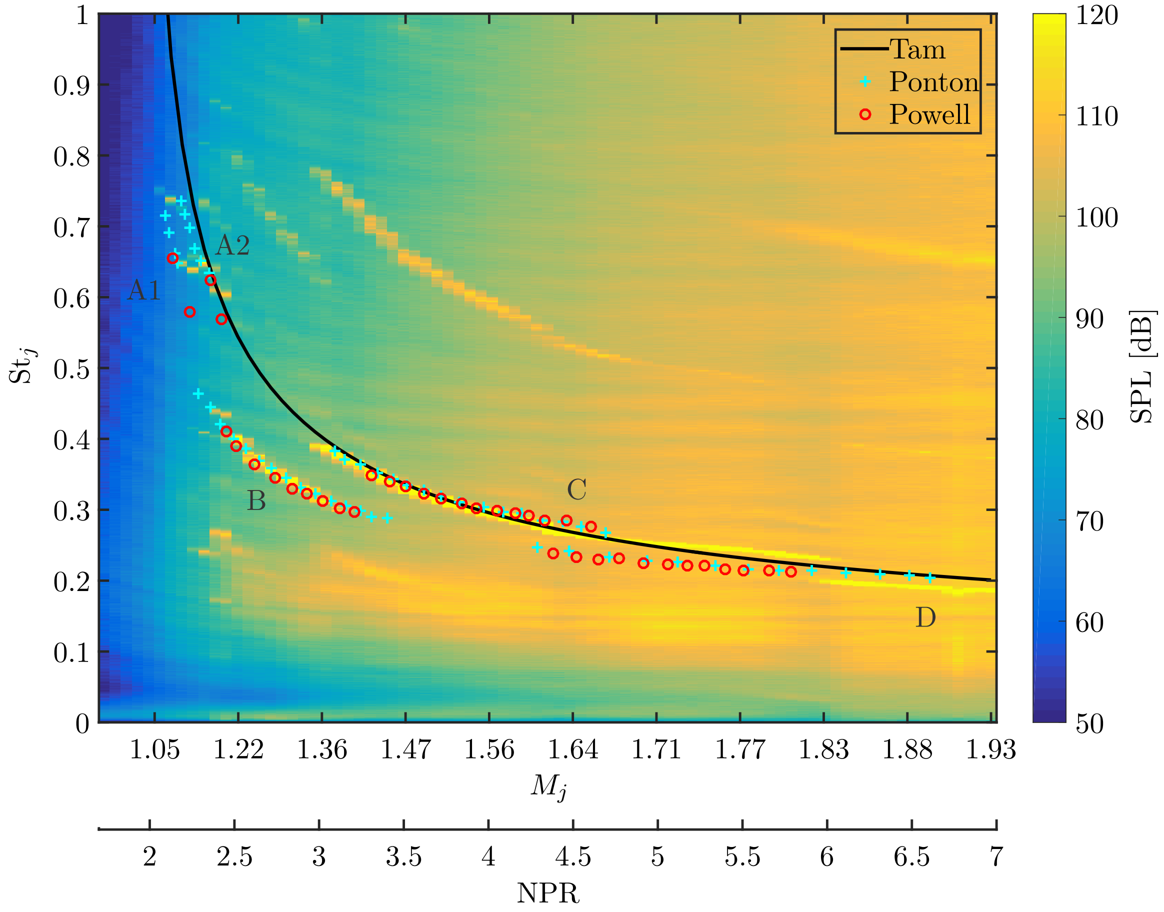

Figure 3.10. Contours of sound pressure level (SPL) as function of jet operating conditions (NPR and Mach number M_j) acquired with microphone number 4 ($\theta = 30°$). The solid black line is the semi-empirical relation proposed by C. Tam et al. (1986), the blue and the red dots are representative of measurements obtained by M. Ponton and J. Seiner (1992) and Powell (1953) respectively.

3.3 Acoustic measurements

3.3.1 Identification of the screech modes

Measurements were performed to characterise the screech frequencies on a wide range of NPR values.

Figure 3.10 was obtained using the first acoustic measurement setup presented in figure 3.9 using only the most downstream microphone (microphone 4 at $\theta = 30°$ from the jet axis). This figure provides contours of SPL as a function of the NPR (or equivalently M_j using Eq. 3.1) and the Strouhal number $St_j \equiv fD_j/U_j$. Screech tones are observed in this figure as thin spectral bands of large SPL decreasing as the NPR increases. The main modes reported in the literature are labelled next to the fundamental spectral bands while the second harmonics are left aside. Together with these acoustic measurements are plotted some classical results reported in the literature. The solid black line corresponds to the semi-empirical law proposed by C. Tam et al. (1986) that reads:

$$St_j = 0.67\left(M_j^2 - 1\right)^{-1/2}\left[1 + 0.7M_j\left(1 + \frac{\gamma - 1}{2}M_j^2\right)^{-1/2}\left(\frac{T_a}{T_{t0}}\right)^{-1/2}\right]^{-1} \quad (3.4)$$

where T_a/T_{t0} is the ratio of the ambient to the total temperature of the jet.

As one can observe, this smooth function provides overall satisfactory estimates of the screech frequencies for modes A, C and D. Note however, that, by design, it cannot account for the modes staging phenomenon and for the frequencies of mode B.

In addition to this curve, experimental results obtained by Powell (1953) and M. Ponton and J. Seiner (1992) for thinner lip configurations are superposed. A satisfactory agreement is obtained for NPR values lower than 4. For NPR > 5, in agreement with the literature mentioned in section 3.1.2.5, the mode C from our thick-lip screeching jet extends over a larger range, up to NPR $= 6.1$. In addition, no screech cessation was observed up to the maximum NPR $= 7$ reached.

Based on these results, six values of NPR were selected to further investigate the different modes of screech using 3D BOS: 2.1 (mode A1), 2.3 (mode A2), 2.7 (mode B), 4.0 and 5.0 (mode C) and 6.6 (mode D). These values were chosen to lie in the middle of each mode spectral band in order to ensure stable conditions and avoid at best modes intermittency and switching.

3.3.2 Analysis of the azimuthal acoustic field

The mean structure of the azimuthal acoustic field generated by the different screech modes is investigated in this section using the acoustic measurements obtained with the ring of microphones previously shown in figure 3.7. Note however that the BOS setup was removed to ensure minimal intrusivity by reducing possible acoustic interferences that could be induced by the metallic structure and BOS panels.

To a perform such an analysis and similarly to Powell et al. (1990) for example, we focus on the acoustic phase-difference between the microphones composing the ring, at the screech frequency. Various techniques can be employed to estimate this phase-difference. Powell et al. (1990) relied on temporal correlograms, but one may also consider Hilbert transforms or cross-power-spectral densities (CPSDs), both providing some information about the phase of a signal. In the present work, we relied on CPSDs that can be understood as the equivalent of correlograms in the frequency domain.

First the signals were digitally filtered with a bandpass filter centred around the screech frequency ($f_s \pm 200$Hz). Cross-power-spectral densities between one arbitrary microphone (here we considered the microphone 1, that is the topmost in figure 3.7 at $\phi = 0°$) and the other ones were then evaluated relying on Welch's method. Finally, the phase difference $\psi_{n,1}$ between the microphones n and the reference one was estimated at the screech frequency by:

$$\psi_{n,1} = \text{angle}\left(\text{cpsd}_{n,1}\left(f_s\right)\right) \tag{3.5}$$

The results for each investigated NPR are shown in figure 3.11 using red circles. In addition, a second estimate of phase difference obtained by averaging the phase differences on a broader range of frequency ($fs\pm$ 100Hz) is plotted in this figure 3.11 using blue markers. This second approach provides an indication of the uncertainty associated with these results in the form of standard deviations evaluated on these spectral bands.

Regarding modes A1 and A2, it results that for all microphones the phase difference is close to zero (figures 3.11a and 3.11b). There are some small phase deviations that may be due an inaccurate positioning of the microphones on the circular ring, such that some microphones could be placed farther or closer to the jet axis, thus inducing slight phase discrepancies; this is more marked for microphones 4, 5 and 6. From these measurements it can be concluded that the jet mode is most likely symmetrical, i.e. toroidal, as already emphasised in the literature (section 3.1.2.1). Interestingly, the phase difference estimates obtained on a spectral band show

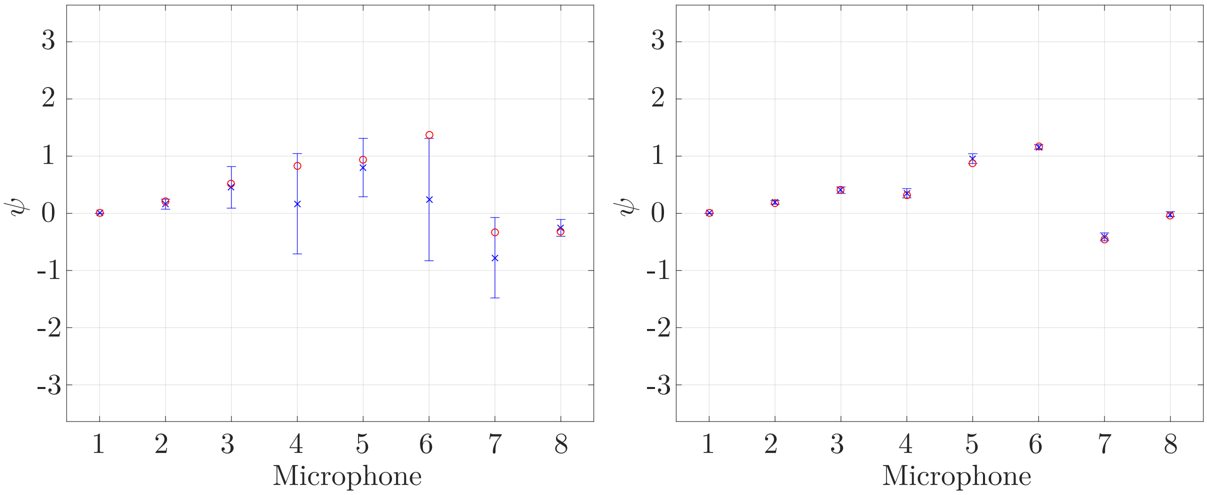

(a) NPR = 2.1, mode A1.

(b) NPR = 2.3, mode A2.

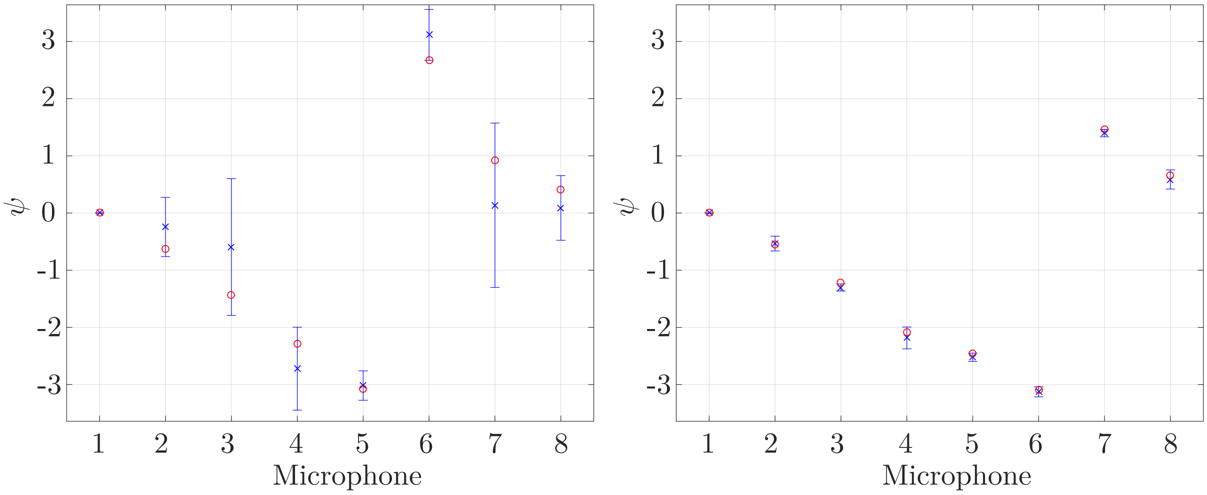

(c) NPR = 2.7, mode B.

(d) NPR = 4.0, mode C.

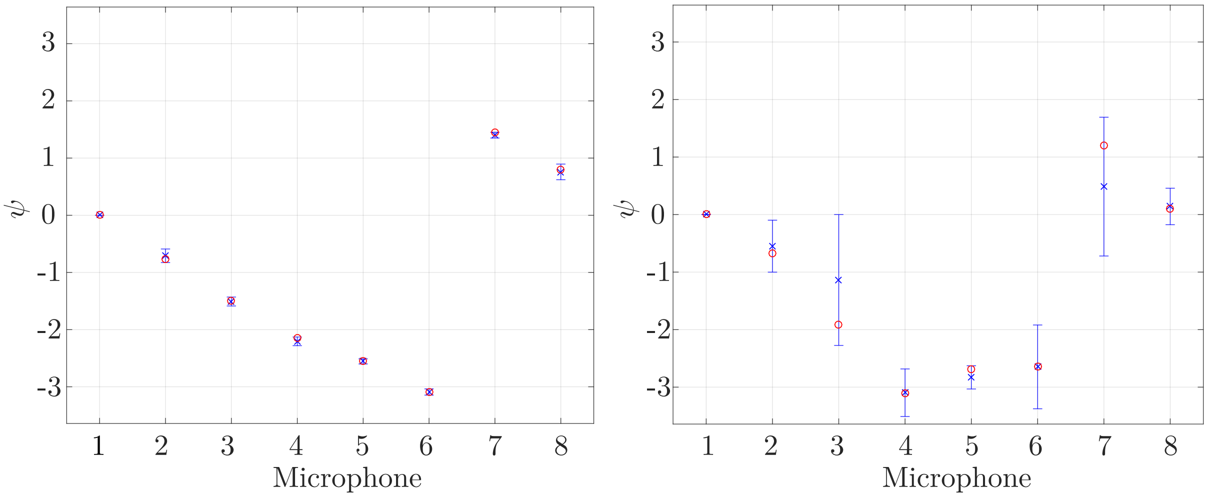

(e) NPR = 5.0, mode C.

(f) NPR = 6.6, mode D.

Figure 3.11. Variation of phase difference ψ for various angular separations of the microphones around the jet axis, for modes A1, A2, B, C and D. The red circle markers ○ provide the phase lag ψ obtained by evaluating the phase at screech frequency f_s, while the blue cross markers × indicate the averaged phase lag computed around the screech frequency $f_s \pm 100$Hz; the error bars provide the standard deviation associated with these phase difference estimates.

that mode A2 yields results with lower variance compared to mode A1, suggesting a more stable condition for this mode A2. Nonetheless, we emphasise that the spectral band over which the standard deviations are evaluated is arbitrary. Reducing it to ±70Hz yields much lower standard deviations for mode A1, suggesting that this mode is also relatively stable but with a narrower spectral content.

Looking at the measurements made at NPR 4 and 5 (figures 3.11d and 3.11e), a similar conclusion can be made for mode C. This mode appears to be very stable and the phase difference varies linearly with the angular position of the microphones. This type of phase difference distribution means that this mode has a helical type of dynamics, with an unit azimuthal wave number (M. K. Ponton and J. M. Seiner 1995).

The interpretation of the results is more difficult for modes B and D, respectively obtained at NPR 2.7 and 6.6 and plotted in figures 3.11c and 3.11f. Standard deviations are observed to be significantly larger than for the other modes, which could indicate more unsteady behaviours. Nonetheless, mode B seems to have a trend similar to the two cases of mode C since the phase difference varies linearly with the angular position of the microphones. This suggests that the jet is here mainly characterised by a helical dynamics and not a sinuous mode with rotating plane as observed by Powell et al. (1992) and M. K. Ponton and J. M. Seiner (1995). Excluding microphone 3 ($\phi = 90°$), the phase measurements for mode D (figure 3.11f) yield values that are either close to 0 or to -π. As emphasised by (M. K. Ponton and J. M. Seiner 1995) this result is consistent with what would be expected for a sinuous, flapping mode.

3.4 Mean density fields results

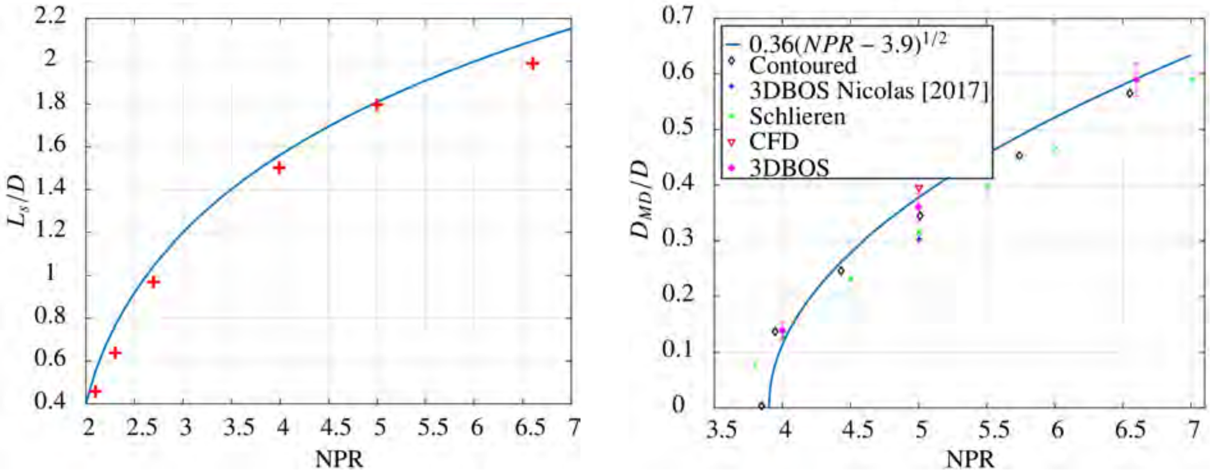

(a) (b)

Figure 3.12. (a) Mean shock spacing L_s/D as a function of jet operating conditions: the solid line is the Prandtl-Pack formula (equation (3.6)) and red plus markers correspond to the present mean 3D BOS results; (b) First Mach disk diameter D_{MD}/D as a function of the jet NPR: the blue solid line is the relation proposed by Addy (1981); the black diamonds are experimental data from Addy (1981); the blue plus markers were obtained from 3D BOS by Nicolas et al. (2017a); the green crosses correspond to Schlieren visualizations; the red inverted triangle is from RANS simulation; the magenta dots correspond to the results of the present experiment. Note that the last four data sets were obtained with the same jet facility.

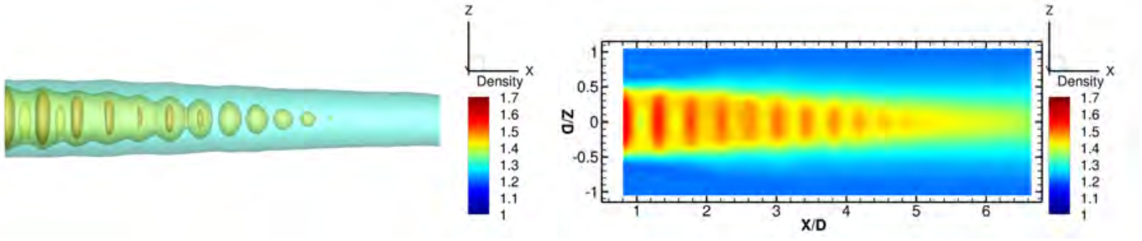

(a) NPR = 2.1

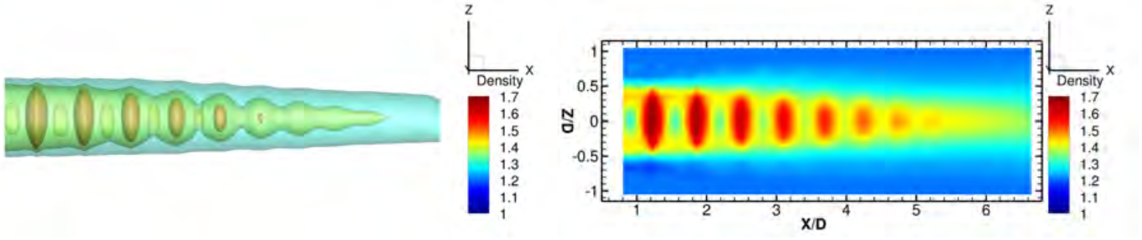

(b) NPR = 2.3

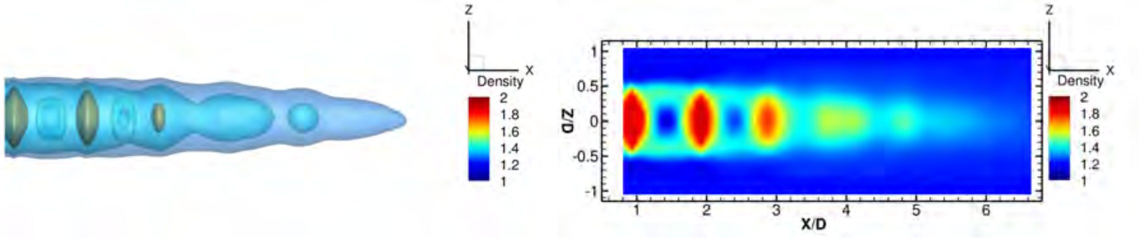

(c) NPR = 2.7

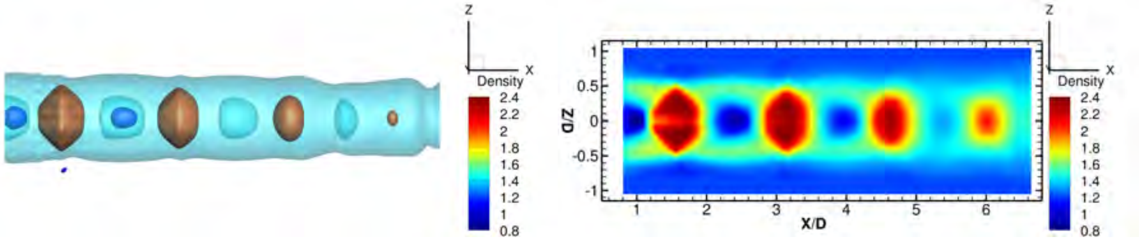

(d) NPR = 4.0

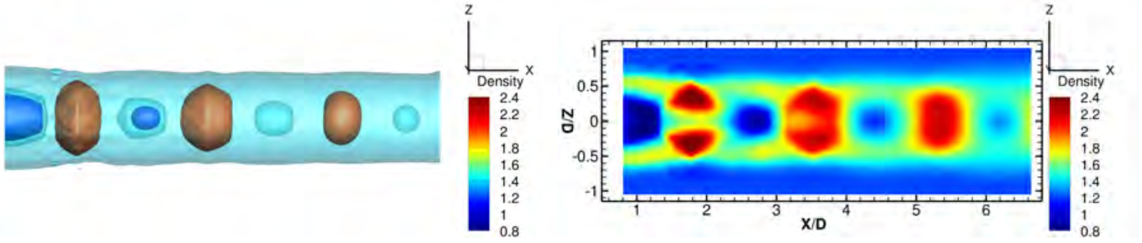

(e) NPR = 5.0

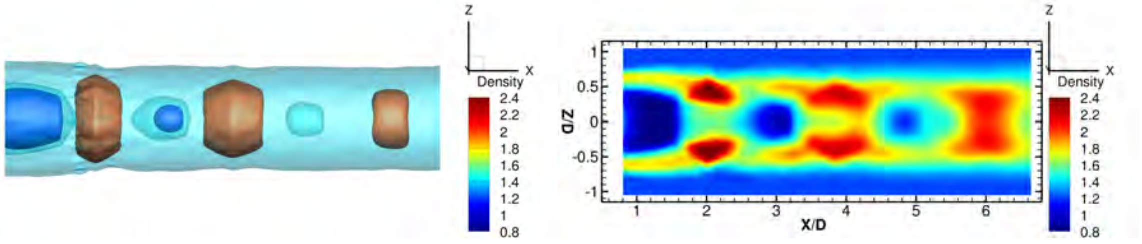

(f) NPR = 6.6

Figure 3.13. Mean 3D BOS results obtained for the six NPR values selected; left column: 3D iso-surfaces of mean density; right column: contours of mean density in the plane $y = 0$.

This section details the properties of the 3D mean density fields obtained by 3D BOS for the six NPR conditions identified in section 3.3.1 using acoustic measurements.

The results are gathered in figure 3.13, displaying 3D density iso-surfaces and density contours in a longitudinal plane (xz). Examining the 3D iso-surface plots, axisymmetric mean density fields are well recovered for all the conditions, which is to be expected. Shock cells appear to be furthermore well captured and one can clearly visualise the increase of the spacing between the cells as the NPR is increased. These shock cells are more readily observed in the density contours extracted from the $y = 0$ plane, which also illustrate the presence of Mach disks for the last three NPR conditions.

In order to compare the mean properties of the present jet with the ones reported in the literature, quantitative data regarding the topology of these jets were extracted from these 3D BOS reconstructions. First, the mean shock spacing L_s was evaluated for each NPR. These results are compared in figure 3.12a with the Prandtl-Pack formula that reads:

$$\frac{L_s}{D} = 1.306 \left(M_j^2 - 1\right)^{1/2} \tag{3.6}$$

A satisfactory agreement is observed, displaying an increase of the shock spacing for increasing values of the NPR.

Second, the average diameter of the first Mach disk D_{MD} appearing for a NPR ≈ 4 was evaluated based on the gradient amplitude of the reconstructed density fields for the three highest NPRs studied (4, 5 and 6.6). These results are compared in figure 3.12b with experimental results reported by Nicolas et al. (2017a) and by Addy (1981) for a contoured nozzle similar to the one here studied. Furthermore, estimates of D_{MD} were also extracted from Schlieren visualizations performed under similar conditions and from a RANS simulation performed by the authors.

The overall agreement with all the results is satisfactory, especially with Addy's, suggesting that the present facility and jet main characteristics do not feature significant geometrical or aerodynamic imperfections. We finally note that the main source of uncertainty in the estimation of D_{MD} from our 3D density results is expected to lie in the spatial resolution of the technique. This uncertainty remains nonetheless sufficiently low to have confidence in the accuracy of the spatial features of the flow evidenced by the 3D BOS technique. Particularly, one can observe an improvement on the estimation of D_{MD} compared to the previous 3D BOS setup used by Nicolas et al. (2017a) at NPR = 5.

3.5 3D density fields of screech modes

The low acquisition rate of the 3D BOS system prevents us from performing a spatio-temporal analysis of the jet dynamics associated with screech. Nonetheless, the absolute instability at the root of screech is expected to significantly alter the jet density field in the form of large coherent oscillations in the jet plume: its coherent imprints should be observed on the instantaneous BOS displacement fields obtained from each camera, as shown in section 3.5.2.

Following the work of Nicolas et al. (2017a) we thus propose to rely on a Proper Orthogonal Decomposition (POD) of the displacement fields (and not the 3D BOS instantaneous density fields for a computational cost reason) in an attempt to isolate the main coherent features associated with the plume instability. A similar approach was also considered by Edgington-Mitchell et al. (2014) to study the dynamics of the screech mode C relying on PIV data.

In the present work, the displacement field **d** obtained with only one camera among the eight available was considered since it was observed to provide sufficiently reliable data for this first investigation. A consequence of this choice is that complex screech dynamics such as flapping

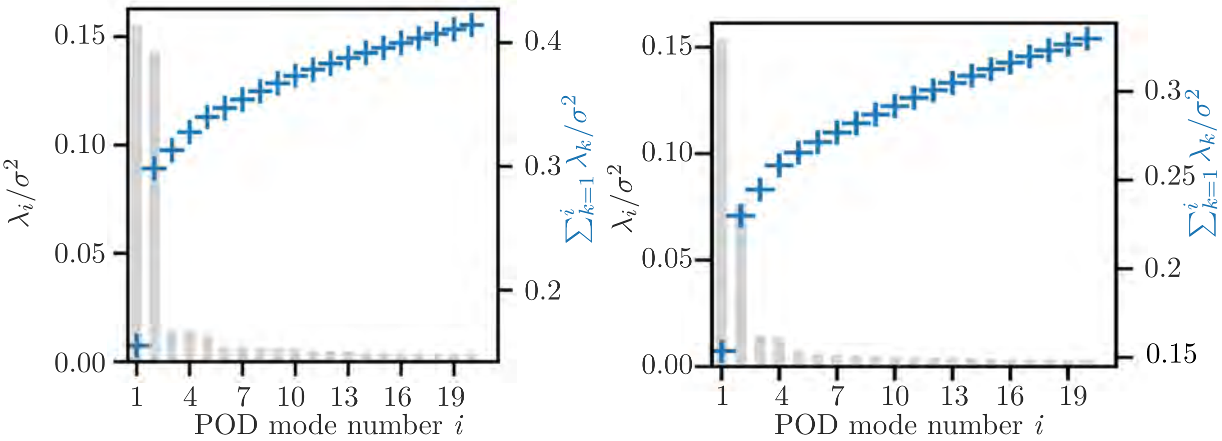

(a) NPR = 2.1 (mode A1) **(b)** NPR = 4.0 (mode C)

Figure 3.14. Normalised POD eigenvalues λ_i/σ^2 obtained on the BOS displacement fields of one camera for two NPR values. These eigenvalues are made dimensionless using the total displacement variance σ^2. The cumulative sum of these eigenvalues (right vertical axis) indicates the fraction of energy captured with an increasing number of modes.

were not satisfactorily captured (that is for modes B and D), and only axisymmetric and purely helical features (modes A and C) were observed to be efficiently isolated. Hence, only these two last modes A and C (that is the two cases where NPR equals 2.1 and 4.0) are further analysed in this section. One perspective for the future will however consider the use of all the cameras to isolate the dominant structures for all the screech modes.

Note that the choice of the camera considered for the following analysis does not modify the results: each camera having a similar point of view on the jet by rotational symmetry around the jet axis, similar decompositions will be obtained.

3.5.1 Proper Orthogonal Decomposition results

POD is performed using the Snapshot POD method proposed by Sirovich (1987) since the number of images acquired per camera (N = 6000) is much lower than the number of displacement vectors evaluated per image (typically around 20000).

We briefly recall that this approach seeks a decomposition of the displacement fluctuation field $\boldsymbol{d}'(\boldsymbol{x}, t_j)$ in the form of orthonormal spatial modes $\boldsymbol{\phi_i}$ that optimally capture the variance of the data. We thus have:

$$\boldsymbol{d}'(\boldsymbol{x}, t_j) = \sum_{i=1}^{N} a_i(t_j)\,\boldsymbol{\phi_i}(\boldsymbol{x}) \tag{3.7}$$

where $a_i(t_j)$ are random variables of the time t_j and with an orthonormal condition on the spatial modes that reads $\langle\boldsymbol{\phi_i}, \boldsymbol{\phi_j}\rangle = \delta_{ij}$.

Note that since the present experiment is not time-resolved, these a_i coefficients are functions of the discrete time variable t_j and do not represent the temporal dynamics of the modes. These spatial modes $\boldsymbol{\phi_i}$ and expansion coefficients a_i are obtained following this classical procedure: first, the (temporal) correlation matrix $\boldsymbol{R}$ associated with the displacement vectors $\boldsymbol{d}'$ is evaluated using the L^2 inner product; second, an eigenvalue decomposition of $\boldsymbol{R}$ provides "temporal" modes a_i and eigenvalues λ_i that represent the energy content of each mode (usually sorted in descending order); finally, spatial POD modes are retrieved by the projection:

$$\boldsymbol{\phi_i}(\boldsymbol{x}) = \frac{1}{N\lambda_i}\sum_{j=1}^{N} a_i\left(t_j\right)\boldsymbol{d}'\left(\boldsymbol{x}, t_j\right) \tag{3.8}$$

Applying this approach to the displacement fields obtained for the two NPRs 2.1 and 4.0 yielded the distribution of eigenvalues λ_i given in figure 3.14. One can clearly observe the emergence of the first two eigenvalues in both cases. For the first case (NPR = 2.1), they contribute to about 30% of the total variance, while for the second case (NPR = 4.0) to about 25%. This observation suggests that it is possible to rely on these two modes to analyse the main coherent organization of the flow in both cases. It appears however for now very uncertain to claim here that they are exactly representative of the spatio-temporal dynamics of screech modes. This point will be further discussed in section 3.5.3.

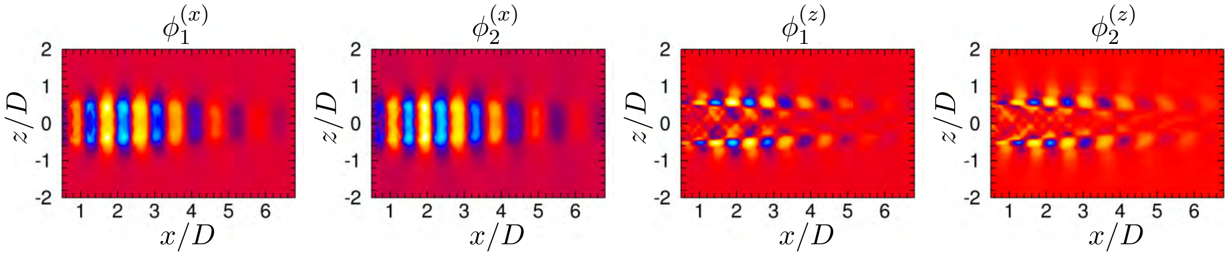

(a) NPR = 2.1

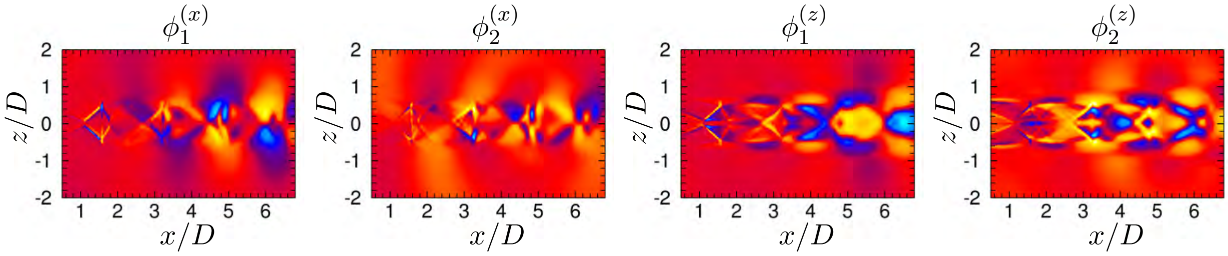

(b) NPR = 4.0

Figure 3.15. Axial $\left(\phi_i^{(x)}\right)$ and vertical $\left(\phi_i^{(z)}\right)$ components of the first two POD spatial modes ($i \in [1..2]$) obtained by considering the BOS displacement fields of one camera for 2 values of NPR.

The spatial POD modes $\boldsymbol{\phi} = \left(\boldsymbol{\phi_i}^{(x)}, \boldsymbol{\phi_i}^{(z)}\right)^T$ associated with these first two eigenvalues for the two NPR cases are displayed in figure 3.15, showing both the horizontal (along x) and vertical (along z) displacement components. Examining these spatial POD modes, it can be observed that for the two aerodynamic conditions, the first two modes selected display a similar spatial structure, with comparable spatial axial wavelength (shifted streamwise by about a quarter-wavelength between the two modes).

For the case NPR = 2.1, the wave-packet-like perturbation is observed to be symmetric along the axis x for the axial component and anti-symmetric for the vertical component. Such a structure is reminiscent of what would be obtained with a Kelvin-Helmholtz-type instability (Edgington-Mitchell et al. 2018).

For the second case NPR = 4.0 we observe that the two spatial modes still display a wave-packet-like structure outside of the jet but with also a significant contribution of fluctuations from the shock cells inside the jet.

The symmetry along the axis x is different compared to the case NPR = 2.1: the axial component of displacement is antisymmetric along x while the vertical component is symmetric.

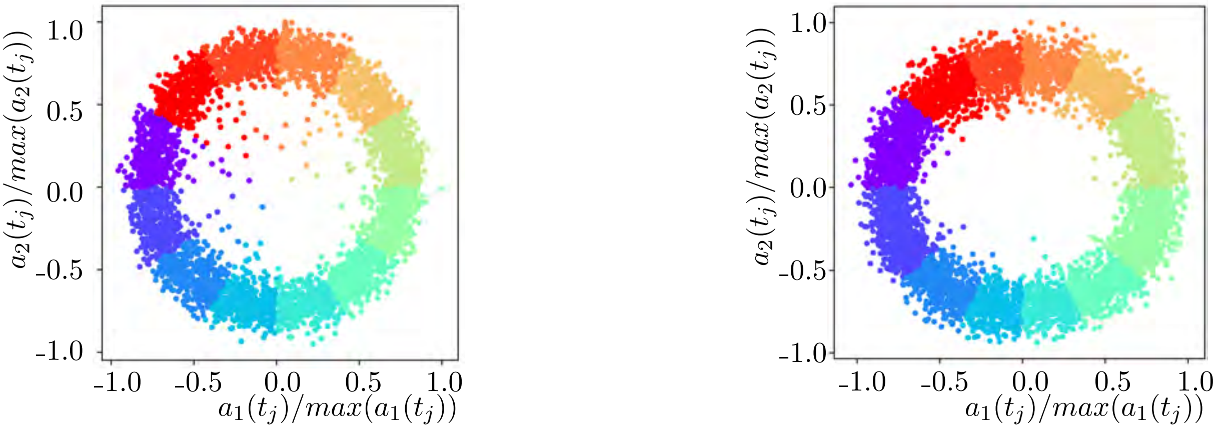

(a) NPR = 2.1 (mode A1) **(b)** NPR = 4.0 (mode C)

Figure 3.16. Scatter plots $(a_1(t_j), a_2(t_j))$ giving the state of all BOS acquisitions (of one camera, $j \in [1..N]$) in the subspace generated by the first two POD spatial modes $\boldsymbol{\phi_i}(\boldsymbol{x})_{i\in[1..2]}$ for the two NPR conditions corresponding to screech modes A1 and C. Colours highlight the division of the scatter plot to define 12 phase classes.

Such a structure is comparable to what would be obtained with an helical instability with unit azimuthal wavenumber (Edgington-Mitchell et al. 2014).

These observations are thus consistent with the general physical behaviour of screech modes reported in the literature for the modes A and C here studied.

The previous observation that the first two dominant POD modes of each NPR case have similar structures suggests that they could be coupled and representative of a similar convective and oscillatory feature like the global instability associated with screech. One way to investigate such a coupling is to plot the state of each BOS acquisition in the subspace generated by the two dominant modes $(\boldsymbol{\phi_1}, \boldsymbol{\phi_2})$, yielding the scatter plot $(a_1(t_j), a_2(t_j))$. If the measurements were temporally resolved, this would lead to a Lissajous figure (or a phase-portrait in terms of dynamic systems) and a purely oscillating dynamics would generate a circle in such a phase-space. The results for the two NPR values considered are displayed in figure 3.16. One can clearly observe that both scatter plots statistically draw a circle with some radial dispersion, supporting a phase-coupling between the two modes that are thus likely representative (statistically) of a convective oscillatory dynamics linked to the plume instability. Further support on this point will be provided in section 3.5.3.

The plots given in figure 3.16 finally offer a way to sort all the BOS images obtained with all the cameras: dividing the two plots in twelve angular sectors, we can define for each BOS acquisition a given "phase" relative to the first two dominant POD modes identified with one camera. This procedure is illustrated in this figure by filling the markers with 12 different colors.

Evaluating the associated phase-average of the displacement fields for each camera based on this sorting procedure yields 12 mean displacement fields for each camera and finally 12 phase-averaged 3D density fields after reconstruction. These 3D results are displayed in figure 3.17. As one can observe, relying on this methodology leads to phase-averaged 3D density fields that are axisymmetric for NPR = 2.1 and helical for NPR = 4.0. These results are in line with the accepted topology of the plume instabilities associated with screech modes A1 and C. This is however the first time to the knowledge of the authors that such average 3D structures are actually reconstructed, assuming that the present methodology provides a representative image of the instabilities associated with screech.

We conclude this section by noting that these phase-averaged reconstructed density fields

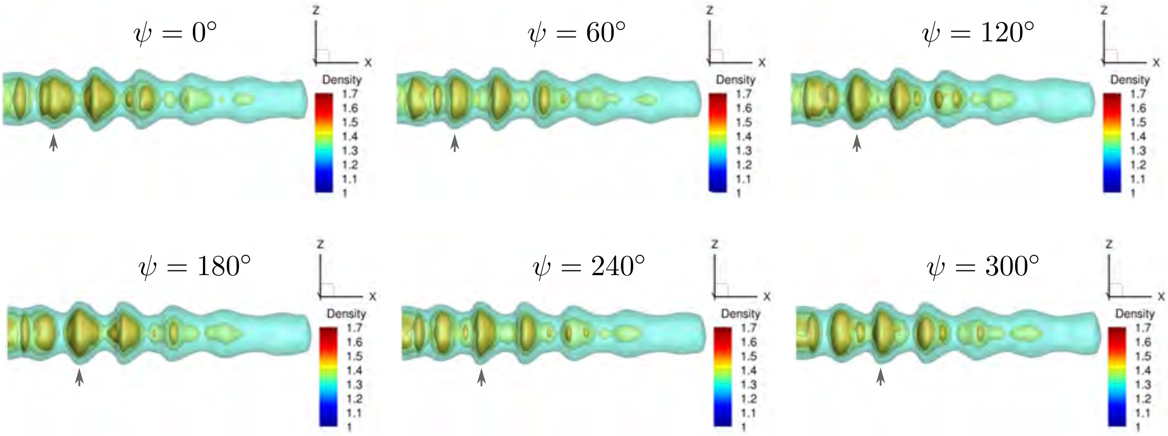

(a) NPR = 2.1

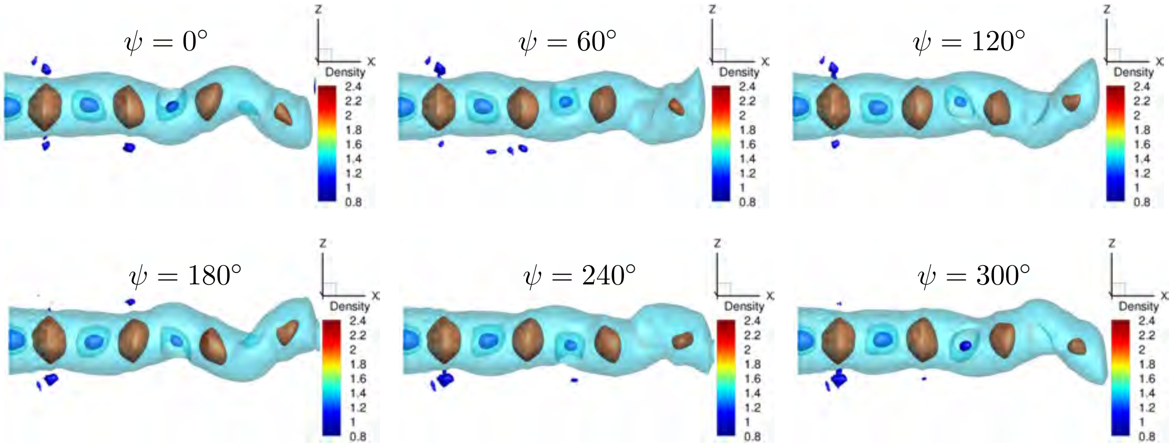

(b) NPR = 4.0

Figure 3.17. Phase-averaged 3D density fields obtained by 3D BOS using the first two spatial-POD modes to sort the images of the 8 cameras for the two NPR conditions corresponding to the screech modes A1 and C.

allow us to qualitatively observe the phase-averaged dynamics of the shock cells for the two NPRs considered. For NPR = 2.1 (mode A1), the first shock cells appear to be significantly disturbed by the perturbation, with forward and backward oscillations. For NPR = 4.0 (mode C), it is observed that the second, third and fourth shock cells remain at the same axial locations but appear to sustain a precession around the x axis, moving in a circular motion within a plane that tilts slightly and periodically with respect to the (yz) plane.

3.5.2 Instantaneous 3D density fields

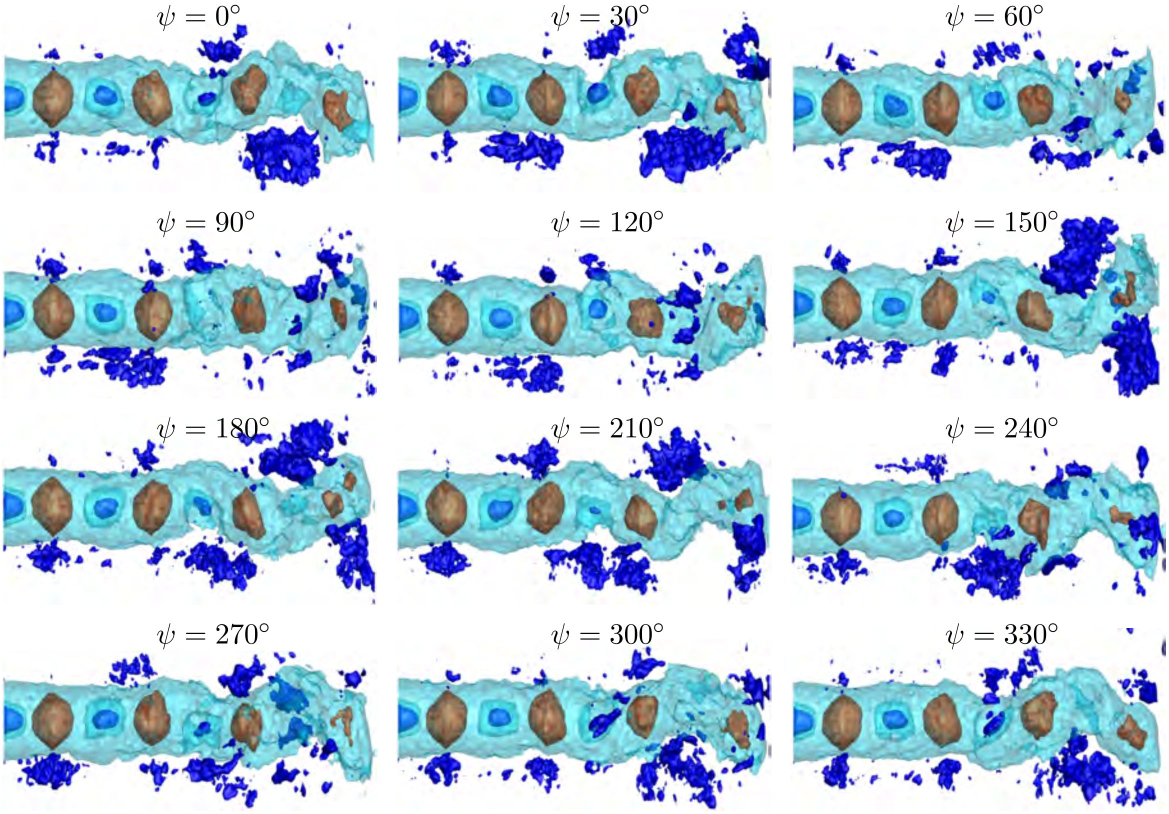

Figure 3.18. Iso-surfaces of 4 instantaneous 3D density fields reconstructed by 3D BOS for the case NPR=4.0; the phase ψ of these fields was evaluated relatively to the first two spatial POD modes.

To highlight the fact that 3D structures identified by the previous methodology relying on POD does not provide completely artificial results, figure 3.18 provides instantaneous 3D density reconstructions obtained for the case NPR = 4.0. These twelve instantaneous fields were arbitrarily chosen from the data shown in the scatter plot of figure 3.16b, one for each angular sectors. While these reconstructions do not provide as smooth density fields as the phase-averaged results, a similar helical organization of the flow can clearly be observed, confirming the physical relevance of the 3D structures previously identified.

3.5.3 On the link between POD results and screech modes

Finally, a central question that one may ask is whether the 3D coherent structures previously identified using (spatial-only) POD are relevant in the description of the (spatio-temporal) screech modes or not. To investigate the possible connection between POD modes and screech noise, 3D BOS measurements were performed together with acoustic measurements using the

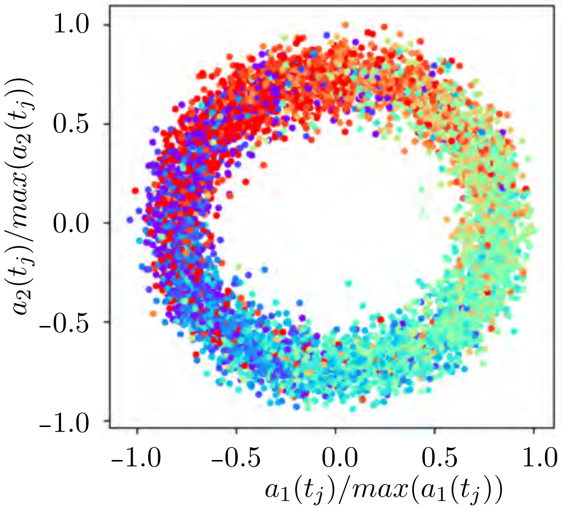

Figure 3.19. Scatter plot similar to figure 3.15b, but with marker colored by the phase value determined by acoustic measurements.

second acoustic setup presented in section 3.2.3, that is with an azimuthal array of microphones shown in figure 3.7. For each BOS acquisition, an oscilloscope acquired the laser Q-switch signal, defining the exact time at which BOS images were recorded, and the acoustic signal of six microphones over at least ten acoustic periods associated with the screech frequency. These acoustic measurements were then post-processed using a narrow digital 100 Hz band-pass filter centred on the screech frequency (with zero phase-shift) and a Hilbert transform to provide a phase estimate of each BOS acquisition with respect to screech. Note that in this process, one actually needs to account for the phase-shift induced by the location of the microphones with respect to the source of screech noise, a distance that is not precise and likely stochastically fluctuates due to the motion of the shock waves. To illustrate the results obtained following this approach, let us consider the case NPR $= 4.0$. Similarly to what was performed with POD, BOS acquisitions were divided into 12 "screech phase" classes. An easy way to visualise the results in comparison with the ones obtained by POD is to consider the scatter plot of POD coefficients in figure 3.16b and to set the colors of the markers as a function of the "screech phase" here evaluated. If the two approaches were equivalent, the coloured version of figure 3.16b would be exactly retrieved.

The plot obtained is shown in figure 3.19: a dispersion of the markers of similar color can be observed, suggesting that some differences exist. Nonetheless, one can notice that this dispersion is not uniform, but that it is centred around each phase class considered, over an angle of about 90°. This figure 3.19 appears as a dispersed version of 3.16b maintaining the overall phase class order previously identified. We thus suggest that, while the details of the two approaches are different, they capture on average the same physics. In other words, we believe that these results support the idea that the POD analysis performed previously is actually relevant in isolating the average modes associated with screech noise. The dispersion observed in the present results is likely the consequence of either some jittering of the screech modes (we observed for example slight variations of its frequency over a complete acquisition sequence) or some spatial fluctuation of the source of screech with respect to the microphone locations; an other possible origin may be the uncertainty in the phase estimation process using the Hilbert transform.

3.6 Conclusion

In this chapter, the non-intrusive and seedless 3D BOS technique was applied to measure the 3D density fields of under-expanded screeching jets.

Compared to the previous work of Nicolas et al. (2017a) a significant improvement on the spatial resolution of the technique was achieved using retro-reflective backgrounds, yielding smaller lens apertures and reduced astigmatism effects. Specifically, the resolution for 3D measures has been improved to about 1mm compared to the 2.5mm obtained in the previous campaign. In addition, the 3D BOS measurements were coupled, for the first time, with acoustic measurements that were used for the analysis of the dynamics of the screech modes.

A first series of acoustic measurements was performed to characterise the screech frequencies and identify the various screech modes obtained with the present installation. In agreement with results reported in the literature, these measurements allowed to highlight a specificity of the present jet issued from a thick-lip nozzle: an earlier transition in terms of NPR between modes B and C, mode C extends over a larger range of NPR values and transition to mode D occurs at higher NPRs.

Furthermore, relying on an azimuthal ring of microphones centred on the jet axis, the mean azimuthal structure of the pressure field generated by the different modes of screech was investigated. For modes A and C, an analysis of the phase-difference between microphones estimated using cross-power-spectral densities highlighted the axisymmetric and helical nature of these modes, respectively. For modes B and D that display more variability in time, the phase-differences between microphones suggested the presence of spinning and flapping modes. This appears to be in relative agreement with the literature but more analysis is required for mode B. For these 2 modes, examining only the average phase difference between microphones is likely inadequate to properly identify their dynamics and different techniques should be considered.

Finally, relying on the BOS measurements, it was shown that the fluctuating density field associated with the main (average) instability wave driving screech for modes A1 and C could be satisfactorily isolated relying on the first two POD modes of the BOS displacement fields. The relevance of these isolated coherent structures in the description of the screech process was evidenced using acoustic measurements. For the first time to our knowledge, a clear 3D visualization of the two modes A1 and C was obtained, displaying axisymmetric and helical structures.

The methodology devised in the present work to study the modes A and C using acoustic and BOS measurements was shown to provide clear insights into the structure of these modes. However, modes B and D appeared more difficult to analyse. Consequently, future work should intend to adapt this methodology to study these modes. One possible way could be to consider not only one camera to identify POD modes, but all the cameras at once. This approach might prove beneficial to study such modes.

Chapter 4

Study of a hot jet in cross-flow using the BOS technique with enhanced spatial resolution

Contents

This chapter is dedicated to the application of 2D and 3D BOS to a hot jet in cross-flow in the presence of a flat plate.

In Section 4.1, we first explain the motivation that led to the study of this type of flow. The next section presents a bibliographic study on jet in cross-flow.

Section 4.3 is dedicated to the description of the conditions of the experiment as the wind tunnel and the devices for the generation of the hot jet. In the following we present the results obtained through measurement techniques such as LDV (laser doppler velocimetry), PIV (particle image velocimetry), thermocouple and infrared and also a CFD simulation. Successively are described the 2D and 3D BOS setups.

Section 4.4 is dedicated to the results obtained with 2D BOS.

In the final section, the results obtained with 3D BOS are presented: a series of 3D density reconstructions from real and synthetic data have been carried out.

Finally, we provide perspectives and some possible suggestions and improvements for future experiences in the presence of a flow with similar constraints.

4.1 Introduction

Helicopters engine exhaust gases are ejected at a temperature up to 600-700°C (figure 4.1). Under these circumstances, two main thermal problems may appear: thermal stress on the helicopter fuselage and hot air recirculation near engine air intake and avionics sensors.

Currently, these problems are evaluated at the very last stage of a new helicopter development, during the flight tests. The risk of a potential problem at this stage means high expenses and long lead time for redesign. It is therefore of the utmost importance to work on the development of CFD methods capable of estimating the thermal impact of exhaust gases on helicopters.

The main challenge is to accurately describe the turbulent mixing between hot exhaust gases, rotor downwash and the main flow.

Before starting to investigate such a complex configuration, there is a need to study similar academic flows: for this reason an experimental campaign on a hot jet in cross-flow was conducted in F2 wind tunnel at ONERA Fauga-Mauzac center. The experimental conditions are

Figure 4.1. Engine exhaust gases visualization for an H160 helicopter hovering in ground effect. Between the red lines the heat produced by the engines warp the image captured by the camera. (Tatjana Obrazcova ©)

typical of a helicopter engine exhaust gases and these specific ranges are very much absent in the literature. For the investigation of such a jet, with strong thermal gradients, Background Oriented Schlieren is very suitable to reconstruct either 3D density or temperature fields. In the present work, 2D and 3D BOS measurements have been carried out using retroreflective panels to ensure maximum spatial resolution.

4.2 Jet in cross-flow bibliography

In literature the term "jet in cross-flow" of JICF is used generically to describe a flow characterized by a jet (liquid or gas) ejected through an orifice of any shape in a non-parallel main flow. In the following, the term outgoing jet will be associated with a circular jet injected perpendicularly to the transverse flow.

This type of flow has been the subject of intense researches and numerous publications. This interest is explained in particular by its presence in many industrial and natural systems. Among the various applications, the following are most frequently cited in the literature:

- Pollutant and plume dispersion (smoke from chimneys or volcanoes, effluent discharges).
- Vertical and/or short take-off and landing (V/STOL) aircraft: the jet from the engine is injected transversely to the main flow during the transition phase between hovering and forward flight.
- Film cooling of combustion chamber walls and turbine blades in turbomachinery: this is achieved by using jets of cold air ejected through perforations in the wall with low blowing rates.
- Dilution jets in the primary combustion zone and at the combustion chamber outlet.
- Fuel injection in conventional and supersonic combustion chambers.
- Vector thrust control of space systems, missiles and aircraft.

Due to the diversity of applications involving jets with transverse flow, it is understandable that a great deal of research has been conducted on the subject. In this context, the articles by Margason (1993) and Mahesh (2013) collect a large part of the studies carried out over the years.

The interaction of a jet with a transverse flow produces a complex flow that is highly three-dimensional and unsteady. The flow dynamics could be described as four coherent vortex structures interacting with each other. As described in figure 4.2, these structures are located in the near field of the jet, where the interactions between the jet and the transverse flow are most intense; they are the following: the pair of contra-rotating vortices, horseshoe vortices, shear layer vortices and wake vortices. The last two are intrinsically unsteady while the first two exist in the average field even though they may have an unsteady behaviour. Furthermore, Kelso et al. (1996) claimed that the global topology observed in low Reynolds extends to high Reynolds.

In order to describe the test conditions, some parameters should be defined. As is the case with a hot jet entering a flow at room temperature, it is necessary to take into account the different temperature of both flows. Callaghan (1948) studied a heated jet and then introduced the ratio of momentum quantities to take into account temperature effects. This parameter is called blowing rate, hereafter C_R:

$$C_R = \frac{\rho_j V_j}{\rho_0 V_0} \tag{4.1}$$

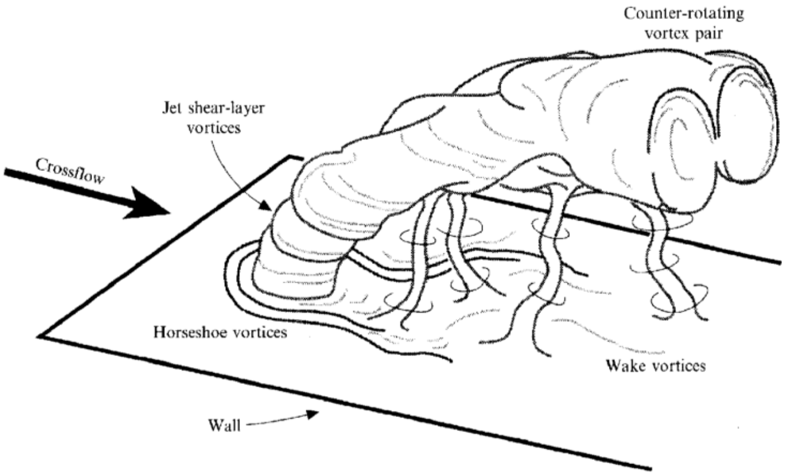

Figure 4.2. Schematic representation of the dynamics of a jet in cross-flow (Fric and Roshko 1994).

where ρ_j and V_j are respectively the density and velocity of the jet and ρ_0 and V_0 are the same quantities but related to the free stream.

Thereafter, Williams and Wood (1965) showed that the blowing rate is not the most appropriate parameter when the effects of temperature and compressibility are no longer negligible. They propose to use a parameter based on the ratio of momentum flows as:

$$R = \sqrt{\frac{\rho_j V_j^2}{\rho_0 V_0^2}} \tag{4.2}$$

Kamotani and Greber (1972) demonstrated that the trajectories based on the local velocity and temperature maxima of a jet flowing at room temperature and a jet heated to 204°C at the same momentum flow ratio overlap perfectly. Harms (1974) shows that at the same momentum flow ratio (R=8), he obtains the same trajectories and positions of the vortex cores for the cold and hot jet. Moreover, at constant R, the velocity fields are very similar between the two jets.

Kamotani and Greber (1972) proposed an empirical equation to describe the location of the maximum temperature as follow:

$$\frac{Z_T}{D} = 0.73\,(J)^{0.52}\left(\frac{\rho_j}{\rho_0}\right)^{0.11}\left(\frac{X}{D}\right)^{0.29} \tag{4.3}$$

Where Z_T is the distance from the flat plate where the maximum temperature is located: it depends on the momentum ratio $J = \rho_j V_j^2/\rho_0 V_0^2$, the density ratio ρ_j/ρ_0 and the distance from the jet X.

In addition the maximum velocity height (Z_V) location writes (Kamotani and Greber 1972):

$$\frac{Z_V}{D} = 0.89\,(J)^{0.47}\left(\frac{X}{D}\right)^{0.36} \tag{4.4}$$

After presenting the main characteristics of the jets in cross-flow and their characteristic quantities necessary to describe their functioning, the experimental set up is presented below to reproduce the conditions sought and to acquire the needed data to study these jets under conditions not covered in the literature and in particular to see the effect of temperature in ranges not previously studied.

4.3 Experimental setup and measurement techniques

4.3.1 Experimental setup

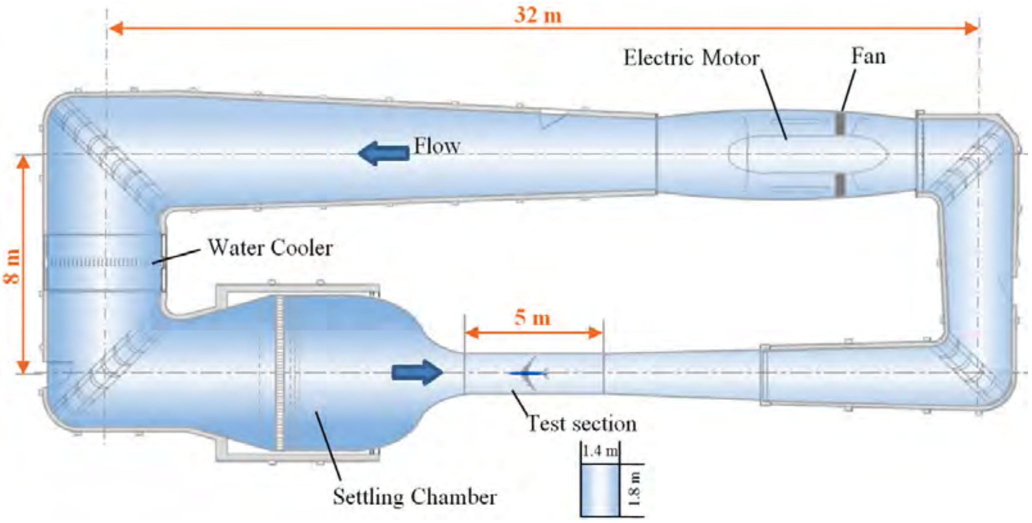

Figure 4.3. Sketch of the F2 subsonic wind tunnel facility at ONERA Fauga-Mauzac center.

The tests were carried out in the ONERA's F2 wind tunnel at Fauga-Mauzac sketched in figure 4.3. This is a closed circuit subsonic wind tunnel characterized by a very low level of turbulence in the test section (<0.05%). The test section has a rectangular shape (1.4×1.8m) and is 5m long. The side walls, made of either transparent or opaque panels, can be modulated as optical measurements are required. The 680kW DC current motor drives a 12 bladed fan and the velocity can be increased from 0 to 100km/h by adjusting the motor speed. The low level of turbulence in the test section is achieved by a contraction ratio of 12 and a set of 4 grids of different sizes, a honeycomb filter and noise dampers on the settling chamber walls.

The configuration under study is described in figure 4.4c. It consists mainly of four parts: a flat plate, a round pipe, a vertical fin (in green) and an air supply system.

1. The flat plate (figure 4.4a and 4.4b), of 1.4m wide and 1.4m long, is fixed directly to the side walls of the test section (not illustrated in the figures). The colors represent the different components of the assembly. Leading and trailing edges are made of aluminium (gray) and are assembled with the flat plate body (in red) that is 24mm thick and consists of Polyfont covered with a layer of fibreglass. The calcium silicate component (purple) protects the upper surface of the flat plate from the hot jet and it is glued to its housing to get a smooth surface.

2. The pipe issuing the jet has an internal diameter of 40mm and is positioned 250mm from the leading edge. Its position has been chosen following a preliminary analysis where the height of the boundary layer at the abscissa of the jet axis was estimated to be about 7mm. This is a compromise between a total relaxation of the boundary layer profile and a very thin boundary layer. A turbulator tape is glued on the flat plate at approximately 30mm from the leading edge and has a thickness of 0.3mm. The software which was used for the calculation of the boundary layer is Clicet (detailed in Aupoix (2010)). The final tube is a 40×50mm drawn pipe. In this section of the pipe is inserted a thermocouple of 0.25mm diameter (to avoid affecting the flow) necessary to adjust the temperature of the jet. The pipe coming out of the wind tunnel floor and feeding the jet is faired with shaped like a

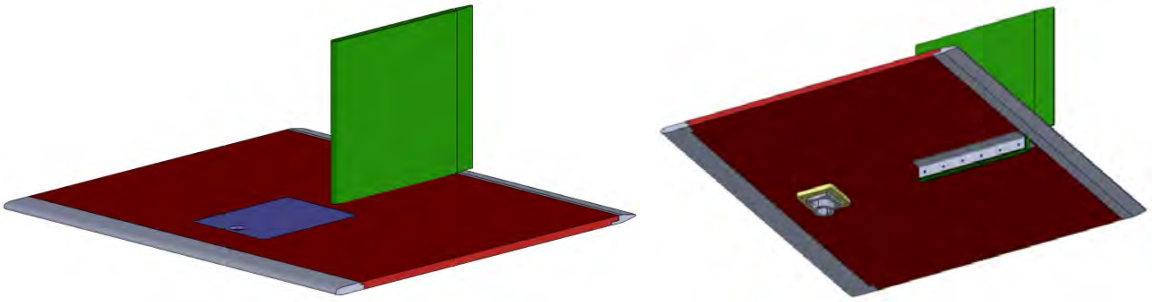

(a) Top view of the flat plate with the vertical aileron in green.

(b) Bottom view of the flat plate: here the inlet of the tube can be observed.

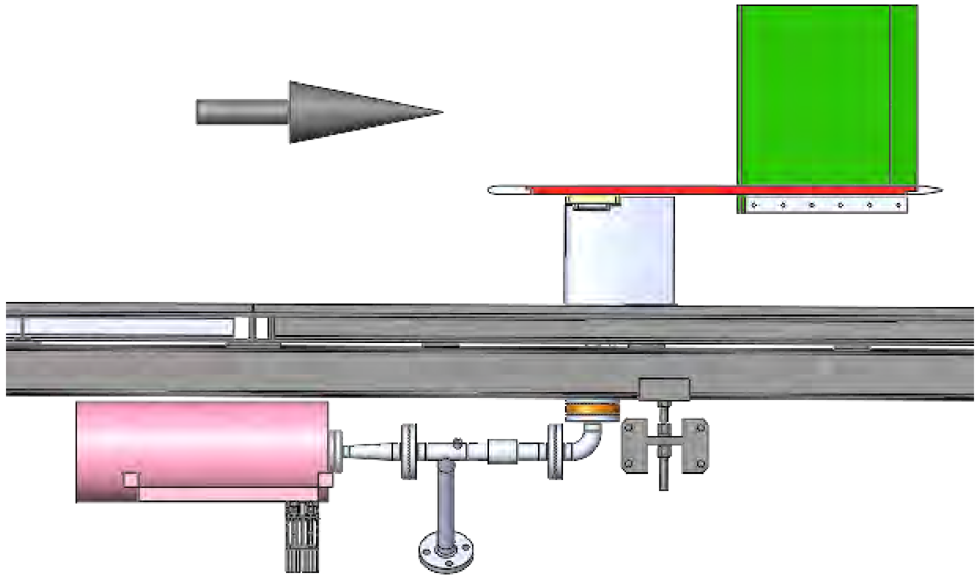

(c)

Figure 4.4. Sketch of the model used for the study of hot jet in cross-flow mounted in the wind tunnel. The various colours represent the different components of the assembly. The arrow indicates the wind direction.

symmetrical wing profile made with 3mm welded aluminium sheet. This fairing is filled with glass wool to prevent the premature cooling of the jet air. The end tube of the jet is clamped to the model by a steel clamp separated from the Polyfont by 25mm of Macor (figure 4.4b in yellow).

3. The dimensions of the fin are 500×500×25mm and the leading edge is located 400mm downstream from the axis of the jet. The leading and trailing edges have simple geometries. The aileron is made of Renshape BM5460 with a 80mm long trailing edge. The leading edge was made with a 12mm round router bit instead of 12.5 mm (not available): this results in a slight flat at the stagnation point. The insulating material used for the aileron allows to visualize with an infrared camera the jet plume. The aileron is painted in mat black to eliminate any kind of light reflection.

4. The hot jet coming out of the model is generated from compressed air supplied supplied from a 300m^3 tank maintained at an average pressure of around 8 bar. The F2 wind tunnel is equipped with a buffer tank to absorb pressure variations and a motorized control valve

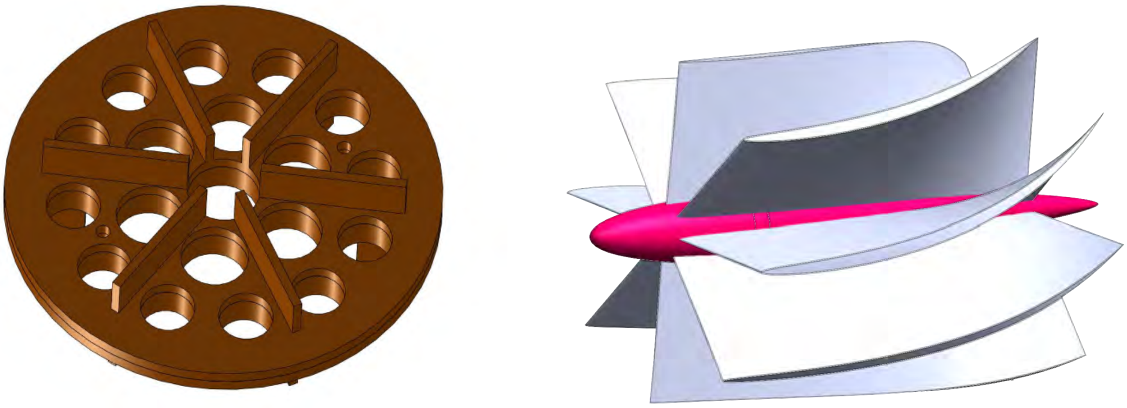

(a) Sketch of the Laws air conditioner places after the 90° elbow.

(b) Sketch of the swirler with 40° exit angles.

Figure 4.5. Details of the devices present in the chain of generation of the hot jet.

to adjust the blowing rate. A rupture disc is mounted on this device to protect the two Leister 16kW heaters (figure 4.4c pink block) from the upstream side. Between the heaters and the model, in the T-piece there is a connection for aerosol injection.

After the 90° elbow, two LAWS air conditioners are mounted to restore the outlet flow to a state close to a fully developed turbulent flow (brown piece in figures 4.4c and 4.5a). The air conditioner used was built according to Gajan et al. (1995). This is made up of an open star with a thickness of D/8 and a Laws plate with a porosity of 70%. The star improves the initial Laws plate and the observed performance is improved. The disc must be symmetrical, resulting in a hole arrangement of 1-6-12 (figure 4.5a). A fully developed velocity profile is obtained 6.5D (260mm) from the conditioner. Thereafter, the next 2 flanges can hold a swirl generator (figure 4.5b) which can be replaced by a smooth ring and a second air conditioner. The swirl is made in Ti6Al4V using a 3D printer to withstand high temperatures.

4.3.1.1 Operating conditions

Measurements were made at different jet and tunnel conditions presented in table 4.1.

In order to meet the required specifications three main parameters were varied: the mass flow rate of the jet, its temperature and the wind tunnel speed. The jet flow rate was set to 70g/s, for the majority of test conditions, to have a ratio of $\mathrm{C_R}$ close to 1 while remaining within the capacity of the air supply. All the configurations that have been tested are shown in table 4.1. All configurations were tested with 2D BOS and infrared while the configurations highlighted in yellow are those that have been chosen for BOS3D, PIV, LDV and thermocouple measurements. These two configurations differ in the jet temperature: in the first case $T_j = 400°\mathrm{C}$ and in the second $T_j = 60°\mathrm{C}$, while jet mass flow rate ($\dot{m}_j = 70\mathrm{g/s}$) and wind tunnel speed ($V_0 = 30\mathrm{m/s}$) were kept constant.

4.3.2 Measurements of the flow dynamics: main results

4.3.2.1 PIV and LDV measurements

LDV measurements were used to characterise the exit conditions of the hot jet and its flow rate through the integration of the velocity profiles. Afterwards, these measurements were used to

	T_j [K]	ρ_j [kg/m^3]	V_j [m/s]	$\dot{m}_j$ [kg/s]	ρ_0 [kg/m^3]	V_0 [m/s]	C_R	R
Test 1	400	0.524	106	70	1.2	20	2.3	3.5
Test 2	400	0.524	106	70	1.2	30	1.5	2.3
Test 3	400	0.524	106	70	1.2	45	1.0	1.5
Test 4	400	0.524	121	80	1.2	20	2.6	4
Test 5	400	0.524	121	80	1.2	30	1.8	2.7
Test 6	300	0.616	90	70	1.2	20	2.3	3.2
Test 7	200	0.746	75	70	1.2	20	2.3	2.9
Test 8	100	0.946	59	70	1.2	20	2.3	2.6
Test 9	60	1.06	53	70	1.2	30	1.5	1.7
Test 10	400	0.524	85	56	1.2	30	1.2	1.9

Table 4.1. Summary table with jet and wind tunnel conditions tested during acquisitions. The lines highlighted in yellow are the held conditions under which acquisitions were made with the 3D BOS.

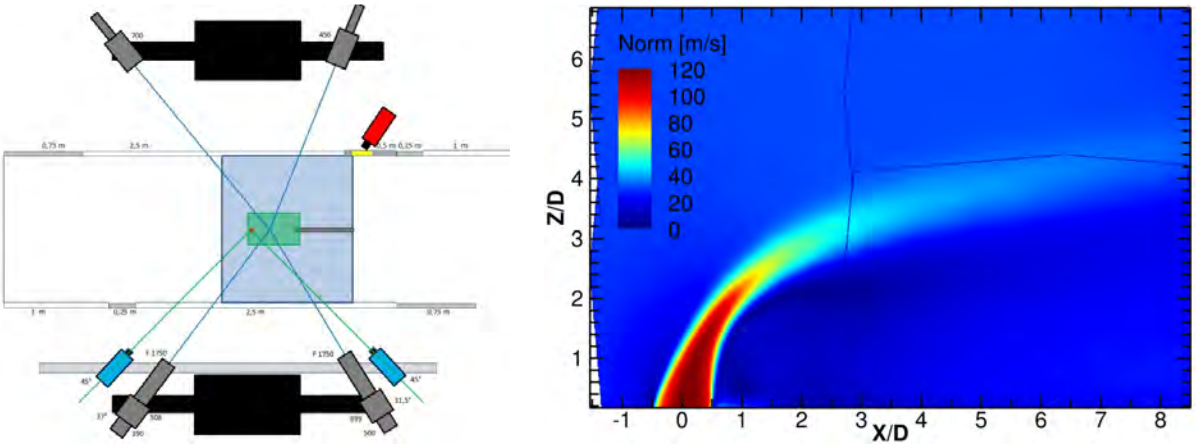

(a) Layout of the apparatus for PIV, LDV and infrared measurements. PIV: camera are in blue and laser beams in green. LDV: receivers in gray and laser beams in blue. Infrared: the camera in red is focused on the aileron (black), the infrared window is in yellow.

(b) Time-averaged velocity norm PIV field at Y/D=0: T_j=400°, ρ_j=0.524kg/m^3, V_j=106m/s, $\dot{m}_j$=70g/s, ρ_0=1.2, V_0=30m/s, C_R=1.5, R=2.3.

Figure 4.6. PIV, LDV and infrared devices arrangement and PIV velocity field.

verify the conditions of exit from the jet and boundary layer profiles were acquired above the flat plate to carry out CFD calculations.

The LDV system used in the F2 wind tunnel allows to evaluate the three velocity components and the assembly is shown in the figure 4.6a.

PIV measurements were carried out in the XZ longitudinal plane at different distances from the centre of the jet. A time-averaged velocity norm field at $Y/D = 0$ is presented in fig. 4.6b, displaying the global appearance of the central part of the jet.

4.3.2.2 Measurements of the thermal behaviour of the flow

Thermal measurements were carried out through thermocouple and infrared measurements.

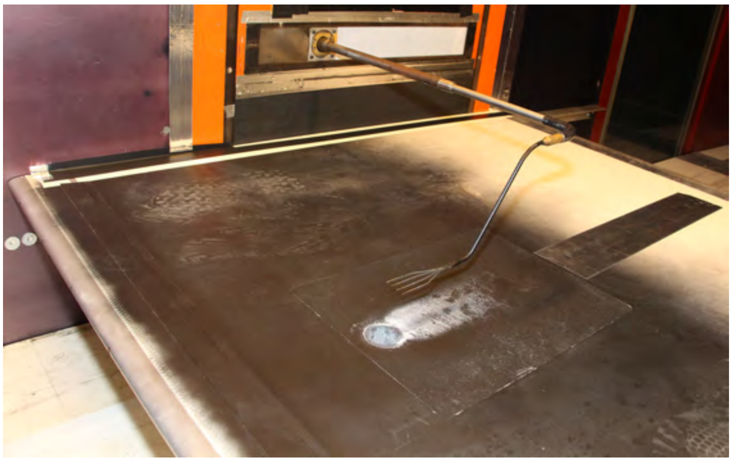

(a) Four thermocouple comb mounted on displacement device. The probe is positioned just downstream of the jet near the wall of the flat plate. In the downstream part, the vertical aileron is removed (black tape).

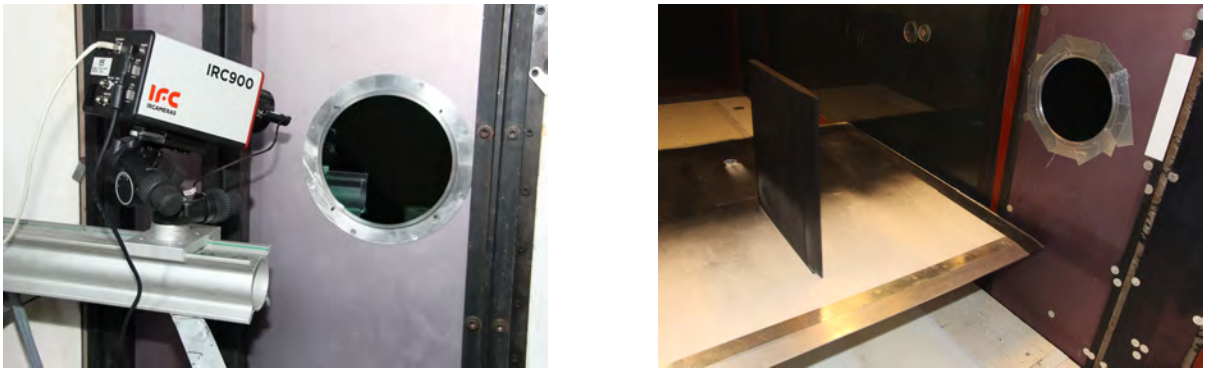

(b) Details of the infrared camera and the IR window.

(c) Details of the IR window and the rear part of the flat plate with the vertical fin painted with matt black ink.

Figure 4.7. Setups details of thermocouple and infrared measurement techniques.

Regarding thermocouple measurements, it was used a four thermocouple comb, shown in figure 4.7a. This comb is attached to the wind tunnel probe displacement device (DS4) located on the right wall of the wind tunnel 2.5m from the vein inlet to perform measurements at the jet outlet and aileron (dismantled during acquisitions). Thermocouple measurements are shown in figures 4.8a, 4.8b and 4.8c.

With regard to infrared measurements a IRCAMERA (model IRC900) infrared camera was used. It was equipped with a 13mm focal length lens, the corresponding field of view is approximately 800 x 650 and it was located on the right wall of the test section (figure 4.7b). The aileron was painted in black with Jelt 700 matt black ink and markers for calibration are glued on it (figure 4.7c). A 875mm × 575mm test pattern composed of a perforated sheet fixed on a wooden support allows a dimensional calibration of the camera's field of view. Image processing to accurately determine the temperature levels in the model reference frame is performed with AfixPSP (Le Sant 2001).

These measurements have allowed us to identify not only the temperature levels but also the structure of the jet, in accordance to literature (section 4.2).

With thermocouple acquisitions we can distinguish the counter-rotating vortex pair that

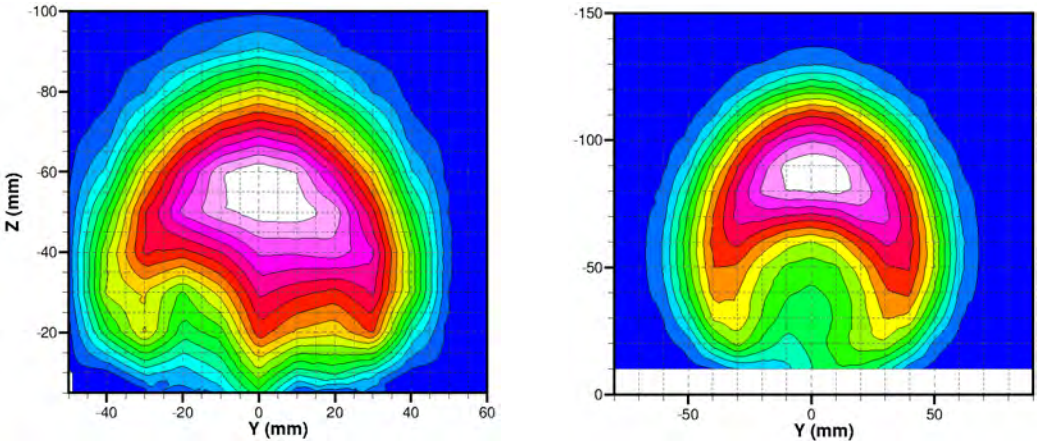

(a) Thermocouple measurements at $X = 0.5D$ (20mm) from the jet axis.

(b) Thermocouple measurements at $X = 1.5D$ (60mm) from the jet axis.

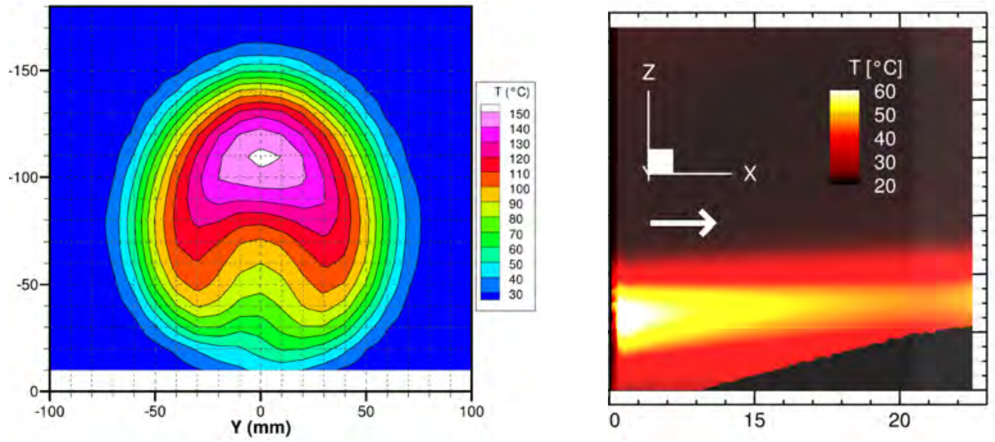

(c) Thermocouple measurements at $X = 3D$ (120mm) from the jet axis.

(d) Infrared measurements on the vertical aileron.

Figure 4.8. Thermocouple and infrared measurements at: T_j=400°, ρ_j=0.524kg/m^3, V_j=106m/s, $\dot{m}_j$=70g/s, ρ_0=1.2, V_0=30m/s, C_R=1.5, R=2.3.

develop downstream of the hot jet outlet. The maximum temperature levels decrease going downstream and the jet increases in size from 100mm in height at X/D=0.5 to 160mm at X/D=3.

The infrared measurements were used to measure the temperature levels at the wall of the aileron affected by the hot jet. A 2D infrared measurement is displayed in figure 4.8d: on the left side of the image we find the leading edge located 400mm downstream from the axis of the jet, where the highest temperatures reach 62°C. The highly turbulent nature of the cross-flow causes the hot flow to mix and cool rapidly. Other infrared measurements are presented in the central images of figures 4.13 and 4.14.

While the thermocouple measurements were used in section 4.5 to compare them with the reconstructions obtained with 3D BOS, the infrared acquisitions were of fundamental importance for their comparison with 2D BOS measurements. These have confirmed that through 2D BOS it is possible to identify the trajectory of a hot jet (further details in section 4.4).

4.3.3 2D and 3D BOS setup

4.3.3.1 2D BOS setup

For 2D BOS measurements, 3 different setups were chosen and described in table 4.2.

Configuration	Preliminary 2D BOS (C1)	Optimum 2D BOS (C2)	3D BOS (C3)
Focal length f [mm]	50	70	23
f-number $f_{\#}$	4	16	11
Camera-flow m [mm]	3100	3100	1000
Flow-background l [mm]	2500	700	1400
Field of view [mm]	520×435	370×310	365×305
Sensitivity [mm/rad]	22.5	13.1	13.5
Spatial resolution [mm]	5.7	1.3	1.5
Background material	plain paper	plain paper	retroreflective

Table 4.2. Summary table of distances and specifications of the BOS setup.

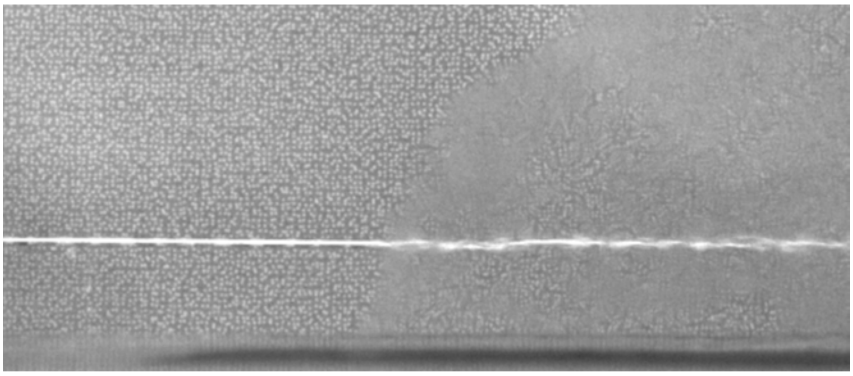

(a) 2D BOS raw image with flow at jet exit using BOS configuration 1 in Table 4.2: at the bottom of the image the surface of the flat plate can be seen. Astigmatism in this area is very strong and alters the background pattern. The horizontal white line corresponds to a tiny space between two panels on which the random background is printed.

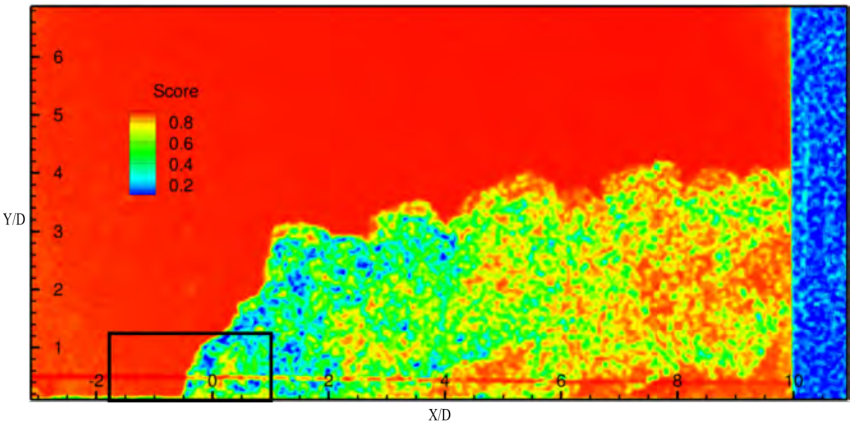

(b) The correlation score is strongly influenced by astigmatism in areas of high density gradients. The black rectangle delimits the area of the raw image of the figure above.

Figure 4.9. Experimental conditions: $T_j = 400^\circ$, $\dot{m}_j = 56$g/s and $V_0 = 30$m/s with 45° swirler.

A first set up (C1) was carried with a single camera with a 50mm lens. The camera-background distance was 3.1m and the jet-background distance was 2.5m.

During the jet adjustment phase, the BOS images with flow were observed in real time, without processing. The boundary area of the plume is easily perceptible by the incessant changes in the pattern and the strong astigmatism that transforms the white dots of the background pattern into larger, grayer spots. Outside the jet, the background pattern remain identical from one image to another (figure 4.9a). This phenomenon is due to the strong astigmatism in the area of the jet outlet: the points of the background are no longer distinguishable and consequently the correlation score, displayed in figure 4.9b, is strongly degraded. This is due to the excessive sensitivity (22.5mm/rad) of the setup and the insufficient spatial resolution (5.7mm) to capture the strong density gradients. Further downstream, after turbulent mixing with the main flow, where the jet temperature decreases, the density gradients are less strong, the image is less degraded by astigmatism and the score is improved compared to the jet exit.

Configuration 2 (C2) is the optimised layout dedicated to 2D BOS which provides the higher level of both sensitivity and resolution, while the configuration 3 (C3) is an adaptation of the previous one in order to fit with the constraints of the 3D setup.

In the configuration C2, a sensitivity of 13mm/rad was chosen to allow the visualization of at least 60°C temperatures. By selecting a 70mm focal length and 370mm field of view, the distances l=0.7m and m=3.1m were identified (table 4.2). The background was printed on paper (obtaining a Lambertian type reflection) and glued on the external wall of the wind tunnel. The size of the dots was optimized and fixed to 3 pixels, obtaining a diameter of 0.55mm. By using a large focal length, the dimensions of the visualized background (450×380mm) are similar to the field visualized at the level of the flow (370×310mm): the light to illuminate the backgrounds can be concentrated in a smaller area than before, consequently it is possible to work with smaller apertures. With this mounting the aperture is fixed to 16 which provides a spatial resolution was equal to 1.3mm.

Configuration C3 aimed at keeping the sensitivity and size of the displayed field fixed, but 3D constraints have arisen in the positioning of the cameras: for this reason a 23mm focal length was selected. The distances that result to respect the characteristics of the mounting are: l=1.4m and m=1m. With this configuration the camera is located 300mm from the walls of the wind tunnel and the background is positioned on the support used in the first configuration. For the 2D BOS test the background was printed on ordinary paper with a dot diameter of 1mm. As a consequence of using a small focal lens and a greater distance between the background and the jet, the surface of the background visualized by the camera is greater (875×735mm) and therefore it was not possible to maintain an aperture equal to 16 but it had to be reduced to 11, obtaining a slightly degraded spatial resolution equal to 1.53mm.

For all three configurations, the camera was tilted so that the lower edge of the field of view was horizontally aligned with the flat plate. In the first configuration the camera was tilted upwards by 4°, in the second by 2.8° and in the third by 8.7°, depending on camera focal length.

In the C1 configuration, 100 images were acquired with the flow, while in the C2 and C3 configurations, to ensure convergence, 1000 images were acquired. The acquisition frequency was 5Hz.

Illumination of the backgrounds was achieved using a 532 nm double-pulse laser (Quantel Big Sky Twin BSL 200). Both laser pulses were used during the cameras exposure time: the maximum laser power was used to obtain the greatest possible amount of light. The exposure time is equal to the sum of the two laser flashes ($\sim$ 20ns) which ensures that the turbulent structures of the flow imaged by the cameras did not move more than about 0.1 px during each acquisition. The laser beam was split into four beams using a separation table made of three 50:50 beamsplitter plates. Four liquid guides equipped with diverging lenses were then used to

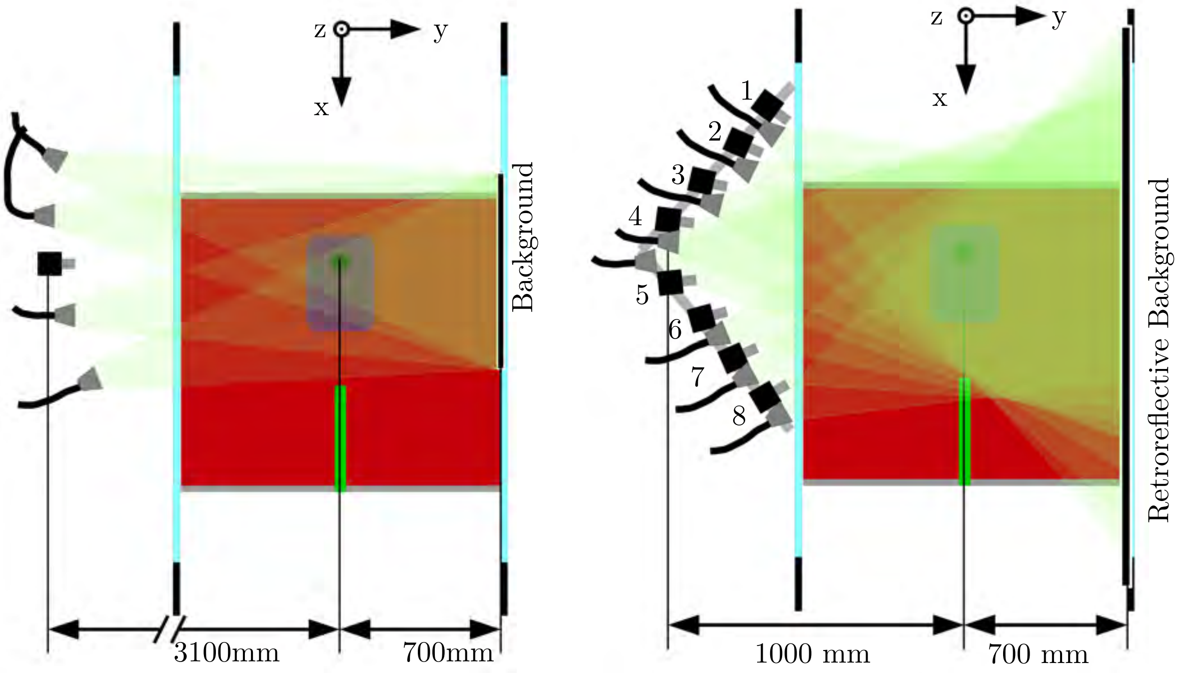

(a) 2D BOS configuration: $f = 70\text{mm}$, $m = 3.1\text{m}$, $l = 700\text{mm}$ and $f\# = 16$.

(b) 3D BOS configuration with 8 camera: : $f = 23\text{mm}$, $m = 1\text{m}$, $l = 700\text{mm}$ and $f\# = 11$.

Figure 4.10. View from above: in red the flat plate, in green the vertical aileron, in purple the calcium silicate plate with the hot jet exit, in turquoise glass walls, in transparent green the light coming out of the laser spots in black the backgrounds attached to the wall of the wind tunnel.

direct this light toward the background.

4.3.3.2 3D BOS setup

For the arrangement of the cameras for 3D BOS we have to handle several difficulties. As studied by Nicolas et al. (2016), and as gained through experience, the recommended arrangement of the cameras to achieve a faithful reconstruction is obtained by a coplanar configuration in a plane orthogonal to the flow main axis and by covering as much as possible the half-circle of view around the object.

But since the studied jet has two main axes (the jet coming out is deviated by 90° by the flow of the wind tunnel), to meet the optimum condition, cameras should be placed on two planes orthogonal to each other. This arrangement of the cameras is shown in the figure 4.11a. In this arrangement the common center of visualization is fixed 115mm downstream from the center of the jet, the 4 cameras on the horizontal plane are spaced 30° apart while those on the vertical plane are spaced 36° apart.

The problem then relies in the positioning of the backgrounds: first, the presence of the model prevents us from positioning the backgrounds at the floor of the wind tunnel because they would be hidden by the model; second, placing them on the model itself would lead to almost null sensitivities because of the small distance l between the background and the flow.

Due to the impossibility of obtaining useful information from the cameras placed in a YZ plane, we chose an arrangement of the cameras in a single XY plane placed at the height of the flat plate (figure 4.10b and 4.11b). This arrangement, according to Nicolas et al. (2016),

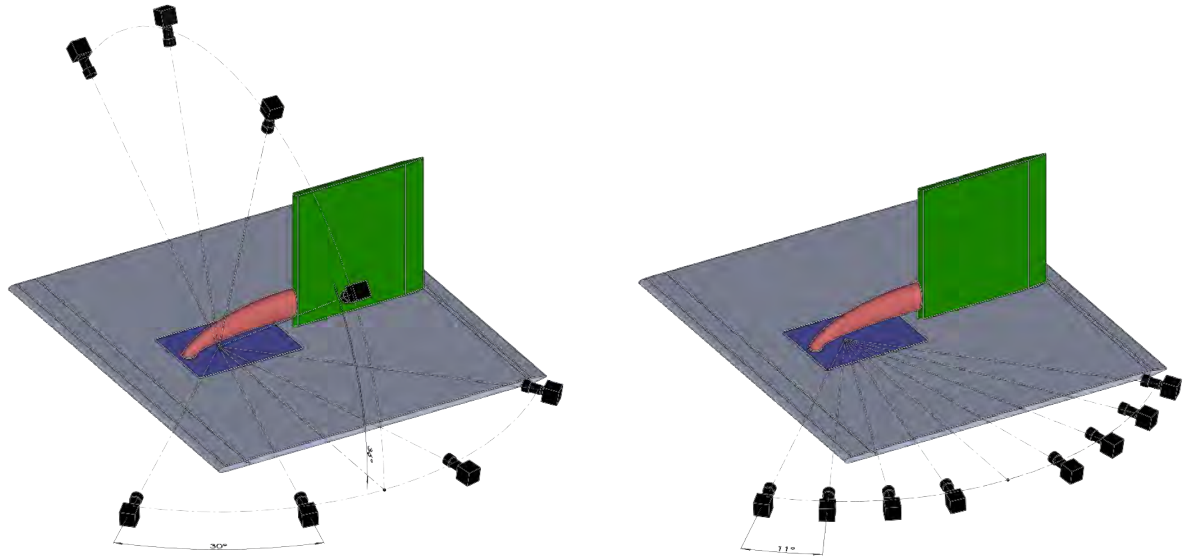

(a) Optimal theoretical camera arrangement: the cameras are positioned equally in two planes perpendicular to the principal axes of the jet.

(b) Arrangement of the cameras that have been used: the cameras are positioned only in the horizontal plane because of the impossibility of obtaining information from the cameras placed in the vertical plane due to the presence of the flat plate.

Figure 4.11. In both arrangements the common center of all the cameras was the point located in the middle of the wind tunnel, on the flat plate and 115mm from the axis of the jet. In red the trajectory followed by the jet

guarantees an optimal reconstruction of the first part of the jet perpendicular to the flat plate, but it is not optimized for the remaining part parallel to the X direction.

In this experience, retro-reflective backgrounds were used. Because with the use of these backgrounds it is necessary to have a light source mounted next to each camera, to simplify the optical setup we chose to use 8 cameras coupled with a separating plate designed to divide the laser beam into 8. This choice is the right compromise between complexity of the installation and quality of the measure (Nicolas et al. 2016).

The flow-camera and flow-background distances varied from one camera to another and are summarized in the table 4.3. The center of the cameras was chosen to be 115mm downstream from the center of the jet, allowing to see the exit of the jet and most of it almost up to the aileron. As we did before, the cameras were tilted by a certain angle, in this case 8.7°, to make the lower part of the image coincide with the surface of the flat plate. With these distances, the flow dimensions recorded by the cameras were about 395×330mm which corresponds to 660×550mm on the background.

	Camera 1, 8	Camera 2, 7	Camera 3, 6	Camera 4, 5
Camera-flow m [mm]	1080	1060	1080	1140
Flow-background l [mm]	730	750	830	950
Focal length f [mm]	23	23	23	23
f-number $f_{\#}$	11	11	11	11
Sensitivity [mm/rad]	9.4	9.65	10.1	10.6
Spatial resolution [mm]	1.17	1.19	1.24	1.3
Entrance angle	80°	69°	57°	45°

Table 4.3. Summary table of distances and specifications of the 3D BOS setup.

As observed in the table 4.3 the sensitivity varies slightly from one camera to another because of the different distances, but it may be considered constant. These small variations are nonetheless taken into account later in the reconstruction through the calibration process.

Due to the different entrance angle and consequently a different response of the retro-reflective background, it was necessary to couple the light guides with the cameras in a certain order to have constant illumination for each camera. In short, the most powerful guides have been chosen to feed the outermost cameras having the highest entrance angle: with this strategy we were able to work at an f-number equal to 11 and a constant illumination for all cameras. The retro-reflective backgrounds used were printed on rigid panels 1×0.5m with matt black ink Minimaki Lus170 on Scotchlite 13150 of 3M made with glass beads. To cover the entire surface viewed by the cameras, 5 panels were used, equal to a surface of 2.5m^2. The diameter of the dots was 1mm equal to about 3-4 pixels depending on the camera.

This setup leads to a resulting spatial resolution that was about 1.2 to 1.3mm and varied little because of the different distances. For a BOS setup we can consider this resolution totally satisfactory: indeed, it has been improved by a factor 3 compared to the previous experience (4.3mm) in the same wind tunnel carried out by Nicolas et al. (2017c) thanks to the use of retro-reflective backgrounds. Excluding the 2D BOS preliminary configuration C1, where the spatial resolution was 5.7mm, the 2D BOS configurations C2 and C3 have a resolution of the same order of magnitude of the 3D BOS.

The laser used was the same as before and was used at its maximum power.

Figure 4.12 shows the result of the optimisation leading to the calibration: the histogram of the reprojection errors in pixels are shown. Despite the dimensions of the system the calibration process is rather efficient, leading to an average reprojection error of 0.26 pixel with a standard deviation of 0.22 pixel. All details of the calibration process can be found in Le Sant et al. (2014).

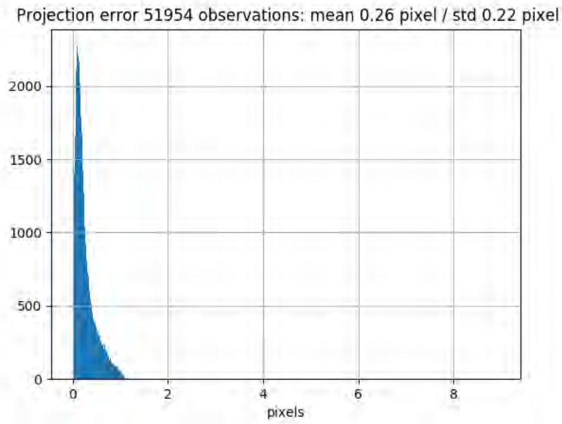

Figure 4.12. Calibration of the 3D BOS multi-camera setup: histogram of reprojection errors (in pixels).

4.4 2D BOS results

This section presents the 2D BOS measurements that were made at all different jet and tunnel conditions presented in table 4.1.

The first subsection is dedicated to 2D BOS measurements made in configuration C1 and the following one to measurements made in the optimised configurations C2 and C3 (details of configurations distances and specifications are given in table 4.2).

4.4.1 C1 configuration

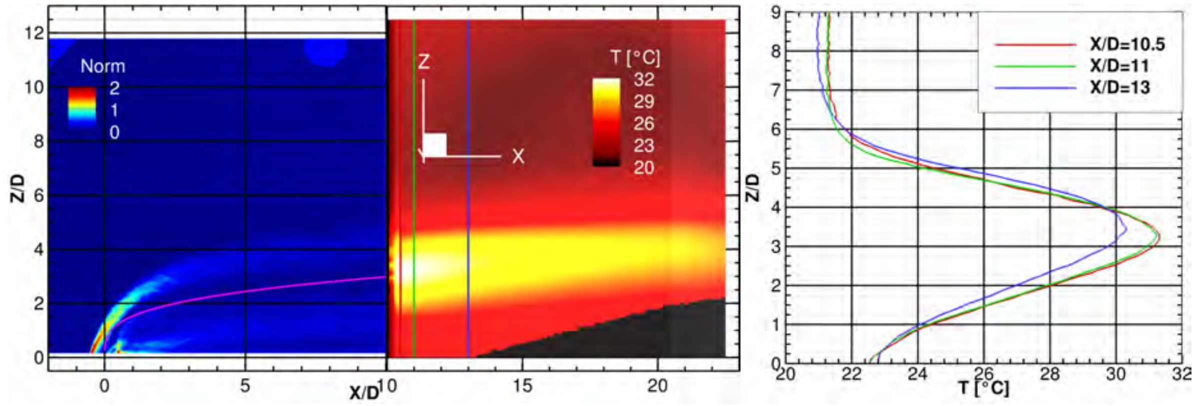

(a) $T_j = 100°\mathrm{C}$, $\dot{m}_j = 56\mathrm{g/s}$, $V_0 = 20\mathrm{m/s}$, $C_R = 2.1$ and $R = 3.2$ without swirler.

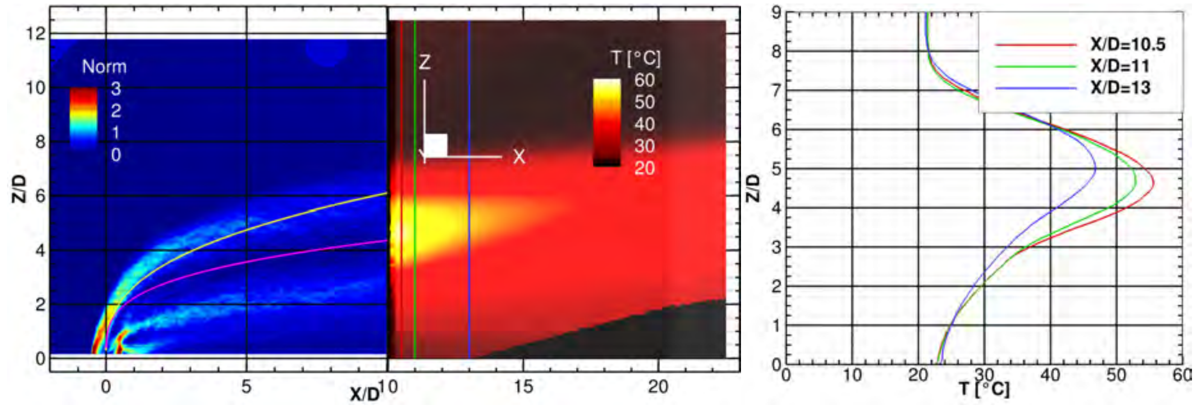

(b) $T_j = 400°\mathrm{C}$, $\dot{m}_j = 64\mathrm{g/s}$, $V_0 = 20\mathrm{m/s}$, $C_R = 1.9$ and $R = 2.1$ without swirler. In yellow the empirical curve proposed by Kamotani and Greber (1972) for the locus of maximum velocity (equation 4.4).

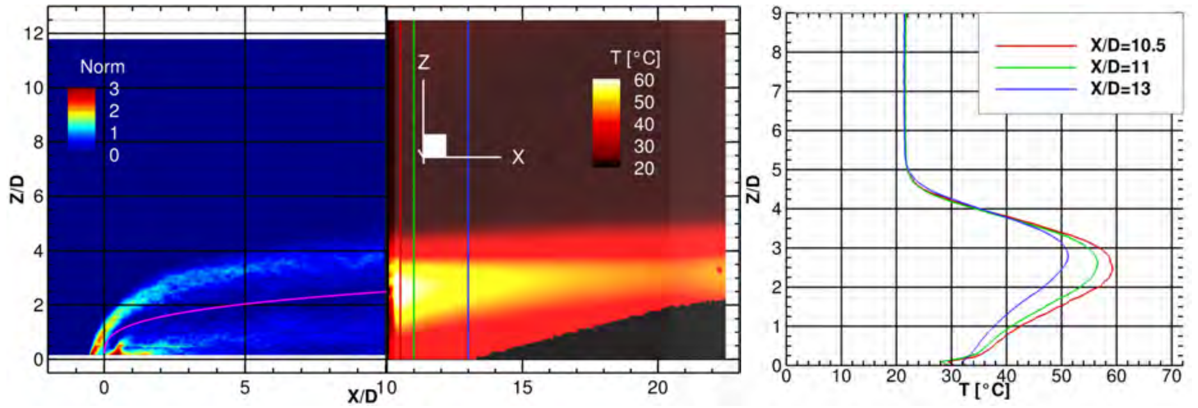

(c) $T_j = 400°\mathrm{C}$, $\dot{m}_j = 56\mathrm{g/s}$, $V_0 = 30\mathrm{m/s}$, $C_R = 1.2$ and $R = 1.9$ with 45° swirler.

Figure 4.13. On the left there is a map of the displacements obtained with the 2D BOS technique in configuration C1 on which the Kamotani curve in magenta has been superimposed (equation 4.3), which identifies the locus of maximum temperature. In the centre the aileron with the infrared measurements, on the right the temperature profiles for three distances from the outlet of the jet.

This section is dedicated to the comparison between 2D BOS and infrared measurements made at several operational conditions to demonstrate that through the 2D BOS it is possible

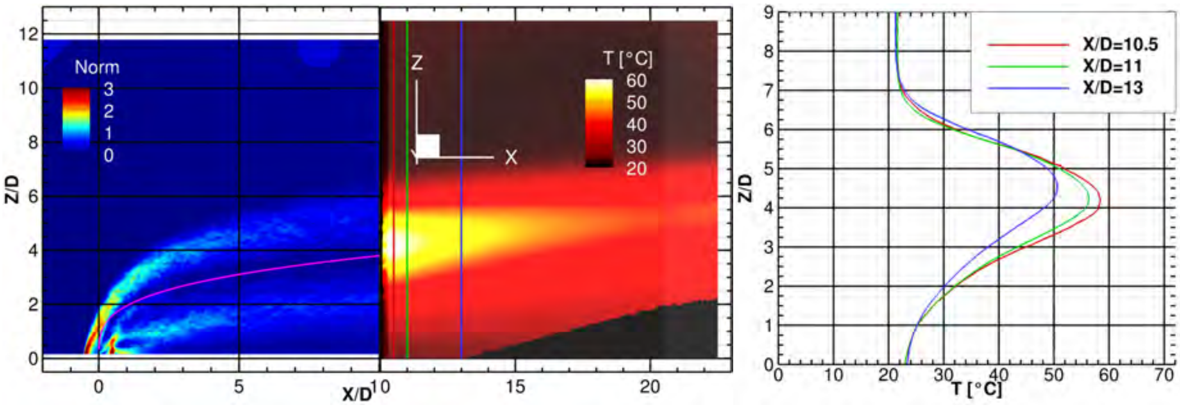

(a) $T_j = 400$°C, $\dot{m}_j = 56$g/s, $V_0 = 20$m/s, $C_R = 1.9$ and $R = 2.8$ without swirler.

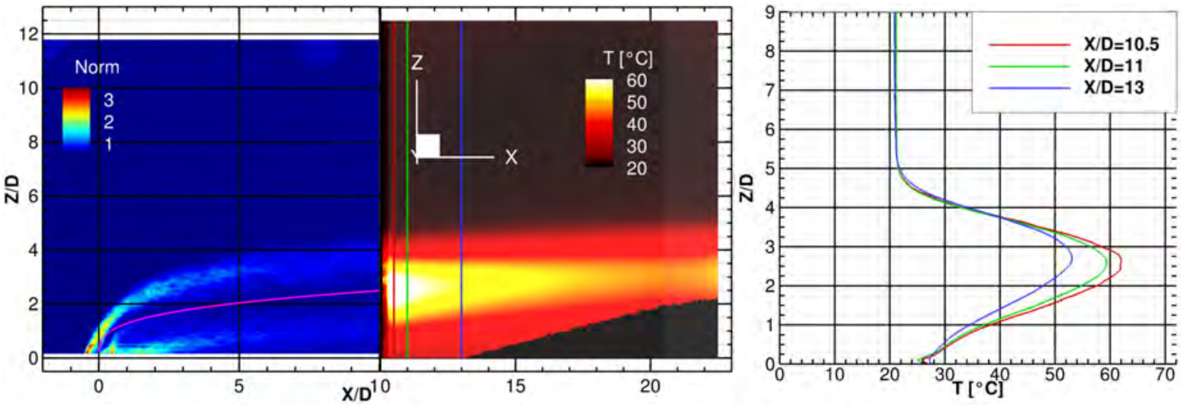

(b) $T_j = 400$°C, $\dot{m}_j = 56$g/s, $V_0 = 30$m/s, $C_R = 1.2$ and $R = 1.9$ without swirler.

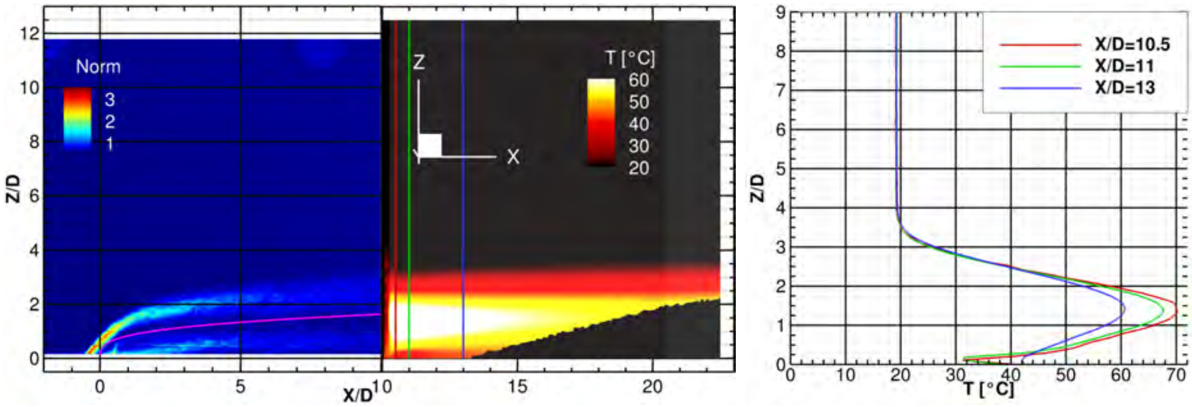

(c) $T_j = 400$°C, $\dot{m}_j = 56$g/s, $V_0 = 45$m/s, $C_R = 0.8$ and $R = 1.3$ without swirler.

Figure 4.14. 2D BOS in configuration C1 and infrared camera measurements at the exit of the jet and on the vertical aileron at 10D (400mm) from the centre of the jet outlet. This figure shows the variations in the trajectory of the jet as the speed of the wind tunnel is changed.

to correctly identify the trajectory of a hot jet.

In figures 4.13 and 4.14, 2D BOS measurements are flanked by measurements made on the vertical aileron with the infrared camera. The 2D BOS measurements were made with the C1 configuration and the result presented is the average of the displacements calculated on 100 images. No full convergence was achieved with the use of 100 images, but the trajectory of the jet is clearly visible up to the vertical aileron. The most important displacements are present at the exit of the jet where are located the highest temperature gradients. Further downstream, because of the turbulent mixing, the flow temperature drops significantly (as confirmed by the infrared camera) and the resulting displacements are weaker.

On the displacements obtained through BOS it has been superimposed in magenta the empirical equation 4.3 proposed by Kamotani and Greber (1972) that describes the location of the maximum temperature.

The 2D BOS does not give us information on the jet temperatures but the curve follows the trend of the displacements obtained. With the measurements obtained through the infrared camera it is possible to see the good accordance between the curve in magenta and the point of maximum temperature on the aileron.

In the figure 4.14 the influence of the wind tunnel air velocity for the same output conditions of the jet ($T_j = 400°C$, $\dot{m}_j = 56g/s$) and wind tunnel temperature ($T_0 = 20°C$) can be observed. When the wind tunnel air velocity is increased (V_0), the momentum ratio R decreases and this strongly influences the path of the jet and to a lesser extent the wall temperature: the jet is pressed against the flat plate and the temperatures on the aileron increase slightly. Heading downstream the maximum temperature continues to decrease for the heat exchanges and its position continues to rise following the equation proposed by Kamotani and Greber (1972).

When the temperatures of the two flows are kept constant, the maximum temperature ordinate depends only on the ratio of the speeds, instead when the temperature of the two flows varies, it is necessary to study the term $(J)^{0.52}\left(\frac{\rho_j}{\rho_0}\right)^{0.11}$ to understand the trend of the maximum temperature height.

Only for figure 4.13b the maximum velocity height (Z_V) proposed by Kamotani and Greber (1972) has been traced in yellow (equation 4.4). This curve does not overlap either the BOS measurement or the measurements made with the IR camera: these two measurement techniques are linked to the temperature and not to the velocity of the flows.

Temperature information obtained from infrared camera measurements cannot be obtained from a 2D BOS measurement: the map of displacements obtained on a single camera is not sufficient to identify temperature levels due to the lack of several point of views and for this purpose a 3D BOS reconstruction is necessary. Nonetheless with a 2D BOS measurement it is possible to correctly obtain the trajectory of a jet in the area where the vertical fin is not present. Coupling 2D BOS with infrared measurement thus allows to estimate the trajectory along the whole development of the hot jet.

4.4.2 C2 and C3 configurations

In this section we present the results obtained with the optimised 2D BOS setup C2 and the reasons that led us to optimise the previous 2D BOS configuration C1.

With an outlet temperature of 400°C, varying $\dot{m}_j$ and V_0, temperatures between 56 and 70°C are obtained at 400mm from the jet outlet on the vertical aileron. As a result, the BOS measurement is relatively complicated due to wide range of temperatures and the impossibility of having different sensitivities in the same measurement. While on the one hand the sensitivity must be increased to improve the signal-to-noise ratio where low temperatures are, on the other hand to reduce the phenomenon of astigmatism at the outlet of the jet the distances must be optimised, decreasing sensitivity and obtaining better spatial resolution.

The choice made for the following measurements was to select a single condition ($T_j = 400°C$, $\dot{m}_j = 70g/s$, $V_0 = 30m/s$, $C_R = 1.5$ and $R = 2.3$) and to decrease the measurement area (from 520×435mm to 370×310) by selecting the portion closest to the outlet of the jet, where temperatures do not decrease excessively, in order to maintain a good signal-to-noise ratio.

The 2D BOS configurations C2 and C3 were used respectively with focal lengths of 70 and

23mm, characterized by the same sensitivity (13mm/rad) and a reduced captured field size (370×310mm). The acquisition of 1000 images has also allowed to reach convergence and the displacements field is significantly improved.

A halved sensitivity, a smaller size of the captured field and a smaller aperture compared to the first configuration have visibly decreased the phenomenon of astigmatism: this is always present but much less important and limited in some areas of the jet. This lead to higher correlation score indicating more faithful displacement fields.

If the image 4.9b is compared with the 4.15c, it is observed that the score is improved in the whole area where the jet is present. Almost everywhere the score is higher than 0.5 and the field of displacements can be considered correct.

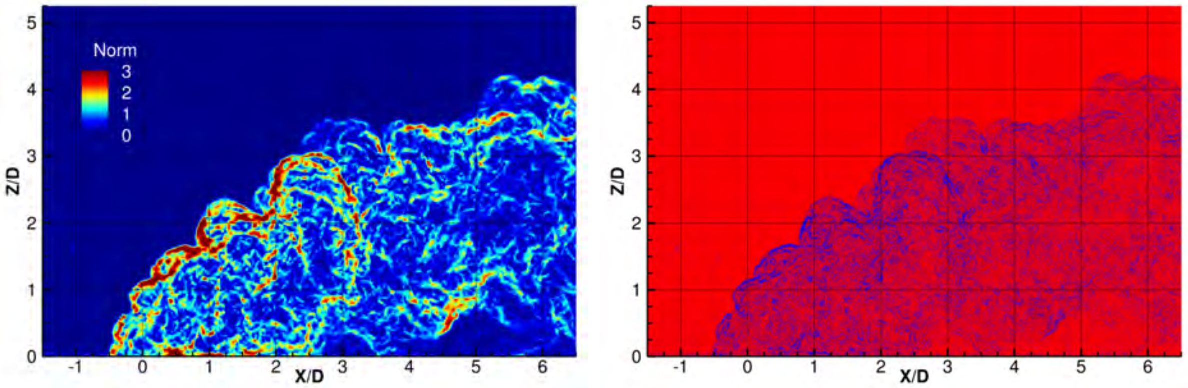

(a) Instantaneous displacements field. **(b)** Gradient of the instantaneous displacements field.

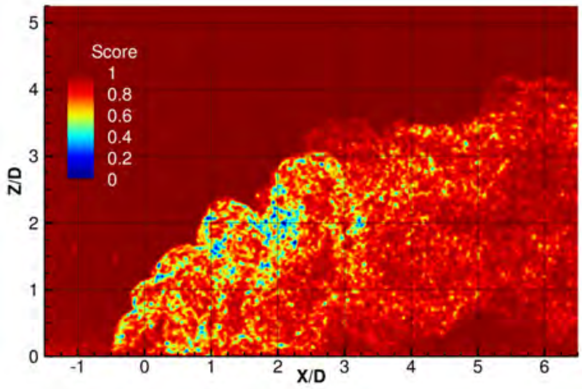

(c) Score of image correlation.

Figure 4.15. Flow conditions: $T_j = 400°\text{C}$, $\dot{m}_j = 56\text{g/s}$, $V_0 = 30\text{m/s}$, $C_R = 1.2$ and $R = 1.9$ without swirler. 2D BOS setup features: f=70mm, $f_{\#}$=16, m=3.1m, l=0.7m, S=13.1mm/rad, δ=1.3mm.

In the previous case (figure 4.9b) the score was on average around 0.4 while now this is about 0.8 (figure 4.15c). There are still some spots where the score is close to zero but remain very limited and isolated areas. These areas correspond to areas of the flow where the displacements and the gradient of the displacements are very high. These are therefore the regions where the refractive index gradients along the optical path are very important, the light is diverted significantly and so astigmatism is produced.

In all the figures in 4.15 are clearly visible the vortices of Kelvin-Helmholtz, in the shape of a ring, which are formed at the leading edge of the jet.

Optimisation of the 2D BOS setup leads to advantages in terms of correlation score and therefore confidence in the measurement, improving image quality by decreasing astigmatism and improving the resolution of the measurement.

4.4.3 Conclusion

In this section the measurements made with the 2D BOS have demonstrated the ability of the technique to visualize in a simple and effective way the trajectory of a hot jet in cross-flow. The Kamotani curve and infrared measurements are coupled with the 2D BOS measurements obtaining an excellent agreement. With the 2D BOS it was therefore possible to visualise the effects of swirl generator, temperature, C_R and R on the jet trajectory (figures 4.13 4.14).

Moreover, it has been demonstrated the importance in optimising the BOS setup and adapting the sensitivity of the measurement in order to limit the distortions induced by astigmatism to improve the correlation scores that determine the quality in the calculation of the displacements.

Although 2D measurements were used to choose the conditions of the experiment and visualize the trajectory of the jet, these are not sufficient to obtain the temperature or density of the flow. For this reason, measurements obtained with 3D BOS are necessary, whose results are presented in the following section.

4.5 3D BOS reconstructions

After 2D BOS acquisitions, useful only from a qualitative point of view, the 3D BOS setup was mounted as shown in figure 4.10b and described in section 4.3.3: 8 cameras positioned on a horizontal plane and retro-reflective backgrounds mounted inside the walls of the wind tunnel.

In the following sub-sections are presented several reconstructions made from experimental data but also a series of synthetic reconstructions. The latter were carried out to understand a series of limitations and problems that occurred during the BOS reconstructions based on experimental data.

All the 3D BOS reconstructions in this section were carried out using the same reconstruction parameters. Since the spatial resolution of the measurement is limited to about 1.2mm, the size of the voxels was fixed at 1mm and the reconstruction volumes vary from one reconstruction to another depending on the 3D mask used: these contain from 38 millions of voxels for the largest mask to about 10 millions of voxels for the smallest. The regularization parameter λ was set at 5×10^{-5} and the number of iterations fixed to 1000. These values were chosen from a parametric study reported in Section 4.5.3.6.

4.5.1 CFD simulation

Some informations on the jet shape prior to 3D BOS reconstruction are provided by thermal measurements, in particular thermocouple estimated profiles given in fig. 4.8. However to better interpret 3D BOS results that will be obtained with available experimental data, and also to propose evolutions of the setup to improve reconstructions, we also rely on a CFD simulation of a cross-flow jet.

The CFD simulation presented in this section was carried out by Romain Paysant during his PhD. It is a RANS calculation performed with ANSYS Fluent software. The mesh is composed of 1.5 million hexahedral cells and the turbulence model used is of type SST k-ω with the wall law (Y+ between 20 and 50). More information may be available shortly in Paysant et al. (2020) and in Paysant's PhD thesis.

From this CFD simulation some characteristics typical of a cross-flow jet can be seen in the simulated 3D density field shown on figure 4.16. These include the typical horseshoe shape of two counter-rotating vortex developing towards downstream (section 4.2). Another characteristic is

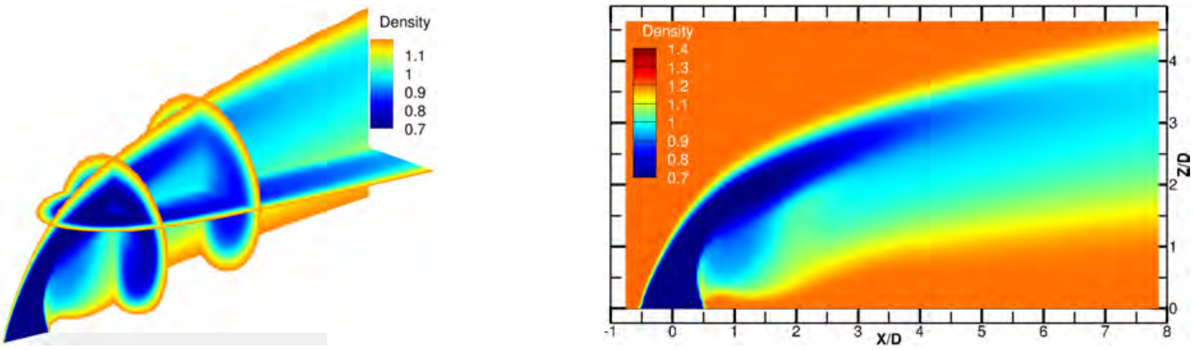

(a) Slices at X=2D, X=4D, Y=0D and Z=2D.

(b) Slice at Y=0D.

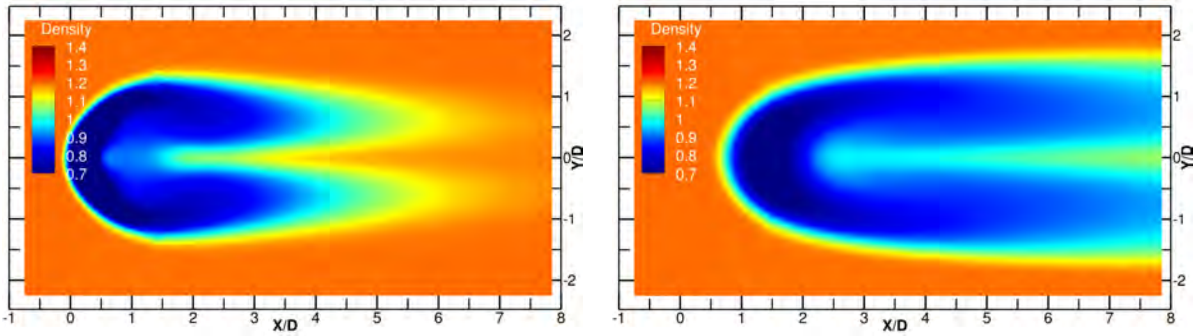

(c) Slice at Z=1D.

(d) Slice at Z=2D.

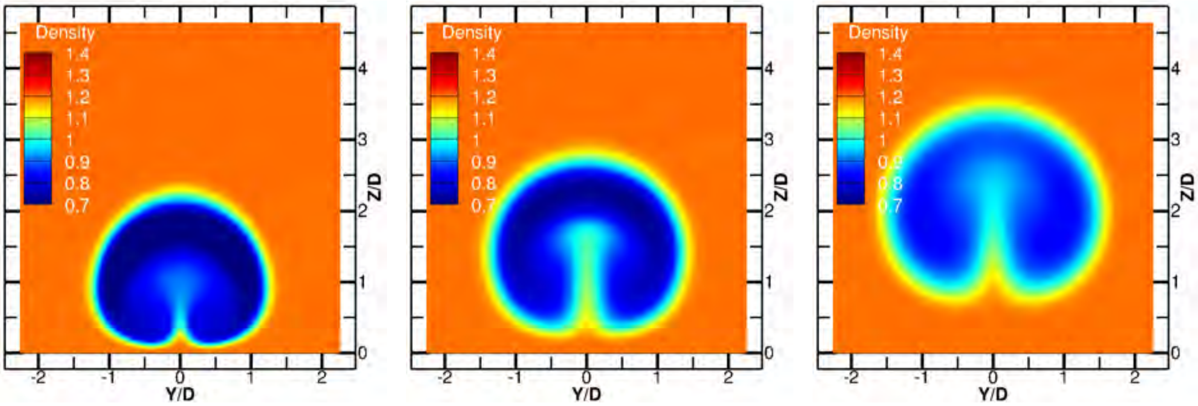

(e) Slice at X=1D.

(f) Slice at X=2D.

(g) Slice at X=4D.

Figure 4.16. Density volume from CFD simulation (Paysant et al. 2020). Simulation conditions $T_j = 400°\mathrm{C}$, $\dot{m}_j = 70\mathrm{g/s}$, $V_0 = 30\mathrm{m/s}$, $C_R = 1.5$ and $R = 2.3$

the recirculation bubble with density values equal to the external one that is located immediately downstream the jet exit, in the area in proximity to the flat plate.

4.5.2 3D BOS reconstructions from experimental data

Acquisitions were made at different jet conditions but only one operation condition is studied here, the acquisition conditions are those of Test 2 in table 4.1: T_j=400°, ρ_j=0.524kg/m^3, V_j=106m/s, $\dot{m}_j$=70g/s, ρ_0=1.2, V_0=30m/s, C_R=1.5 and R=2.3.

The convergence of the displacement fields is largely ensured by the acquisition of 2800

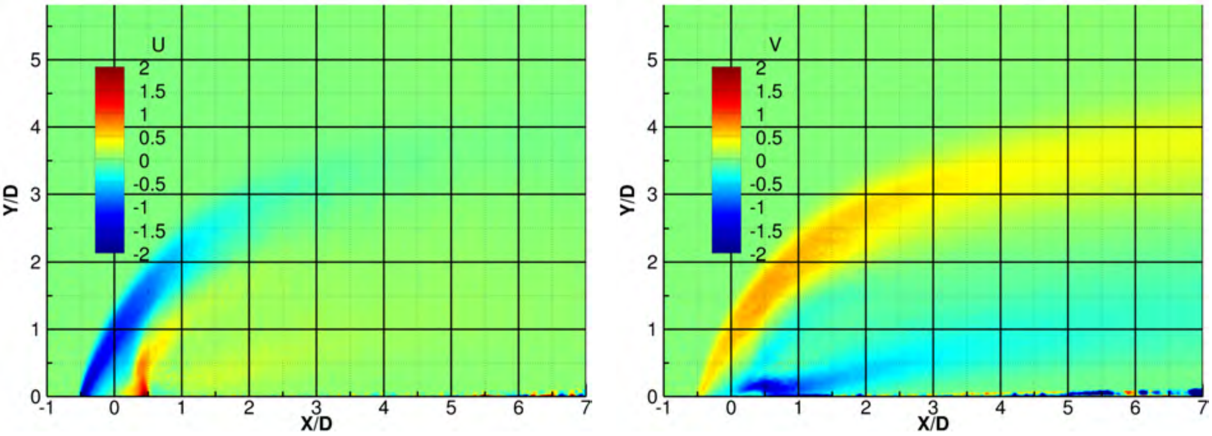

(a) Horizontal displacements field U in pixels. **(b)** Vertical displacements field V in pixels.

Figure 4.17. Mean displacements fields obtained by the camera number 1 by averaging 2800 images.

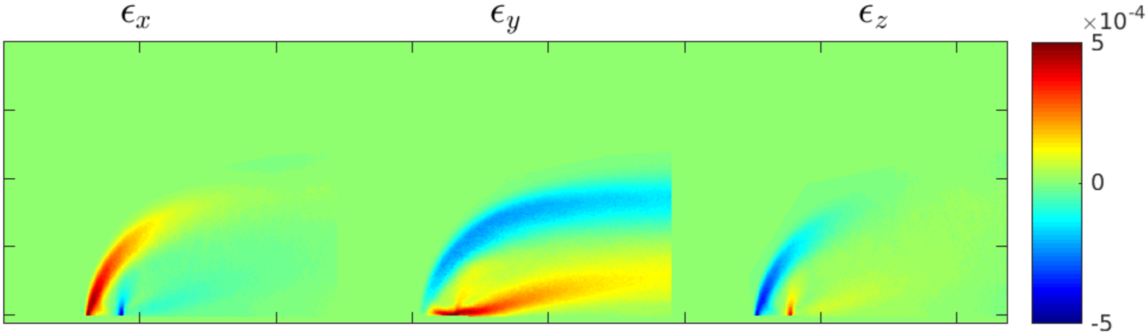

Figure 4.18. Deviations in radians obtained through experimental data in the three directions x, y and z of camera number 1.

images for each of the 8 cameras. The figure 4.17 shows the displacement maps for camera number 1 (figure 4.10b). The displacements are stronger at the outlet of the jet, where there are the highest density gradients, and then decrease rapidly in the downstream direction.

After calculating the mean displacement fields for the 8 cameras, the deviations in the three directions x, y and z were evaluated taking into account the different sensitivity of the cameras due to the different distances l and m (table 4.3): this is taken into account through the calibration process as described in Nicolas et al. (2016). Figure 4.18 shows the deviations ϵ_x, ϵ_y and ϵ_z, in radians for camera 1.

These deviations were used for the following 3D reconstructions.

4.5.2.1 3D BOS standard reconstruction

In this section we apply the classical process of mask definition and 3D reconstruction which is usually done at ONERA (see Section 1.7), to the 3D BOS data at hand and comment the limitations observed on the results.

Starting from the estimated displacement norm, for each camera, the user draws by hand a 2D mask. Then, each voxel of the original volume is initialized to zero and projected onto the image plane of each camera and its value is increased if the projection is within the corresponding 2D mask. The corresponding 3D mask is composed of all the voxels of the volume that are retained when their value is higher than a threshold set by the user. This means that only the voxels

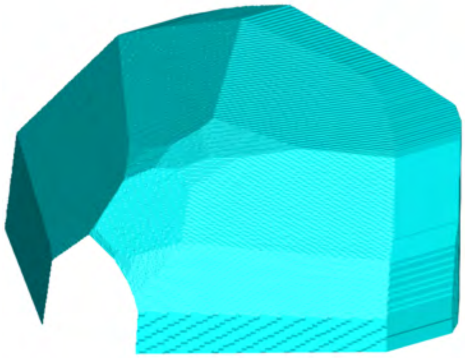

(a) 3D mask M1: mask obtained by hand drawing 8 2D masks based on the real displacements of the 8 cameras placed on the horizontal plane.

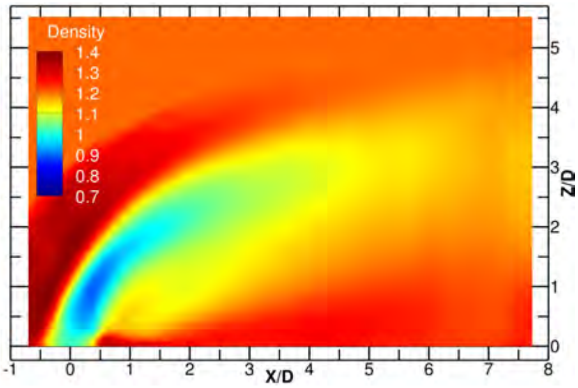

(b) Mean density field, slice at Y=0D.

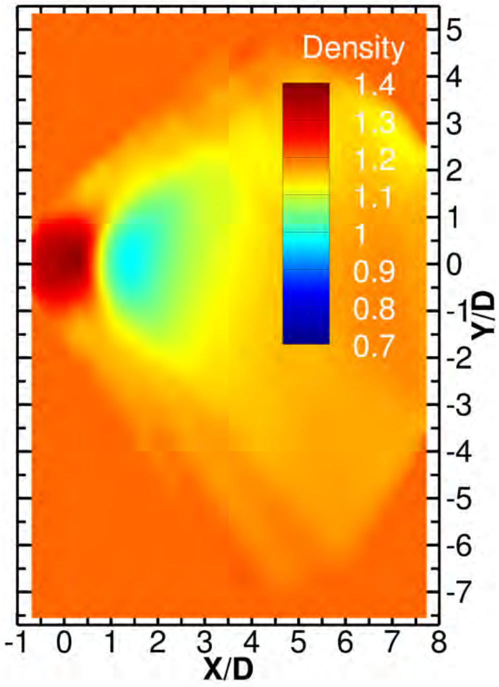

(c) Mean density field, slice at Z=2D.

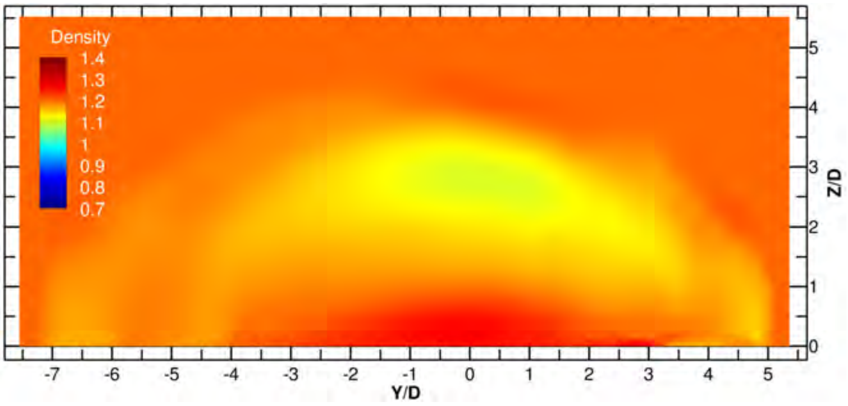

(d) Mean density field, slice at X=4D.

Figure 4.19. 3D BOS reconstruction from the real data acquired by the eight cameras arranged on the horizontal plane (figure 4.10b) and using the mask in figure 4.19a.

that are inside the 2D masks of a certain number of cameras are kept.

A boundary condition equal to the external density is directly imposed on the 3D mask edges, while where the mask is perforated or where there is no edge, freestream boundary conditions are imposed.

Comparing the results obtained with the 3D BOS reconstructions (figures 4.19b, 4.19c and 4.19d) and those obtained with CFD (figure 4.16), several problems may be identified:

1. There are areas where the density is higher than the density of the air at ambient temperature: surely these values are not correct because the flow of the wind tunnel is at a temperature of 20° and the jet is heated to 400°. These areas are located upstream and outside of the jet and in the lower part, in contact with the flat plate.
2. Abnormal density values inside the jet. This jet comes out at a temperature of 400° and then it is expected a density of 0.524kg/m^3 instead the minimum density reached is equal to 0.95kg/m^3.
3. No typical characteristics of the cross-flow jet topology can be distinguished. These include the typical horseshoe shape of two counter-rotating vortex developing towards downstream and the recirculation bubble that is located immediately downstream the jet exit.

These problems are associated both to the reconstruction volume that is much larger than the actual volume of the jet and to the arrangement of the cameras: the reconstruction procedure spreads the information throughout the volume and the placement of the cameras does not allow to capture the width of the jet.

4.5.2.2 Effect of an optimised 3D mask

As noticed in the previous section, the 3D mask is too wide compared to the width of the jet. For this reason, using the data acquired through PIV and thermocouple measurements it was possible to draw with a CAD software a 3D mask much smaller than the previous one to try to contain the information and better reconstruct the jet.

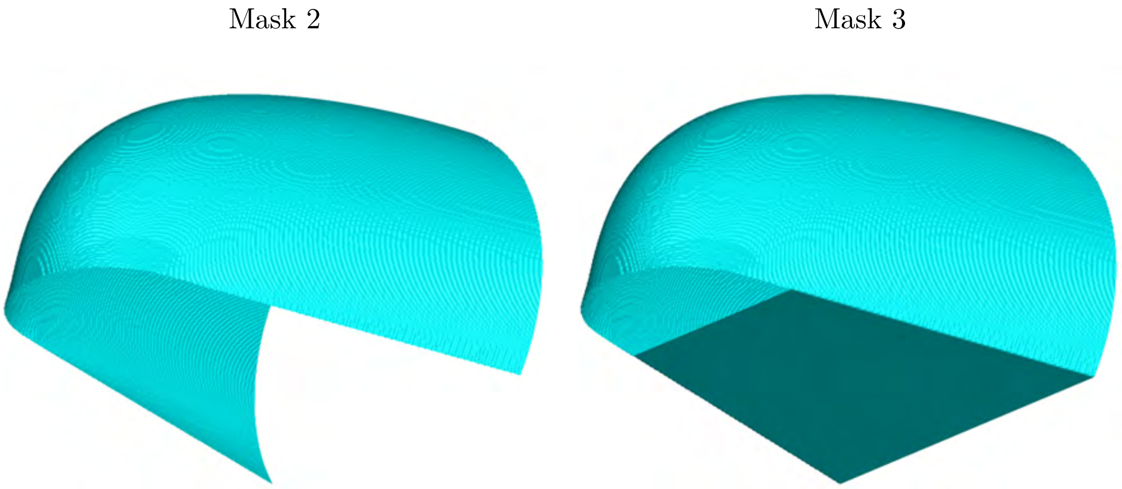

(a) CAD-designed mask from PIV and thermocouple data.

(b) In this mask the external boundary conditions are also imposed in contact with the flat plate, except in the zone of exit of the jet.

Figure 4.20. Two 3D CAD-designed masks from PIV and thermocouple data with different boundary conditions in contact with the flat plate.

The masks that have been obtained with this process are displayed in figure 4.20a (Mask 2) and 4.20b (Mask 3). On Mask 2, the external density conditions are imposed only on the outermost part of the jet and neither in contact with the flat plate nor in the downstream part where the jet goes through the mask. On Mask 3, the external density is also imposed in part of the area in contact with the flat plate. This imposition of boundary conditions was possible thanks to the data of the thermocouple shown in figure 4.8c: at a distance of 3 diameters from the centre of the jet, the wall temperature is to be considered equal to the external temperature.

Looking at the reconstructions obtained with these two masks (figure 4.21) and with the same reconstruction parameters as before, the reconstruction is significantly improved thanks to the use of optimised masks around the jet, but some difficulties remain.

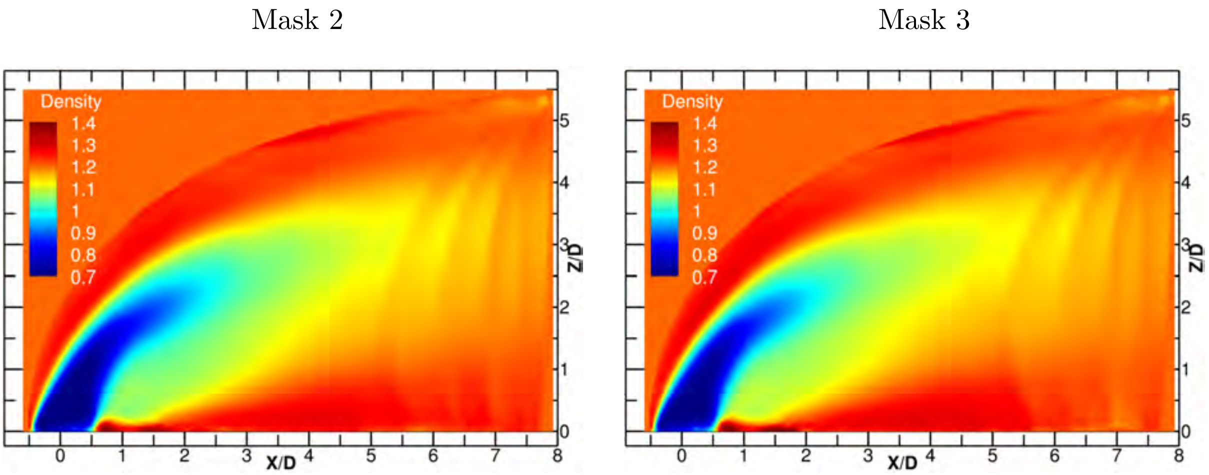

(a) Slice at Y=0D. **(b)** Slice at Y=0D.

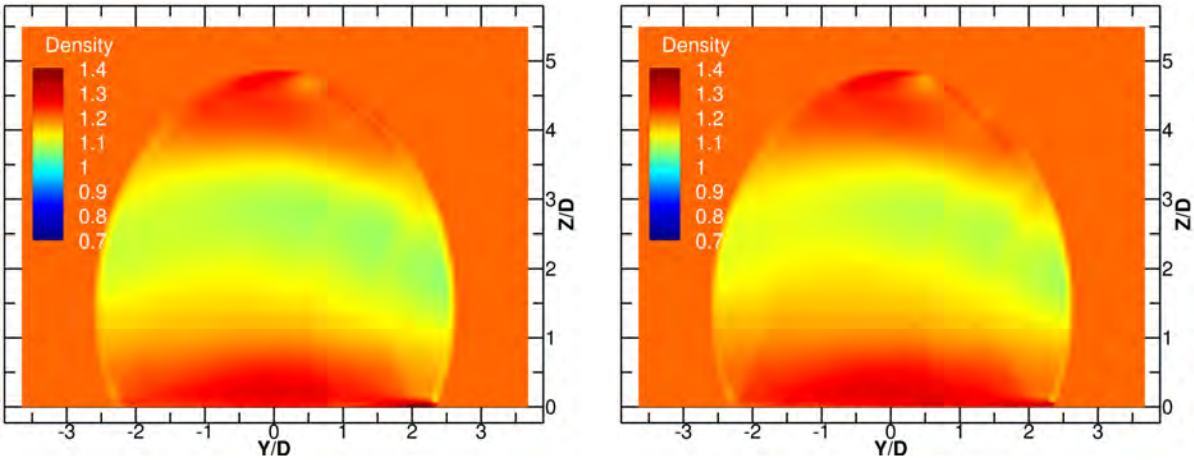

(c) Slice at X=4D. **(d)** Slice at X=4D.

Figure 4.21. 3D BOS mean density field reconstructions using the same mask with different boundary conditions. On the left the reconstruction corresponding to the mask of figure 4.20a on the right with that of figure 4.20b

The imposition of the external density in contact with the flat plate does not bring significant improvements as both reconstructions using Mask 2 or Mask 3 appear almost identical.

The density levels are more similar to CFD simulation (figure 4.16) than in the previous case but there are always regions where the result is not physically reliable. At the jet outlet the minimum density reached is equal to 0.65kg/m^3 corresponding to 270°C. In addition, there are always higher density levels than the external density in the upstream part of the jet and in the area immediately downstream of the jet in the area between it and the flat plate.

These reconstructions clearly show the effect of the ray-validation procedure during the reconstruction process (section 1.7.8). Due to the arrangement of the cameras, a large part of the deviations captured by the outermost cameras must be eliminated and are not used in the reconstruction process as these rays went through a flow region outside of the reconstructed volume. This means that in the downstream part of the 3D reconstruction, the information comes from a limited number of cameras and therefore from a limited number of viewpoints, resulting in a strongly degraded result. The effect of the validation can be seen in the images 4.21a and 4.21b: on the right side there are vertical stripes and clearly observable density jumps.

Looking at the reconstructions of images 4.21c and 4.21d it can be observed that the reconstruction is not able to reproduce the shape of the two counter-rotating vortices and the recirculation bubble located immediately downstream the jet exit observed in the CFD simulation (figure 4.16) and are still different from the thermocouple measurements (figure 4.8). The classic JICF dynamic is totally lost. Due to the arrangement of the cameras on a single plane, the information is distributed over the entire width of the volume.

After these two reconstructions we can conclude by saying that the choice of the mask certainly influences the 3D reconstruction but it does not solve the problems related to the geometrical configuration of the cameras.

Since the reconstructions from the real data are not satisfactory, it was necessary to continue the investigation of the problems related to the reconstruction of this jet. This topic is discussed in the next section where further investigation will be done on numerical simulations.

4.5.3 Synthetic 3D BOS reconstruction from CFD simulation

In the following subsections, a series of 3D BOS synthetic reconstructions are presented which should improve the reconstruction and explain the errors present in the reconstructions obtained from the experimental data.

This section uses the CFD simulation presented earlier in section 4.5.1 to obtain simulated deviations that are obtained as exposed in section 4.5.3.1.

First of all a BOS reconstruction was made with synthetic data in the same experimental configuration and then the influence of rays validation was studied. Subsequently a series of reconstructions with an arrangement of the cameras on two different planes and orthogonal to each other are proposed: with this arrangement of the cameras the effect of the use of a tailored mask and the influence of the number of cameras was studied. Finally, the choice of the regularization parameter and its effect on the reconstruction are presented.

4.5.3.1 Simulation of BOS data from CFD

The 3D BOS synthetic reconstructions have as starting input not a displacements field obtained from images correlation but the synthetic deviations field. The process to obtain the deviations starts with choosing the configuration of the cameras: for each camera, integrated deviations (ϵ_x, ϵ_y and ϵ_z) are computed through ray tracing within the simulated volume. To take into account the imperfections of the measures, a white and homogeneous Gaussian noise has been added to synthetic deviations. The variance noise has been fixed at $\sigma = 510 \times 10^{-5}$rad resulting from a displacement noise of 0.1 pixel (value typical of random errors of digital image correlation in cases where the correlation score is good). This deviation calculation procedure has been used for all the simulations presented below.

4.5.3.2 Simulation replay of the experimental set-up

This section is intended to examine whether the errors in the reconstructions presented up to now are related to the configuration of the 3D BOS setup or if they can be related in some way to some errors committed during the acquisition of experimental data.

In the present case, to compare the reconstruction with the previous ones, the configuration of the cameras used is the same as the experimental one in figure 4.10b: 8 cameras are placed in the horizontal plane corresponding to the plane passing through the flat plate.

The tomographic reconstruction was carried out with the same parameters used in the previous case. The 3D mask chosen for the reconstruction is the Mask 2 (figure 4.20a), the one without the imposition of the external density in contact with the flat plate. The number of iterations (1000) and the parameter of regularization, $\lambda = 5 \times 10^{-5}$, have not been changed.

The results achieved in this procedure can be found in figure 4.22 in the right column. To ease the comparison, we present again (on the left) the result obtained with the experimental data (figure 4.21). At first glance, reconstructions are quite similar from that obtained from the experimental data under the same conditions.

The 3D BOS synthetic reconstruction is not able to reconstruct correctly the CFD simulated ground truth density volume and the anomalies that were observed and presented in section 4.5.2.2 remain.

From images 4.22a and 4.22b at Y/D=0 we notice that the density distributions within the jet are partly different between the two reconstructions. The bubble-shaped area of the center X/D=1 and Z/D=1, where the densities are lower (higher temperatures), is more marked in the synthetic case than in the real one. The other main difference is located in the downstream part: in the real case the jet is more mixed and therefore there are higher densities while in the synthetic case the jet in this area is still well defined and there is a net border with the outside region with stronger gradients in the boundary area of the jet.

As regards the density at the outlet of the jet, the values are lower in the synthetic reconstruction and therefore more similar to the expected values.

These discrepancies can be attributed to differences between CFD simulation and reality and to errors related to the measurement of BOS distances (m and l).

With the synthetic data it is not possible to reconstruct in the YZ plane at X/D=4 the mushroom-shaped area due to the contra-rotative vortices (figure 4.22f). On this plane the information is spread along the entire width of the mask in a strip between the two extremes that correspond to the extremes in Z where the jet is located in the CFD simulation.

In the reconstruction based on synthetic deviations, in the furthest downstream part of the jet, we find those streaks associated with rays validation (figure 4.22b).

In conclusion, through the reconstruction based on the deviations obtained from the CFD simulation we have demonstrated that all the problems related to the reconstruction are not due to the experimental data acquisition but come mainly from the coplanar arrangement of the cameras and to a lesser extent from the 3D mask, boundary conditions and ray validations.

While maintaining the same layout of cameras, in the next section are investigated a tight mask and ideal boundary conditions.

4.5.3.3 Synthetic reconstruction with a tight mask and ideal boundary conditions

In this section is discussed the effect of using a tight mask with ideal boundary conditions with the 8 coplanar camera configuration (figure 4.10b).

To eliminate any kind of effect related to the 3D mask and the boundary conditions, it was preferred to create a mask as narrow as possible around the jet. Since the reconstructions proposed to investigate this aspect are synthetic reconstructions, the volume obtained from the CFD simulation was used to create this type of 3D mask. The mask is then obtained by selecting the iso-surface where the density is equal to the external density (figure 4.23). As boundary conditions, freestream conditions have been imposed in the downstream part and at the exit of the jet, elsewhere the external density is imposed. With this choice the Mask 4 is as small as possible without eliminating any part of the jet.

As expected, and as seen in sections 4.5.2.1 and 4.5.2.2, by modifying the mask the reconstruction changes considerably and by using a mask even more adjusted to the shape of the jet,

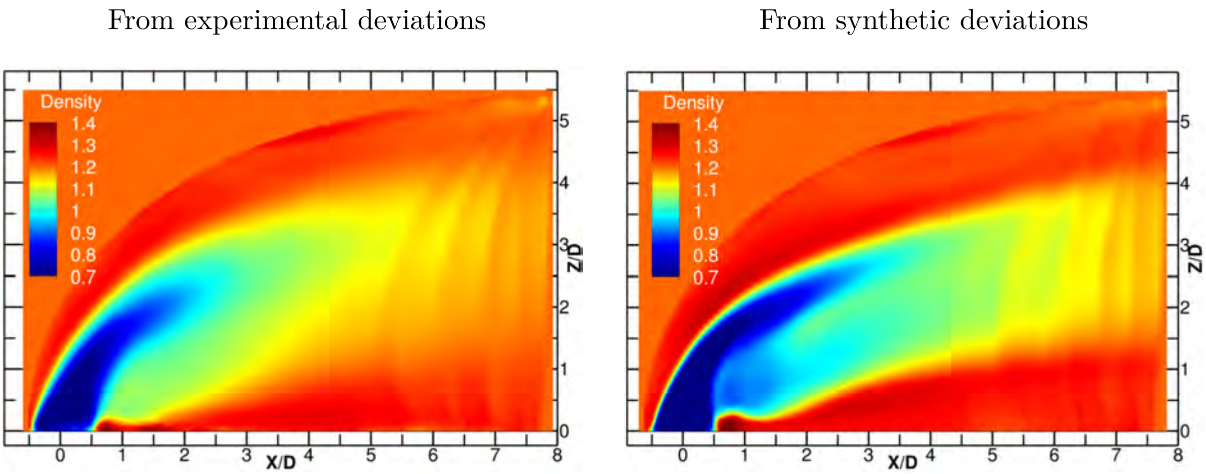

(a) Slice at Y=0D. **(b)** Slice at Y=0D.

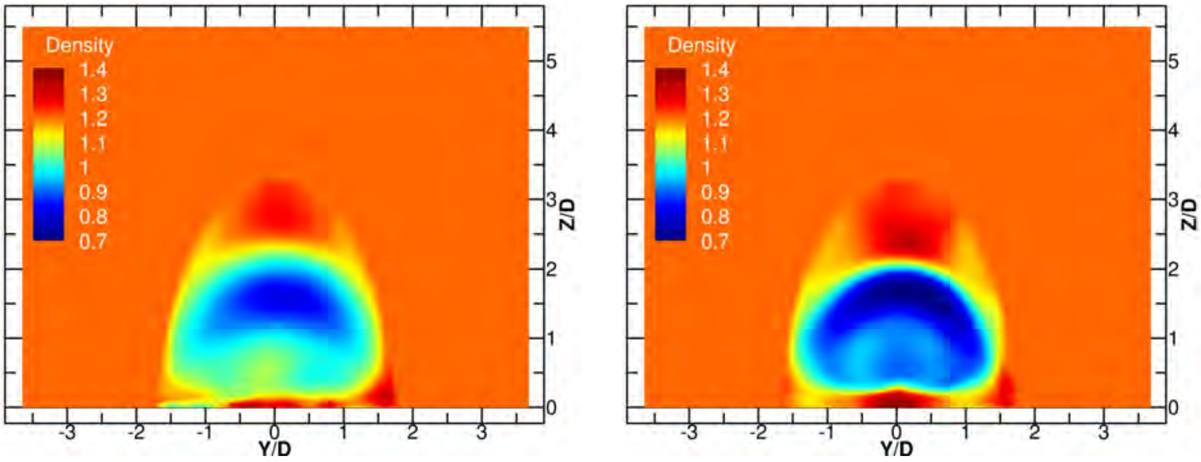

(c) Slice at X=1D. **(d)** Slice at X=1D.

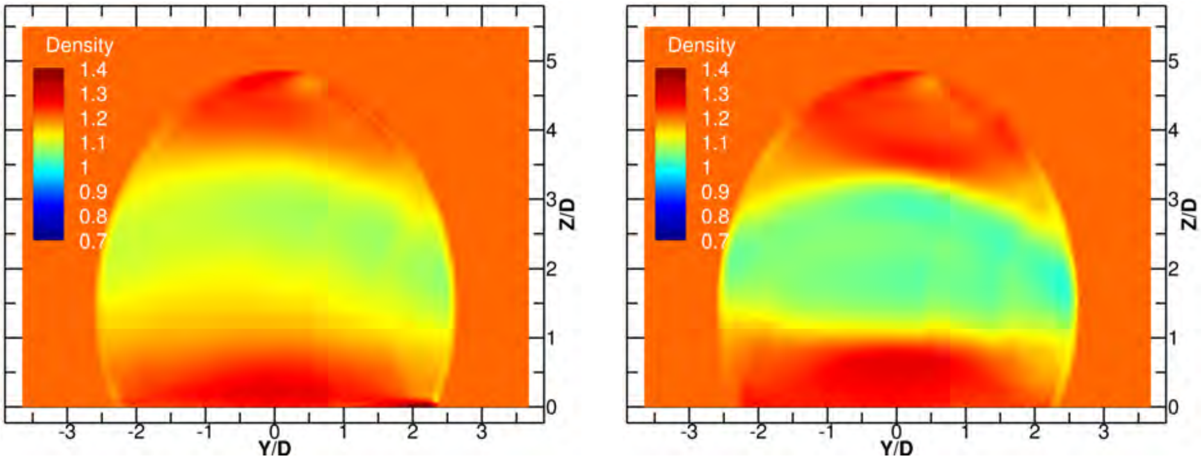

(e) Slice at X=4D. **(f)** Slice at X=4D.

Figure 4.22. 3D BOS mean density field reconstructions using the Mask 2. On the left the reconstruction using experimental deviations (figure 4.21); on the right using synthetic deviations.

the reconstruction is improved. The images that are to be compared to evaluate this improvement are the reconstructions in figures 4.22b and 4.22f with Mask 2 (figure4.20a) and in figures

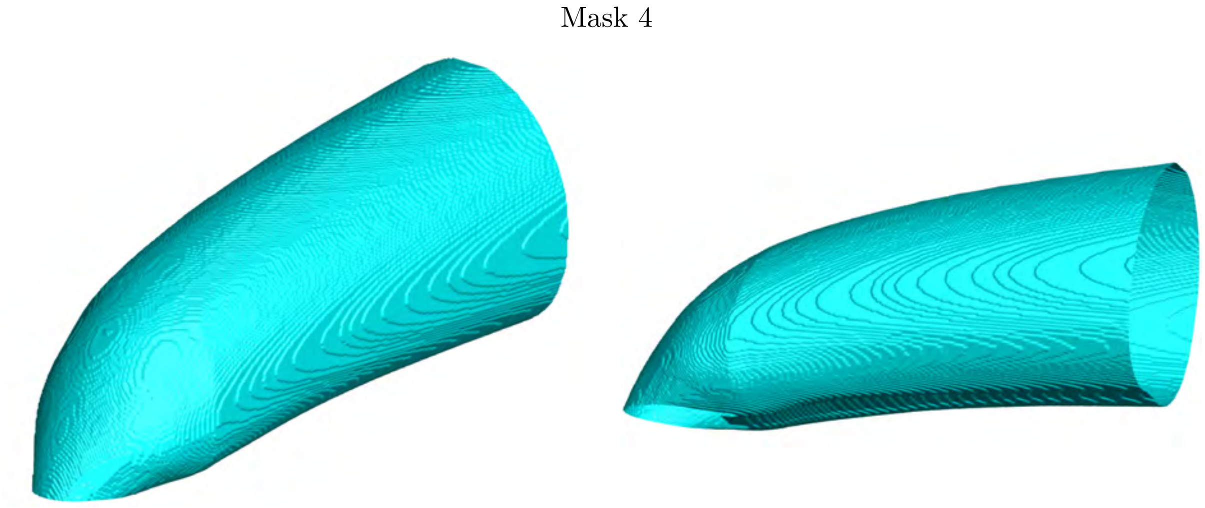

(a) **(b)**

Figure 4.23. 3D mask obtained from the CFD simulation by selecting the iso-surface where the density is equal to the external density.

4.25a and 4.25e with Mask 4 (figure 4.23).

Using the most tailored mask there are no more areas where the density is higher than the external density and consequently the density values inside the jet are more similar to those of the CFD simulation; moreover the information is not assigned to the outside of the jet, changing its appearance. The only area where the density is slightly higher than the external density (1.30kg/m^3) is located in the area immediately downstream of the jet, between this and the flat plate.

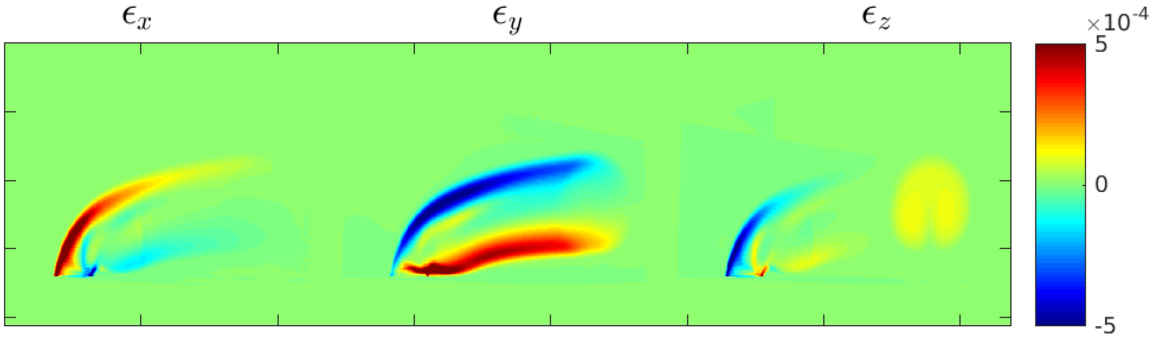

Figure 4.24. Deviations in radians in the three directions x, y and z of camera number 1 obtained with ray tracing through the cut CFD volume.

When the shape and size of the 3D mask varies, so do the rays that are retained after the ray validation process and then used for the 3D reconstruction. For this reason, since Mask 4 towards the downstream is narrower than Mask 2, the part of the deviations discarded during the rays validation is smaller and therefore its effect, although present, remains less marked than in previous cases.

Remembering that a ray is considered valid when no gradient density is encountered outside the mask, to eliminate the step of the rays validation and to obtain a reconstruction faithful to the input deviations of the reconstruction process, it is necessary to carry out a ray tracing only through the volume that is then effectively reconstructed. For this reason the CFD simulation which continues up to 20 diameters downstream of the orifice, was cut to 8D downstream of the outlet to adapt it to the dimensions of the 3D mask and 3D BOS reconstruction. Ray tracing was made through this reduced volume and therefore all the deviations obtained must be considered as valid. This step is used only for the purpose of investigation and it would be impossible and incorrect not to perform the rays validation in a real case.

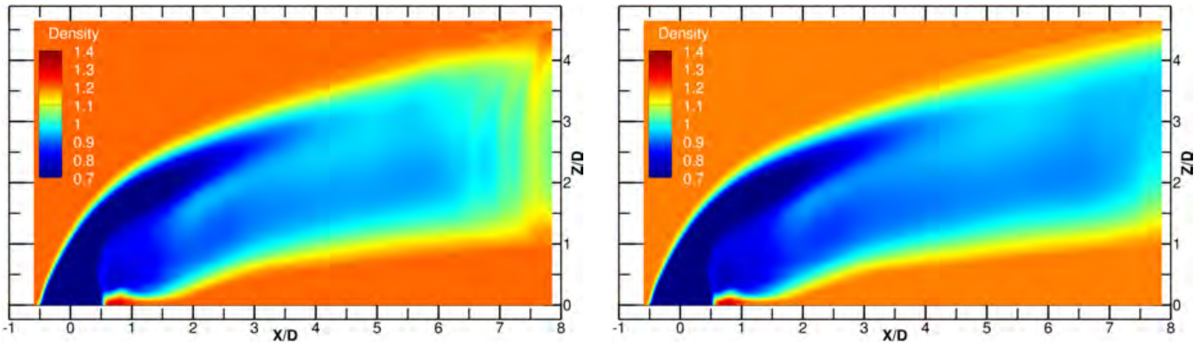

(a) Slice at Y=0D.

(b) Slice at Y=0D.

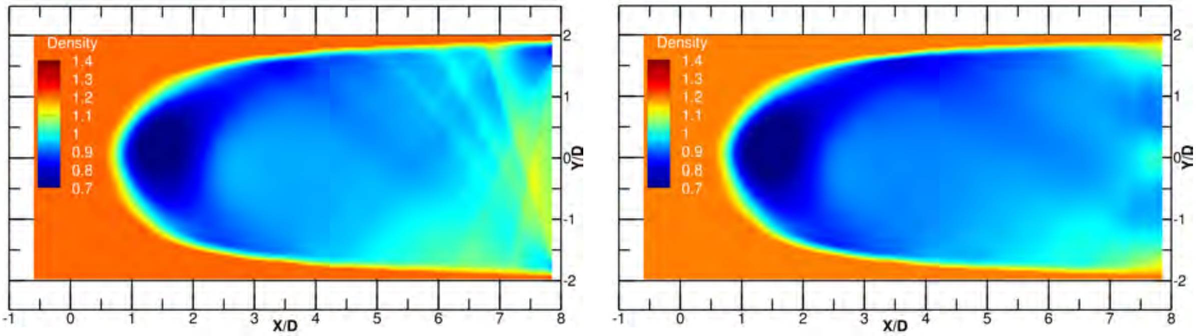

(c) Slice at Z=2D.

(d) Slice at Z=2D.

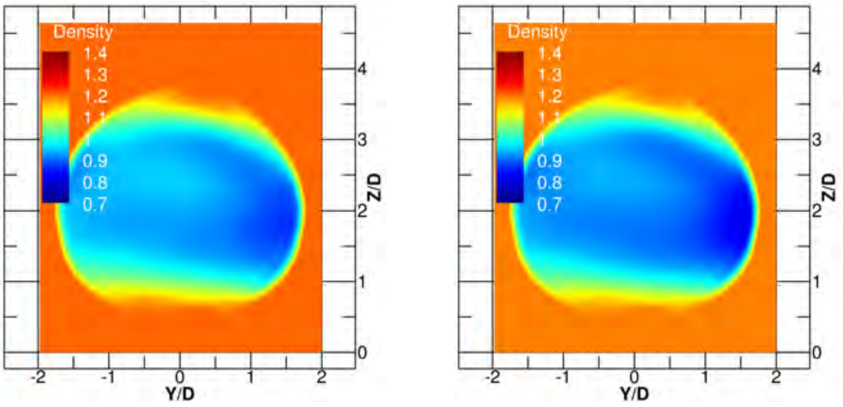

(e) Slice at X=4D.

(f) Slice at X=4D.

Figure 4.25. 3D BOS mean density field reconstructions using the super-tailored 3D mask of figure 4.23. On the left the reconstruction with rays validation; on the right without rays validation.

Figure 4.24 shows the deviations in the three directions on camera 1. Since this is the outermost camera together with camera 8, it is the one where in the validation phase most of the deviations are discarded. By comparing the experimental deviation map (figure 4.18) with the one obtained with the procedure described above (figure 4.24), it can be seen that in the downstream part (right side), the circular zone where the rays enter the lateral part of the 3D mask and exit at the rearmost part, there are substantial differences. The deviations thus obtained take into account a sudden jump: the density passes from that present inside the jet to the external one. The rays validation is therefore very important: reconstructing without the validation would mean to adding to the reconstruction a part of the information coming from outside the reconstruction volume.

In reconstructions the validation of the rays mainly influences the region of the volume where the deviations are eliminated, and therefore the region downstream of the jet. In the reconstruction carried out without the validation we do not find the density jumps (figures 4.25b and 4.25d), in this case in the form of vertical (in the XZ plan) or diagonal (in the XY plan) strips, which were present in previous cases (figures 4.25a and 4.25c). These density jumps stems from the fact that, when ray validation is done, the volume near the free edge is reconstructed with less cameras.

Thanks to the reconstructions of this section, we demonstrate that even with a tight 3D mask and ideal boundary conditions, it is not possible to correctly reconstruct the internal structures in the jet: the 3D BOS reconstruction remains inaccurate.

In this section is presented the best reconstruction achievable from a planar configuration of the cameras, while the next section will show what can be achieved with a different geometric configuration of the cameras.

4.5.3.4 Synthetic 3D BOS using a two-planes configuration

As already extensively explained in section 4.3.3, because of the two principal axes of the jet, vertical and horizontal, a coplanar arrangement of the camera is suboptimal: here we investigate the benefit in the 3D reconstruction of a non coplanar configuration. The cameras were arranged on two planes and distributed on them: four cameras on the horizontal plane and four on the vertical plane, as shown in figure 4.11a and explained in section 4.3.3.

The cameras located in the vertical plane (plane YZ) are optimized to reconstruct the horizontal part of the jet, parallel to the flat plates, while the cameras in the horizontal plane (plane XY) are optimized to reconstruct the vertical part of the jet, the first part at the exit.

Let us recall that this configuration is not feasible experimentally because of the presence of the model which prevents us from positioning the background at a sufficient distance from the cameras.

The mask built from the PIV and thermocouple data, Mask 3 of figure 4.20b, has been used as the 3D mask for the BOS reconstruction. During the ray validation process, for cameras located on the horizontal plane, deviations next to the opening in the most downstream part of the mask are eliminated, while for cameras located on the vertical plane, deviations next to the hot jet outlet are eliminated.

By analysing the transversal planes of the jet, at X=2D and X=4D (figure 4.26c and 4.26d), the typical shape of the counter-rotating vortices is well reconstructed on both planes and in the whole jet, these two slices must be compared with the images of the CFD simulation 4.16f and 4.16g. This aspect can also be verified by the image 4.26b, on the horizontal plane passing through Z=2D: the U-shape is a sign that the jet is well reconstructed and this characteristic was not present with the previous configuration of the cameras (figures 4.25c and 4.25d). From these results it can be deduced that the optimised camera arrangement has a positive impact on the reconstruction.

These results have never been obtained with previous configurations, demonstrating the importance of the arrangement of the cameras in 3D BOS.

Despite the encouraging results obtained there are still problems in the reconstruction. First of all the downstream part of the jet is not reconstructed: this part, because of the arrangement of the cameras, is only seen by one camera (camera 3 in figure 4.11a, the third from the left on the horizontal plane, that has the right end parallel to the end of the 3D mask) and therefore it

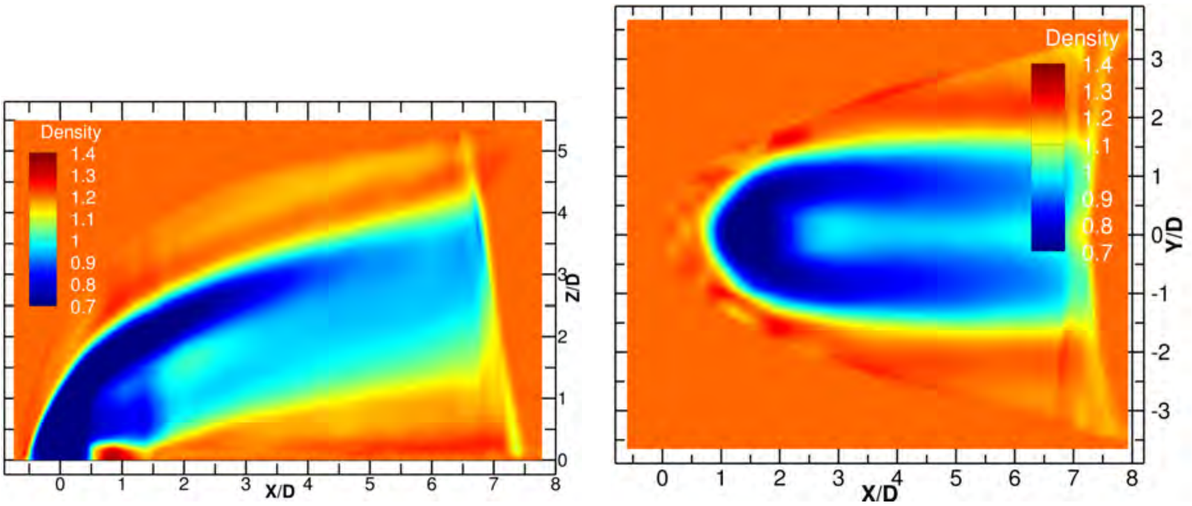

(a) Slice at Y=0D. **(b)** Slice at Z=2D.

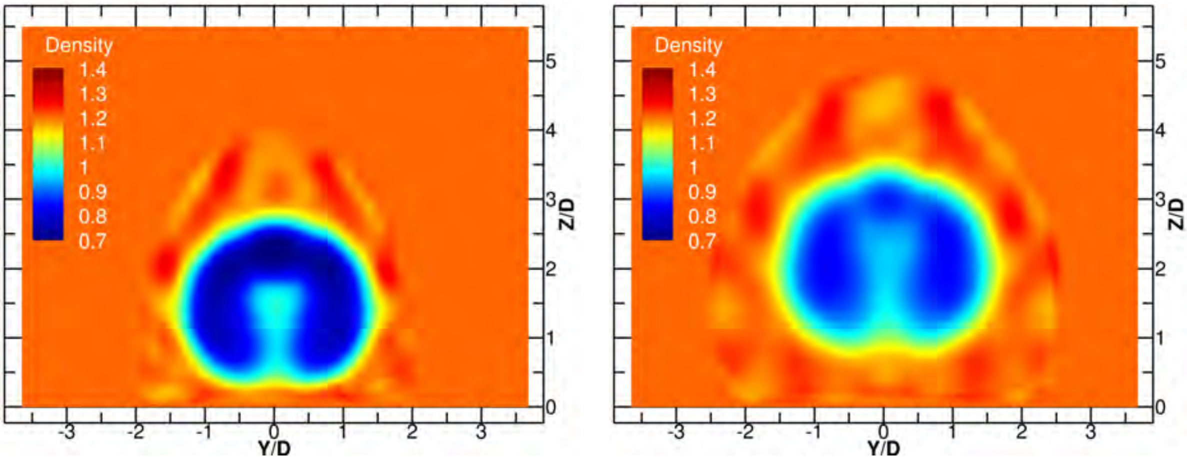

(c) Slice at X=2D. **(d)** Slice at X=4D.

Figure 4.26. 3D BOS mean density field reconstructions using the 3D mask of figure 4.20b with 8 cameras arranged on two orthogonal planes.

is not possible to reconstruct it. In the future, to reconstruct even this part, it will be necessary to arrange the cameras of the vertical plane with the extreme part of the sensor tangent to the downstream side of the 3D mask, in other words it would be sufficient to tilt the cameras in the vertical by a few degrees upstream.

At the jet outlet, due to the hole in the 3D mask clearly larger than the diameter of the jet outlet, a large part of the deviations resulting from the cameras of the vertical plane is eliminated. The zone where the density is higher than the external density, between the jet and the flat plate, is probably linked to rays validation.

The other main difference compared to the ground truth density field obtained by CFD calculation is the presence of some spots, outside the jet but inside the 3D mask, where the density is higher than the external density. Consequently, the information is not correctly distributed and the density levels inside the jet remain higher than expected.

To improve this issue, the strategy already implemented in the previous section was chosen: the proposed solution was to use the 3D mask more tailored to the shape of the jet (Mask 4 of figure 4.23). With this mask the code is forced to distribute the density within a certain volume and those artefacts disappear. Moreover, the density values reached inside the jet do not differ much from the starting values of the CFD simulation.

Thanks to the narrower mask a smaller part of the deviations is eliminated during the ray validation process. This leads to improvements that can be seen on the reconstruction in figures 4.27a and 4.27b, mainly in the downstream part of the jet and at the jet outlet: the area where the flow is seen by a single camera is very limited and therefore the area not reconstructed is less important and density values are closer to the levels of the CFD simulation.

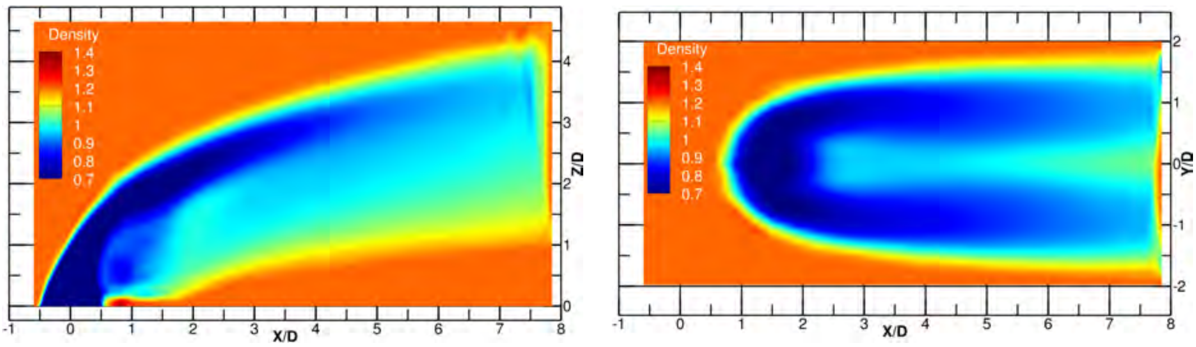

(a) Slice at Y=0D. **(b)** Slice at Y=0D.

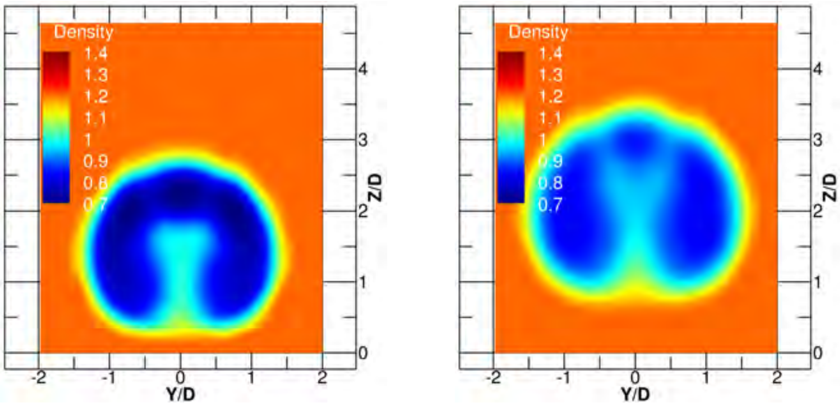

(c) Slice at X=2D. **(d)** Slice at X=4D.

Figure 4.27. 3D BOS mean density field reconstructions using the 3D tailored mask of figure 4.23 with 8 cameras arranged on two orthogonal planes.

An effect, already present in the previous case (figure 4.26d), but previously not as significant as the other problems present, is the V-shaped artefact where the density is lower than the density around this area. Verifying the arrangement of the cameras, this phenomenon is due to the angular distance between the two cameras placed in the upper part: the angle between these two cameras corresponds to the one formed by the V in the reconstruction.

Since the number of cameras is lower than that used in previous experiences during the doctorates of Todoroff (2013) and Nicolas (2017), their number has been increased to try to improve the reconstruction.

A configuration with 6 cameras in the horizontal plane and 8 in the vertical plane was chosen. The six cameras on the horizontal plane are tilted so as to have the lower part parallel to the flat plate, are spaced at an angle of 18° forming an angle of 90° between the two extreme cameras. The cameras on the vertical plane are 20° spaced and considering the cameras on the horizontal plane, an angle of view of 160° is covered by cameras around the jet.

The mask used is the same as in the previous case (Mask 4 of figure 4.23), so that only the

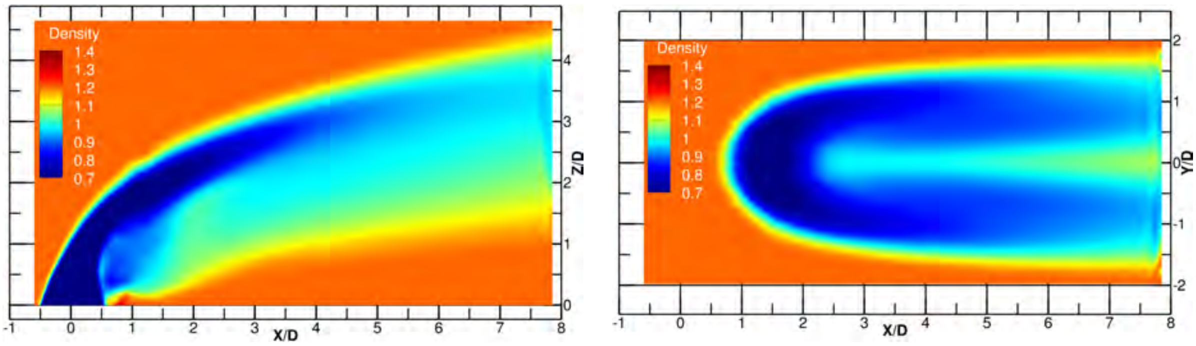

(a) Slice at Y=0D. **(b)** Slice at Z=2D.

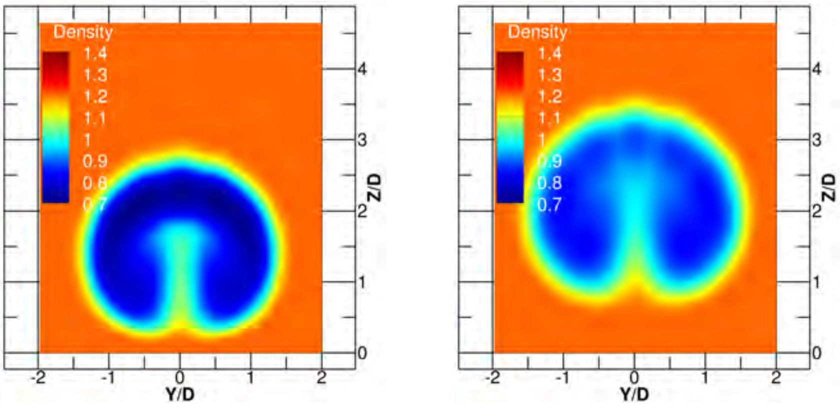

(c) Slice at X=2D. **(d)** Slice at X=4D.

Figure 4.28. 3D BOS mean density field reconstructions using the 3D tailored mask of figure 4.23 with 14 cameras arranged on two orthogonal planes: 6 on the horizontal plane and 8 on the vertical plane.

influence of the number of cameras can be investigated.

Looking at the reconstruction for Y=0 we notice some slight improvements in particular to the low-density zone at X=2D and Z=2D: the shape of this zone is better reconstructed compared to previous reconstructions.

The biggest differences are noticed in figures 4.28b, 4.28c and 4.28d. On the plane at Z=2D, the horseshoe shape is better reconstructed, especially the central part, at low density, is more similar to the CFD calculation compared to the reconstruction obtained with the same mask but with only 8 cameras. Moreover the downstream area, influenced by the beam validation, is slightly improved: this is due to the fact that increasing the number of cameras this area is seen and then reconstructed by a greater number of cameras.

For the transversal cut for X=2D, the low density vertical zone, between the two counter-rotating vortices is reconstructed more faithfully than in the previous case.

The same can be said for the cut for X=4D. The problem presented above, related to the V shape where the density is lower than the surrounding zone, is always present: this artefact is less marked and the angle formed by the V sides depends on the position of the cameras, in this case the V is narrower than in the previous case because the angle between the cameras is smaller.

Despite the fact that it has been shown to be effective in using more cameras, the benefits are limited compared to the complexity and increase in the amount of data and calculation time needed to obtain a reconstruction with a larger number of cameras.

4.5.3.5 Practical issues in mask construction

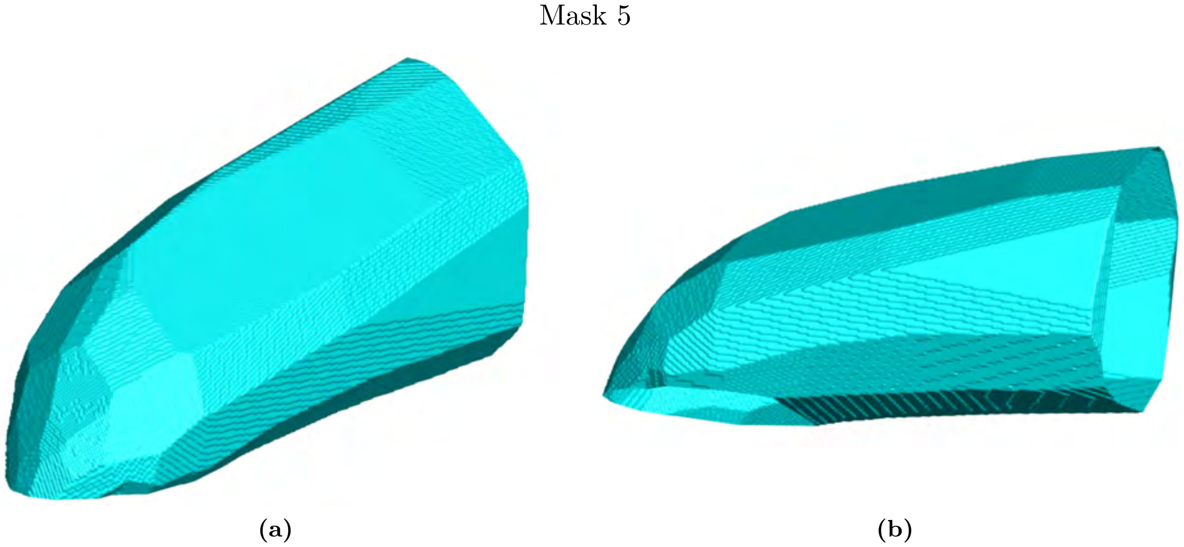

Figure 4.29. 3D mask obtained by hand drawing 8 2D masks based on the synthetic deviations of the 8 cameras placed arranged on two orthogonal planes. b) The hole in the mask corresponding to the jet outlet is significantly larger than the diameter of the jet outlet.

Before the 3D reconstruction it is necessary to make a 3D mask from the available data, in this section we study some practical problems that may arise in this operation.

For this purpose it is therefore necessary to design a 3D mask based on the BOS deviations of each camera and not use the mask obtained from a CFD calculation or derived from experimental data obtained by measurements such as PIV or thermocouple.

The process used to design the 3D mask is the same as the one detailed in section 4.5.2.1. The mask that is obtained (figure 4.29, Mask 5), thanks to the arrangement of the cameras on two planes, is tight around the jet. Since the 2D masks that are used to create the 3D mask are drawn by hand, the latter results very squared and not symmetrical with respect to the two principal axes.

These asymmetries lead to important artefacts in the 3D reconstruction (figure 4.30): major reconstruction problems ranging from the jet exit to X/D=3, where the aperture in the mask ends. The whole part in correspondence of the jet outlet is strongly influenced by the elimination of a large number of deviations, which even if they should be retained are discarded because the 3D mask is not adapted to the outlet diameter of the jet.

The series of errors present in the reconstruction presented above shows that improvements are still necessary: for this purpose, the mask represented in figure 4.31 has been created. This 3D mask has been designed with a CAD software starting from mask in figure 4.29. By knowing the position and the outlet diameter of the jet, it was possible to considerably reduce the outlet aperture of the jet in the 3D mask: this was fixed to the diameter of the jet (40mm) plus 2mm. Moreover, this new mask is symmetrical and consists of the minimum envelope that encloses within it the previous mask. With this mask only a small part (the minimum necessary) of the deviations at the jet outlet are eliminated and it is very adjusted to the jet.

The reconstruction thus obtained (figure 4.32) is deprived of the errors previously present. This can be compared with the reconstruction of figure 4.27, obtained with the Mask 4 of figure 4.23 (obtained from the CFD simulation). A first difference is associated to the size of the mask: in the region outside the jet but inside the 3D mask, the density values are not equal to the external density but slightly higher. This effect, although present, is much less pronounced than

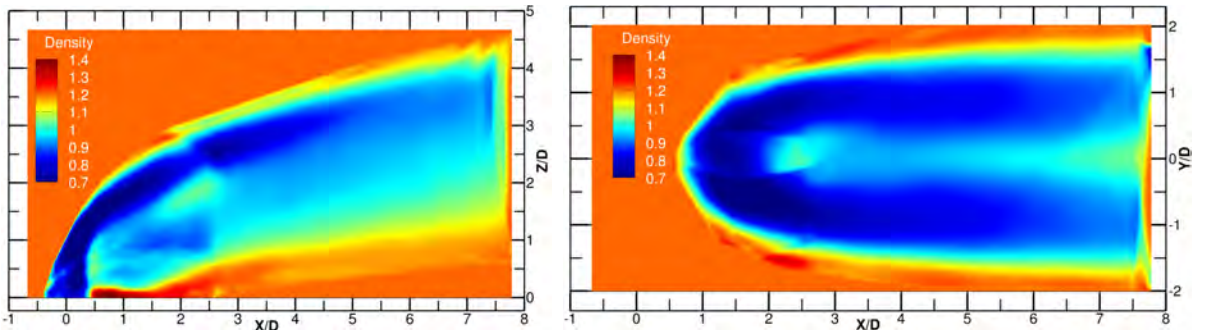

(a) Slice at Y=0D.

(b) Slice at Z=2D.

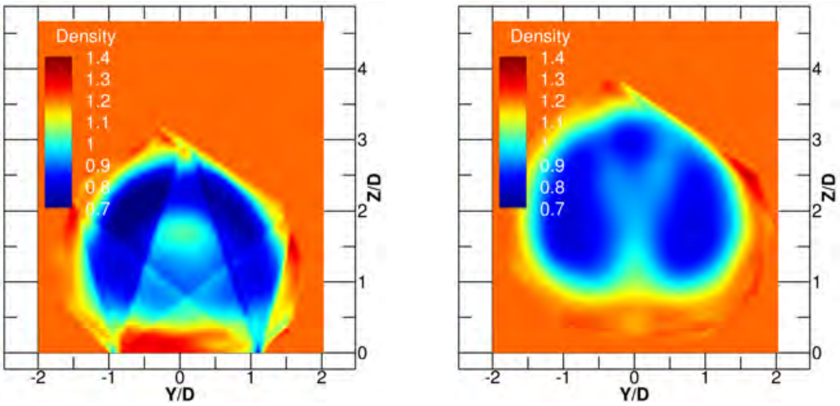

(c) Slice at X=2D.

(d) Slice at X=2D.

Figure 4.30. 3D BOS mean density field reconstructions using the hand drawing 3D mask of figure 4.29 with 8 cameras arranged on two orthogonal planes. The asymmetry of the mask and rays validation leads to problems with reconstruction.

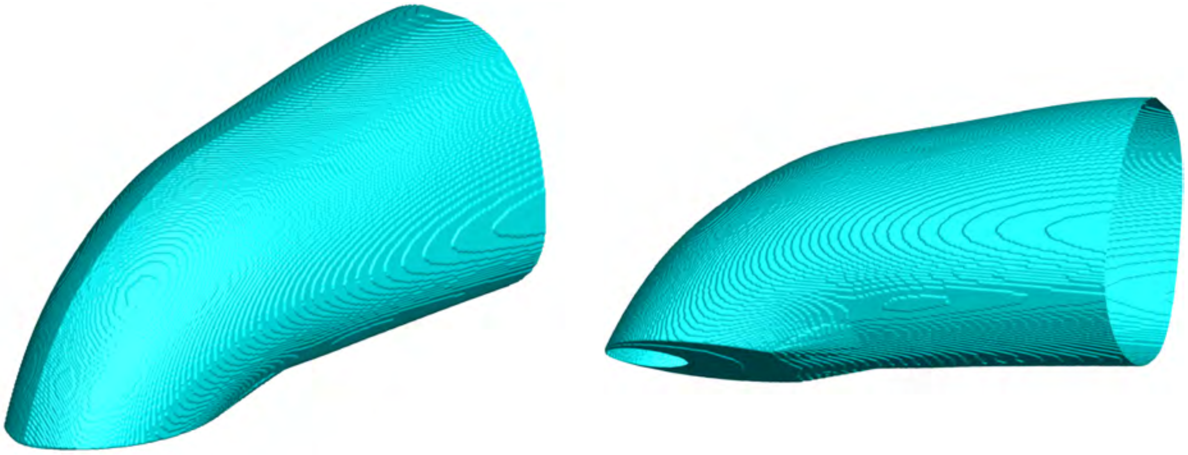
Mask 6

(a)

(b)

Figure 4.31. 3D mask obtained from the mask of figure 4.29 and modified with a CAD software to make it symmetrical and reduce the outlet hole of the jet: the hole was set to the diameter of the jet (40mm) plus 2mm.

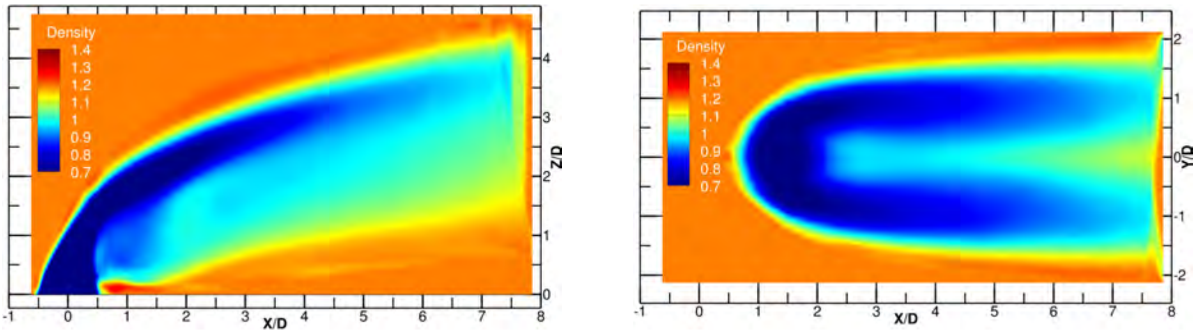

(a) Slice at Y=0D.

(b) Slice at Z=2D.

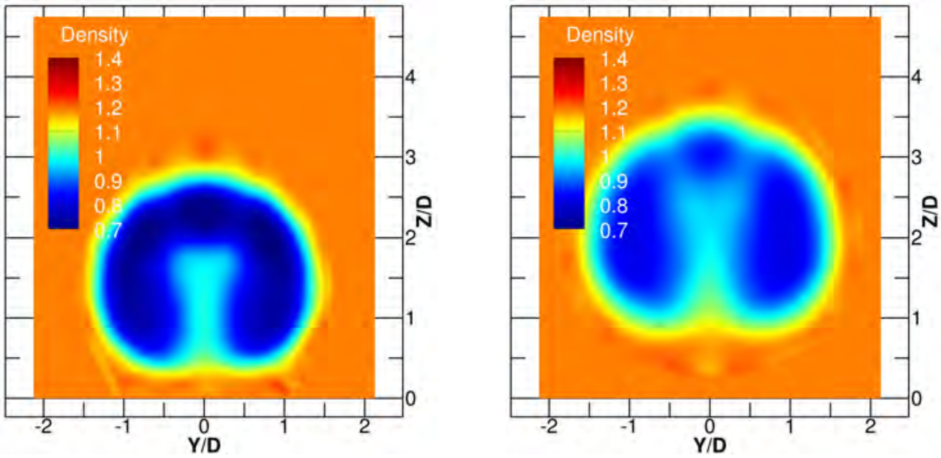

(c) Slice at X=2D.

(d) Slice at X=4D.

Figure 4.32. 3D BOS mean density field reconstructions using the CAD modified 3D mask of figure 4.31 with 8 cameras arranged on two orthogonal planes.

the reconstruction 4.26 obtained with Mask 3 (figure 4.20b): the reconstruction in this case is improved because Mask 6 is narrower around the jet and the regularization does not have the necessary space to create those high density spots outside the jet and the density values inside the jet reach the expected levels.

This section has shown that it is possible to build an optimised 3D mask with the use of CAD software and its beneficial effects on the 3D BOS reconstruction. One perspective for the future is certainly the implementation of the 3D mask optimisation process for future BOS reconstructions.

4.5.3.6 Choice of the regularization parameter through L-curve

In this last section the choice of the regularization parameter and its effect on the reconstruction are examined. The configuration on which the λ has been determined is that presented in section 4.5.3.4, the one that leads to the best reconstruction: 14 cameras are arranged on two planes, 6 on the horizontal plane and 8 on the vertical one, the mask used is the most tailored (figure 4.23) and for each of the nine cases 2500 iterations have been carried out.

As described in the chapter state of art, in section 1.7.8.2, the approach is based on the minimization of the compound criterion:

$$\mathcal{J}(\rho) = \|A\rho - \varepsilon\|^2 - \lambda\mathcal{R}(\rho) \tag{4.5}$$

sum of the least-square criterion $\|A\rho - \varepsilon\|^2$ and the regularization term $\lambda\mathcal{R}(\rho)$, and it is strongly dependent on the regularization parameter $\lambda > 0$.

The regularization adopted is a first order Tikhonov and Arsenin (1977) regularization implemented by choosing the $\mathcal{L}2$ norm of the density spatial gradient as the regularization term, such as:

$$\mathcal{R}(\rho) = \|\bar{D}\rho\|^2 = -\rho^T \Delta\rho$$

where $\bar{D}$ is the up-winded discrete gradient operator and Δ the discrete Laplacian operator. The choice of this type of regularization leads to a well-known quadratic behaviour. While it helps the reconstruction by enforcing smoothness and reducing the effect of noise, it tends to over smooth the density discontinuities that may be present in the flow.

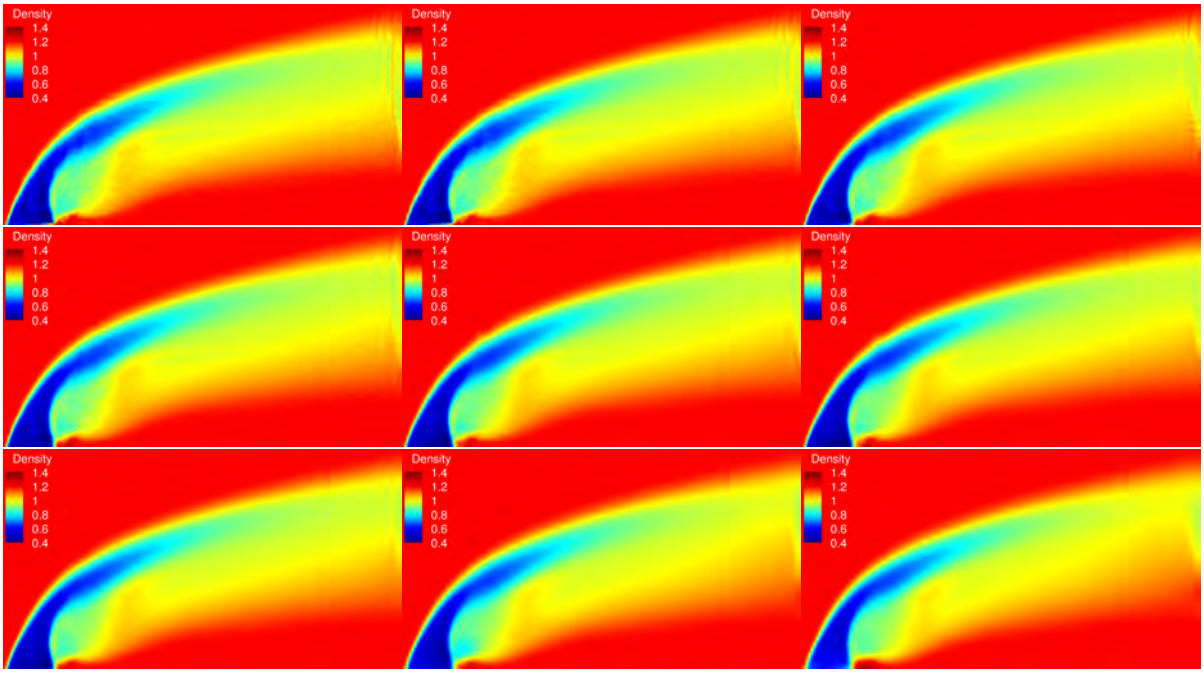

Figure 4.33. Different 3D BOS reconstructions using different regularization parameters λ: it increases from left to right and from top to bottom.

The effectiveness of the regularization is shown in the 9 reconstructions of figure 4.33 obtained with 9 different regularization parameters ($\lambda = 5 \times 10^{-7}$, 1×10^{-6}, 5×10^{-6}, 1×10^{-5}, 3×10^{-5}, 5×10^{-5}, 1×10^{-4}, 5×10^{-4} and 1×10^{-3}) chosen a priori. The regularization parameter increases from left to right and from top to bottom: the solution is smoothed by the quadratic regularization. The reconstructions obtained are quite stable despite the variation of the regularization parameter: this may be due to the fact that a very narrow mask and a large number of cameras with a rather low noise level added on synthetic deviations are used ($\sigma = 510\times10^{-5}$rad). The variations are quite limited but significant for very low (small oscillations) and very high (smoothing) regularization parameters.

To determine the optimal parameter of the regularization has been used the approach proposed by Hansen (1992) and recalled in Idier (2008). This method is known as L-curve from the shape of the plot that is obtained by plotting the gradient norm as a function of the data term for several density reconstructions obtained using various regularization parameters λ. Once the L-curve graph is traced a good choice for the optimum parameter corresponds to the point of maximum curvature. At this point both terms of the global criterion are close to their minimum and it is also proven to minimize the average risk in a quadratic setting.

In the present case looking at the curve of figure 4.34a, the point of maximum curvature of the L-curve is obtained for a value of $\lambda = 5\times10^{-5}$, this choice tends to balance the sensitivity of both terms of equation 4.5. At each point of the L-curve in figure 4.34a, obtained with a different regularization parameter λ, corresponds a reconstruction of figure 4.33. The reconstruction corresponding to the optimal point is the sixth (second row and third column), moreover other slices on different planes of the same reconstruction have been presented previously in section 4.5.3.4 figure 4.28.

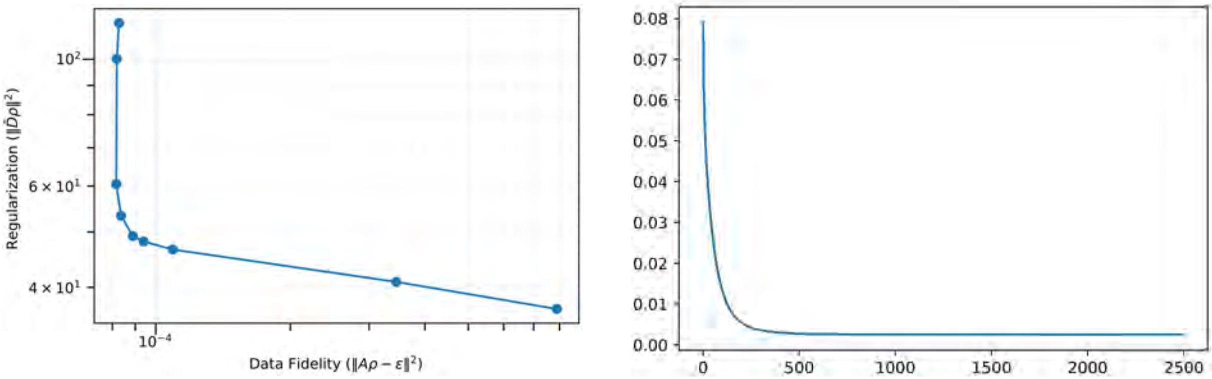

(a) L-curve **(b)** Global criterion convergence with $\lambda = 5\times10^{-5}$

Figure 4.34. The L-curve is obtained with 9 different regularisation values: $\lambda = 5\times10^{-7}$, 1×10^{-6}, 5×10^{-6}, 1×10^{-5}, 3×10^{-5}, 5×10^{-5}, 1×10^{-4}, 5×10^{-4} and 1×10^{-3}.

The former parametric study is quite computationally demanding as each run of 2500 iterations for a single parameter leads to 12h of computing time. Hence, we have decided to reuse the same parameter ($\lambda = 5\times10^{-5}$) for all our behavioural study (sec. 1.3-1.6). Indeed, as noticed in Nicolas (2017), the choice of the parameter mainly depends on the type of flow considered.

Looking at figure 4.34b it is observed that the global criterion converges quite quickly after about 500 iterations. Consideration of the global criterion hides the fact, that we have observed in a more detailed analysis of the convergence, that the two criteria of equations 4.5 behaves differently with the number of iterations. The data term converges quickly, while the term of regularization, after a first oscillation converges more slowly than the first one, after about 800 iterations. For this reason we have decided to perform 1000 iterations in the calculations presented above to make sure that we are at convergence without an excessive number of iterations.

4.6 Conclusion and perspectives

During the experimental campaign on a hot jet in cross-flow conducted in the F2 wind tunnel, different measurements have been made. Some of the results obtained through LDV, PIV, thermocouple and infrared measurement techniques and CFD are presented in section 4.3.2. Nevertheless, the chapter is dedicated to present the results obtained with 2D and 3D BOS measurements using retroreflective panels to ensure maximum spatial resolution.

In the preliminary part of the campaign, the 2D BOS has proved useful to go to adjust the parameters of the experiment such as temperature and mass flow rate of the jet and speed of the primary flow of the wind tunnel. The strong astigmatism in the BOS image has been used in our favour: in the presence of the jet the background formed by high-frequency pattern is no longer recognizable and becomes a more or less uniform gray spot (figure 4.9a). While this method has been useful for characterizing in real time the trajectory of the jet, flow-induced displacement measurements are impossible due to the lack of image correlation in the areas most affected by astigmatism (figure 4.9b). The relationship proposed by Kamotani and Greber (1972) is correctly superimposed on the acquisitions made with the 2D BOS.

In 3D BOS set up, with the help of retro-reflective backgrounds, the spatial resolution is significantly improved compared to the previous experience carried out by Nicolas et al. (2017c). In addition, the use of these backgrounds allows to work at higher f-numbers greatly reducing astigmatism and thus improving the image correlation quality. The choice of the arrangement of the cameras on a single plane (the horizontal one passing through the surface of the flat plate), imposed by the spatial configuration of the set-up, proved to be unsuitable to obtain a satisfactory 3D reconstruction of the jet. The use of a tight mask (Mask 3), obtained from PIV and thermocouple measurement, improved reconstruction, but not enough to restore internal flow structures.

Subsequently, with the 3D BOS simulations, it was possible to investigate factors on which it would not have been possible through experimental measurements. In particular, reconstruction process applied to a synthetic jet in cross flow according to different cameras layout highlights the key role of the points of view arrangement and the influence of the 3D mask.

Hence, through the two orthogonal planes configuration which has been presented in the beginning of the chapter, we can reconstruct correctly the typical geometries of this type of flow: the 3D reconstructions thus obtained are presented in Figure 4.26. When due to geometrical limitations it is not possible to arrange the cameras in an optimal way with respect to the flow geometry, it is impossible to reconstruct the jet correctly: in our case it was not possible to obtain a faithful reconstruction using the data acquired with the cameras arranged on a single plane (figure 4.11b).

Moreover, benefits of using an increased number of cameras are limited compared to the complexity and increase in the amount of data and calculation time needed to obtain a reconstruction with a larger number of cameras. Consequently, arrangement optimisation of the cameras is much more important than their number.

In this simulation study we also have shown the gain brought by a proper optimization of the 3D mask constructed from 2D mask, so as to respect smoothness and symmetries which are expected for the jet at hand.

Considering the need to place cameras in the vertical plane to obtain a correct reconstruction, I feel like proposing a technical solution that could be implemented in the future. The main problem is related to the positioning of the backgrounds: due to the presence of the flat plate it is impossible to position them on the walls of the wind tunnel, while placing them directly on the flat plate the distance between the background and the flow would be negligible and consequently the sensitivity of the measurement. The solution I propose is to equip the surface of the flat plate with a high light reflective film and position the BOS backgrounds at the level of the cameras. In this way the distance between the BOS background and the flow (l) is increased and a sensitivity different from zero is obtained. With this configuration it must be taken into account that the light passes twice through the flow and is then diverted twice: this changes the sensitivity of the measurement compared to a classic configuration.

A point to be studied in the future is how to eliminate those areas where the density is greater than the external density without having to define a "super-tailored" 3D mask.

During an experimental campaign there are not always additional informations such as a CFD computation or additional experimental measurements to design a tailored 3D mask around the flow. This leads to artefacts causing an incorrect 3D reconstruction. An example is the effect of quadratic regularisation that leads to non-physical areas, more precisely to points outside the jet where the density is higher than the external one. We would like to have a more adaptive method

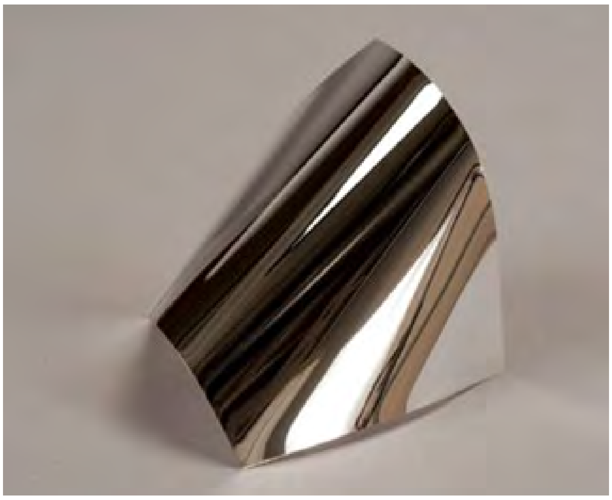

Figure 4.35. Film providing high specular reflection of visible light. (SirVisual ©)

according to a change in flow, in order to reduce the dependence of the 3D BOS reconstruction on the 3D mask. For this purpose, a total variation regularization L1L2 type could be studied ((Li et al. 2007), (Dong and Liu 2009) and (Zhao et al. 2010)). The criterion L1L2 is as follows:

$$\mathcal{J}(\rho) = \|\varepsilon - A\rho\|^2 + \lambda\sqrt{\|\nabla\rho\|^2 + \delta^2} \tag{4.6}$$

With this type of regularization it is necessary to choose two parameters: the regularisation parameter λ and the threshold associated with the transition from L1 to L2, δ: their choice results tricky and time costly to adjust.

An other promising way to gain access to 3D density and to overcome the current limitations of 3DBOS may be found in data assimilation techniques aiming at providing numerical simulations closely resembling the experimental data (Foures et al. 2014). This solution implies large cost of investment in numerical aspects, for the design of workable models and efficient optimization process.

Conclusion and perspectives

This study is part of the development of measurement methods for 3D flows visualisation in the domain of fluid mechanics. The purpose of these measurement techniques is to allow the validation of numerical computation codes or the study of complex phenomena inaccessible to current calculation codes. The optical methods that have been developed in recent years have enabled great progress to be made towards the acquisition of increasingly accurate and exhaustive data. This work focuses on the 3D BOS, a technique of high interest that has been a great success since its inception. The reasons for this are surely due to the simple set-up and implementation, but also to its ability to build large fields and the possibility of having a non-intrusive and quantitative measure. ONERA has developed this technique through the PhDs of Violaine Todoroff and Francois Nicolas and a team of experts in different fields. The system developed consists of 12 cameras thanks to which it is possible to reconstruct 3D instantaneous density fields. Thanks to the work of Nicolas, the possibility of its use in large wind tunnels has been demonstrated.

After a careful bibliographic study, some useful solutions for improving the spatial resolution of 3D BOS have been identified. These include retroreflective backgrounds, telecentric lenses and the use of speckle to generate the BOS background. In a classic BOS configuration, it is only by adjusting the lens aperture that the measurement resolution can be improved.

The use of retroreflective backgrounds allow to reflect as much light as possible and therefore to close the lens diaphragm at maximum. In our tests we gained a factor 16 in terms of light, being able to perform measurements at much higher $f_{\#}$ improving the resolution of the measurement. Retroreflective backgrounds have proved to be a valid solution to perform measurements with several 8 cameras without having to increase the aperture of the camera, thus obtaining instantaneous measurements of unsteady flows at high resolution (Chapter 3 and 4).

The theoretical study of the equations that characterize spatial resolution of telecentric lenses show that their use increases the resolution of the measurement only in certain specific conditions. Telecentric lens appears advantageous mainly for small flows (<100mm) and requires cameras with large sensors. Using such lenses in our experimental settings would have resulted in high costs and a difficult setup to adjust, so we did not explore this approach further.

During speckle tests we have shown how the use of the speckle introduces spurious displacements and degradation of the correlation scores. These two effects are caused by the change of shape and light intensity induced by the flow on the speckle pattern between a reference image and one with the flow. These changes are dependent on the type of flow observed: stronger density gradients lead to larger changes in the speckle, so measurements in the presence of strong gradients are almost impossible due to the great loss of confidence in the calculation of the displacements. The inline speckle setup was useful to understand that speckle pattern changes are not linked to the sensitivity of the measurement but are introduced by the flow itself. Thereafter, a classic BOS setup was compared to the double-pass speckle setup proposed by A. H. Meier and Roesgen (2013). In the configuration at hand, the effects introduced by the speckle on the measurement are important and the noise is high. It is therefore difficult to conclude if the double-pass speckle BOS setup brings improvements in the resolution of the measurement.

The experimental campaign that has been carried out on the F113 bench to study the under-expanded screeching jets brought a significant improvement on the spatial resolution, compared to the previous work of Nicolas et al. (2017a). This was achieved using retro-reflective backgrounds, yielding smaller lens apertures and reduced astigmatism effects. Specifically, the resolution for 3D measures has been improved to about 1mm compared to the 2.5mm obtained in the previous campaign. In addition, the 3D BOS measurements were coupled, for the first time, with acoustic measurements that were used for the analysis of the dynamics of the screech modes.

A first series of acoustic measurements was performed to characterise the screech frequencies and identify the various screech modes obtained with the present installation. In agreement with results reported in the literature, these measurements allowed to highlight a specificity of the present jet issued from a thick-lip nozzle: an earlier transition in terms of NPR between modes B and C, mode C extending over a larger range of NPR values and transition to mode D occurring at higher NPRs.

For modes A and C, an analysis of the phase-difference between microphones estimated using cross-power-spectral densities highlighted the axisymmetric and helical nature of these modes, respectively. For modes B and D that display more variability in time, the phase-differences between microphones suggested the presence of spinning and flapping modes. This appears to be in relative agreement with the literature but more analysis is required for mode B. For these 2 modes, examining only the average phase difference between microphones is likely inadequate to properly identify their dynamics and different techniques should be considered.

Satisfactory mean and instantaneous 3D density reconstructions were obtained, enabling analysis of the structure of the 3D shock cells such as determining the mean shock spacing (L_s) and the Mach disk diameter (D_{MD}).

Finally, relying on the BOS measurements, it was shown that the fluctuating density field associated with the main (average) instability wave driving screech for modes A1 and C could be satisfactorily isolated relying on the first two POD modes of the BOS displacement fields. The relevance of these isolated coherent structures in the description of the screech process was evidenced using acoustic measurements. For the first time to our knowledge, a clear 3D experimental visualization of the two modes A1 and C was obtained, displaying axisymmetric and helical structures.

During the experimental campaign on a hot jet in cross-flow conducted in the F2 wind tunnel, 2D and 3D BOS measurements have been carried out using retroreflective panels to ensure maximum spatial resolution. The 2D BOS has proved useful to adjust the parameters of the experiment such as temperature and mass flow rate of the jet and speed of the primary flow of the wind tunnel. The empirical equation to describe the location of the maximum temperature proposed by Kamotani and Greber (1972) is correctly superimposed on the acquisitions made with the 2D BOS.

The spatial resolution of the 3D BOS set up, with the help of retro-reflective backgrounds, is significantly improved compared to the previous experience carried out by Nicolas et al. (2017c). In addition, the use of these backgrounds allows to work at higher f-numbers greatly reducing astigmatism and thus improving the image correlation quality. The choice of the arrangement of the cameras on a single plane, imposed by the spatial configuration constraints, proved to be unsuitable to obtain a satisfactory 3D reconstruction of the jet. The use of an optimised 3D mask, obtained from PIV and thermocouple measurement, improved reconstruction, but not enough to restore internal flow structures.

Through 3D BOS simulations, it was possible to investigate factors on which it would not have been possible through experimental measurements. In particular, reconstruction process applied to a synthetic jet in cross flow according to different cameras layout highlights the key role of the points of view arrangement and the influence of the 3D mask. The main result here is that the two orthogonal planes configuration, makes it possible to reconstruct correctly the typical geometries of this type of flow.

Benefits of using an increased number of cameras are limited compared to the increase in the amount of data and calculation time needed to obtain a reconstruction.

Finally, through this simulation study we also have shown the gain brought to the the 3D BOS reconstruction by a proper optimization of the 3D mask with the use of CAD software, so as to respect smoothness and symmetries which are expected for the jet.

Perspectives

Regarding the acoustic data I acquired on the under-expanded screeching jets during this work, many advanced acoustic analyses are still possible. The methodology devised here to study the screech modes A and C using acoustic and BOS measurements was shown to provide clear insights into the structure of these modes. However, modes B and D appeared more difficult to analyse. Consequently, future work should intend to adapt this methodology to study these modes. One possible way could be to consider not only one camera to identify POD modes, but all the cameras at once. This approach might prove beneficial to study such modes.

As identified during the wind tunnel tests presented in Chapter 4, the arrangement of the cameras in the presence of a flow of complex geometry is vital to achieve a realistic 3D BOS reconstruction. In order to overcome space and geometrical constraints, it is necessary to find new original solutions in order to be able to position the cameras so as to obtain correct reconstructions. For example, one of these solutions is the one presented at the end of Chapter 4. It consists of equipping the surface of the flat plate with a high light reflective film and position the BOS backgrounds close to cameras. In this way the distance between the BOS background and the flow (l) is increased and a sensitivity different from zero is obtained. With this configuration it must be taken into account that the light passes twice through the flow and is then diverted twice: this changes the sensitivity of the measurement compared to a classic configuration.

Given the great influence of 3D masks that has been observed in Chapter 4, it is vital to review and find a method to make the reconstruction code less mask dependent. For this purpose, a total variation regularization L1L2 type could be studied (Li et al. (2007), Dong and Liu (2009) and Zhao et al. (2010)). This would allow to obtain good results even with masks not super tailored to the flow. With this type of regularization it is necessary to choose two parameters: the regularisation parameter λ and the threshold associated with the transition from L1 to L2, δ. Their choice can be tricky and time costly to adjust.

When, in addition to BOS acquisitions, other data from different techniques are present (PIV, LDV, CFD, thermocouple, infrared, pressure data), data assimilation techniques can be undertaken (Foures et al. 2014). In this way a number of limitations of 3D BOS could be overcome, but certainly at the cost of a large investment in numerical aspects, for the design of workable models and efficient optimization process.

Bibliography

Addy, A. L. (1981). “Effects of axisymmetric sonic nozzle geometry on Mach disk characteristics”. In: *AIAA Journal* 19.1, pp. 121–122. DOI: `10.2514/3.7751` (cit. on pp. 96, 98).

Ahuja, K., K. Massey, M. D’Agostino, K. Ahuja, K. Massey, and M. D’Agostino (1997). “Flow/acoustic interactions in open-jet wind tunnels”. In: *3rd AIAA/CEAS Aeroacoustics Conference*, p. 1691 (cit. on p. 88).

André, B. (2012). “Etude expérimentale de l’effet du vol sur le bruit de choc de jets supersoniques sous-détendus”. PhD thesis (cit. on p. 86).

Aoki, T., Y.-H. Kweon, Y. Miyazato, H.-D. Kim, and T. Setoguchi (2006). “An experimental study of the nozzle lip thickness effect on supersonic jet screech tones”. In: *Journal of Mechanical Science and Technology* 20.4, pp. 522–532. DOI: `10.1007/bf02916483` (cit. on p. 88).

Assunção, T. L. de (2018). “Experimental study of underexpanded round jets: nozzle lip thickness effects and screech closure mechanisms investigation”. PhD thesis (cit. on pp. 88, 89).

Atcheson, B., W. Heidrich, and I. Ihrke (2009). “An evaluation of optical flow algorithms for background oriented schlieren imaging”. In: *Experiments in Fluids* 46, pp. 467–476 (cit. on pp. 24, 25).

Atcheson, B., I. Ihrke, W. Heidrich, A. Tevs, D. Bradley, M. Magnor, and H. Seidel (2008). “Time-resolved 3D Capture of Non-stationary Gas Flows”. In: *ACM Transactions on Graphics (Proc. SIGGRAPH Asia)* 27.5, p. 132 (cit. on pp. xx, 17, 18, 29, 34, 37).

Augenstein, E., F. Leopold, H. Richard, and M. Raffel (2001). “Schlieren Techniques in Comparison: The Background Oriented Method versus Visualization with Holographic Filters”. In: (cit. on p. 29).

Aupoix, B. (2010). “Couches Limites Bidimensionnelles Compressibles. Descriptif et Mode D’emploi du Code CLICET—Version 2010”. In: *ONERA, Octobre, Technical Report No. RT* 1, p. 117015 (cit. on p. 111).

Barthe, C. (2006). “Etude Aérothermique de Jets Supersoniques Chauds.” MA thesis. SUPAERO (cit. on p. 17).

Bauknecht, A., C. B. Merz, and M. Raffel (2014a). “Airborne Application of the Background Oriented Schlieren Technique to a Helicopter in Forward Flight”. In: *Lisbon* (cit. on p. 26).

Bauknecht, A., C. B. Merz, M. Raffel, A. Landolt, and A. H. Meier (2014b). “Blade-tip vortex detection in maneuvering flight using the background-oriented schlieren technique”. In: *Journal of Aircraft* 51.6, pp. 2005–2014 (cit. on p. 25).

Bencs, P., S. Szabó, R. Bordás, K. Zähringer, and D. Thévenin (2011). “Synchronization of particle image velocimetry and background oriented schlieren measurement techniques”. In: *Proc. 8th Pacific Symposium on Flow Visualization and Image Processing*, pp. 1–6 (cit. on p. 30).

Berger, C. (2002). “Design of telecentric imaging systems for noncontact velocity sensors”. In: *Optical Engineering* 41.10, pp. 2599–2607 (cit. on p. 52).

Bichal, A. and B. Thurow (2013). “On the application of background oriented schlieren for wavefront sensing”. In: *Measurement Science and Technology* 25.1, p. 015001 (cit. on pp. 18, 24).

Bichal, A. (2015). “Development of 3D background oriented schlieren with a plenoptic camera”. PhD thesis (cit. on p. 32).

Buhlmann, P. (2020). “Laser Speckle Background Oriented Schlieren Imaging for Near-Wall Measurements”. PhD thesis. ETH Zurich (cit. on pp. 44, 69).

Callaghan, E. E. (1948). *Investigation of the penetration of an air jet directed perpendicularly to an air stream.* Vol. 1615. National Advisory Committee for Aeronautics (cit. on p. 109).

Champagnat, F., A. Plyer, G. Le Besnerais, S. Davoust, and Y. Le Sant (2011). “Fast and Accurate PIV computation using highly parallel iterative correlation maximization”. In: *Experiment in Fluids* 50, pp. 1169–1182 (cit. on p. 34).

Cozzi, F., E. Göttlich, L. Angelucci, V. Dossena, and A. Guardone (2017). “Development of a background-oriented schlieren technique with telecentric lenses for supersonic flow”. In: *Journal of Physics: Conference Series* 778.1, p. 012006 (cit. on pp. 25, 31, 44, 51, 52, 58, 60).

Dalziel, S., G. Hughes, and B. Sutherland (2000). “Whole-field density measurements by ’synthetic schlieren’”. In: *Experiment in Fluids* 28, pp. 322–335 (cit. on pp. xx, 16).

Davies, M. and D. Oldfield (1962). “Tones from a choked axisymmetric jet. I. Cell structure, eddy velocity and source locations”. In: *Acta Acustica united with Acustica* 12.4, pp. 257–267 (cit. on p. 86).

Debrus, S., M. Francon, C. Grover, M. May, and M. Roblin (1972). “Ground glass differential interferometer”. In: *Applied optics* 11.4, pp. 853–857 (cit. on p. 15).

Desse, J. (2002). “Real-time color holographic interferometry”. In: *Applied Optics* 41, pp. 5326–5333 (cit. on p. 10).

Desse, J. and J. Tribillon (2009). “real-time three-color holographic interferometer”. In: *Applied Optics* 48, pp. 6870–6877 (cit. on p. 10).

Dong, F. and Z. Liu (2009). “A new gradient fidelity term for avoiding staircasing effect”. In: *Journal of Computer Science and Technology* 24, pp. 1162–1170 (cit. on pp. 147, 151).

Donjat, D., F. Nicolas, O. Leon, F. Micheli, G. Le Besnerais, and F. Champagnat (2017). “Exploration of Under-Expanded Free and Impinging Supersonic Jet Flows”. In: *International Symposium on Shock Waves.* Springer, pp. 1163–1170 (cit. on p. 85).

Edgington-Mitchell, D. (2019). “Aeroacoustic resonance and self-excitation in screeching and impinging supersonic jets – A review”. In: *International Journal of Aeroacoustics* 18.2-3, pp. 118–188. DOI: `10.1177/1475472x19834521` (cit. on p. 87).

Edgington-Mitchell, D., V. Jaunet, P. Jordan, A. Towne, J. Soria, and D. Honnery (2018). “Upstream-travelling acoustic jet modes as a closure mechanism for screech”. In: *Journal of Fluid Mechanics* 855. DOI: `10.1017/jfm.2018.642` (cit. on pp. 87, 100).

Edgington-Mitchell, D., K. Oberleithner, D. Honnery, and J. Soria (2014). “Coherent structure and sound production in the helical mode of a screeching axisymmetric jet”. In: *Journal of Fluid Mechanics* 748, pp. 822–847. DOI: `10.1017/jfm.2014.173` (cit. on pp. 98, 101).

Elsinga, G., B. Van Oudheusden, F. Scarano, and D. Watt (2004). “Assessment and application of quantitative schlieren methods: Calibrated color schlieren and background oriented schlieren”. In: *Experiments in Fluids* 36.2, pp. 309–325 (cit. on pp. 17, 25).

Fomin, N., E. Lavinskaya, and K. Takayama (2006). “Limited projections laser speckle tomography of complex flows”. In: *Optics and lasers in engineering* 44.3, pp. 335–349 (cit. on p. 16).

Foures, D., N. Dovetta, D. Sipp, and P. J. Schmid (2014). “A data-assimilation method for Reynolds-averaged Navier–Stokes-driven mean flow reconstruction”. In: (cit. on pp. 147, 151).

Franquet, E., V. Perrier, S. Gibout, and P. Bruel (2015). “Free underexpanded jets in a quiescent medium: A review”. In: *Progress in Aerospace Sciences* 77, pp. 25–53 (cit. on p. 84).

Fric, T. and A. Roshko (1994). “Vortical structure in the wake of a transverse jet”. In: *Journal of Fluid Mechanics* 279, pp. 1–47 (cit. on p. 110).

Gajan, P., A. Strzelecki, and A. Bontemps (1995). “Etude bibliographique sur les conditionneurs d’écoulements.” In: *ONERA, RT 1/2590-00/dermes.* 1, p. 117015 (cit. on p. 113).

Gojani, A. B., B. Kamishi, and S. Obayashi (2013). “Measurement sensitivity and resolution for background oriented schlieren during image recording”. In: *Journal of Visualization* 16.3, pp. 201–207. DOI: `10.1007/s12650-013-0170-5` (cit. on pp. 18, 20, 21).

Gojon, R., C. Bogey, and M. Mihaescu (2018). “Oscillation Modes in Screeching Jets”. In: *AIAA Journal* 56.7, pp. 2918–2924. DOI: `10.2514/1.j056936` (cit. on p. 87).

Goldhahn, E. and J. Seume (2007). “The background oriented schlieren technique: sensitivity, accuracy, resolution and application to a three-dimensional density field”. In: *Experiments in Fluids* 43, pp. 241–249 (cit. on pp. 17, 18).

Goodman, J. W. (2007). *Speckle phenomena in optics: theory and applications.* Roberts and Company Publishers (cit. on pp. 62, 63).

Hansen, P. C. (1992). “Analysis of discrete ill-posed problems by means of the L-curve”. In: *SIAM review* 34.4, pp. 561–580 (cit. on pp. 37, 144).

Hargather, M. and G. Settles (2010a). “Natural-background-oriented schlieren imaging”. In: *Experiments in Fluids* 48 (1), pp. 59–68 (cit. on p. 17).

— (2010b). “Natural-background-oriented schlieren imaging”. In: *Experiments in Fluids* 48 (1), pp. 59–68 (cit. on p. 26).

Hargather, M. J., G. S. Settles, and M. J. Madalis (2010). “Schlieren imaging of loud sounds and weak shock waves in air near the limit of visibility”. In: *Shock Waves* 20.1, pp. 9–17 (cit. on p. 14).

Harms, L. (1974). *Experimental Investigation of the Flow Field of a Hot Turbulent Jet With Lateral Flow.* NASA (cit. on p. 110).

Heineck, J. T., D. Banks, E. T. Schairer, E. A. Haering, and P. Bean (2016). “Background oriented schlieren (BOS) of a supersonic aircraft in flight”. In: *AIAA Flight Testing Conference*, p. 3356 (cit. on pp. 25, 28).

Heineck, J. T., E. T. Schairer, L. Walker, and L. Kushner (2010). “Retroreflective background oriented schlieren (rbos)”. In: (cit. on pp. 25, 30).

Hernandez, R., B. Heine, O. Schneider, P. Chernukha, and M. Raffel (2013). “Visualization and Computation of Quantified Density Data of the Rotor Blade Tip Vortex”. In: *New Results in Numerical and Experimental Fluid Mechanics VIII.* Springer, pp. 321–329 (cit. on p. 30).

Howes, W. L. (1983). “Rainbow schlieren”. In: (cit. on p. 14).

Idier, J. (2008). *Bayesian Approach to Inverse Problems.* Ed. by J. Idier (cit. on p. 144).

Iffa, E., A. Aziz, and A. Malik (2011). “Velocity field measurement of a round jet using quantitative schlieren”. In: *Applied Optics* 50, pp. 618–625 (cit. on p. 17).

Ihrke, I. and M. Magnor (2004). “Image-Based Tomographic Reconstruction of Flames”. In: *Eurographics/ACM SIGGRAPH Symposium on Computer Animation.* Ed. by D. P. R. Boulic (cit. on p. 37).

Ihrke, I. (2008). “Reconstruction and rendering of time varying natural phenomena.” PhD thesis. Saarland University (cit. on pp. xx, 18, 38).

Jin, J., I. V. Mursenkova, N. Sysoev, N. A. Vinnichenko, I. A. Znamenskaya, and F. N. Glazyrin (2011). “Experimental investigation of blast waves from plasma sheet using the background oriented schlieren and shadow methods”. In: *Journal of Flow Visualization and Image Processing* 18.4 (cit. on p. 29).

Kamotani, Y. and I. Greber (1972). “Experiments on a turbulent jet in a cross flow”. In: *AIAA journal* 10.11, pp. 1425–1429 (cit. on pp. 110, 122, 124, 146, 150).

Keagy Jr, W. and H. Ellis (1948). “The application of the schlieren method to the quantitative measurement of mixing gases in jets”. In: *Symposium on Combustion and Flame, and Explosion Phenomena.* Vol. 3. 1. Elsevier, pp. 667–674 (cit. on p. 47).

Kelso, R. M., T. Lim, and A. Perry (1996). “An experimental study of round jets in cross-flow”. In: *Journal of fluid mechanics* 306, pp. 111–144 (cit. on p. 109).

Kindler, K., E. Goldhahn, F. Leopold, and M. Raffel (2007). “Recent developments in background oriented Schlieren methods for rotor blade tip vortex measurements”. In: *Experiments in Fluids* 43 (2). 10.1007/s00348-007-0328-9, pp. 233–240 (cit. on p. 26).

Kirmse, T., J. Agocs, A. Schröder, J. M. Schramm, S. Karl, and K. Hannemann (2011). “Application of particle image velocimetry and the background-oriented schlieren technique in the high-enthalpy shock tunnel Göttingen”. In: *Shock waves* 21.3, pp. 233–241 (cit. on pp. 18, 20, 22, 29, 42).

Klemkowsky, J. N., T. W. Fahringer, C. J. Clifford, B. F. Bathel, and B. S. Thurow (2017). “Plenoptic background oriented schlieren imaging”. In: *Measurement Science and Technology* 28.9, p. 095404 (cit. on pp. 31, 32).

Klinge, F., T. Kirmse, and J. Kompenhans (2003). “Application of quantitative Background Oriented Schlieren (BOS): Investigation of a wing tip vortex in a transonic windtunnel”. In: (cit. on p. 17).

Ko, H. S., S. S. Ahn, and H. J. Kim (2011). “Measurement of impinging butane flame using combined optical system with digital speckle tomography”. In: *Optics and Lasers in Engineering* 49.11, pp. 1320–1329 (cit. on pp. 16, 18).

Kumar, R., M. Y. Ali, F. S. Alvi, and L. Venkatakrishnan (2011). “Generation and control of oblique shocks using microjets”. In: *AIAA journal* 49.12, pp. 2751–2759 (cit. on p. 29).

Le Sant, Y. (2001). “Afix 2: an image processing software for wind tunnel applications”. In: *ONERA–The French Aerospace Lab TR* 211, p. 05458 (cit. on p. 115).

Le Sant, Y., V. Todoroff, A. Bernard-Brunel, G. Le Besnerais, F. Micheli, and D. Donjat (2014). “Multi-camera calibration for 3DBOS”. In: *17th International Symposium on Applications of Laser Techniques to Fluid Mechanics* (cit. on pp. 34, 121).

Leopold, F. (2007). “The Application of the Colored Background Oriented Schlieren Technique (CBOS) to Free-Flight and In-Flight Measurements”. In: *Instrumentation in Aerospace Simulation Facilities, 2007. ICIASF 2007. 22nd International Congress on.* IEEE, pp. 1–10 (cit. on pp. 25, 26).

Leopold, F., F. Jagusinski, C. Demeautis, M. Ota, and D. Klatt (2012). “Increase of accuracy for CBOS by background projection”. In: *Proceedings of 15th international symposium on flow visualization (ISFV15-087), Minsk, Belarus* (cit. on pp. 23, 52).

Leopold, F., M. Ota, D. Klatt, and K. Maeno (2013). “Reconstruction of the Unsteady Supersonic Flow around a Spike Using the Colored Background Oriented Schlieren Technique”. In: *Journal of Flow Control, Measurement & Visualization* 1, pp. 69–76 (cit. on pp. 17, 26, 31, 35, 51).

Li, F., C. Shen, J. Fan, and C. Shen (2007). “Image restoration combining a total variational filter and a fourth-order filter”. In: *Journal of Visual Communication and Image representation* 18, pp. 322–330 (cit. on pp. 147, 151).

Loose, S., H. Richard, M. Dewhirst, and M. Raffel (2000). “Background oriented schlieren (BOS) and particle image velocimetry (PIV) applied for transonic turbine blade investigations.” In: *10th International Symposium on Applications of Laser Techniques to Fluid Mechanics, Lisbon, Portugal* (cit. on p. 17).

Mahesh, K. (2013). “The interaction of jets with crossflow”. In: *Annual review of fluid mechanics* 45, pp. 379–407 (cit. on p. 109).

Margason, R. J. (1993). “Fifty years of jet in cross flow research”. In: *ceaj* (cit. on p. 109).

Meier, A. H. and T. Roesgen (2013). “Improved background oriented schlieren imaging using laser speckle illumination”. In: *Experiments in fluids* 54.6, p. 1549 (cit. on pp. 27, 28, 44, 61, 63–66, 69, 80, 149).

Meier, G. (2002). “Computerized background-oriented schlieren”. In: *Experiments in Fluids* 33.1, pp. 181–187 (cit. on p. 16).

Merle, M. (1956). “SUR LA FREQUENCE DES ONDES SONORES EMISES PAR UN JET DAIR A GRANDE VITESSE”. In: *COMPTES RENDUS HEBDOMADAIRES DES SEANCES DE L ACADEMIE DES SCIENCES* 243.5, pp. 490–493 (cit. on p. 86).

Michalski, Q., C. J. B. Parejo, A. Claverie, J. Sotton, and M. Bellenoue (2018). “An application of speckle-based background oriented schlieren for optical calorimetry”. In: *Experimental Thermal and Fluid Science* 91, pp. 470–478 (cit. on p. 76).

Mizukaki, T., K. Wakabayashi, T. Matsumura, and K. Nakayama (2013). “Background-oriented schlieren with natural background for quantitative visualization of open-air explosions”. In: *Shock Waves*, pp. 1–10 (cit. on p. 25).

Nicolas, F., D. Donjat, O. Léon, G. L. Besnerais, F. Champagnat, and F. Micheli (2017a). “3D reconstruction of a compressible flow by synchronized multi-camera BOS”. In: *Experiments in Fluids* 58.5. DOI: `10.1007/s00348-017-2325-y` (cit. on pp. 84, 85, 96, 98, 105, 150).

Nicolas, F., V. Todoroff, A. Plyer, G. Le Besnerais, D. Donjat, F. Micheli, F. Champagnat, P. Cornic, and Y. Le Sant (2016). “A direct approach for instantaneous 3D density field reconstruction from background-oriented schlieren (BOS) measurements”. In: *Experiments in fluids* 57.1, p. 13 (cit. on pp. 29, 33, 36, 42, 44, 119, 120, 128).

Nicolas, F. (2017). “Reconstruction de champs instantanés de masse volumique par BOS 3D. Applications à l’étude d’écoulements complexes en grande soufflerie”. PhD thesis. Toulouse, ISAE (cit. on pp. xx, 21, 32, 34–36, 139, 145).

Nicolas, F., D. Donjat, O. Léon, G. Le Besnerais, F. Champagnat, and F. Micheli (2017b). “3D reconstruction of a compressible flow by synchronized multi-camera BOS”. In: *Experiments in Fluids* 58.5, p. 46 (cit. on pp. 39, 42, 43, 84).

Nicolas, F., D. Donjat, A. Plyer, F. Champagnat, G. Le Besnerais, F. Micheli, P. Cornic, Y. Le Sant, and J. Deluc (2017c). “Experimental study of a co-flowing jet in ONERA’s F2 research wind tunnel by 3D background oriented schlieren”. In: *Measurement Science and Technology* 28.8, p. 085302 (cit. on pp. 22, 29, 42, 121, 146, 150).

Nocedal, J. and S. Wright (1999). *Numerical Optimization*. Ed. by P. Glynn. Springer (cit. on p. 37).

Norum, T. D. (1983). “Screech suppression in supersonic jets”. In: *AIAA Journal* 21.2, pp. 235–240. DOI: `10.2514/3.8059` (cit. on p. 88).

Norum, T. D. and J. G. Shearin (1984). “Effects of simulated flight on the structure and noise of underexpanded jets”. In: (cit. on p. 87).

Olchewsky, F. (2017). “Caractérisation des écoulements instationnaires 3D par tomographie holographique numérique multidirectionnelle”. PhD thesis (cit. on p. 9).

Olchewsky, F., J.-M. Desse, D. Donjat, and F. Champagnat (2019). “Vertical digital holographic bench for underexpanded jet gas density reconstruction”. In: *Digital Holography and Three-Dimensional Imaging*. Optical Society of America, Th2B–3 (cit. on p. 10).

Olchewsky, F., Z. Essaidi, J.-M. Desse, and F. Champagnat (2018a). “3D reconstructions of jets by multidirectional digital holographic tomography”. In: *Proceedings 18th International Symposium on Flow Visualization*. ETH Zurich (cit. on p. 11).

Olchewsky, F., J.-M. Desse, et al. (2018b). “Multidirectional holographic interferometer for 3D gas density reconstruction”. In: *3D Image Acquisition and Display: Technology, Perception and Applications.* Optical Society of America, 3W5G–4 (cit. on p. 18).

Ota, M., K. Hamada, H. Kato, and K. Maeno (2011). “Computed-tomographic density measurement of supersonic flow field by colored-grid background oriented schlieren (CGBOS) technique”. In: *Measurement Science and Technology* 22, pp. 104–111 (cit. on pp. 18, 26, 27, 35).

Ota, M., H. Kato, and K. Maeno (2012). “Three-dimensional density measurement of supersonic and axisymmetric flow field by colored grid background oriented schlieren (CGBOS) technique”. In: *International Journal of Aerospace Innovations* 4.1-2, pp. 1–12 (cit. on p. 35).

Ota, M., F. Leopold, R. Noda, and K. Maeno (2015). “Improvement in spatial resolution of background-oriented schlieren technique by introducing a telecentric optical system and its application to supersonic flow”. In: *Experiments in Fluids* 56.3, p. 48 (cit. on pp. 20, 21, 31, 51, 52, 54).

Ota, M. and K. Maeno (2008). “A trial of density measurement of supersonic flow in shock tunnel experiment by specially structured background oriented schlieren (SSBOS) technique”. In: (cit. on p. 17).

Paysant, R., E. Laroche, P. Millan, and P. Buet (2020). “RANS modelling of a high temperature jet in crossflow: from eddy viscosity models to advanced anisotropic approaches”. In: THMT 10, St Petersbourg (cit. on pp. 126, 127).

Pérez, J.-P. (2000). *Optique. Fondements et applications.* Ed. by M. Sciences. Dunod (cit. on pp. 4, 6).

Ponton, M. K. and J. M. Seiner (1995). “Acoustic study of B helical mode for choked axisymmetric nozzle”. In: *AIAA Journal* 33.3, pp. 413–420. DOI: `10.2514/3.12402` (cit. on pp. 86, 96).

Ponton, M. and J. Seiner (1992). “The effects of nozzle exit lip thickness on plume resonance”. In: *Journal of Sound and Vibration* 154.3, pp. 531–549. DOI: `10.1016/0022-460x(92)90784-u` (cit. on pp. 88, 93, 94).

Powell, A. (1953). “On the Mechanism of Choked Jet Noise”. In: *Proceedings of the Physical Society. Section B* 66.12, pp. 1039–1056. DOI: `10.1088/0370-1301/66/12/306` (cit. on pp. 86–88, 93, 94).

Powell, A., Y. Umeda, and R. Ishii (1990). “The screech of round choked jets, revisited”. In: *13th Aeroacoustics Conference*, p. 3980 (cit. on pp. 87, 94).

Powell, A., Y. Umeda, and R. Ishii (1992). “Observations of the oscillation modes of choked circular jets”. In: *The Journal of the Acoustical Society of America* 92.5, pp. 2823–2836 (cit. on pp. 86, 96).

Rabal, H. J. and R. A. Braga Jr (2018). *Dynamic laser speckle and applications.* CRC press (cit. on p. 62).

Raffel, M. (2015). “Background-oriented schlieren (BOS) techniques”. In: *Experiments in Fluids* 56.3, pp. 1–17 (cit. on p. 16).

Raffel, M., J. Heineck, E. Schairer, F. Leopold, and K. Kindler (2014). “Background-Oriented Schlieren Imaging for Full-Scale and In-Flight Testing”. In: *Journal of the American Helicopter Society* 59.1, pp. 1–9 (cit. on pp. 17, 25, 26).

Raffel, M., H. Richard, and G. Meier (2000a). “On the applicability of background oriented optical tomography for large scale aerodynamic investigations”. In: *Experiments in Fluids* 28.5, pp. 477–481 (cit. on pp. xx, 16).

Raffel, M., H. Richard, Y. Yu, and G. Meier (2000b). “Background Oriented Stereoscopic Schlieren (BOSS) for full scale helicopter vortex characterization”. In: *In 9th international symposium on flow visualization.* Heriot-Watt University, Edinburgh, UK (cit. on p. 16).

Raffel, M., C. E. Willert, F. Scarano, C. J. Kähler, S. T. Wereley, and J. Kompenhans (2018). *Particle image velocimetry: a practical guide.* Springer (cit. on p. 24).

Raman, G. (1997). "Cessation of screech in underexpanded jets". In: *Journal of Fluid Mechanics* 336, pp. 69–90. DOI: `10.1017/s002211209600451x` (cit. on p. 88).

— (1998). "Advances in understanding supersonic jet screech: Review and perspective". In: *Progress in aerospace sciences* 34.1-2, pp. 45–106 (cit. on p. 86).

Ramanah, D., S.Raghunath, D. Mee, T.Rösgen, and P. Jacobs (2007). "Background oriented schlieren for flow visualisation in hypersonic impulse facilities". In: *Shock waves* 17, pp. 65–70 (cit. on pp. 25, 29).

Richard, H. and M. Raffel (2001). "Principle and applications of the background oriented schlieren (BOS) method". In: *Measurement Science and Technology* 12, pp. 1576–1585 (cit. on pp. 25, 29).

Rouser, K., P. King, F. Schauer, R. Sondergaard, L. Goss, and J. Hoke (2011). "Time-accurate flow field and rotor speed measurements of a pulsed detonation driven turbine". In: *49th AIAA Aerospace Sciences Meeting including the New Horizons Forum and Aerospace Exposition*, p. 577 (cit. on p. 29).

Schairer, E., L. K. Kushner, and J. T. Heineck (2013). "Measurements of tip vortices from a full-Scale UH-60A rotor by retro-reflective background oriented schlieren and stereo photogrammetry". In: (cit. on p. 30).

Schardin, H. (1942). "Die schlierenverfahren und ihre anwendungen". In: *Ergebnisse der exakten Naturwissenschaften.* Springer, pp. 303–439 (cit. on p. 12).

Schröder, A., R. Geisler, D. Schanz, J. Agocs, D. Pallek, M. Schroll, J. Klinner, M. Beversdorff, M. Voges, and C. Willert (2014). "Application of image based measurement techniques for the investigation of aeroengine performance on a commercial aircraft in ground operation". In: *17th International Symposium on Applications of Laser Techniques to Mechanics, Lisbon, Portugal, July*, pp. 7–10 (cit. on pp. 24, 25).

Settles, G. S. (2018). "Smartphone schlieren and shadowgraph imaging". In: *Optics and Lasers in Engineering* 104, pp. 9–21 (cit. on p. 17).

Settles, G. S., T. Grumstrup, J. Miller, M. Hargather, L. Dodson, and J. Gatto (2005). "Full-scale high-speed "Edgerton" retroreflective shadowgraphy of explosions and gunshots". In: *Fifth Pacific Symposium on Flow Visualisation and Image Processing* (cit. on p. 70).

Settles, G. (2001). *Schlieren and Shadowgraph Techniques: Visualizing Phenomena in Transparent Media.* Ed. by Springer (cit. on pp. 12, 46).

Shen, H. and C. K. W. Tam (2000). "Effects of Jet Temperature and Nozzle-Lip Thickness on Screech Tones". In: *AIAA Journal* 38.5, pp. 762–767. DOI: `10.2514/2.1055` (cit. on p. 88).

Shen, H. and C. K. Tam (2002). "Three-dimensional numerical simulation of the jet screech phenomenon". In: *AIAA journal* 40.1, pp. 33–41 (cit. on p. 87).

Sirovich, L. (1987). "Turbulence and the dynamics of coherent structures. I. Coherent structures". In: *Quarterly of applied mathematics* 45.3, pp. 561–571 (cit. on p. 99).

Sivasubramanian, M., R. Cole, and P. Sukanek (1984). "Optical temperature gradient measurements using speckle photography". In: *International journal of heat and mass transfer* 27.5, pp. 773–780 (cit. on p. 15).

Sourgen, F., F. Leopold, and D. Klatt (2012). "Reconstruction of the density field using the colored background oriented schlieren technique (CBOS)". In: *Optics and Lasers in Engineering* 50.1, pp. 29–38 (cit. on p. 18).

Tam, C. K. and F. Q. Hu (1989). "On the three families of instability waves of high-speed jets". In: *Journal of Fluid Mechanics* 201, pp. 447–483 (cit. on p. 87).

Tam, C. K. and H. Tanna (1982). "Shock associated noise of supersonic jets from convergent-divergent nozzles". In: *Journal of Sound and Vibration* 81.3, pp. 337–358 (cit. on p. 85).

Tam, C., J. Seiner, and J. Yu (1986). "Proposed relationship between broadband shock associated noise and screech tones". In: *Journal of Sound and Vibration* 110.2, pp. 309–321. DOI: `10.1016/s0022-460x(86)80212-7` (cit. on p. 93).

Tikhonov, A. and V. Arsenin (1977). *Solutions of ill-posed problems*. Winston (cit. on pp. 36, 144).

Todoroff, V. (2013). "Mesure d'un champ de masse volumique par Background Oriented Schlieren 3d. Etude d'un dispositif expérimental et des méthodes de traitement pour la résolution du problème inverse." PhD thesis (cit. on pp. xx, 32, 139).

Todoroff, V., G. Le Besnerais, D. Donjat, F. Micheli, A. Plyer, and F. Champagnat (2014). "Reconstruction of instantaneous 3D flow density fields by a new direct regularized 3DBOS method". In: *Int. Symp. on Applications of Laser Techniques to Fluid Mechanic, Lisbon* (cit. on pp. 35, 36).

Tropea, C., A. Yaris, and J. Foss, eds. (2006). *Handbook of experimental fluid mechanics*. Springer (cit. on pp. 8–11, 13).

Venkatakrishnan, L. (2005). "Density measurements in an axisymmetric underexpanded jet by background-oriented schlieren technique". In: *AIAA journal* 43.7, pp. 1574–1579 (cit. on p. 29).

Venkatakrishnan, L. and P. Suriyanarayanan (2009). "Density field of supersonic separated flow past an afterbody nozzle using tomographic reconstruction of BOS data". In: *Experiments in Fluids* 47.3, pp. 463–473 (cit. on p. 17).

Venkatakrishnan, L., P. Suriyanarayanan, and G. Jagadeesh (2013). "Density field visualization of a Micro-explosion using background-oriented schlieren". In: *Journal of visualization* 16.3, pp. 177–180 (cit. on p. 29).

Vinnichenko, N., A. Uvarov, and Y. Plaksina (2012). "Accuracy of background oriented schlieren for different background patterns and means of refraction index reconstruction". In: *15th International Symposium on Flow Visualization* (cit. on p. 25).

Walker, S. H. and F. O. Thomas (1997). "Experiments characterizing nonlinear shear layer dynamics in a supersonic rectangular jet undergoing screech". In: *Physics of Fluids* 9.9, pp. 2562–2579 (cit. on p. 88).

Weinstein, L. M. (1994). "An optical technique for examining aircraft shock wave structures in flight". In: (cit. on p. 28).

Wernekinck, U. and W. Merzkirch (1987). "Speckle photography of spatially extended refractive-index fields". In: *Applied optics* 26.1, pp. 31–32 (cit. on p. 15).

Williams, J. and M. N. Wood (1965). *Aerodynamic Interference Effects with Jet-lift Schemes on V/STOL Aircraft at Forward Speeds*. RAE (cit. on p. 110).

Wilson, S., G. Gustafson, D. Lincoln, K. Murari, and C. Johansen (2015). "Performance evaluation of an overdriven LED for high-speed schlieren imaging". In: *Journal of Visualization* 18.1, pp. 35–45 (cit. on p. 30).

Yamamoto, S., Y. Tagawa, and M. Kameda (2014). "The evolution of a shock wave pressure induced by a laser pulse in a liquid filled thin tube using the background-oriented schlieren technique". In: *Lisbonne* (cit. on p. 29).

Zhao, F., M. Shi, and T. Xu (2010). "A new image restoration model based on the adaptive total variation". In: *2010 International Conference on Digital Manufacturing and Automation* (cit. on pp. 147, 151).